PROGRAMA DE DOUTORAMENTO EM ENGENHARIA MECÂNICA

U.PORTO

FEUP FACULDADE DE ENGENHARIA
UNIVERSIDADE DO PORTO

Non-linear Vibrations of Tow Placed Variable Stiffness Composite Laminates

Hamed Akhavan

Doctoral Program in Mechanical Engineering

Supervisor: Pedro Manuel Leal Ribeiro

October 2015

Abstract

Vibrations of structures and mechanical systems have plenty of advantages, but also disadvantages. Notably, vibrations can lead to failures or damage of equipment. Therefore, knowing more about the vibratory behaviour helps engineers to control damage and to take preventive measures in order to avoid damages or malfunctions.

For a long time, optimising material properties was a goal in material design. An important aspect in the optimisation of fibrous composite materials is the fibre angles in different layers of the laminate. In traditional composite laminates, the fibre orientation is constant in a ply, but some researchers paid attention to the possibility of changing the fibre orientation angle inside a ply. A laminate with plies which have curvilinear fibre paths is considered as a variable stiffness composite laminate (VSCL). Due to the variation of in-plane stiffness in a VSCL, these laminates find special applications in naval, aerospace, or other structures (e.g. in solar array wings, aircraft wings, fuselages and tail sections).

Vibrations of VSCL plates are analysed in this thesis. To define a curvilinear fibre path, it is assumed that the fibre angle varies linearly along one of the Cartesian axes, say x, from a value T_0 at the centre of the panel to the value T_1 at the panel edges, $x = \pm a/2$, where the panel has length a. The fibre path defined in this fashion is called the reference fibre path; other fibre paths in the ply can be produced by shifting - or copying - this path with a constant distance through direction y. During the manufacture process, there is a limitation on the fibre curvature radius; if the fibre path curvature is less than a determined amount, there will be kinking or buckling of the tows in the ply.

In this thesis, a p-version finite element based on a third-order shear deformation theory is used to model the displacements. Non-linear terms based on von Kármán strain–displacement relations are included. Using the principle of virtual work, the equations of motion are obtained in matrix form. The order of the equations of motion (regarded as the order of the full model) can be reduced using static condensation and modal coordinates (reduced-order models). The transient responses of the equations of motion of VSCL models are obtained using Newmark method; the same method is employed to obtain solutions in static problems, using time as an auxiliary parameter. The program is implemented in an in-house Visual Fortran code. To find the periodic oscillations of VSCL plates in free and forced vibrations, the shooting method is used, together with a Runge-Kutta-Fehlberg method for integration, again in an in-house Visual Fortran computational code.

In a traditional composite laminate the stiffness does not change - at the macro scale - in the laminate, while, in a VSCL laminate stiffnesses change spatially with respect to at least one coordinate. It is found that this change in local stiffness changes the natural frequencies and mode shapes of vibration of the laminate, both in the linear and the non-linear regimes. Using VSCL, the stress field and the strengths in the laminate may change in a different way from what would occur in a laminate with rectilinear fibres. Consequently, the load magnitudes at which damage onset appears, as well as the position of damage onset, can be changed.

The effect of geometrical imperfections (out-of-planarity) is included in the *p*-version finite element too. The free and forced, non-linear, periodic vibrations of VSCL plates are analysed using displacement time-histories, phase plane plots, frequency spectra and shapes assumed by the plates. Bifurcations from main branches of the backbone of frequency response curves are detected and analysed. The effect of imperfection of the plate on the hardening and softening of the free vibration backbone curves are detailed.

Resumo

Materiais compósitos laminados são frequentemente utilizados em elementos estruturais sujeitos a vibrações. Um aspeto importante na otimização de materiais compósitos reforçados com fibras é a orientação destas últimas. Em laminados compósitos tradicionais, a orientação das fibras dispostas na mesma lâmina é constante, mas alguns investigadores têm explorado a possibilidade de alterar a orientação das fibras numa lâmina, utilizando fibras curvilíneas. Um laminado com fibras curvilíneas é um laminado compósito com rigidez variável (VSCL do inglês *Variable Stiffness Composite Laminates*).

Vibrações e a deformação em regime estático de placas VSCL são analisadas nesta tese. Considera-se, em particular, o caso de fibras cujo ângulo é uma função bilinear de um dos eixos cartesianos. Limitações impostas à curvatura das fibras pelo processo de fabrico e pela ocorrência de encurvadura são tomadas em consideração.

Um aspeto fundamental desta tese, é o desenvolvimento de um elemento finito da versão *p* para placas VSCL, baseado numa teoria de deformação de corte de terceira ordem. Os termos não-lineares das relações entre deformações e deslocamentos de von Kármán são considerados, para se conseguir estudar grandes deslocamentos (regime geometricamente não-linear). Usando o princípio dos trabalhos virtuais, as equações de movimento são obtidas na forma matricial. O número de equações de movimento do modelo completo foi reduzido utilizando condensação estática e coordenadas modais (modelos de ordem reduzida). No que concerne à resolução das equações do movimento, foram essencialmente utilizados dois métodos. Para obter soluções em regime estático e respostas dinâmicas em regime transiente, as equações do movimento foram resolvidas pelo método de Newmark, no primeiro caso utilizando o tempo como um parâmetro artificial auxiliar. Para encontrar as oscilações periódicas de placas, tanto em vibrações livres como forçadas, foi utilizado o método do disparo (método *shooting*), em conjunto com um método Runge-Kutta-Fehlberg para a integração no tempo das equações do movimento. Em todos os casos, recorreu-se a códigos computacionais escritos em Fortran 90.

Enquanto numa placa laminada compósita com fibras retilíneas a rigidez não muda - à escala macro - de um ponto para o outro do plano médio, numa placa VSCL a rigidez muda espacialmente. Verificou-se que esta alteração na rigidez local provoca alterações nas frequências naturais e nos modos de vibração do laminado, tanto em regime linear como no regime geometricamente não linear. Usando VSCL, o campo de tensões e a resistência do laminado muda de uma forma diferente do que ocorreria num laminado com fibras retilíneas. Por conseguinte, as magnitudes de carga para a qual dano se inicia, bem como o local em que se dá esse início, são alterados.

O efeito de imperfeições geométricas (alteração da planaridade) foi incluído no elemento finito da versão *p* desenvolvido. Vibrações periódicas nos regimes livre e forçado, não lineares, de placas VSCL foram analisadas utilizando gráficos dos deslocamentos em função do tempo, planos de fase, espectros de frequência e as formas assumidas pelas placas. Bifurcações de ramos principais da curvas dorsais (*backbone curves*) e de curvas de resposta de frequência foram detetadas e analisadas. O efeito de imperfeições geométricas da placa sobre a inclinação das curvas dorsais

foi descrito.

Acknowledgments

I am grateful to Almighty Allah, whose blessings have always been enormous, who gave me the ability to complete this task. I express my heartiest thanks to my parents and family members who encouraged me at every stage of life and saw in me a successful person.

It is a great honor and privilege for me to record this deep sense of gratitude and indebtedness to my supervisor Professor Pedro Ribeiro[1] who guided me during all the course of this work. He was always there to help me find my way out of any problems. His critical observations helped me improve the analytical skills required for the research process as well as the writing skills required for disseminating the results.

I am also thankful to Professor Marcelo Moura[1] and to Professor José Rodrigues[1] who extended every help to me to have a better understanding of the subject. Here, I am going to appreciate the support from Professor Bogdan Epureanu[2] who received me very well during a short visit at the University of Michigan, Ann Arbor. I do not forget all the supports from Professor Antonio Ferreira[1] during my study in Porto. I appreciate his great helps.

Joining the program in University of Porto proved to be a door to make friends from around the world, know new cultures and understand new perspectives of life. I would also like to mention my colleagues and friends whose silent support led me to achieve the goal of completing this work. They are Dr. Julija Vasiljevska, Dr. Rosa Crespo, Dr. Stanislav Stoykov, Dr. Hadi Fanaee, Dr. Marzieh Moeenfard, Dr. Arif Ur Rahman, Dr. Gloria Lema, Dr. Jakov Krstulovic, Dr. David Miranda, Dr. Mariana Seabra, Dr. Mohsen Mirkhalaf, Eng. Tiago Lima, Eng. Romina Fernandes, Eng. Raul Moreira, Eng. Gonçalo Carneiro, and Eng. João Reis. Also, during my stay in Ann Arbor, I had very good time with Dr. Hossein Rokni and his wife. It was a wonderful experience with all of them.

During part of this work, I benefited from a research grant of project "Vibrations of variable stiffness composite laminated panels", reference PTDC / EME-PME / 098967 / 2008, a project funded by the Portuguese Science and Technology Foundation (Fundação para a Ciência e a Tecnologia - FCT[3]), with national funds (PIDDAC). Also, I would like to mention the support by another grant from FCT with reference number SFRH / BD / 81707 / 2011. These supports are gratefully acknowledged.

Finally, but most importantly, I wish to thank my wife Dr. Maryam Bagheri for her patience, assistance, support and faith in me.

HAMED AKHAVAN
Porto, Portugal
December 2015

[1] Department of Mechanical Engineering, Faculty of Engineering, University of Porto, Porto, Portugal
[2] Department of Mechanical Engineering, University of Michigan, Ann Arbor, MI
[3] http://www.fct.pt

"We think someone else, someone smarter than us,
someone more capable, someone with more resources will solve that problem.
But there isn't anyone else."

Regina Dugan

Contents

List of Figures

List of Tables

Notation

a	length of the plate
b	width of the plate
c	$c = 4/3h^2$
$\mathbf{C}$	damping matrix
D	flexural rigidity
E_1,E_2	major and minor Young's moduli
f_i, g_i, h_i	p-version out-of-plane, in-plane and rotation shape functions
$f_u, f_v, f_w, f_{\phi_x}, f_{\phi_y}$	in-plane, out-of-plane, and rotational loads (forces and moments per unit area)
f^*	interaction parameter in damage criterion
$\mathbf{f_i}$	generalised external force
G_{ij}	shear moduli
h	thickness of the plate
h_0	imperfection magnitude
$\mathbf{I}$	identity matrix
$\mathbf{K}$	stiffness matrix
$\mathbf{K_L}^{ij}, \mathbf{K_{L1}}^{ij}, \mathbf{K_{L2}}^{ij}, \mathbf{K_{L3}}^{ij}$	linear stiffness sub-matrices
$\overline{\mathbf{K}}_\mathbf{L}$	modal linear stiffness matrix
$\mathbf{K_{NL}}^{ij}$	non-linear stiffness sub-matrices
$\overline{\mathbf{K}}_\mathbf{NL}$	modal non-linear stiffness matrix
$\mathbf{M}$	mass matrix
$\mathbf{M}^{ij}$	mass sub-matrices
$\overline{\mathbf{M}}$	modal mass matrix
$\mathbf{N^u}$	vector of in-plane shape functions
$\mathbf{N^w}$	vector of out-of-plane shape functions
$\mathbf{N^{\phi_x}}, \mathbf{N^{\phi_y}}$	vectors of rotation shape functions
p_u	number of in-plane shape functions
p_w	number of out-of-plane shape functions
$p_{\phi_x}, p_{\phi_y}, p_\phi$	numbers of rotation shape functions
$\mathbf{q_i}$	generalised displacement vector
$\mathbf{q_m}$	modal displacement vector
Q_{ij}	elastic constants
S, S_{12}, S_{23}	shear strengths
t	time
T	period
T_0	fibre angle at the centre of a lamina
T_1	fibre angle at the edges of a lamina
u	in-plane displacement in the longitudinal direction
v	in-plane displacement in the width direction
V	volume of the plate

w	transverse displacement
u^0, v^0, w^0	mid-plane displacements
w_i	imperfection
w_{max}	maximum amplitude of transverse displacement in a periodic cycle
X_t, X_c	longitudinal tensile and compressive strengths
$\mathbf{X}$	phase-space vector
Y_t, Y_c	transverse tensile and compressive strengths
α	proportional damping parameter
δW_j	virtual work of the inertia force
δW_{in}	virtual work of the elastic (internal) force
δW_{ex}	virtual work of external force
$\varepsilon_x, \varepsilon_y, \varepsilon_z, \gamma_{xy}, \gamma_{xz}, \gamma_{yz}$	normal and shear strains in the xyz coordinates
$\varepsilon_1, \varepsilon_2, \gamma_{12}, \gamma_{13}, \gamma_{23}$	normal and shear strains in the material coordinates
$\boldsymbol{\varepsilon}_o^p$	linear in-plane strain
$\boldsymbol{\varepsilon}_o^b$	linear bending strain
$\boldsymbol{\varepsilon}_o^{b1}$	linear out-of-plane strain
$\boldsymbol{\varepsilon}_o^{p1}$	linear strain due to imperfection and/or non-linear in-plane strain
$\boldsymbol{\gamma}_o^p$	transverse shear strains
λ	safety factor
$\nu, \nu_{12}, \nu_{13}, \nu_{23}$	Poisson's ratios
ω, ω_{li}	natural linear frequencies
Ω	area of the plate
ϕ_x, ϕ_y	rotations of the normal to the middle surface about the y and x axis
$\boldsymbol{\phi}_i$	normal modes of vibration
$\boldsymbol{\Phi}$	reduced modal matrix
ρ	density
$\sigma_x, \sigma_y, \tau_{xy}, \tau_{xz}, \tau_{yz}$	normal and shear stresses in the xyz coordinates
$\sigma_1, \sigma_2, \tau_{12}, \tau_{13}, \tau_{23}$	normal and shear stresses in the material coordinates
θ	fibre path angle
$\{\}$	column vector
$\lfloor \rfloor$	row vector
$[\,]$	matrix

Acronyms

CCCC	clamped plate
CPT	classical plate theory
CLPT	classical laminate plate theory
CSCL	constant stiffness composite laminate
FFFF	free plate
FSDT	first-order shear deformation theory
DOF	degree of freedom
HSDT	higher-order shear deformation theory
SSSS	simply-supported plate
TSDT	third-order shear deformation theory
VSCL	variable stiffness composite laminate

Chapter 1

Variable Stiffness Composite Laminates

1.1 Introduction

Composite materials are made of at least two constituent materials that remain separated in the finished structure. Laminated fibre-reinforced composites are a popular type of composites, which have a number of advantages in comparison to metal based structures, including the facts that they offer lightweight and stiff surfaces, which resist well to corrosion and are also believed to have a relatively long fatigue life. Most commonly, fibre reinforced composite materials have straight and unidirectional fibres, which are homogeneously distributed in each lamina, hence, in a macroscopic sense, it can be considered that the stiffness does not vary in the laminate domain.

While many techniques for optimising traditional composite materials (constant stiffness composite laminates - CSCL) have been developed, modern processing methods allow for more complex composite structures to be conceived and created. The appearance of automated tow-placement technology (see a photo of this machine by NLR - Nationaal Lucht- en Ruimtevaartlaboratorium or the National Aerospace Laboratory of the Netherlands - in Figure 1.1), as a modern composite manufacturing mechanism, turned the production of laminates with curved fibres (variable stiffness composite laminates - VSCL) easier. Variable stiffness designs allow for the composite to be tailored to a wider range of properties than traditional straight-fibre laminates. In some applications, including in aerospace and naval structures, it may be quite interesting to design laminated plates using curvilinear fibres instead of straight ones, since by using a VSCL the natural frequencies change and vibrational resonance can be avoided; or one can expect a different stress field, displacement, damage onset or also different response to the forced vibrations in the non-linear regime. Here, without incurring weight penalties, the vibration response can be optimised by tailoring the fibre angles of different layers.

This dissertation concentrates on VSCL panels where the fibre orientation angle is not constant in a ply and acronym 'VSCL' will be mostly used for this specific type of panel. Fibres can be placed together in a curvilinear path to make a variable stiffness composite ply. This can be done using an automated tow-placement machine with rotating head (see Figure 1.1). Two variable stiffness composite laminates with different fibre paths are presented in Figure 1.2. Composite

Figure 1.1: Tow-placement machine producing plies with curvilinear fibre path. Courtesy of NLR.

materials where the stiffness is purposely made to vary in the laminate have, particularly since the nineties [1–5], deserved greater interest, because they may lead to more efficient designs.

There are several techniques to obtain VSCL panels. The main ones, represented in Figure 1.3 - with variable stiffness in surface of the panel - are: using curvilinear fibres [6–8], varying the volume fraction of fibres [9, 10], and dropping or adding plies to the laminate [11–13]. Attaching discrete stiffeners to the laminate [14–16], Figure 1.3(d), can be regarded as a procedure that varies the stiffness. Functionally graded plates [17] in which the material properties change in the in-plane directions [18, 19] may be regarded as VSCL plates. It is also worth noting that materials whose stiffness varies in space appear in nature [20].

Not negating that other ways of varying the stiffness may, for technological or economic reasons, be more adequate in specific situations, varying the fibre orientation has a few advantages.

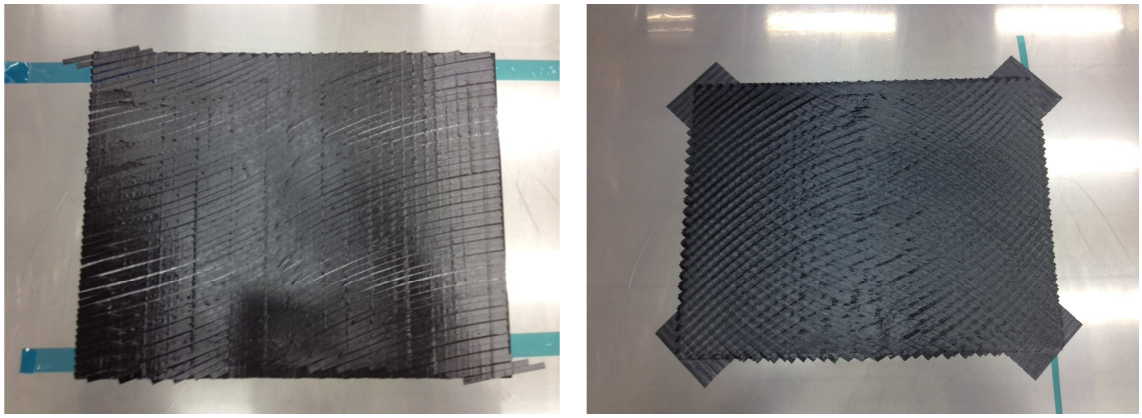

Figure 1.2: Two different VSCL plates with curvilinear fibres, right figure is a multi-layer laminate and left is a single-layer ply. Courtesy of NLR.

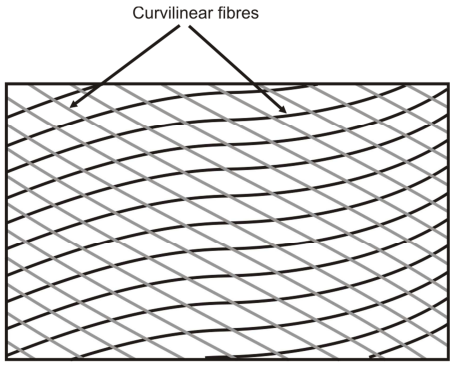

(a) Laminate with curvilinear fibres

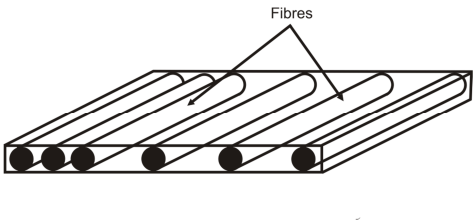

(b) Lamina with variable fibre volume fraction

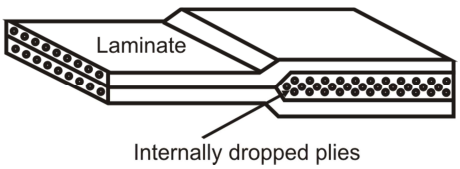

(c) Laminate with internally dropped plies.

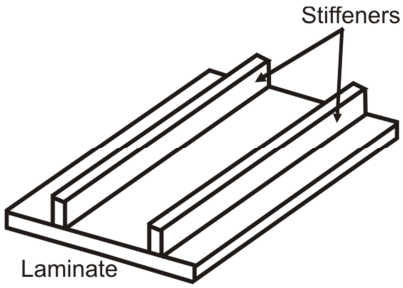

(d) Plate with stiffeners

Figure 1.3: Examples of four types of variable stiffness composite panels [43].

One of them is that the stiffness varies continuously with the membrane coordinates, in opposition to what occurs either when stiffeners are attached to a laminate or when plies are terminated at different locations. The two last options lead to abrupt changes in the thickness direction, which produce stress concentration and out-of-plane, interlaminar, stresses [11, 13]. Moreover, unlike stiffeners, curvilinear fibres do not introduce major geometry variations. Curved fibres offer a wider degree of possibilities than variations of rectilinear fibre volume fraction and provide a solution to the problem of continuity when one considers manufacturing a structure with different fibre angles in adjoining elements [1, 3, 21]. Furthermore, curvilinear fibres also offer a way to diminish stress concentrations that occur, e.g., around holes or cut-outs.

The objectives of this thesis are summarised in the next section. Manufacturing of VSCL and the definition of fibre paths are addressed after. Finally, the organization of the thesis is described.

1.2 Objectives

The objective of this thesis is to investigate the vibrations of VSCL panels, identifying the consequences of using curvilinear instead of linear fibre paths on the vibrational mode shapes, natural frequencies, forced response, stress distribution and failure onset. Taking into account the applications in aircraft and spacecraft panels, vibrations with large amplitude displacements will be considered. In fact, vibrations of those panels often occur in the non-linear regime, because the panels are thin and subjected to large dynamic excitations and therefore vibrate with large displacements. Due to existence of geometrical imperfection in the built panels, the effect of out-of-plane imperfection is considered. Changes in the free vibration behaviour of the panel from hardening to softening due to geometrical imperfection will be showed.

1.3 Manufacturing VSCL with Curvilinear Fibres

Here, a short review on manufacturing aspects of variable stiffness composites is given. Literature reviews on the static analysis, damage, free and forced oscillations in the non-linear regime plus linear vibration of variable stiffness panels will be presented in the following chapters.

One of the reasons behind the increasing availability of curved fibre laminates is that present tow-placement machines are capable of controlling fibre tows individually. Tow-placement machines have a computer controlled robotic arm with a fibre placement head, allowing for a precise control of the fibre orientation and providing the possibility to curve the fibres within the plane of the laminate; they also have cut/restart capabilities [22, 23]. This technology opens the door to an enlarged design space, with respect to the traditional straight-fibre reinforced composites, offering new possibilities for weight reduction and better performance, which is particularly important in means of transport [24]. For instance, the application of this technology to aircraft fuselage regions dominated by bending, linked to regions where shear deformation mostly affects the response, is suggested[1]. In such a case, plies with fibres aligned along a certain axis should turn to plies where

[1] http://aerospaceengineeringblog.com/variable-stiffness-composites/

the fibres that make 45 degrees with relation to the same axis. With curvilinear fibres, these two regions can be connected in a continuous fashion.

Automated fibre placement (AFP) with advanced machines (also written as Automated Tow-Placement Machines) is the chief procedure to obtain laminates with curvilinear fibres and – as written above – benefits from the machines' capability to control tow-placement [24]; but it also induces defects [25, 26]. Gaps and overlaps as defects of variable stiffness plies are visible in Figure 1.2. This technology is, maybe for the first time, mentioned in a series of works presented at the International SAMPE Symposiums, including [27–29]. Tow overlapping and tow dropping result in fibre and resin rich or poor regions. A novel fibre placement technique, designated as "Continuous Tow Shearing (CTS)" which uses shear deformation characteristics of dry tows, has been presented in Ref. [30]. Tests indicate that CTS can decrease process-induced defects such as fibre wrinkling, resin rich areas and fibre discontinuity.

Another type of advanced fibre placement – different from the one mentioned in a previous paragraph and, for example, in Refs. [22] and [23] – is tailored fibre placement (TFP), an automated textile process for the production of reinforcing structures [31,32]. This process apparently allows manufacturing textile preforms for composite parts with fibre layouts of arbitrary direction using embroidery technology; the desired fibre quantities and orientations can be transferred into fibre preforms.

1.4 Variable Stiffness Laminate with Curvilinear Fibres

The fibres in each unique lamina are straight in a similar direction in constant stiffness composite laminates, Figure 1.4(a), or they can be in curved forms (leading to variable stiffness composite laminates), Figure 1.4(b). In CSCL plates, the fibre orientations in each lamina do not change, but from one lamina to another they can be altered. To date, the main focus of researchers has been finding the best stacking sequence for the layers in these CSCL plates, which can result in a better design for deformations, frequencies, and vibration mode shapes.

In this thesis we consider laminated plates with variable fibre angle through a ply, Figure 1.4(b). Theoretically, this variation could obey any pattern. One pattern for fibre paths to develop is a curvilinear form. The other fibre paths may be attained using the curvilinear reference fibre path.

1.4.1 Definition of Reference Fibre Path

The fibre path orientation θ is here defined as

$$\theta(x) = 2(T_1 - T_0)\frac{|x|}{a} + T_0 \tag{1.1}$$

in which T_0 and T_1 are the path orientation angles in the centre and vertical edges of a rectangular plate, with length a and width b, where x and y Cartesian coordinates system is used, Figure

Accessed: 29 September 2015

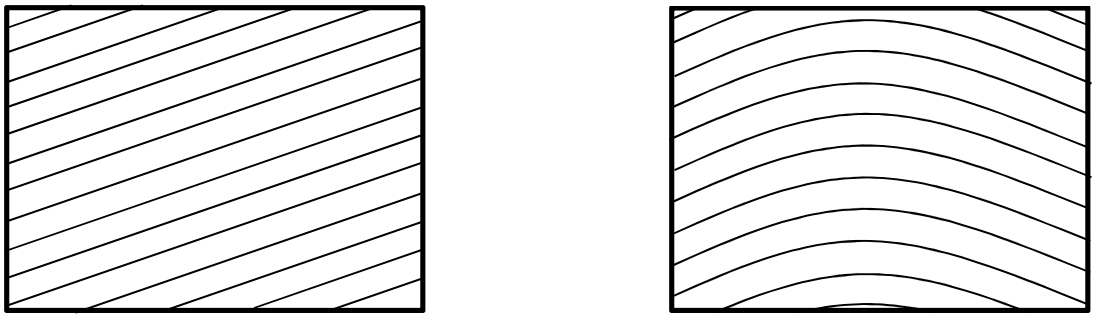

(a) Constant stiffness lamina

(b) Variable stiffness lamina

Figure 1.4: Lamina with straight fibres versus lamina with curved fibres.

1.5. Here, the fibre orientations change spatially. To introduce a VSCL plate with k layers the notation $\left[\langle T_0,T_1\rangle^{(1)},\langle T_0,T_1\rangle^{(2)},\ldots,\langle T_0,T_1\rangle^{(k)}\right]$ is used, here $\langle T_0,T_1\rangle^{(k)}$ shows the fibre angles at the centre and the edge of the kth lamina. Also, $\left[\langle T_0,T_1\rangle^{1},\ldots,\langle T_0,T_1\rangle^{i},\ldots,\langle T_0,T_1\rangle^{k}\right]_{sym}$ means that the laminate has $2\times k$ layers which are symmetric about the mid-plane.

1.4.2 Shifted Curvilinear Fibres

Once the reference fibre path is defined, it is easy to find the remaining fibre paths. There are two methods to find the other fibre paths: parallel and shifted methods. The shifting of the reference fibre path along an axis to create the remaining paths is more straight-forward than the use of parallel paths. The first fibre path created is the reference fibre path. The next fibre path is made by shifting the reference fibre path a fixed amount in the y direction. The remaining fibre paths for the lamina are made in the same manner, with the only difference being the amount that each path is shifted along the y axis. The completed shifted fibre $\langle 0^o,45^o\rangle$ lamina can be seen in Figure

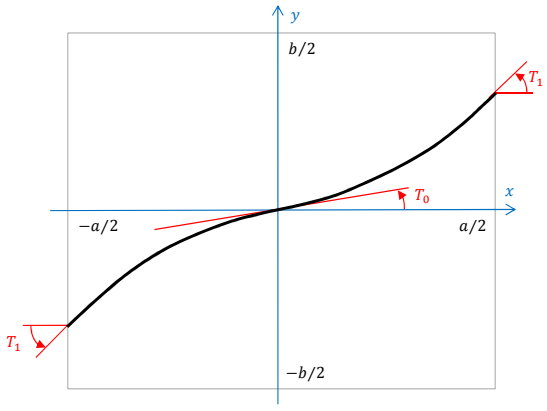

Figure 1.5: Reference fibre path in VSCL with curvilinear fibres

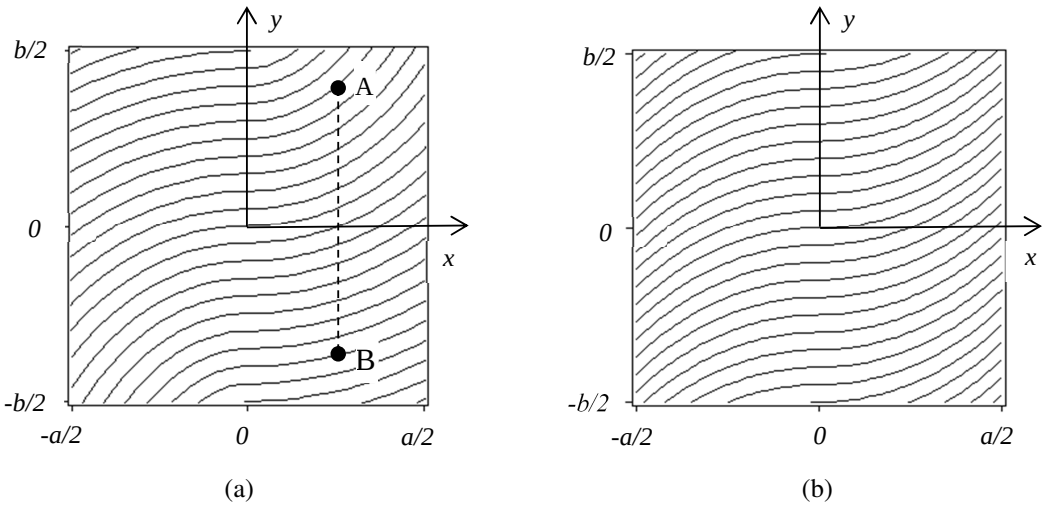

Figure 1.6: A $\langle 0^o, 45^o \rangle$ lamina created by (a) shifted fibre method, and (b) parallel fibre method.

1.6(a). Note that here the change in fibre orientation only takes place along the x axis. In shifted fibre method, a single analytical expression for the fibre orientation angle exists that is valid for all fibre paths.

1.4.3 Parallel Curvilinear Fibres

The parallel method creates fibre paths so that each path is defined as a set of points lying a constant distance from the reference curve. In this pattern, any fibre curve is created parallel to another fibre curve. Unlike in the shifted fibre method, in the parallel fibre method, the reference path obeys an analytical expression that is not obeyed by the other paths. The completed parallel fibre $\langle 0^o, 45^o \rangle$ lamina can be seen in Figure 1.6(b). Unlike the shifted fibre, two points, A and B, which have the same x coordinate no longer have identical fibre orientations. In this investigation, the shifted fibre paths are used. For more details on this, one can refer to Ref. [6].

1.4.4 Manufacturing Limitations on VSCL by Shifted Curvilinear Fibres

In order to create the variable-stiffness laminates here considered, it is necessary to actually curve the tow paths. If a fibre is curved too much, then it is quite possible that a kink in the fibre develops. In an effort to limit the degree of this kinking, the curvature of the fibre paths should be less than a prescribed maximum value. The paths of shifted fibres in the ply are identical to the reference fibre path. The definition of curvature for a function of a single variable $f(x)$ is given by

$$K = \frac{f''(x)}{\left(1 + (f'(x))^2\right)^{\frac{3}{2}}} \tag{1.2}$$

Recognising that the reference fibre path of a given ply is defined by the single variable x, its curvature can be found by substituting the fibre path equation for $f(x)$ in the above equation. Only

the curvature of this path in the positive portion of the panel needs to be calculated, since the reference fibre path is antisymmetric about the y axis. So the fibre orientation is

$$\theta(x) = (T_1 - T_0)\frac{x}{\frac{a}{2}} + T_0, \qquad 0 < x < \frac{a}{2} \tag{1.3}$$

and the fibre path equation is

$$f(x) = \int \tan\left((T_1 - T_0)\frac{x}{\frac{a}{2}} + T_0\right) dx \tag{1.4}$$

or

$$f(x) = \frac{a}{2(T_0 - T_1)}\left\{ln\left[\cos\left((T_1 - T_0)\frac{x}{\frac{a}{2}} + T_0\right)\right] - ln\left[\cos(T_0)\right]\right\}. \tag{1.5}$$

At each location along the reference fibre path, the curvature is required to be less than the maximum allowable curvature of 3.28 m^{-1} [6], to insure that the laminate could be made (this value may change depending on the material, layup rate, and compaction pressure used in the manufacturing process. Ref. [33] gives different values for different tow properties). In the numerical examples that follow, results are computed only if the curvature is less than this critical value. When the curvature exceeded the maximum allowable curvature, no analysis is performed since the laminate should not be, according to Ref. [6], manufactured. Therefore, the following constraint inequality is respected:

$$K = \frac{2(T_1 - T_0)}{a}\cos\left((T_1 - T_0)\frac{x}{\frac{a}{2}} + T_0\right) < 3.28 \tag{1.6}$$

1.5 Organization of this Dissertation

The thesis is organised into 7 chapters. Chapter 1 introduces VSCL plates with curvilinear fibre which follow a reference fibre path. Two different methods (parallel and shifted) are presented to make the variable stiffness ply using the reference fibre path. The manufacturing limitations of VSCL plates are presented here. Linear modelling of VSCL plate with a p-version finite element with hierarchical set of shape functions, using a third order shear deformation theory (TSDT), is developed in Chapter 2. Here, the solution to the eigenvalue problem of VSCL plates is given and the natural frequencies and mode shapes of vibration are calculated and compared for clamped, simply-supported and free plates. The third chapter is self-contained with the development of the theory. In the next chapters, improved formulations to include non-linearities are developed.

The non-linear model and equations of equilibrium based on the virtual work principle are introduced in Chapter 3, which is devoted to static problems. Newmark method is used to solve the equations of equilibrium in the non-linear regime. Numerical results for large deflection and stresses are presented and compared.

Damage onset of VSCL plates under different types of static and dynamic loads are thoroughly studied in Chapter 4. Here, Tsai-Wu damage criterion is used and the equations of motion are

solved by Newmark method . The transient behaviour of VSCL plates under different loadings is presented.

Static condensation and modal summation method, that reduce the number of degrees of freedom in non-linear VSCL models are presented in Chapter 5, where the shooting method is used to find free periodic oscillations of VSCL plates. Results for non-linear frequencies are compared and backbone curves, bifurcations, time history responses, phase-plane diagrams and frequency spectra of deflection amplitude and stresses are presented. Here, free oscillations of imperfect VSCL plates are also addressed.

The shooting method is also used in Chapter 6 to find forced periodic oscillations of VSCL plates. Frequency response curves for different VSCL plates are presented, where bifurcations are detected. Steady-state time histories, phase-plane plots and frequency spectra for deflection amplitude, and stresses in a periodic cycle in different points of bifurcated and fundamental branch of the response are studied. Damage onset is analysed.

Chapter 7 points out the conclusions of the thesis. Based on the conclusions, some new subjects are suggested to investigate in the future.

Chapter 2

Linear Vibrational Modes of VSCL Plates

2.1 Introduction

In this chapter, natural frequencies and vibrational mode shapes of variable stiffness composite laminated (VSCL) plates with curvilinear fibres are studied. The plates are rectangular either perfect or with geometric imperfections (out-of-planarity). In each ply of the rectangular VSCLs, the fibre-orientation angle changes linearly with respect to the horizontal coordinate, Equation (1.1).

To define the modes of vibration of the laminates, a *p*-version finite element with hierarchical basis functions is presented. This element follows a third-order shear deformation theory (TSDT), because this theory allows one to consider shear deformation and is hence more accurate than classical plate theory. In addition, deformation through the thickness is more truthfully represented in a TSDT than in a FSDT (first-order shear deformation theory) and, unlike the latter, a TSDT does not require a shear correction factor. On the other hand, a TSDT is still an equivalent single layer theory, and hence has smaller implementation and computational costs than layerwise theories or three-dimensional elasticity (for more details see Refs. [34–39]).

The convergence properties of this new element are investigated. Taking manufacturing restrictions regarding the fibre curvatures into account, maps of natural frequencies as functions of tow-orientation angles are determined in demonstrative examples. This manufacturing limitation arises from a fact that the curvature of fibres should not be larger than a specific value, in order to prevent the occurrence of fibre kinking [6]. It is verified that the use of curvilinear fibres instead of the traditional straight fibres introduces a greater degree of flexibility, which can be used to adjust frequencies and vibrational mode shapes. Some experimental results for VSCL plates with free edges are given and further compared with numerical results of the linear model.

2.1.1 Literature Review

There are several publications on vibrations of constant stiffness composite laminate (CSCL) plates and shells, i.e., in laminates with straight fibres. But, in spite of the fact that VSCL panels find application in fields where they are prone to experience vibrations, there is a very limited number of studies on the vibrations of these panels. Wu and Lee [40] studied the frequencies of a conical shell with variable stiffness, as the function of circumferential coordinate, and achieved changes of 20% and 7% in the fundamental frequencies of shells with simply-supported and clamped boundary conditions, respectively.

In another reference [41], the effect of transverse shear deformation and embedded manufacturing defects (gaps and overlaps) on the linear natural frequencies was presented. The governing equations obtained via classical and shear deformation theories and then the authors solved the equations by using the hybrid Fourier–Galerkin method. It was declared that for moderately-thick plates with length-to-thickness ratio $a/h = 10$, major differences emerge between classical laminate plate theory and TSDT predictions. In particular, discrepancy up to 15% was observed for the fundamental frequency.

In Ref. [42], a layerwise formulation for free vibrations of symmetric and unsymmetric VSCL plates was applied taking into account a linear variation of the in-plane displacement fields in each layer of plate. The authors in Ref. [42] concluded that increasing the fibre orientation angle at the edge of laminates always leads to lower fundamental natural frequencies; where the same is not necessarily true in what regards the fibre angle at the centre of the laminates. In comparison between symmetric and unsymmetric laminates with the same properties, they found that the maximum fundamental natural frequencies occur in the symmetric laminate. However, they mentioned that the frequency values of higher modes were often larger for unsymmetric VSCL plates.

Ref. [43] includes a review on VSCL panels as well as a comparison between natural frequencies obtained by p-version and h-version finite element models of VSCL plates. Another reference includes a small discussion on the linear vibration of VSCL plates in terms of the number of in-plane, out-of-plane and rotation shape functions in p-version finite element [44].

In another research [45], Ritz solutions used to find natural frequencies and vibration modes of laminated plates having curvilinear reinforcing fibers. VSCL plates with quadratically, cubically, and arbitrarily shaped fibers, defined using spline functions, were studied. It was showed that the effect of the fiber shapes diminish by inserting symmetric layers toward the outermost layer into the inner layers. Also, plates with thin outer layers and thick inner layers which are symmetric to the outer layer presented higher frequencies than those with thick outermost layers [45].

In variable stiffness panels, the stiffness properties are continuous functions of position. Ideally, by varying the fibre steering geometry, the stiffness properties at each point in the panel can be independently varied. The additional freedom in locally tailoring the stiffness properties means that the performance of variable stiffness panels can be highly improved over constant stiffness (straight fibres) panels. However, this additional freedom comes at the price of having a significantly enlarged design space. In this fashion, optimisation can be used to find a VSCL panel with

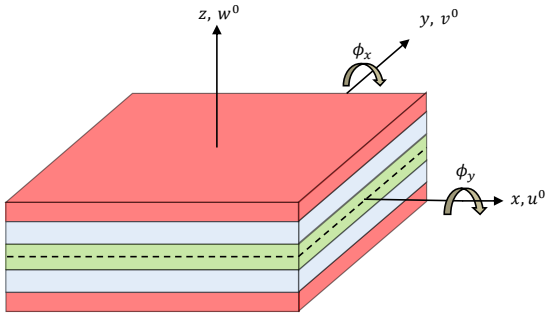

Figure 2.1: Coordinates of a laminated plate

maximized fundamental frequency; two examples are provided by Refs. [46, 47], where variable stiffness shells are analised using classical lamination theory. Most of the results presented in this chapter are published in Ref. [48].

2.2 Linear Formulation for of VSCL Plates with Curvilinear Fibres and with Imperfections

A right-handed three-dimensional Cartesian coordinate system is adopted, with the x and y axis on the middle plane of the undeformed plate and the z axis positive upwards. The origin of the coordinate system is located in the geometric centre of the undeformed plate (Figure 2.1).

In the TSDT used here, the displacement components in the x, y, and z directions, represented by u, v, and w are given (see Refs. [34, 37, 39] for displacement field without imperfection) by Equations (2.1)

$$u(x,y,z,t) = u^0(x,y,t) + z\phi_x(x,y,t) - cz^3\left(\phi_x(x,y,t) + \frac{\partial w^0(x,y,t)}{\partial x}\right),$$

$$v(x,y,z,t) = v^0(x,y,t) + z\phi_y(x,y,t) - cz^3\left(\phi_y(x,y,t) + \frac{\partial w^0(x,y,t)}{\partial y}\right),$$

$$w(x,y,z,t) = w^0(x,y,t) + w_i(x,y), \tag{2.1}$$

where u^0, v^0, and w^0 are the values of u, v, and w at the mid-plane and ϕ_x and ϕ_y are the independent rotations of the normal to the middle surface about the y and x axis, respectively (as shown in the Figure 2.1). t is time, $c = 4/3h^2$, and h is the plate thickness. Initial geometric imperfection in the normal direction, w_i, associated with zero initial stress, is considered in the formulation. If $c = 0$, one can obtain the displacement field of FSDT. The displacement field of this TSDT accommodates quadratic variation of transverse shear strains (and hence stresses) through the thickness and vanishing of transverse shear stresses on the top and bottom of a plate. Unlike FSDT, mentioned TSDT requires no shear correction factors.

In the following equations, function arguments are not always given. Herein, the mid-plane displacements are given by

$$\begin{Bmatrix} u^0(x,y,t) \\ v^0(x,y,t) \\ w^0(x,y,t) \\ \phi_x(x,y,t) \\ \phi_y(x,y,t) \end{Bmatrix} = \begin{bmatrix} \mathbf{N^u}(x,y)^T & \mathbf{0} & \mathbf{0} & \mathbf{0} & \mathbf{0} \\ \mathbf{0} & \mathbf{N^u}(x,y)^T & \mathbf{0} & \mathbf{0} & \mathbf{0} \\ \mathbf{0} & \mathbf{0} & \mathbf{N^w}(x,y)^T & \mathbf{0} & \mathbf{0} \\ \mathbf{0} & \mathbf{0} & \mathbf{0} & \mathbf{N^{\phi_x}}(x,y)^T & \mathbf{0} \\ \mathbf{0} & \mathbf{0} & \mathbf{0} & \mathbf{0} & \mathbf{N^{\phi_y}}(x,y)^T \end{bmatrix} \begin{Bmatrix} \mathbf{q_u}(t) \\ \mathbf{q_v}(t) \\ \mathbf{q_w}(t) \\ \mathbf{q_{\phi_x}}(t) \\ \mathbf{q_{\phi_y}}(t) \end{Bmatrix} \tag{2.2}$$

where $\mathbf{N^i}(x,y)$ are vector of shape functions and $\mathbf{q_i}(t)$ are generalised displacement vectors (**i**= **u**, **v**, **w**, $\phi_\mathbf{x}$, and $\phi_\mathbf{y}$). Vector $\mathbf{N^u}(x,y)$ is constituted by p_u^2 in-plane shape functions, $\mathbf{N^w}(x,y)$ is constituted by p_w^2 out-of-plane shape functions. $\mathbf{N^{\phi_x}}(x,y)$ and $\mathbf{N^{\phi_y}}(x,y)$ are the vectors of shape functions for the rotations of the cross section about the y and x axis, respectively. If the boundary conditions permit, we have the same number of terms, for $\mathbf{N^{\phi_x}}(x,y)$ and $\mathbf{N^{\phi_y}}(x,y)$, given by $p_\phi^2 = p_{\phi_x}^2 = p_{\phi_y}^2$. Also, the vector of shape functions for displacements in the y direction $\mathbf{N^v}(x,y)$ are the same as the one for displacements in the x direction, $\mathbf{N^u}(x,y)$.

Here, $\lfloor\ \rfloor$ and $\{\ \}$ mean a row and column vectors, respectively. The row vectors of bi-dimensional surface or membrane, transverse and rotational shape functions that appear in Equation (2.2) are, respectively

$$\mathbf{N^{u}}^T(\xi,\eta) = \mathbf{N^{v}}^T(\xi,\eta) = \lfloor g_1(\xi)g_1(\eta), g_1(\xi)g_2(\eta), \ldots, g_{p_u}(\xi)g_{p_u}(\eta)\rfloor,$$

$$\mathbf{N^{w}}^T(\xi,\eta) = \lfloor f_1(\xi)f_1(\eta), f_1(\xi)f_2(\eta), \ldots, f_{p_w}(\xi)f_{p_w}(\eta)\rfloor,$$

$$\mathbf{N^{\phi_x}}^T(\xi,\eta) = \lfloor h_1(\xi)h_1(\eta), h_1(\xi)h_2(\eta), \ldots, h_{p_{\phi_x}}(\xi)h_{p_{\phi_x}}(\eta)\rfloor,$$

$$\mathbf{N^{\phi_y}}^T(\xi,\eta) = \left\lfloor h_1(\xi)h_1(\eta), h_1(\xi)h_2(\eta), \ldots, h_{p_{\phi_y}}(\xi)h_{p_{\phi_y}}(\eta)\right\rfloor \tag{2.3}$$

where g, f and h are surface, transverse and rotation one-dimensional displacement shape functions (see Appendix A); $p_u = p_v$, p_w, p_{ϕ_x} and p_{ϕ_y} are the numbers of respective displacement shape functions employed. η and ξ are the local co-ordinates, and related to principal coordinates of x and y by $x = \frac{a}{2}\xi$, $y = \frac{b}{2}\eta$, where a and b are the length and width of the plate, and ξ and η change from -1 to 1.

p-Version finite element method as a discretization procedure for solving partial differential equations is used. In this method, the finite element mesh is fixed and the polynomial degrees of elements are increased. This is in contrast with the widely used discretization procedure h-version finite element method in which the polynomial degrees of elements are fixed and the mesh is refined. In the linear elastic mechanics problem, it is demonstrated that solutions based on the p-version converge faster than solutions based on the h-version [49]. Additional computational

results and evidence of faster convergence of the p-version finite element were presented in Ref. [50]. In the p-version finite element method, one is free to choose the number and the set of displacement shape functions to use in the element definition, being each of the displacement components - u, v, w, ϕ_x, and ϕ_y - associated with a particular set of shape functions (see Appendix A).

The strain displacement relations by Green deformation tensor is expressed as (after Ref. [51])

$$\varepsilon_x = \frac{1}{2}\left(2\frac{\partial u}{\partial x} + \frac{\partial u}{\partial x}\frac{\partial u}{\partial x} + \frac{\partial v}{\partial x}\frac{\partial v}{\partial x} + \frac{\partial w}{\partial x}\frac{\partial w}{\partial x}\right),$$

$$\varepsilon_y = \frac{1}{2}\left(2\frac{\partial v}{\partial y} + \frac{\partial u}{\partial y}\frac{\partial u}{\partial y} + \frac{\partial v}{\partial y}\frac{\partial v}{\partial y} + \frac{\partial w}{\partial y}\frac{\partial w}{\partial y}\right),$$

$$\varepsilon_z = \frac{1}{2}\left(2\frac{\partial w}{\partial z} + \frac{\partial u}{\partial z}\frac{\partial u}{\partial z} + \frac{\partial v}{\partial z}\frac{\partial v}{\partial z} + \frac{\partial w}{\partial z}\frac{\partial w}{\partial z}\right),$$

$$\varepsilon_{xy} = \frac{1}{2}\left(\frac{\partial u}{\partial y} + \frac{\partial v}{\partial x} + \frac{\partial u}{\partial x}\frac{\partial u}{\partial y} + \frac{\partial v}{\partial x}\frac{\partial v}{\partial y} + \frac{\partial w}{\partial x}\frac{\partial w}{\partial y}\right),$$

$$\varepsilon_{xz} = \frac{1}{2}\left(\frac{\partial u}{\partial z} + \frac{\partial w}{\partial x} + \frac{\partial u}{\partial x}\frac{\partial u}{\partial z} + \frac{\partial v}{\partial x}\frac{\partial v}{\partial z} + \frac{\partial w}{\partial x}\frac{\partial w}{\partial z}\right),$$

$$\varepsilon_{yz} = \frac{1}{2}\left(\frac{\partial v}{\partial z} + \frac{\partial w}{\partial y} + \frac{\partial u}{\partial y}\frac{\partial u}{\partial z} + \frac{\partial v}{\partial y}\frac{\partial v}{\partial z} + \frac{\partial w}{\partial y}\frac{\partial w}{\partial z}\right),$$

$$\gamma_{xy} = 2\varepsilon_{xy}, \gamma_{xz} = 2\varepsilon_{xz}, \gamma_{yz} = 2\varepsilon_{yz}. \tag{2.4}$$

where ε_i is the normal strain acting on the surface normal to i in direction i, and ε_{ij} is the shear strain acting on the surface normal to i in direction j. Strains, with some simplifications by neglecting higher order terms except the term which include imperfection, can be expressed as (again, as will be often done in this text, for simplicity we write $u_0(x,y,t)$ as u_0, etc.)

$$\varepsilon_x(x,y,z,t) = \frac{\partial u^0}{\partial x} + \left(z - cz^3\right)\frac{\partial \phi_x}{\partial x} - cz^3\left(\frac{\partial^2 w^0}{\partial x^2}\right) + \frac{\partial w^0}{\partial x}\frac{\partial w_i}{\partial x},$$

$$\varepsilon_y(x,y,z,t) = \frac{\partial v^0}{\partial y} + \left(z - cz^3\right)\frac{\partial \phi_y}{\partial y} - cz^3\left(\frac{\partial^2 w^0}{\partial y^2}\right) + \frac{\partial w^0}{\partial y}\frac{\partial w_i}{\partial y},$$

$$\varepsilon_z(x,y,z,t) = 0,$$

$$\gamma_{xy}(x,y,z,t) = \frac{\partial u^0}{\partial y} + \frac{\partial v^0}{\partial x} + \left(z - cz^3\right)\left(\frac{\partial \phi_x}{\partial y} + \frac{\partial \phi_y}{\partial x}\right) - 2cz^3\frac{\partial^2 w^0}{\partial x \partial y} + \frac{\partial w^0}{\partial x}\frac{\partial w_i}{\partial y} + \frac{\partial w^0}{\partial y}\frac{\partial w_i}{\partial x},$$

$$\gamma_{yz}(x,y,z,t) = \left(1-3cz^2\right)\left(\phi_y(x,y,t)+\frac{\partial w^0}{\partial y}\right),$$

$$\gamma_{xz}(x,y,z,t) = \left(1-3cz^2\right)\left(\phi_x(x,y,t)+\frac{\partial w^0}{\partial x}\right). \tag{2.5}$$

These expressions are in general accurate enough for linear vibrations of plates. If more accurate expressions are needed, the Equations (2.5) can be improved retaining all the non-linear terms. Strains can be presented in the matrix form as

$$\left\{\begin{array}{c}\varepsilon_x\\ \varepsilon_y\\ \gamma_{xy}\end{array}\right\} = \left[\begin{array}{cccccccc}1&0&0&z&0&0&-cz^3&0&0\\0&1&0&0&z&0&0&-cz^3&0\\0&0&1&0&0&z&0&0&-cz^3\end{array}\right]\boldsymbol{\varepsilon}$$

$$\boldsymbol{\varepsilon} = \left\{\begin{array}{c}\boldsymbol{\varepsilon}_o^p\\ \boldsymbol{\varepsilon}_o^b\\ \boldsymbol{\varepsilon}_o^b\end{array}\right\} + \left\{\begin{array}{c}\boldsymbol{\varepsilon}_o^{p1}\\ \mathbf{0}\\ \boldsymbol{\varepsilon}_o^{b1}\end{array}\right\} \tag{2.6}$$

in which $\boldsymbol{\varepsilon}_o^p$ is the linear in-plane strain

$$\boldsymbol{\varepsilon}_o^p = \left\{\begin{array}{c}u^0_{,x}\\ v^0_{,y}\\ u^0_{,y}+v^0_{,x}\end{array}\right\} \tag{2.7}$$

Here, partial derivation is represented by a comma. $\boldsymbol{\varepsilon}_o^b$ is the linear bending strain

$$\boldsymbol{\varepsilon}_o^b = \left\{\begin{array}{c}\phi_{x,x}\\ \phi_{y,y}\\ \phi_{x,y}+\phi_{y,x}\end{array}\right\} \tag{2.8}$$

and $\boldsymbol{\varepsilon}_o^{b1}$ is another linear strain

$$\boldsymbol{\varepsilon}_o^{b1} = \left\{\begin{array}{c}w^0_{,xx}\\ w^0_{,yy}\\ 2w^0_{,xy}\end{array}\right\} \tag{2.9}$$

$\boldsymbol{\varepsilon}_o^{p1}$ is the linear strain due to imperfection as

$$\boldsymbol{\varepsilon}_o^{p1} = \left\{\begin{array}{c}w^0_{,x}w_{i,x}\\ w^0_{,y}w_{i,y}\\ w^0_{,x}w_{i,y}+w^0_{,y}w_{i,x}\end{array}\right\} \tag{2.10}$$

The following linear strain displacement relation is employed for the transverse shear strains in the TSDT model:

$$\begin{Bmatrix} \gamma_{yz} \\ \gamma_{xz} \end{Bmatrix} = \begin{bmatrix} (1-3cz^2) & 0 \\ 0 & (1-3cz^2) \end{bmatrix} \boldsymbol{\gamma}_o^p$$

$$\boldsymbol{\gamma}_o^p = \begin{Bmatrix} w^0_{,y} + \phi_y \\ w^0_{,x} + \phi_x \end{Bmatrix} \tag{2.11}$$

By introducing mid-plane displacements of Equation (2.2) in the definitions above,

$$\boldsymbol{\varepsilon}_o^p = \begin{bmatrix} \mathbf{N}^{\mathbf{u}\,T}_{,x} & \mathbf{0} \\ \mathbf{0} & \mathbf{N}^{\mathbf{u}\,T}_{,y} \\ \mathbf{N}^{\mathbf{u}\,T}_{,y} & \mathbf{N}^{\mathbf{u}\,T}_{,x} \end{bmatrix} \begin{Bmatrix} \mathbf{q_u} \\ \mathbf{q_v} \end{Bmatrix},$$

$$\boldsymbol{\varepsilon}_o^b = \begin{bmatrix} \mathbf{N}^{\boldsymbol{\phi}_\mathbf{x}\,T}_{,x} & \mathbf{0} \\ \mathbf{0} & \mathbf{N}^{\boldsymbol{\phi}_\mathbf{y}\,T}_{,y} \\ \mathbf{N}^{\boldsymbol{\phi}_\mathbf{x}\,T}_{,y} & \mathbf{N}^{\boldsymbol{\phi}_\mathbf{y}\,T}_{,x} \end{bmatrix} \begin{Bmatrix} \mathbf{q}_{\boldsymbol{\phi}_\mathbf{x}} \\ \mathbf{q}_{\boldsymbol{\phi}_\mathbf{y}} \end{Bmatrix},$$

$$\boldsymbol{\varepsilon}_o^{b1} = \begin{Bmatrix} \mathbf{N}^{\mathbf{w}\,T}_{,xx} \\ \mathbf{N}^{\mathbf{w}\,T}_{,yy} \\ 2\mathbf{N}^{\mathbf{w}\,T}_{,xy} \end{Bmatrix} \mathbf{q_w},$$

$$\boldsymbol{\varepsilon}_o^{p1} = \frac{1}{2} \begin{Bmatrix} w_{i,x}\mathbf{N}^{\mathbf{w}}_{,x} \\ w_{i,y}\mathbf{N}^{\mathbf{w}}_{,y} \\ w_{i,x}\mathbf{N}^{\mathbf{w}}_{,y} + w_{i,y}\mathbf{N}^{\mathbf{w}}_{,x} \end{Bmatrix} \mathbf{q_w},$$

$$\boldsymbol{\gamma}_o^p = \begin{bmatrix} \mathbf{N}^{\mathbf{w}T}_{,y} & \mathbf{0} & \mathbf{N}^{\boldsymbol{\phi}_\mathbf{y}\,T} \\ \mathbf{N}^{\mathbf{w}T}_{,x} & \mathbf{N}^{\boldsymbol{\phi}_\mathbf{x}\,T} & \mathbf{0} \end{bmatrix} \begin{Bmatrix} \mathbf{q_w} \\ \mathbf{q}_{\boldsymbol{\phi}_\mathbf{x}} \\ \mathbf{q}_{\boldsymbol{\phi}_\mathbf{y}} \end{Bmatrix}. \tag{2.12}$$

A variable stiffness composite lamina can be considered as an orthotropic composite plate in each point of its surface. So, the stress-strain relation in the k^{th} lamina in the material coordinates is (see Refs. [34, 52])

$$\begin{Bmatrix} \sigma_1 \\ \sigma_2 \\ \tau_{23} \\ \tau_{13} \\ \tau_{12} \end{Bmatrix}^{(k)} = \begin{bmatrix} Q_{11} & Q_{12} & 0 & 0 & 0 \\ Q_{21} & Q_{22} & 0 & 0 & 0 \\ 0 & 0 & Q_{44} & 0 & 0 \\ 0 & 0 & 0 & Q_{55} & 0 \\ 0 & 0 & 0 & 0 & Q_{66} \end{bmatrix}^{(k)} \begin{Bmatrix} \varepsilon_1 \\ \varepsilon_2 \\ \gamma_{23} \\ \gamma_{13} \\ \gamma_{12} \end{Bmatrix}^{(k)} \tag{2.13}$$

in which index 1 is direction of the fibre, 2 is perpendicular to the fibre orientation in the lamina surface, and 12, 13, and 23 are shear directions. Q_{ij} are elastic properties of the lamina. Elastic constants are (see Refs. [34, 35]):

$$Q_{11}^{(k)} = \frac{E_1^{(k)}}{1-\nu_{12}^{(k)}\nu_{21}^{(k)}},$$

$$Q_{12}^{(k)} = \frac{\nu_{12}^{(k)}E_2^{(k)}}{1-\nu_{12}^{(k)}\nu_{21}^{(k)}},$$

$$Q_{22}^{(k)} = \frac{E_2^{(k)}}{1-\nu_{12}^{(k)}\nu_{21}^{(k)}},$$

$$Q_{44}^{(k)} = G_{23}^{(k)},$$

$$Q_{55}^{(k)} = G_{13}^{(k)},$$

$$Q_{66}^{(k)} = G_{12}^{(k)}, \tag{2.14}$$

where, $E_1^{(k)}$ is the major elasticity modulus, $E_2^{(k)}$ the lower elasticity modulus, $G_{12}^{(k)}$, $G_{13}^{(k)}$, and $G_{23}^{(k)}$ the shear moduli, and $\nu_{12}^{(k)}$ the Poisson ratio in the k^{th} layer. To apply the principle of virtual work, as described in Ref. [53], it is convenient to transform the stresses and strains from principal fibre coordinates (1,2, and 3) to xyz coordinates. For that purpose, the following transformation matrices are used (Refs. [34, 35]):

$$\begin{Bmatrix} \sigma_x \\ \sigma_y \\ \tau_{yz} \\ \tau_{xz} \\ \tau_{xy} \end{Bmatrix} = \begin{bmatrix} \cos^2\theta & \sin^2\theta & 0 & 0 & -2\sin\theta\cos\theta \\ \sin^2\theta & \cos^2\theta & 0 & 0 & 2\sin\theta\cos\theta \\ 0 & 0 & \cos\theta & \sin\theta & 0 \\ 0 & 0 & -\sin\theta & \cos\theta & 0 \\ \sin\theta\ \cos\theta & -\sin\theta\cos\theta & 0 & 0 & -\sin^2\theta+\cos^2\theta \end{bmatrix} \begin{Bmatrix} \sigma_1 \\ \sigma_2 \\ \tau_{23} \\ \tau_{13} \\ \tau_{12} \end{Bmatrix} \tag{2.15}$$

$$\begin{Bmatrix} \varepsilon_x \\ \varepsilon_y \\ \gamma_{yz} \\ \gamma_{xz} \\ \gamma_{xy} \end{Bmatrix} = \begin{bmatrix} \cos^2\theta & \sin^2\theta & 0 & 0 & -\sin\theta\cos\theta \\ \sin^2\theta & \cos^2\theta & 0 & 0 & \sin\theta\ \cos\theta \\ 0 & 0 & \cos\theta & \sin\theta & 0 \\ 0 & 0 & -\sin\theta & \cos\theta & 0 \\ 2\sin\theta\ \cos\theta & -2\sin\theta\ \cos\theta & 0 & 0 & -\sin^2\theta+\cos^2\theta \end{bmatrix} \begin{Bmatrix} \varepsilon_1 \\ \varepsilon_2 \\ \gamma_{23} \\ \gamma_{13} \\ \gamma_{12} \end{Bmatrix} \tag{2.16}$$

where θ is the fibre angle. One should note that in opposition to CSCL plates, the fibre orientation is changing in VSCL plates and so the fibre coordinates (the material coordinate) are not constant. Using Equation (2.13) and transformation matrices above, the stress-strain relation in the global coordinates is

$$\begin{Bmatrix} \sigma_x \\ \sigma_y \\ \tau_{yz} \\ \tau_{xz} \\ \tau_{xy} \end{Bmatrix}^{(k)} = \begin{bmatrix} \bar{Q}_{11} & \bar{Q}_{12} & 0 & 0 & \bar{Q}_{16} \\ \bar{Q}_{21} & \bar{Q}_{22} & 0 & 0 & \bar{Q}_{26} \\ 0 & 0 & \bar{Q}_{44} & \bar{Q}_{45} & 0 \\ 0 & 0 & \bar{Q}_{54} & \bar{Q}_{55} & 0 \\ \bar{Q}_{61} & \bar{Q}_{62} & 0 & 0 & \bar{Q}_{66} \end{bmatrix}^{(k)} \begin{Bmatrix} \varepsilon_x \\ \varepsilon_y \\ \gamma_{yz} \\ \gamma_{xz} \\ \gamma_{xy} \end{Bmatrix}^{(k)} \tag{2.17}$$

with transformed reduced stiffnesses ($\bar{Q}_{ij}$) depending on the fibre orientation θ defined as (similar formulations but for lamina with straight fibres can be found in Refs. [34, 54])

$$\bar{Q}_{11} = Q_{11}\cos^4\theta + 2\left(Q_{12} + 2Q_{66}\right)\sin^2\theta\cos^2\theta + Q_{22}\sin^4\theta,$$

$$\bar{Q}_{12} = \bar{Q}_{21} = \left(Q_{11} + Q_{22} - 4Q_{66}\right)\sin^2\theta\cos^2\theta + Q_{12}\left(\sin^4\theta + \cos^4\theta\right),$$

$$\bar{Q}_{22} = Q_{11}\sin^4\theta + 2\left(Q_{12} + 2Q_{66}\right)\sin^2\theta\cos^2\theta + Q_{22}\cos^4\theta,$$

$$\bar{Q}_{16} = \bar{Q}_{61} = \left(Q_{11} - Q_{12} - 2Q_{66}\right)\sin\theta\cos^3\theta + \left(Q_{12} - Q_{22} + 2Q_{66}\right)\sin^3\theta\cos\theta,$$

$$\bar{Q}_{26} = \bar{Q}_{62} = \left(Q_{11} - Q_{12} - 2Q_{66}\right)\sin^3\theta\cos\theta + \left(Q_{12} - Q_{22} + 2Q_{66}\right)\sin\theta\cos^3\theta,$$

$$\bar{Q}_{66} = \left(Q_{11} - 2Q_{12} + Q_{22} - 2Q_{66}\right)\sin^2\theta\cos^2\theta + Q_{66}\left(\sin^4\theta + \cos^4\theta\right),$$

$$\bar{Q}_{44} = Q_{44}\cos^2\theta + Q_{55}\sin^2\theta,$$

$$\bar{Q}_{45} = \bar{Q}_{54} = \left(-Q_{44} + Q_{55}\right)\sin\theta\cos\theta,$$

$$\bar{Q}_{55} = Q_{44}\sin^2\theta + Q_{55}\cos^2\theta. \tag{2.18}$$

As follows, by introducing coefficients $U_i,\ (i = 1-7)$, the transformed reduced stiffnesses ($\bar{Q}_{ij}$) can be simplified. Similar expressions but for lamina with straight fibres can be found in Ref. [55].

$$U_1 = \frac{1}{8}\left(3Q_{11} + 2Q_{12} + 3Q_{22} + 4Q_{66}\right),$$

$$U_2 = \frac{1}{2}\left(Q_{11} - Q_{22}\right),$$

$$U_3 = \frac{1}{8}\left(Q_{11} - 2Q_{12} + Q_{22} - 4Q_{66}\right),$$

$$U_4 = \frac{1}{8}\left(Q_{11} + 6Q_{12} + Q_{22} - 4Q_{66}\right),$$

$$U_5 = \frac{1}{8}\left(Q_{11} - 2Q_{12} + Q_{22} + 4Q_{66}\right),$$

$$U_6 = \frac{1}{2}\left(Q_{44} + Q_{55}\right),$$

$$U_7 = \frac{1}{2}\left(Q_{44} - Q_{55}\right), \tag{2.19}$$

and so

$$\bar{Q}_{11}^{(k)} = U_1 + U_2\cos 2\theta_k + U_3\cos 4\theta_k,$$

$$\bar{Q}_{12}^{(k)} = U_4 - U_3\cos 4\theta_k,$$

$$\bar{Q}_{22}^{(k)} = U_1 - U_2\cos 2\theta_k + U_3\cos 4\theta_k,$$

$$\bar{Q}_{16}^{(k)} = \frac{1}{2}U_2\sin 2\theta_k + U_3\sin 4\theta_k,$$

$$\bar{Q}_{26}^{(k)} = \frac{1}{2}U_2\sin 2\theta_k - U_3\sin 4\theta_k,$$

$$\bar{Q}_{66}^{(k)} = U_5 - U_3\cos 4\theta_k,$$

$$\bar{Q}_{44}^{(k)} = U_6 + U_7\cos 2\theta_k,$$

$$\bar{Q}_{45}^{(k)} = -U_7\sin 2\theta_k,$$

$$\bar{Q}_{55}^{(k)} = U_6 - U_7\cos 2\theta_k. \tag{2.20}$$

The following coefficients are going to be used as coefficients in the virtual work principle (here, n stands for number of layers):

$$(A_{ij}, B_{ij}, C_{ij}, D_{ij}, E_{ij}, F_{ij}) = \sum_{k=1}^{n}\int_{z_{k-1}}^{z_k} \bar{Q}_{ij}^{(k)}\left(1, z, z^2, -cz^3, -cz^4, c^2z^6\right)dz,\ i,j = 1,2 \text{ and } 6$$

$$(G_{ij}, H_{ij}, I_{ij}) = \sum_{k=1}^{n} \int_{z_{k-1}}^{z_k} \bar{Q}_{ij}^{(k)} \left(1, -3cz^2, 9c^2z^4\right) dz, \; i, j = 4 \text{ and } 5 \tag{2.21}$$

Replacing Equations (2.20) in Equations (2.21), one obtains

$$\mathbf{A}(x) = \sum_{k=1}^{n} h_k \left(\begin{bmatrix} U_1 & U_4 & 0 \\ U_4 & U_1 & 0 \\ 0 & 0 & U_5 \end{bmatrix} + U_2 \begin{bmatrix} 1 & 0 & 0 \\ 0 & -1 & 0 \\ 0 & 0 & 0 \end{bmatrix} \cos 2\theta_k(x) + U_3 \begin{bmatrix} 1 & -1 & 0 \\ -1 & 1 & 0 \\ 0 & 0 & -1 \end{bmatrix} \right.$$

$$\left. \cos 4\theta_k(x) + \frac{U_2}{2} \begin{bmatrix} 0 & 0 & 1 \\ 0 & 0 & 1 \\ 1 & 1 & 0 \end{bmatrix} \sin 2\theta_k(x) + U_3 \begin{bmatrix} 0 & 0 & 1 \\ 0 & 0 & -1 \\ 1 & -1 & 0 \end{bmatrix} \sin 4\theta_k(x) \right),$$

$$\mathbf{B}(x) = 0,$$

$$\mathbf{C}(x) = \sum_{k=1}^{n} \frac{z_k^3 - z_{k-1}^3}{3} \left(\begin{bmatrix} U_1 & U_4 & 0 \\ U_4 & U_1 & 0 \\ 0 & 0 & U_5 \end{bmatrix} + U_2 \begin{bmatrix} 1 & 0 & 0 \\ 0 & -1 & 0 \\ 0 & 0 & 0 \end{bmatrix} \cos 2\theta_k(x) + U_3 \begin{bmatrix} 1 & -1 & 0 \\ -1 & 1 & 0 \\ 0 & 0 & -1 \end{bmatrix} \right.$$

$$\left. \cos 4\theta_k(x) + \frac{U_2}{2} \begin{bmatrix} 0 & 0 & 1 \\ 0 & 0 & 1 \\ 1 & 1 & 0 \end{bmatrix} \sin 2\theta_k(x) + U_3 \begin{bmatrix} 0 & 0 & 1 \\ 0 & 0 & -1 \\ 1 & -1 & 0 \end{bmatrix} \sin 4\theta_k(x) \right),$$

$$\mathbf{D}(x) = 0,$$

$$\mathbf{E}(x) = \sum_{k=1}^{n} \left(-c \frac{z_k^5 - z_{k-1}^5}{5} \right) \left(\begin{bmatrix} U_1 & U_4 & 0 \\ U_4 & U_1 & 0 \\ 0 & 0 & U_5 \end{bmatrix} + U_2 \begin{bmatrix} 1 & 0 & 0 \\ 0 & -1 & 0 \\ 0 & 0 & 0 \end{bmatrix} \cos 2\theta_k(x) + U_3 \right.$$

$$\left. \begin{bmatrix} 1 & -1 & 0 \\ -1 & 1 & 0 \\ 0 & 0 & -1 \end{bmatrix} \cos 4\theta_k(x) + \frac{U_2}{2} \begin{bmatrix} 0 & 0 & 1 \\ 0 & 0 & 1 \\ 1 & 1 & 0 \end{bmatrix} \sin 2\theta_k(x) + U_3 \begin{bmatrix} 0 & 0 & 1 \\ 0 & 0 & -1 \\ 1 & -1 & 0 \end{bmatrix} \sin 4\theta_k(x) \right),$$

$$\mathbf{F}(x) = \sum_{k=1}^{n} \left(c^2 \frac{z_k^7 - z_{k-1}^7}{7} \right) \left(\begin{bmatrix} U_1 & U_4 & 0 \\ U_4 & U_1 & 0 \\ 0 & 0 & U_5 \end{bmatrix} + U_2 \begin{bmatrix} 1 & 0 & 0 \\ 0 & -1 & 0 \\ 0 & 0 & 0 \end{bmatrix} \cos 2\theta_k(x) + \right.$$

$$U_3 \begin{bmatrix} 1 & -1 & 0 \\ -1 & 1 & 0 \\ 0 & 0 & -1 \end{bmatrix} \cos 4\theta_k(x) + \frac{U_2}{2} \begin{bmatrix} 0 & 0 & 1 \\ 0 & 0 & 1 \\ 1 & 1 & 0 \end{bmatrix} \sin 2\theta_k(x) + U_3 \begin{bmatrix} 0 & 0 & 1 \\ 0 & 0 & -1 \\ 1 & -1 & 0 \end{bmatrix} \sin 4\theta_k(x) \Bigg),$$

$$\mathbf{G}(x) = \sum_{k=1}^{n} h_k \left(U_6 \begin{bmatrix} 1 & 0 \\ 0 & 1 \end{bmatrix} + U_7 \begin{bmatrix} 1 & 0 \\ 0 & -1 \end{bmatrix} \cos 2\theta_k(x) + U_7 \begin{bmatrix} 0 & -1 \\ -1 & 0 \end{bmatrix} \sin 2\theta_k(x) \right),$$

$$\mathbf{H}(x) = \sum_{k=1}^{n} -c\left(z_k^3 - z_{k-1}^3\right) \left(U_6 \begin{bmatrix} 1 & 0 \\ 0 & 1 \end{bmatrix} + U_7 \begin{bmatrix} 1 & 0 \\ 0 & -1 \end{bmatrix} \cos 2\theta_k(x) + U_7 \begin{bmatrix} 0 & -1 \\ -1 & 0 \end{bmatrix} \sin 2\theta_k(x) \right),$$

$$\mathbf{I}(x) = \sum_{k=1}^{n} \frac{9}{5} c^2 \left(z_k^5 - z_{k-1}^5\right) \left(U_6 \begin{bmatrix} 1 & 0 \\ 0 & 1 \end{bmatrix} + U_7 \begin{bmatrix} 1 & 0 \\ 0 & -1 \end{bmatrix} \cos 2\theta_k(x) + U_7 \begin{bmatrix} 0 & -1 \\ -1 & 0 \end{bmatrix} \sin 2\theta_k(x) \right). \tag{2.22}$$

Because only symmetric laminated plates will be analised, there is no coupling between in-plane stretching and transverse bending, therefore **B** and **D** are null matrices. The plate equations of motion are derived by equating the sum of the virtual works of inertia forces (δW_j) and elastic (internal) restoring forces (δW_{in}) to zero.

$$\delta W_j + \delta W_{in} = 0 \tag{2.23}$$

The virtual work of the elastic restoring (internal) forces is:

$$\delta W_{in} = -\int_V \begin{Bmatrix} \delta\varepsilon_x \\ \delta\varepsilon_y \\ \delta\gamma_{xy} \\ \delta\gamma_{yz} \\ \delta\gamma_{xz} \end{Bmatrix}^T \begin{Bmatrix} \sigma_x \\ \sigma_y \\ \tau_{xy} \\ \tau_{yz} \\ \tau_{xz} \end{Bmatrix} dV \tag{2.24}$$

Extending strains and stresses in the equation above, the internal work is (for simplicity, matrix $\mathbf{A}(x)$ is denoted by **A** and etc.)

$$\delta W_{in} = -\int_\Omega \Big(\delta\boldsymbol{\varepsilon}_o^{pT} \mathbf{A} \boldsymbol{\varepsilon}_o^p + \delta\boldsymbol{\varepsilon}_o^{bT} (\mathbf{C} + 2\mathbf{E} + \mathbf{F}) \boldsymbol{\varepsilon}_o^b + \delta\boldsymbol{\varepsilon}_o^{bT} (\mathbf{E} + \mathbf{F}) \boldsymbol{\varepsilon}_o^{b1} + \delta\boldsymbol{\varepsilon}_o^{b1T} (\mathbf{E} + \mathbf{F}) \boldsymbol{\varepsilon}_o^b +$$

$$\delta\boldsymbol{\varepsilon}_o^{b1T} \mathbf{F} \boldsymbol{\varepsilon}_o^{b1} + \delta\boldsymbol{\gamma}_o^{pT} (\mathbf{G} + 2\mathbf{H} + \mathbf{I}) \boldsymbol{\gamma}_o^p + \delta\boldsymbol{\varepsilon}_o^{p1T} \mathbf{A} \boldsymbol{\varepsilon}_o^p + \delta\boldsymbol{\varepsilon}_o^{pT} \mathbf{A} \boldsymbol{\varepsilon}_o^{p1} + \delta\boldsymbol{\varepsilon}_o^{p1T} \mathbf{A} \boldsymbol{\varepsilon}_o^{p1} \Big) d\Omega \tag{2.25}$$

where Ω is the surface of the plate. According to the Equation (2.25), the virtual work of internal forces has nine terms; one can calculate the first term as

$$\delta\boldsymbol{\varepsilon}_o^{pT}\mathbf{A}\boldsymbol{\varepsilon}_o^p = \left\{\begin{array}{c}\delta\mathbf{q_u}\\ \delta\mathbf{q_v}\end{array}\right\}^T \left[\begin{array}{ccc}\mathbf{N}^{\mathbf{u}}_{,x} & \mathbf{0} & \mathbf{N}^{\mathbf{u}}_{,y}\\ \mathbf{0} & \mathbf{N}^{\mathbf{u}}_{,y} & \mathbf{N}^{\mathbf{u}}_{,x}\end{array}\right]\mathbf{A}\left[\begin{array}{cc}\mathbf{N}^{\mathbf{u}\,T}_{,x} & \mathbf{0}\\ \mathbf{0} & \mathbf{N}^{\mathbf{u}\,T}_{,y}\\ \mathbf{N}^{\mathbf{u}\,T}_{,y} & \mathbf{N}^{\mathbf{u}\,T}_{,x}\end{array}\right]\left\{\begin{array}{c}\mathbf{q_u}\\ \mathbf{q_v}\end{array}\right\} =$$

$$\left\{\begin{array}{c}\delta\mathbf{q_u}\\ \delta\mathbf{q_v}\end{array}\right\}^T \left[\begin{array}{cc}\mathbf{K}^{11}_{\mathbf{L1}} & \mathbf{K}^{12}_{\mathbf{L1}}\\ \mathbf{K}^{21}_{\mathbf{L1}} & \mathbf{K}^{22}_{\mathbf{L1}}\end{array}\right]\left\{\begin{array}{c}\mathbf{q_u}\\ \mathbf{q_v}\end{array}\right\}. \tag{2.26}$$

The second term is

$$\delta\boldsymbol{\varepsilon}_o^{bT}(\mathbf{C}+2\mathbf{E}+\mathbf{F})\boldsymbol{\varepsilon}_o^b = \left\{\begin{array}{c}\delta\mathbf{q}_{\boldsymbol{\phi}_\mathbf{x}}\\ \delta\mathbf{q}_{\boldsymbol{\phi}_\mathbf{y}}\end{array}\right\}^T \left[\begin{array}{ccc}\mathbf{N}^{\boldsymbol{\phi}_\mathbf{x}}_{,x} & \mathbf{0} & \mathbf{N}^{\boldsymbol{\phi}_\mathbf{x}}_{,y}\\ \mathbf{0} & \mathbf{N}^{\boldsymbol{\phi}_\mathbf{y}}_{,y} & \mathbf{N}^{\boldsymbol{\phi}_\mathbf{y}}_{,x}\end{array}\right](\mathbf{C}+2\mathbf{E}+\mathbf{F})\left[\begin{array}{cc}\mathbf{N}^{\boldsymbol{\phi}_\mathbf{x}\,T}_{,x} & \mathbf{0}\\ \mathbf{0} & \mathbf{N}^{\boldsymbol{\phi}_\mathbf{y}\,T}_{,y}\\ \mathbf{N}^{\boldsymbol{\phi}_\mathbf{x}\,T}_{,y} & \mathbf{N}^{\boldsymbol{\phi}_\mathbf{y}\,T}_{,x}\end{array}\right]$$

$$\left\{\begin{array}{c}\mathbf{q}_{\boldsymbol{\phi}_x}\\ \mathbf{q}_{\boldsymbol{\phi}_y}\end{array}\right\} = \left\{\begin{array}{c}\delta\mathbf{q}_{\boldsymbol{\phi}_\mathbf{x}}\\ \delta\mathbf{q}_{\boldsymbol{\phi}_\mathbf{y}}\end{array}\right\}^T \left[\begin{array}{cc}\mathbf{K}^{44}_{\mathbf{L1}} & \mathbf{K}^{45}_{\mathbf{L1}}\\ \mathbf{K}^{54}_{\mathbf{L1}} & \mathbf{K}^{55}_{\mathbf{L1}}\end{array}\right]\left\{\begin{array}{c}\mathbf{q}_{\boldsymbol{\phi}_\mathbf{x}}\\ \mathbf{q}_{\boldsymbol{\phi}_\mathbf{y}}\end{array}\right\}. \tag{2.27}$$

The third term is

$$\delta\boldsymbol{\varepsilon}_o^{bT}(\mathbf{E}+\mathbf{F})\boldsymbol{\varepsilon}_o^{b1} = \left\{\begin{array}{c}\delta\mathbf{q}_{\boldsymbol{\phi}_\mathbf{x}}\\ \delta\mathbf{q}_{\boldsymbol{\phi}_\mathbf{y}}\end{array}\right\}^T \left[\begin{array}{ccc}\mathbf{N}^{\boldsymbol{\phi}_\mathbf{x}}_{,x} & \mathbf{0} & \mathbf{N}^{\boldsymbol{\phi}_\mathbf{x}}_{,y}\\ \mathbf{0} & \mathbf{N}^{\boldsymbol{\phi}_\mathbf{y}}_{,y} & \mathbf{N}^{\boldsymbol{\phi}_\mathbf{y}}_{,x}\end{array}\right](\mathbf{E}+\mathbf{F})\left\{\begin{array}{c}\mathbf{N}^{\mathbf{w}\,T}_{,xx}\\ \mathbf{N}^{\mathbf{w}\,T}_{,yy}\\ 2\mathbf{N}^{\mathbf{w}\,T}_{,xy}\end{array}\right\}\mathbf{q_w}$$

$$= \left\{\begin{array}{c}\delta\mathbf{q}_{\boldsymbol{\phi}_\mathbf{x}}\\ \delta\mathbf{q}_{\boldsymbol{\phi}_\mathbf{y}}\end{array}\right\}^T \left[\begin{array}{c}\mathbf{K}^{43}_{\mathbf{L1}}\\ \mathbf{K}^{53}_{\mathbf{L1}}\end{array}\right]\mathbf{q_w}; \tag{2.28}$$

the fourth term in Equation (2.25) is defined as the transpose of the third term. It can be shown as

$$\delta\boldsymbol{\varepsilon}_o^{b1\,T}(\mathbf{E}+\mathbf{F})\boldsymbol{\varepsilon}_o^b = \delta\mathbf{q_w}^T\left[\begin{array}{c}\mathbf{K}^{43\,T}_{\mathbf{L1}}\\ \mathbf{K}^{53\,T}_{\mathbf{L1}}\end{array}\right]\left\{\begin{array}{c}\delta\mathbf{q}_{\boldsymbol{\phi}_\mathbf{x}}\\ \delta\mathbf{q}_{\boldsymbol{\phi}_\mathbf{y}}\end{array}\right\} = \delta\mathbf{q_w}^T\left[\begin{array}{cc}\mathbf{K}^{34}_{\mathbf{L1}} & \mathbf{K}^{35}_{\mathbf{L1}}\end{array}\right]\left\{\begin{array}{c}\delta\mathbf{q}_{\boldsymbol{\phi}_\mathbf{x}}\\ \delta\mathbf{q}_{\boldsymbol{\phi}_\mathbf{y}}\end{array}\right\}. \tag{2.29}$$

The fifth term is expressed as

$$\delta\boldsymbol{\varepsilon}_o^{b1\,T}\mathbf{F}\boldsymbol{\varepsilon}_o^{b1} = \delta\mathbf{q_w}^T\left[\begin{array}{ccc}\mathbf{N}^{\mathbf{w}}_{,xx} & \mathbf{N}^{\mathbf{w}}_{,yy} & 2\mathbf{N}^{\mathbf{w}}_{,xy}\end{array}\right]\mathbf{F}\left\{\begin{array}{c}\mathbf{N}^{\mathbf{w}\,T}_{,xx}\\ \mathbf{N}^{\mathbf{w}\,T}_{,yy}\\ 2\mathbf{N}^{\mathbf{w}\,T}_{,xy}\end{array}\right\}\mathbf{q_w} = \delta\mathbf{q_w}^T\mathbf{K}^{33}_{\mathbf{L1}}\mathbf{q_w}. \tag{2.30}$$

The sixth term is defined as

$$\delta\boldsymbol{\gamma}_o^{pT}\left(\mathbf{G}+2\mathbf{H}+\mathbf{I}\right)\boldsymbol{\gamma}_o^{p}=\left\{\begin{array}{c}\delta\mathbf{q_w}\\ \delta\mathbf{q}_{\boldsymbol{\phi}_\mathbf{x}}\\ \delta\mathbf{q}_{\boldsymbol{\phi}_\mathbf{y}}\end{array}\right\}^T\left[\begin{array}{cc}\mathbf{N}^{\mathbf{w}}_{,y} & \mathbf{N}^{\mathbf{w}}_{,x}\\ \mathbf{0} & \mathbf{N}^{\boldsymbol{\phi}_\mathbf{x}}\\ \mathbf{N}^{\boldsymbol{\phi}_\mathbf{y}} & \mathbf{0}\end{array}\right]\left(\mathbf{G}+2\mathbf{H}+\mathbf{I}\right)\left[\begin{array}{ccc}\mathbf{N}^{\mathbf{w}T}_{,y} & \mathbf{0} & \mathbf{N}^{\boldsymbol{\phi}_\mathbf{y}T}\\ \mathbf{N}^{\mathbf{w}T}_{,x} & \mathbf{N}^{\boldsymbol{\phi}_\mathbf{x}T} & \mathbf{0}\end{array}\right]$$

$$\left\{\begin{array}{c}\mathbf{q_w}\\ \mathbf{q}_{\boldsymbol{\phi}_\mathbf{x}}\\ \mathbf{q}_{\boldsymbol{\phi}_\mathbf{y}}\end{array}\right\}=\left\{\begin{array}{c}\delta\mathbf{q_w}\\ \delta\mathbf{q}_{\boldsymbol{\phi}_\mathbf{x}}\\ \delta\mathbf{q}_{\boldsymbol{\phi}_\mathbf{y}}\end{array}\right\}^T\left[\begin{array}{ccc}\mathbf{K}^{33}_{\mathbf{L2}} & \mathbf{K}^{34}_{\mathbf{L2}} & \mathbf{K}^{35}_{\mathbf{L2}}\\ \mathbf{K}^{43}_{\mathbf{L2}} & \mathbf{K}^{44}_{\mathbf{L2}} & \mathbf{K}^{45}_{\mathbf{L2}}\\ \mathbf{K}^{53}_{\mathbf{L2}} & \mathbf{K}^{54}_{\mathbf{L2}} & \mathbf{K}^{55}_{\mathbf{L2}}\end{array}\right]\left\{\begin{array}{c}\mathbf{q_w}\\ \mathbf{q}_{\boldsymbol{\phi}_\mathbf{x}}\\ \mathbf{q}_{\boldsymbol{\phi}_\mathbf{y}}\end{array}\right\}. \tag{2.31}$$

The seventh, eighth and ninth terms are affected by imperfection, where the seventh term is

$$\delta\boldsymbol{\varepsilon}_o^{p1^T}\mathbf{A}\boldsymbol{\varepsilon}_o^{p}=\frac{1}{2}\delta\mathbf{q_w}^T\left\{\begin{array}{c}w_{i,x}\mathbf{N}^{\mathbf{w}}_{,x}\\ w_{i,y}\mathbf{N}^{\mathbf{w}}_{,y}\\ w_{i,x}\mathbf{N}^{\mathbf{w}}_{,y}+w_{i,y}\mathbf{N}^{\mathbf{w}}_{,x}\end{array}\right\}^T\mathbf{A}\left[\begin{array}{cc}\mathbf{N}^{\mathbf{u}\,T}_{,x} & \mathbf{0}\\ \mathbf{0} & \mathbf{N}^{\mathbf{u}\,T}_{,y}\\ \mathbf{N}^{\mathbf{u}\,T}_{,y} & \mathbf{N}^{\mathbf{u}\,T}_{,x}\end{array}\right]\left\{\begin{array}{c}\mathbf{q_u}\\ \mathbf{q_v}\end{array}\right\}=$$

$$\delta\mathbf{q_w}^T\left[\begin{array}{cc}\mathbf{K}^{31}_{\mathbf{L3}} & \mathbf{K}^{32}_{\mathbf{L3}}\end{array}\right]\left\{\begin{array}{c}\mathbf{q_u}\\ \mathbf{q_v}\end{array}\right\} \tag{2.32}$$

The eighth term is the transpose of the seventh term as

$$\delta\boldsymbol{\varepsilon}_o^{pT}\mathbf{A}\boldsymbol{\varepsilon}_o^{p1}=\left\{\begin{array}{cc}\delta\mathbf{q_u} & \delta\mathbf{q_v}\end{array}\right\}^T\left[\begin{array}{c}\mathbf{K}^{13}_{\mathbf{L3}}\\ \mathbf{K}^{23}_{\mathbf{L3}}\end{array}\right]\mathbf{q_w} \tag{2.33}$$

while

$$\left[\begin{array}{c}\mathbf{K}^{13}_{\mathbf{L3}}\\ \mathbf{K}^{23}_{\mathbf{L3}}\end{array}\right]=\left[\begin{array}{cc}\mathbf{K}^{31}_{\mathbf{L3}} & \mathbf{K}^{32}_{\mathbf{L3}}\end{array}\right]^T \tag{2.34}$$

The ninth term is defined as

$$\delta\boldsymbol{\varepsilon}_o^{p1^T}\mathbf{A}\boldsymbol{\varepsilon}_o^{p1}=\frac{1}{4}\delta\mathbf{q_w}^T\left\{\begin{array}{c}w_{i,x}\mathbf{N}^{\mathbf{w}}_{,x}\\ w_{i,y}\mathbf{N}^{\mathbf{w}}_{,y}\\ w_{i,x}\mathbf{N}^{\mathbf{w}}_{,y}+w_{i,y}\mathbf{N}^{\mathbf{w}}_{,x}\end{array}\right\}^T\mathbf{A}\left\{\begin{array}{c}w_{i,x}\mathbf{N}^{\mathbf{w}}_{,x}\\ w_{i,y}\mathbf{N}^{\mathbf{w}}_{,y}\\ w_{i,x}\mathbf{N}^{\mathbf{w}}_{,y}+w_{i,y}\mathbf{N}^{\mathbf{w}}_{,x}\end{array}\right\}\mathbf{q_w}=\delta\mathbf{q_w}^T\mathbf{K}^{33}_{\mathbf{L3}}\mathbf{q_w} \tag{2.35}$$

So the internal virtual work, given in Equation (2.25), can be written as

$$\delta W_{in}=-\int_\Omega\delta\left\{\begin{array}{c}\mathbf{q_u}\\ \mathbf{q_v}\\ \mathbf{q_w}\\ \mathbf{q}_{\boldsymbol{\phi}_\mathbf{x}}\\ \mathbf{q}_{\boldsymbol{\phi}_\mathbf{y}}\end{array}\right\}^T\left[\begin{array}{ccccc}\mathbf{K}^{11}_{\mathbf{L}} & \mathbf{K}^{12}_{\mathbf{L}} & \mathbf{K}^{13}_{\mathbf{L}} & \mathbf{0} & \mathbf{0}\\ & \mathbf{K}^{22}_{\mathbf{L}} & \mathbf{K}^{23}_{\mathbf{L}} & \mathbf{0} & \mathbf{0}\\ & & \mathbf{K}^{33}_{\mathbf{L}} & \mathbf{K}^{34}_{\mathbf{L}} & \mathbf{K}^{35}_{\mathbf{L}}\\ & & & \mathbf{K}^{44}_{\mathbf{L}} & \mathbf{K}^{45}_{\mathbf{L}}\\ sym & & & & \mathbf{K}^{55}_{\mathbf{L}}\end{array}\right]\left\{\begin{array}{c}\mathbf{q_u}\\ \mathbf{q_v}\\ \mathbf{q_w}\\ \mathbf{q}_{\boldsymbol{\phi}_\mathbf{x}}\\ \mathbf{q}_{\boldsymbol{\phi}_\mathbf{y}}\end{array}\right\}d\Omega \tag{2.36}$$

Above, generalised coordinate vectors $\mathbf{q_k}, (\mathbf{k} = \mathbf{u}, \mathbf{v}, \mathbf{w}, \boldsymbol{\phi}_\mathbf{x}, \boldsymbol{\phi}_\mathbf{y})$ are variables and linear stiffness sub-matrices $\mathbf{K}_\mathbf{L}^{ij}, (i, j = 1-5)$ are constant. These sub-matrices are defined as

$$\begin{bmatrix} \mathbf{K}_\mathbf{L}^{11} & \mathbf{K}_\mathbf{L}^{12} & \mathbf{K}_\mathbf{L}^{13} & \mathbf{0} & \mathbf{0} \\ & \mathbf{K}_\mathbf{L}^{22} & \mathbf{K}_\mathbf{L}^{23} & \mathbf{0} & \mathbf{0} \\ & & \mathbf{K}_\mathbf{L}^{33} & \mathbf{K}_\mathbf{L}^{34} & \mathbf{K}_\mathbf{L}^{35} \\ & & & \mathbf{K}_\mathbf{L}^{44} & \mathbf{K}_\mathbf{L}^{45} \\ sym & & & & \mathbf{K}_\mathbf{L}^{55} \end{bmatrix} = \begin{bmatrix} \mathbf{K}_\mathbf{L1}^{11} & \mathbf{K}_\mathbf{L1}^{12} & \mathbf{0} & \mathbf{0} & \mathbf{0} \\ & \mathbf{K}_\mathbf{L1}^{22} & \mathbf{0} & \mathbf{0} & \mathbf{0} \\ & & \mathbf{K}_\mathbf{L1}^{33} & \mathbf{K}_\mathbf{L1}^{34} & \mathbf{K}_\mathbf{L1}^{35} \\ & & & \mathbf{K}_\mathbf{L1}^{44} & \mathbf{K}_\mathbf{L1}^{45} \\ sym & & & & \mathbf{K}_\mathbf{L1}^{55} \end{bmatrix}$$

$$+ \begin{bmatrix} \mathbf{0} & \mathbf{0} & \mathbf{0} & \mathbf{0} & \mathbf{0} \\ & \mathbf{0} & \mathbf{0} & \mathbf{0} & \mathbf{0} \\ & & \mathbf{K}_\mathbf{L2}^{33} & \mathbf{K}_\mathbf{L2}^{34} & \mathbf{K}_\mathbf{L2}^{35} \\ & & & \mathbf{K}_\mathbf{L2}^{44} & \mathbf{K}_\mathbf{L2}^{45} \\ sym & & & & \mathbf{K}_\mathbf{L2}^{55} \end{bmatrix} + \begin{bmatrix} \mathbf{0} & \mathbf{0} & \mathbf{K}_\mathbf{L3}^{13} & \mathbf{0} & \mathbf{0} \\ & \mathbf{0} & \mathbf{K}_\mathbf{L3}^{23} & \mathbf{0} & \mathbf{0} \\ & & \mathbf{K}_\mathbf{L3}^{33} & \mathbf{0} & \mathbf{0} \\ & & & \mathbf{0} & \mathbf{0} \\ sym & & & & \mathbf{0} \end{bmatrix} \tag{2.37}$$

Above, $\mathbf{K}_\mathbf{L1}^{ij}$ and $\mathbf{K}_\mathbf{L2}^{ij}$ are the linear stiffness sub-matrices for a perfect VSCL plate and $\mathbf{K}_\mathbf{L3}^{ij}$ are the linear stiffness sub-matrices due to an imperfection.

The virtual work of inertia forces is

$$\delta W_j = -\int_{-\frac{h}{2}}^{\frac{h}{2}} \int_\Omega \rho \left(\delta u \ddot{u} + \delta v \ddot{v} + \delta w \ddot{w}\right) d\Omega dz \tag{2.38}$$

Here, two over-dots is the second derivation with respect to time, and ρ is the density of the plate. Using Equations (2.1) and (2.2), the virtual work of inertia forces can be written as

$$\delta W_j = \int_\Omega \delta \begin{Bmatrix} \mathbf{q_u} \\ \mathbf{q_v} \\ \mathbf{q_w} \\ \mathbf{q}_{\boldsymbol{\phi}_\mathbf{x}} \\ \mathbf{q}_{\boldsymbol{\phi}_\mathbf{y}} \end{Bmatrix}^T \begin{bmatrix} \mathbf{M}^{11} & \mathbf{0} & \mathbf{0} & \mathbf{0} & \mathbf{0} \\ & \mathbf{M}^{22} & \mathbf{0} & \mathbf{0} & \mathbf{0} \\ & & \mathbf{M}^{33} & \mathbf{M}^{34} & \mathbf{M}^{35} \\ & & & \mathbf{M}^{44} & \mathbf{0} \\ sym & & & & \mathbf{M}^{55} \end{bmatrix} \begin{Bmatrix} \ddot{\mathbf{q}}_\mathbf{u} \\ \ddot{\mathbf{q}}_\mathbf{v} \\ \ddot{\mathbf{q}}_\mathbf{w} \\ \ddot{\mathbf{q}}_{\boldsymbol{\phi}_\mathbf{x}} \\ \ddot{\mathbf{q}}_{\boldsymbol{\phi}_\mathbf{y}} \end{Bmatrix} d\Omega \tag{2.39}$$

The mass sub-matrices are defined as

$$\mathbf{M}^{11} = \mathbf{M}^{22} = \rho h \int_\Omega \mathbf{N}^\mathbf{u} \mathbf{N}^{\mathbf{u}T} d\Omega,$$

$$\mathbf{M}^{33} = \rho h \int_\Omega \mathbf{N}^\mathbf{w} \mathbf{N}^{\mathbf{w}T} d\Omega + \frac{\rho h^3}{252} \int_\Omega \left(\mathbf{N}^\mathbf{w}_{,x} \mathbf{N}^{\mathbf{w}T}_{,x} + \mathbf{N}^\mathbf{w}_{,y} \mathbf{N}^{\mathbf{w}T}_{,y}\right) d\Omega,$$

$$\mathbf{M}^{34} = -\frac{4\rho h^3}{315} \int_\Omega \mathbf{N}^\mathbf{w}_{,x} \mathbf{N}^{\boldsymbol{\phi}_\mathbf{x}T} d\Omega,$$

$$\mathbf{M}^{35} = -\frac{4\rho h^3}{315} \int_\Omega \mathbf{N}^\mathbf{w}_{,y} \mathbf{N}^{\boldsymbol{\phi}_\mathbf{y}T} d\Omega,$$

$$\mathbf{M}^{44} = -\frac{17\rho h^3}{315}\int_{\Omega} \mathbf{N}^{\boldsymbol{\phi}_x}{\mathbf{N}^{\boldsymbol{\phi}_x}}^T d\Omega,$$

$$\mathbf{M}^{55} = -\frac{17\rho h^3}{315}\int_{\Omega} \mathbf{N}^{\boldsymbol{\phi}_y}{\mathbf{N}^{\boldsymbol{\phi}_y}}^T d\Omega. \tag{2.40}$$

Considering harmonic oscillations, the second derivatives of generalised displacements with respect to time are $\ddot{\mathbf{q}}(t) = -\omega^2\mathbf{q}(t)$; then, as a result of the virtual work principle, Equation (2.23), one can obtain

$$\begin{bmatrix} \mathbf{M}^{11} & \mathbf{0} & \mathbf{0} & \mathbf{0} & \mathbf{0} \\ & \mathbf{M}^{22} & \mathbf{0} & \mathbf{0} & \mathbf{0} \\ & & \mathbf{M}^{33} & \mathbf{M}^{34} & \mathbf{M}^{35} \\ & & & \mathbf{M}^{44} & \mathbf{0} \\ sym & & & & \mathbf{M}^{55} \end{bmatrix} \begin{Bmatrix} \ddot{\mathbf{q}}_{\mathbf{u}} \\ \ddot{\mathbf{q}}_{\mathbf{v}} \\ \ddot{\mathbf{q}}_{\mathbf{w}} \\ \ddot{\mathbf{q}}_{\boldsymbol{\phi}_x} \\ \ddot{\mathbf{q}}_{\boldsymbol{\phi}_y} \end{Bmatrix} + \begin{bmatrix} \mathbf{K}_{\mathbf{L}}^{11} & \mathbf{K}_{\mathbf{L}}^{12} & \mathbf{K}_{\mathbf{L}}^{13} & \mathbf{0} & \mathbf{0} \\ & \mathbf{K}_{\mathbf{L}}^{22} & \mathbf{K}_{\mathbf{L}}^{23} & \mathbf{0} & \mathbf{0} \\ & & \mathbf{K}_{\mathbf{L}}^{33} & \mathbf{K}_{\mathbf{L}}^{34} & \mathbf{K}_{\mathbf{L}}^{35} \\ & & & \mathbf{K}_{\mathbf{L}}^{44} & \mathbf{K}_{\mathbf{L}}^{45} \\ sym & & & & \mathbf{K}_{\mathbf{L}}^{55} \end{bmatrix} \begin{Bmatrix} \mathbf{q}_{\mathbf{u}} \\ \mathbf{q}_{\mathbf{v}} \\ \mathbf{q}_{\mathbf{w}} \\ \mathbf{q}_{\boldsymbol{\phi}_x} \\ \mathbf{q}_{\boldsymbol{\phi}_y} \end{Bmatrix} = \begin{Bmatrix} \mathbf{0} \\ \mathbf{0} \\ \mathbf{0} \\ \mathbf{0} \\ \mathbf{0} \end{Bmatrix} \tag{2.41}$$

From Equation (2.41), an eigenvalue problem can be derived, where the eigenvalues are the square of linear natural frequencies ω_{li} and the eigenvectors $\boldsymbol{\phi}_i$ define the corresponding mode shapes of vibration.

2.3 Numerical Results

In this section, natural frequencies and mode shapes of vibration of various plates are given. The superior convergence rate of the *p*-version finite element method in smooth linear problems has been proved by well-posed theoretical arguments [56]. Numerical tests, where the high convergence rate of displacement based plate *p*-version finite elements was confirmed in linear and nonlinear problems, can, for example, be found in [57–63]. The aim of this study is to show the convergence properties of the *p*-element proposed for VSCL, to investigate how does the variable stiffness influence the natural modes of vibration, and if plates with different thickness and with different boundary conditions are affected in a diverse way by the variation of the fibre orientation. The properties of the plates analised are defined in Table 2.1.

2.3.1 Convergence Study

Convergence studies were carried out and some of them are here shown, with the goal of demonstrating that an accurate *p*-version model can be constructed with a small number of DOF. Tables

Table 2.1: Characteristics of the plates studied.

a (m)	b (m)	h (m)	E_1 (GPa)	E_2 (GPa)	G_{12} (GPa)	G_{13} (GPa)	G_{23} (GPa)	ν_{12}	ρ (kg/m^3)
Plate 1 VSCL									
1	1	0.01-0.1	173	7.2	3.76	3.76	3.76	0.29	1540
Plate 2 CSCL									
1	1	0.1	173	33.1	9.38	8.27	3.24	0.25	1000
Plate 3 CSCL									
0.48	0.32	0.001	120.5	90.63	3.58	3.58	3.58	0.32	1540
Plate 4 CSCL									
0.2	0.1	0.001	131.7	9.86	4.21	4.21	4.21	0.28	1600
Plate 5 VSCL (experiment)									
0.4	0.3	0.00177	126.3	8.765	4.92	4.92	3.35	0.334	1580
Plate 6 VSCL (with imperfection)									
0.2085	0.21	0.0003	198	198	76.15	76.15	76.15	0.3	7850
Plate 7 VSCL (with imperfection)									
1	1	0.1	207.79	207.79	79.92	79.92	79.92	0.3177	8166

2.2 and 2.3 show the convergence of the linear natural frequency of a VSCL plate with the number of in-plane, rotational and out-of-plane shape functions used. The VSCL plate considered here is a three-layer $[\langle 0^o, 45^o\rangle, \langle -45^o, -60^o\rangle, \langle 0^o, 45^o\rangle]$ laminate plate with characteristics given in Table 2.1 as Plate 1. Taking as reference the model with $p = p_u = p_w = p_\phi = 19$, the maximum relative error of natural frequencies computed with the model taking $p = p_u = p_w = p_\phi = 10$ is 0.21%. Here, ten out-of-plane, in-plane, and rotational shape functions (500 DOF totally) give a very good approximation to the first eight linear natural frequencies, and this element is used in the analyses that follow in this chapter, unless otherwise specified.

2.3.2 Comparison with Numerical Results

The model here employed is validated by comparing its results with the linear natural frequencies obtained elsewhere (including Refs. [61, 64–69]). For that purpose, the model is applied to CSCL plates with different thickness to length ratios in Tables 2.4, 2.5, and 2.6. The linear vibration results of the model for VSCLs plate are compared with experimental results in Section 2.3.3.

The following boundary conditions are considered: simply-supported with movable edges (SSSS-2), clamped, and free (see Appendix A). These comparisons show a good agreement between the results of the present TSDT model and published data, computed via models based on classical, first-order, or higher-order shear deformation theories. Ref. [64] used a layerwise B-spline finite strip method (LWB). A layerwise plate theory (LWPT), an exact 3-D elasticity solution, a higher-order shear deformable plate theory (HSDPT), a first-order shear deformable plate theory (FSDPT or FSDT), and a classical plate theory (CPT) are used in Ref. [65]. Classical plate theory is used in Ref. [66], and FSDT is applied in Refs. [61, 67]. Ref. [68] applied a higher-order theory with FEM and Ref. [69] a thin plate theory with Rayleigh Ritz. The characteristics of the plates used here are given in Table 2.1. Plate 2, in Table 2.4, is a three-layer $[0^o, 90^o, 0^o]$ laminate

Table 2.2: Convergence of the linear natural frequency of a VSCL plate with in-plane and rotation shape functions.

p_u, p_w, p_ϕ	Mode							
	1	2	3	4	5	6	7	8
$4,10,4$	3881.9	5792.0	7912.9	8659.4	9519.6	11714	12643	14032
$5,10,5$	3874.3	5738.0	7788.8	8606.9	9450.0	11568	12533	12675
$6,10,6$	3871.0	5732.1	7778.9	8434.2	9379.0	11405	12420	12648
$7,10,7$	3867.8	5721.1	7768.5	8417.1	9367.6	11333	12164	12414
$8,10,8$	3858.6	5715.8	7759.6	8412.4	9344.3	11308	12142	12381
$9,10,9$	3858.0	5712.8	7739.3	8408.9	9329.6	11298	12136	12371
$10,10,10$	3856.6	5711.7	7738.7	8405.9	9327.6	11294	12135	12341
$11,11,11$	3855.7	5709.9	7734.9	8398.7	9324.2	11287	12128	12332
$12,12,12$	3853.8	5707.1	7733.2	8396.3	9319.5	11281	12119	12328
$13,13,13$	3853.8	5706.7	7730.7	8393.7	9317.5	11278	12117	12328
$14,14,14$	3852.9	5705.5	7729.3	8392.2	9314.9	11274	12113	12322
$15,15,15$	3852.7	5705.1	7728.9	8390.9	9314.4	11273	12112	12320
$17,17,17$	3852.2	5704.5	7728.3	8389.8	9313.2	11271	12109	12319
$19,19,19$	3852.1	5704.2	7728.2	8389.3	9313.0	11271	12109	12318

Table 2.3: Convergence of the linear natural frequency of a VSCL plate with out-of-plane shape functions.

p_u, p_w, p_ϕ	Mode							
	1	2	3	4	5	6	7	8
$10,4,10$	3901.9	5762.8	7867.8	8494.5	9532.7	11491	12431	12522
$10,5,10$	3874.5	5750.8	7819.7	8473.5	9409.1	11404	12358	12449
$10,6,10$	3872.1	5731.7	7772.6	8460.6	9376.8	11379	12234	12412
$10,7,10$	3862.1	5726.4	7767.0	8425.4	9359.4	11341	12224	12370
$10,8,10$	3860.4	5716.9	7748.2	8417.4	9344.3	11317	12155	12366
$10,9,10$	3856.8	5715.1	7743.7	8406.8	9332.7	11299	12145	12344
$10,10,10$	3856.6	5711.7	7738.7	8405.9	9327.6	11294	12135	12341
$13,13,13$	3853.8	5706.7	7730.7	8393.7	9317.5	11278	12117	12328
$14,14,14$	3852.9	5705.5	7729.3	8392.2	9314.9	11274	12113	12322
$15,15,15$	3852.7	5705.1	7728.9	8390.9	9314.4	11273	12112	12320
$17,17,17$	3852.2	5704.5	7728.3	8389.8	9313.2	11271	12109	12319
$19,19,19$	3852.1	5704.2	7728.2	8389.3	9313.0	11271	12109	12318

plate. Plate 3, in Table 2.5, is an eight-layer $[2\theta,-\theta,\theta,0^{o}]_{sym}$ laminate plate and Plate 4, in Table 2.6, is a thirty two-layer $[(-45^{o},45^{o})_{8}]_{sym}$ laminate plate.

Table 2.4: Natural frequency parameters $\omega h\sqrt{\rho/E_2}$ of simply-supported CSCL Plate 2.

Method	Mode							
	1	2	3	4	5	6	7	8
LWB [64]	0.06715	0.12819	0.17230	0.20811	0.22868	0.28423	0.29358	0.31807
LWPT [65]	0.06716	0.12816	0.17225	0.20808	0.22864	0.28415	0.29549	0.31973
Exact [65]	0.06715	0.12811	0.17217	0.20798	-	-	-	-
HSDPT [65]	0.06839	0.11301	0.17921	0.21526	-	-	-	-
FSDPT [65]	0.06931	0.12886	0.18674	0.22055	-	-	-	-
CPT [65]	0.07769	0.15185	0.26599	0.31077	-	-	-	-
Present								
$p=9$	0.06858	0.13046	0.17952	0.21563	0.23160	0.29165	0.30622	0.33103
$p=10$	0.06858	0.13046	0.17952	0.21563	0.23158	0.29164	0.30621	0.33103
$p=13$	0.06858	0.13046	0.17952	0.21563	0.23158	0.29164	0.30621	0.33103

Table 2.5: Natural frequencies (rad/s) of clamped CSCL Plate 3. (Present results are calculated using $p=10$)

Method	Mode							
	1	2	3	4	5	6	7	8
$\theta=45^{o}$								
CPT [66]	511.387	645.281	886.217	-	-	-	-	-
FSDT [67]	511.083	644.870	885.608	1231.88	1339.55	1470.12	1692.10	1698.88
Present	511.103	644.876	885.586	1231.81	1339.69	1470.22	1690.36	1698.92
$\theta=60^{o}$								
FSDT [67]	473.502	606.411	829.030	1129.90	1238.95	1366.27	1539.49	1606.11
Present	473.505	606.409	829.022	1129.87	1238.97	1366.23	1538.39	1606.08
$\theta=90^{o}$								
FSDT [67]	433.776	680.754	1070.14	1153.52	1213.96	1557.11	1824.91	2059.33
Present	433.756	680.765	1069.99	1153.61	1213.84	1557.07	1825.18	2058.83

The TSDT results of Table 2.4 are always more accurate than the CPT ones. Table 2.4 also shows that the present TSDT based model provides results that, with one exception, are closer to the exact ones than the FSDT results of Ref. [65]. It is recalled that another advantage of TSDT over FSDT is the fact that the former does not require a shear correction factor. In Table 2.5, the present natural frequencies computed using $p=10$ shape functions (equal to 500 DOF) agree very well with natural frequencies by FSDT [67]; the maximum relative error is 0.1% for the 7^{th} mode when $\theta=45^{o}$. The present natural frequencies in Table 2.6 are in good agreement with the results of CPT (by Ritz method) [69] and FSDT [61] (here $h/b=0.01$).

Table 2.6: Natural frequency parameters $\omega a^2 h\sqrt{\rho/E_2}$ of free CSCL Plate 4.

Method	Mode							
	1	2	3	4	5	6	7	8
Ref. [61] - FSDT	8.569	23.197	28.946	45.612	48.267	66.202	67.218	77.978
Ref. [68] - HSDT	8.60	23.38	29.44	46.10	48.80	67.57	68.14	-
Ref. [69] - CPT	8.58	23.38	29.19	45.79	48.68	66.74	68.02	78.81
Present - $p = 10$	8.5883	23.459	29.179	45.660	48.824	67.088	67.541	78.284
Present - $p = 13$	8.5843	23.431	29.105	45.601	48.730	66.845	67.363	78.126

2.3.3 Comparison with the Experimental Results

In this section, vibrational modes of a VSCL plate are compared with experimental results. The analysis is carried out on a VSCL in order to extract the modes of vibration, obtaining results for model validation. The layup of the plate analysed is the following: $[\langle 30^o, 10^o\rangle, \langle -30^o, -10^o\rangle, \langle 30^o, 10^o\rangle, \langle -30^o, -10^o\rangle, \langle 90^o, 90^o\rangle]_{sym}$. The material used is Hexply AS4/8552, a high performance material for aerospace structures. The material properties of Plate 5 of Table 2.1 were specified by the manufacturer. The boundary conditions of the plate are free. To see the experiment setup and procedure refer to Appendix B.

Table 2.7 presents the first seven natural frequencies computed using present TSDT model and FSDT finite elements alongside the identified natural frequencies (after Ref. [70]). The column on the right-hand side of the table contains the relative difference between the numeric values, computed with the present TSDT, and the experimental values.

Table 2.7: Comparison between numerical and experimental natural frequencies (Hz) of the VSCL plate 5 of Table 2.1.

Mode	TSDT	FSDT (Ref. [70])	Experimental	Relative difference (%)
1	48.057	46.879	50.897	-5.6
2	50.365	49.059	57.522	-12.4
3	85.951	84.155	85.777	0.2
4	108.24	106.31	109.28	-0.9
5	117.87	115.61	120.14	-1.9
6	161.88	156.95	162.36	-0.3
7	203.01	200.19	195.64	3.8

The modes of vibration obtained experimentally [70] are compared in Figure 2.2 with the ones defined by two types of finite element models, one of the *h*-version FSDT [70] and the other of the present *p*-version TSDT. Although gaps and overlaps [1], which are consequence of the tow placement, exist in the real plate and were not taken into account in the models, the models provide natural frequency values and mode shapes quite close to the experimental ones.

Most natural frequencies are rather well predicted by the TSDT model. The exception is the natural frequency of the second mode, where a difference of 12% between theory and experiments was found. This may be explained by the particularity that the excitation point is not far from a nodal line of this mode. Other reasons justify the differences encountered. One of them regards the

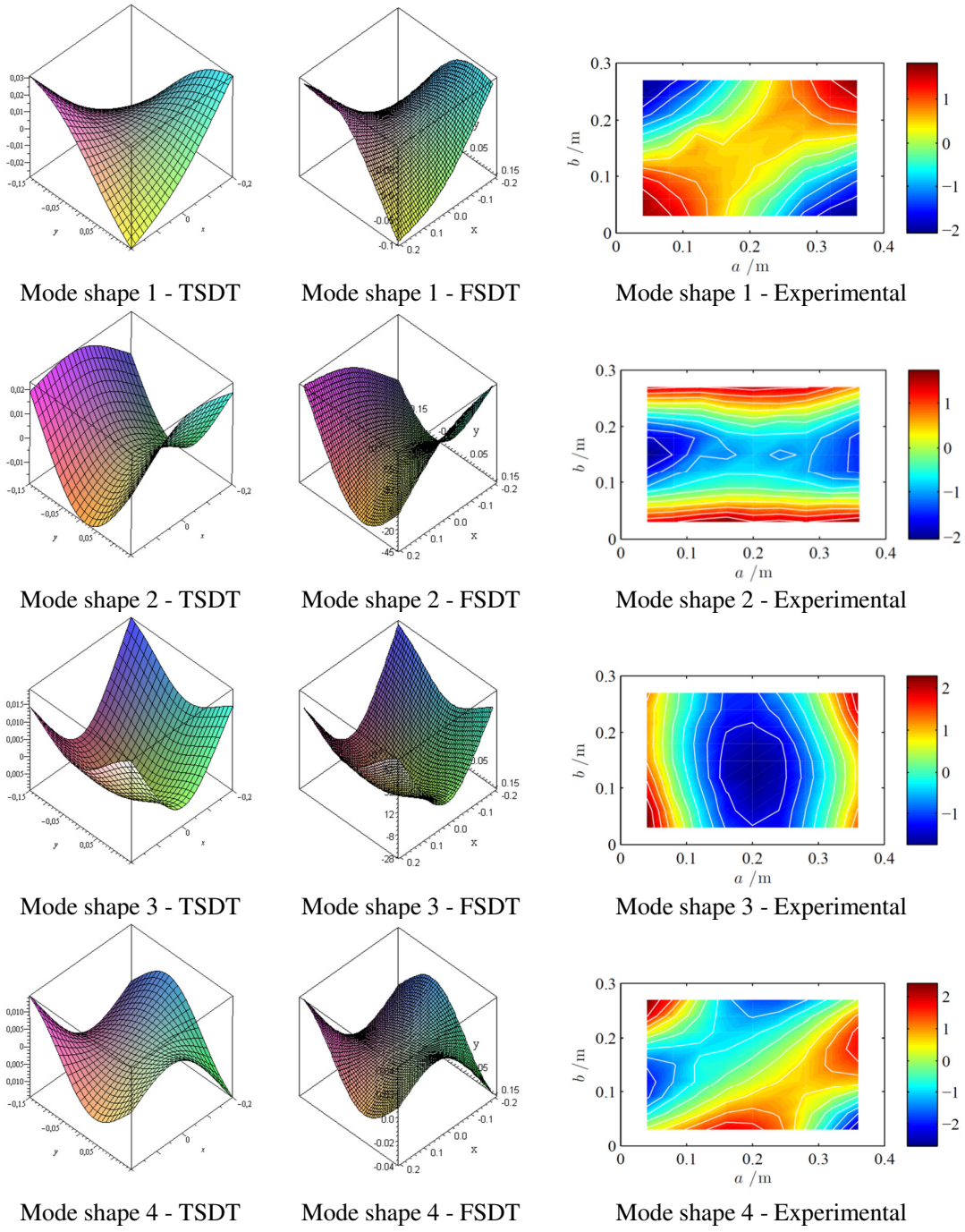

Figure 2.2: Numerical and experimental vibration mode shapes: first to fourth modes [70].

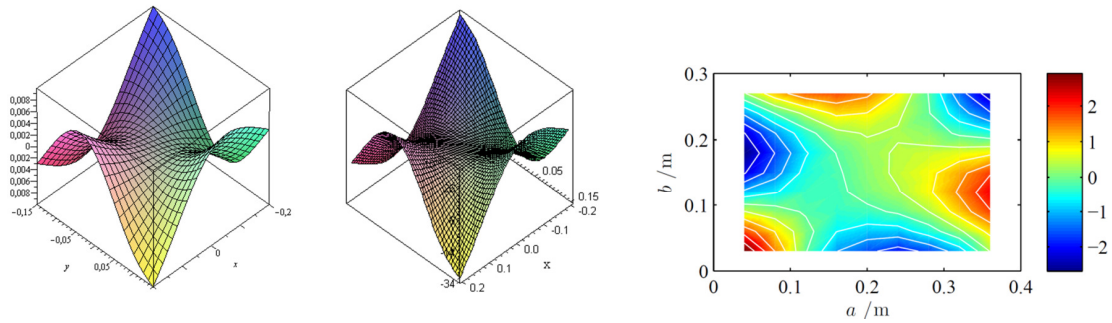

Mode shape 5 - TSDT | Mode shape 5 - FSDT | Mode shape 5 - Experimental

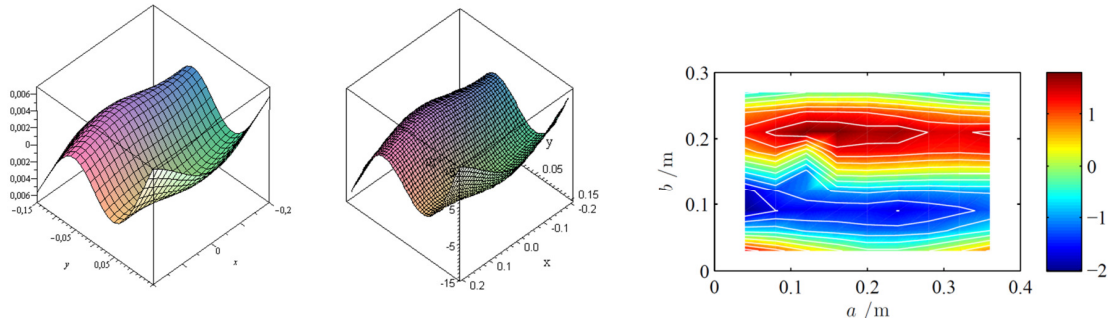

Mode shape 6 - TSDT | Mode shape 6 - FSDT | Mode shape 6 - Experimental

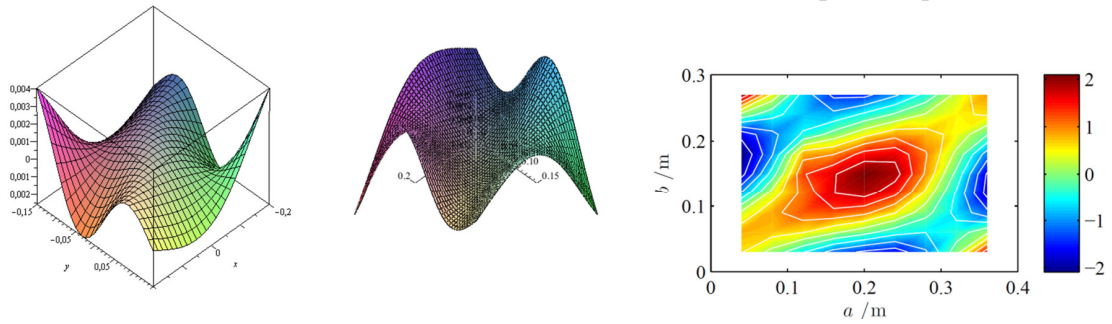

Mode shape 7 - TSDT | Mode shape 7 - FSDT | Mode shape 7 - Experimental

Figure 2.3: Numerical and experimental vibration mode shapes: fifth to seventh modes [70].

material constants: the in-plane elasticity and shear moduli are tabulated, they should be approximately correct, but it was not possible to verify if they are completely accurate; the transverse shear moduli were not given by the supplier and we guessed the values. The second reason is related with the orientation of the fibres. In the model, it is assumed that the fibres are perfectly shifted, all obeying the same analytical formula, but in truth this does not occur, as only the central tow is shifted, the other tows are parallel to it. The real plate shows gaps or overlaps that are not in the theoretical model.

2.3.4 Dependence of Vibration Modes on the Fibre Orientation

In some situations in industry, designers need to change the natural frequencies to higher or lower values in order to avoid resonance. This aim may be achieved by using a VSCL instead of a CSCL plate, without changing the plate dimensions or the constitutive materials, because in a VSCL plate the frequencies are also sensitive to variations of the fibre orientation within each particular layer. In this section, numerical experiments are carried out to illustrate how the natural frequencies and mode shapes change with the fibre orientation. To obtain Figure 2.4, a VSCL plate with a wide range of fibre orientations is analised. For a VSCL plate as the one used in Table 2.2 (Plate 1 of Table 2.1, but with $a = b = 0.5$ m), the maximum relative difference in the frequency computation between a model with 320 and 500 DOF, among the first nine frequencies, is less than 0.4%. To be time-efficient, just in Figures 2.4 and 2.5, eight in-plane, out-of-plane, and rotational shape functions (320 DOF) are used.

Figure 2.4 shows the possible frequencies for a four-layer clamped VSCL with $h/a = 0.1$ and fibre-orientation angles as $[\langle T_0, T_1\rangle, \langle 90^o + T_0, 90^o + T_1\rangle]_{sym}$ (the mechanical properties and geometry is the same as the VSCL plate used in Table 2.2). As written in Section 1.4.4, the variation of the fibre orientations is not totally free, due to manufacturing constraints [6]. The VSCL plates with fibre-orientation angles located in the hatched area in Figure 2.4 should not be manufactured, due to the curvature constrain defined by the tow-placement machine. A dashed-line in the figures represents the CSCL plates where both angles T_0 and T_1 are the same. As this figure shows, for some modes of vibration, the CSCL dashed-line does not cross the areas of maximum or minimum frequency. So, in these cases, the maximum and/or minimum value of the natural frequency is obtained with VSCL plates. The reachable difference between the highest and lowest frequency in this VSCL plate is 10% for the first frequency, 15% for fifth frequency, and 3% for eighth frequency (for other frequencies till the ninth, this difference is between 3% and 15%).

Using VSCL with diverse fibre orientation also leads to changes in the mode shapes. This feature is shown in Figure 2.5, where the first six modes of vibration for the VSCL plates with fibre-orientation angles varying as $[\langle 45^o, 90^o\rangle, \langle -45^o, 0^o\rangle]_{sym}$, $[\langle 0^o, -40^o\rangle, \langle 90^o, 50^o\rangle]_{sym}$, $[\langle 30^o, 60^o\rangle, \langle -60^o, -30^o\rangle]_{sym}$, and $[\langle 90^o, 60^o\rangle, \langle 0^o, -30^o\rangle]_{sym}$ are illustrated. The plates considered here have the same geometrical and mechanical properties as the one used in Figure 2.4. So, the natural frequencies of these modes were given in Figure 2.4. The difference for the second to sixth mode

shapes, ordered according to the growing natural frequency, is obvious and notable for the different VSCL plates considered. In the case of the first mode, Figure 2.5 is not so illustrative, but Figure 2.6, which shows sections ($y = 0$) of the fundamental mode shapes of these four VSCL plates, demonstrates that also in this case there is some variation.

To understand how the boundary conditions and the plate thickness relate with the fibre variation, Tables 2.8, 2.9 and 2.10 show the first nine frequencies of three-layer square VSCL plates of diverse thickness, for simply-supported with movable edges (SSSS-2), clamped, and free boundary conditions, respectively. The geometric and material properties are as Plate 5 in Table 2.1 and the fibre-orientation angles are $[\langle 0^o, 45^o\rangle, \langle -45^o, -60^o\rangle, \langle 0^o, 45^o\rangle]$,$[\langle 30^o, 0^o\rangle, \langle 45^o, 90^o\rangle, \langle 30^o, 0^o\rangle]$, and $[\langle 90^o, 45^o\rangle, \langle 60^o, 30^o\rangle, \langle 90^o, 45^o\rangle]$. VSCL plates with thickness to length ratio h/a equal either to 0.01 or to 0.1 are investigated here. In these tables, the results are obtained with ten in-plane, out-of-plane, and rotational shape functions (500 DOF). Although, any change in the fibre angles results to an alteration in the natural frequency, the boundary condition of the VSCL plate has a decisive role on the change trend. As an example, we note that by changing fibre angles from $[\langle 0^o, 45^o\rangle, \langle -45^o, -60^o\rangle, \langle 0^o, 45^o\rangle]$ to $[\langle 30^o, 0^o\rangle, \langle 45^o, 90^o\rangle, \langle 30^o, 0^o\rangle]$, in the VSCL plate studied in Tables 2.8, 2.9 and 2.10, the frequencies decrease in the simply-supported and free boundary conditions while they increase in the clamped conditions. From plate's thickness point of view, changing fibre orientations may result in a more significant change - in relative terms - in the natural frequencies of a thin VSCL plate in comparison with a thick one.

Table 2.8: Linear natural frequencies (Hz) for simply-supported VSCL plates.

h/a	Mode								
	1	2	3	4	5	6	7	8	9
	$[\langle 0^o, 45^o\rangle, \langle -45^o, -60^o\rangle, \langle 0^o, 45^o\rangle]$								
0.01	358.488	589.9	960.361	1075.21	1327.88	1474.67	1726.71	2137.13	2262.35
0.1	2934.69	4688.3	7000.96	7324.22	8471.78	10448.8	10907	11653.3	12812.9
	$[\langle 30^o, 0^o\rangle, \langle 45^o, 90^o\rangle, \langle 30^o, 0^o\rangle]$								
0.01	308.799	503.799	845.509	1131.31	1279.85	1307.4	1701.66	1758.95	2342
0.1	2620.4	4225.74	6704.11	7121.26	8383.48	9317.14	11079.5	11762	12154.1
	$[\langle 90^o, 45^o\rangle, \langle 60^o, 30^o\rangle, \langle 90^o, 45^o\rangle]$								
0.01	329.688	539.407	886.392	1091.2	1279.9	1401.87	1755.53	1809.82	2216.58
0.1	2746.66	4402.32	6915.87	7058.72	8254.38	9626.07	11158.9	11486.5	12375.6

2.3.5 Verification of the Model Including Geometrical Imperfection

Although any type of geometry imperfection can be integrated in the model, sinusoidal imperfection, $w_i = h_0 \times \cos(\pi x/a)\cos(\pi y/b)$, is applied into the formulation, as was done in Refs. [71,72], in which h_0 is the imperfection magnitude at the centre of the plate. To validate the linear model, some examples of linear frequencies of imperfect laminates are compared with published data. Because data on imperfect VSCL plates are not available, the comparisons are made with isotropic and CSCL plates. In all comparison studies on imperfect plates, a specific simply-supported

Table 2.9: Linear natural frequencies (Hz) for clamped VSCL plates.

h/a	Mode								
	1	2	3	4	5	6	7	8	9
	$[\langle 0^o, 45^o\rangle, \langle -45^o, -60^o\rangle, \langle 0^o, 45^o\rangle]$								
0.01	579.398	821.532	1225.79	1493.76	1726.96	1775.16	2135.76	2443.53	2706.78
0.1	3856.6	5711.95	7743.34	8406.57	9329.84	11295.2	12134.7	12343.9	13516.2
	$[\langle 30^o, 0^o\rangle, \langle 45^o, 90^o\rangle, \langle 30^o, 0^o\rangle]$								
0.01	667.177	862.919	1234.64	1701.04	1775.56	1902.48	2269.83	2310.69	2879.58
0.1	4144.85	5696.2	8166.79	8214.53	9562.22	10805.3	12216.5	12720.3	13552.6
	$[\langle 90^o, 45^o\rangle, \langle 60^o, 30^o\rangle, \langle 90^o, 45^o\rangle]$								
0.01	710.771	912.183	1335.49	1689.69	1836.71	1987.55	2278.23	2466.75	2920.42
0.1	4284.2	5761.83	8193.46	8247.32	9210.52	10770	12062.6	12503.6	12566.9

Table 2.10: Linear natural frequencies (Hz) for free VSCL plates.

h/a	Mode								
	1	2	3	4	5	6	7	8	9
	$[\langle 0^o, 45^o\rangle, \langle -45^o, -60^o\rangle, \langle 0^o, 45^o\rangle]$								
0.01	140.946	170.21	344.57	477.563	592.531	715.99	718.893	872.198	1007.9
0.1	1267.89	1624.7	2951.58	4175.95	4800.67	5450.35	5674.65	6416.61	7095.51
	$[\langle 30^o, 0^o\rangle, \langle 45^o, 90^o\rangle, \langle 30^o, 0^o\rangle]$								
0.01	110.436	177.48	266.529	459.734	468.741	618.25	658.132	771.549	856.679
0.1	1046.35	1699.37	2455.55	4019.93	4021.99	5080.01	5256.28	6123.58	6971.14
	$[\langle 90^o, 45^o\rangle, \langle 60^o, 30^o\rangle, \langle 90^o, 45^o\rangle]$								
0.01	123.172	151.348	277.543	389.523	404.515	577.629	622.333	693.601	840.149
0.1	1146.96	1450.12	2466.98	3519.31	3528.15	4808.8	5257.86	5536.84	6343.97

boundary condition, with restrained normal displacement at the plate edges and fully free in-plane displacements (SSSS-3), has been used (see Appendix A) [71–73].

For the comparison example in Figure 2.7, an isotropic imperfect plate with mechanical properties of plate 6 in Table 2.1 are used. First - and second - mode frequencies versus imperfection are compared with data from Ref. [71]. The difference between frequencies of the imperfect plate (with $h_0/h = 1$) with two methods is about 2%. It seems to us that this difference is due to the different methods used to model the plate; in Ref. [71], Kirchhoff hypothesis was used.

Another comparison study is shown in Table 2.11, which gives linear frequency parameters $\omega_{li}a^2\pi^2\sqrt{\rho/D}$ - with $D = Eh^3/12\left(1-\nu^2\right)$ - of a square stainless steel imperfect plate ($h_0 = 0.2h$) with properties of plate 7 of Table 2.1. The boundary conditions are simply-supported (SSSS-3). Good correlation is achieved.

Table 2.11: Comparison of linear frequency parameters $\omega_i a^2\pi^2\sqrt{\rho/D}$ for a simply-supported (SSSS-3) square plate with imperfection ($h_0 = 0.2h$).

Mode number i	Kitipornchai et al. [73]	Rafiee et al. [72]	Present
1	1.9379	1.9494	1.9473
2	4.6088	4.7912	4.6162
3	4.6088	4.7912	4.6162
4	7.0676	7.0698	7.0443

2.4 Conclusions

In this chapter, variable stiffness composite laminated plates with curvilinear fibres were analysed with a *p*-version finite element, using a third order shear deformation theory. The effects of using curvilinear fibres instead of straight fibres in laminated composite plates on the mode shapes and natural frequencies of vibration were investigated. Several boundary conditions and plate thicknesses were considered. It is found that using VSCL plates can change mode shapes of vibration meaningfully and may lead to a significant decrease or increase in the natural frequencies. Apparently, thicker plates are less influenced, relatively, than thinner plates, a behavior that may be explained by the fact that the alteration considered in the fibre variation, with respect to traditional laminates, only occurs in a plane. This conjecture is a result of a limited number of case studies and requires further validation. Also, the laminate model including imperfection parameters in the out-of-plane direction was verified.

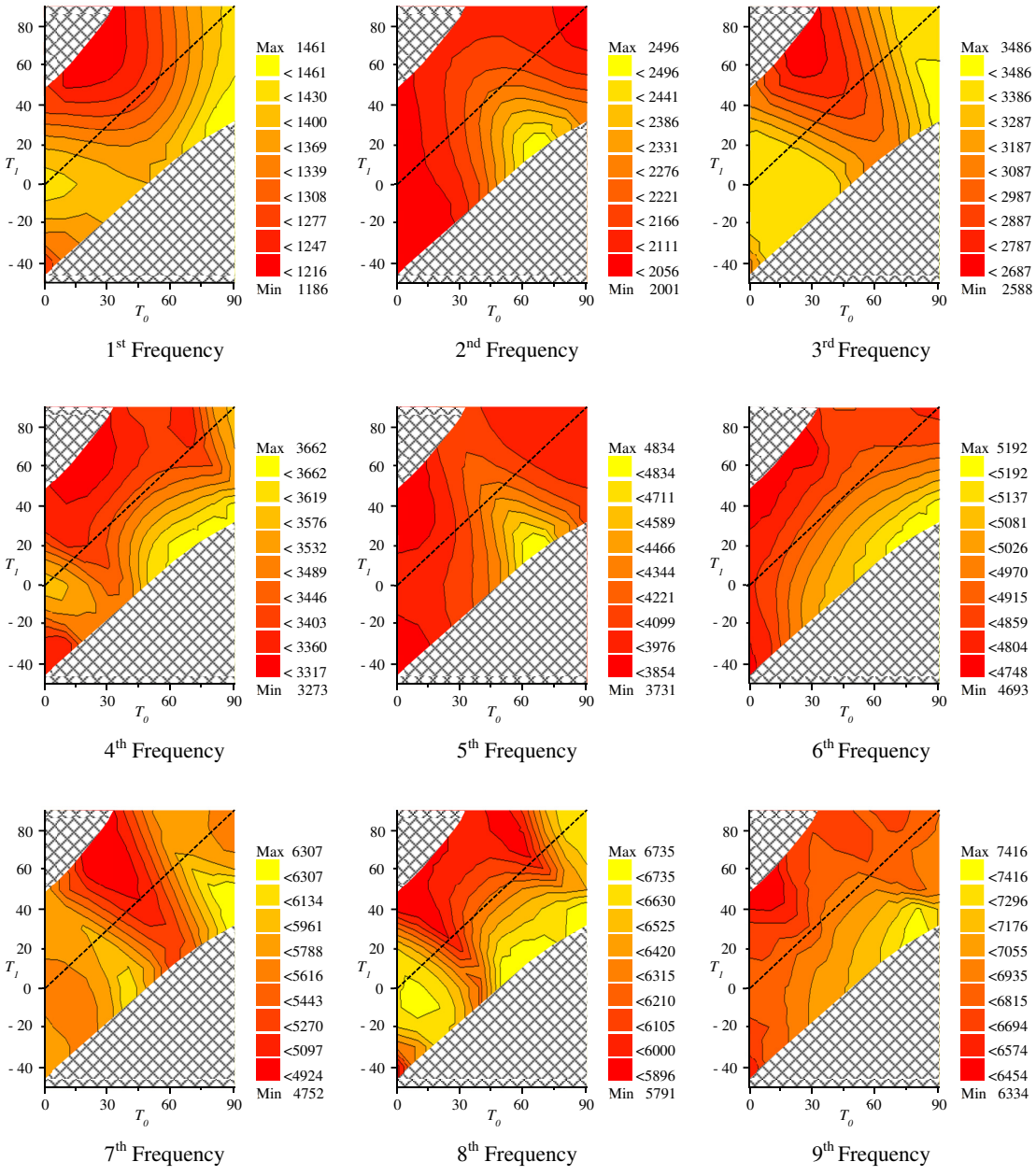

Figure 2.4: Contour plots of natural frequencies against T_0 and T_1 as fibre angles in a VSCL.

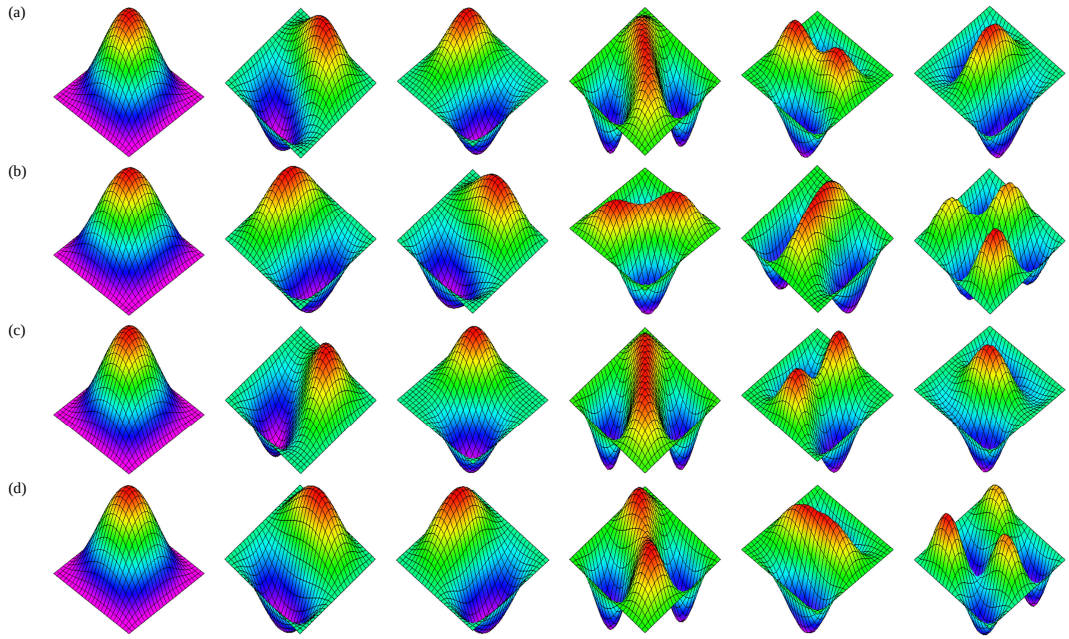

Figure 2.5: Mode shapes of vibration of VSCL with (a) $\langle T_0, T_1 \rangle = \langle 45^o, 90^o \rangle$; (b) $\langle T_0, T_1 \rangle = \langle 0^o, -40^o \rangle$; (c) $\langle T_0, T_1 \rangle = \langle 30^o, 60^o \rangle$; (d) $\langle T_0, T_1 \rangle = \langle 90^o, 60^o \rangle$.

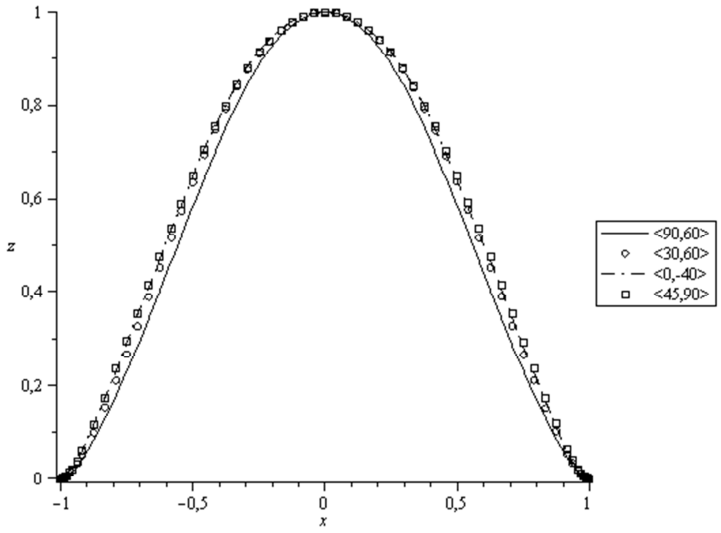

Figure 2.6: First mode shapes of vibrations for four different VSCL plates ($y = 0$).

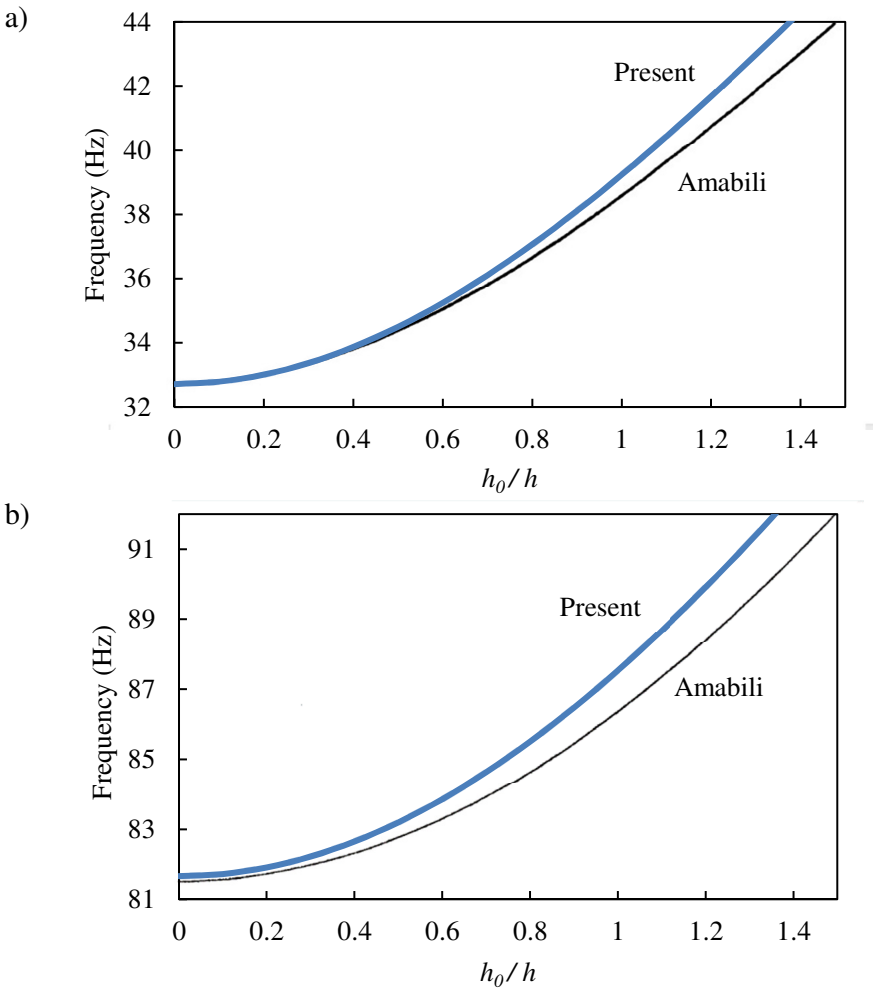

Figure 2.7: Comparison of (a) the first and (b) the second natural frequencies versus the geometric imperfection calculated by the present method and given by Ref. [71].

Chapter 3

Static Analysis of VSCL Plates in the Geometrically Non-Linear Regime

3.1 Introduction

The present chapter aims at computing large deflections (taking geometric non-linearity into account) and stresses of diverse VSCL plates with curvilinear fibres, and showing that the fibre variation may indeed be used to reduce deflections and stresses in some static loadings. The current tailoring concept may allow one to implement the best fibre angles for minimising deflections and/or to find VSCLs with lower stresses, for the same constitutive materials, overall panel dimensions and loadings. To carry out the analysis, a *p*-version finite element that follows third-order shear deformation theory (TSDT) [34–36] is developed. A linear version of this element has been applied to determine the linear modes of vibration of VSCLs in Chapter 2. The new non-linear element is employed in diverse test cases on CSCLs taken from the literature. We found, as is typical in *p*-elements, that accurate results are computed with a relatively small number of degrees of freedom. Deflections, normal stresses and shear stresses are determined as functions of tow-orientation angles in demonstrative examples. Shear transverse stresses are calculated with both constitutive and equilibrium equations. The effects of geometric non-linearity on the deflection and stresses of VSCLs are shown. The model presented allows to continue searching for advantages of VSCL plates and to better understand the behaviour of these plates in different loading conditions.

3.1.1 Literature Review

With the expansion of the idea of using VSCLs with curvilinear fibres, investigators [6–8] discussed the novelties of such laminates in buckling, failure, stresses, and static deformation when the plates are subjected to in-plane uniaxial loading and end shortening. These novelties were due to the ability of VSCLs to re-distribute stresses via the spatial variation of fibre angles [74]. After these achievements, Tatting and Gürdal developed a design tool, where a solver designated as

STAGS was integrated with a laminate design software [22,23]. With the help of the software developed, Tatting and Gürdal succeeded to continue analysing buckling, prebuckling, deformation, and stress distributions in a VSCL plate subjected to in-plane loading (with emphasis in plates with a hole - because of the usefulness of VSCLs in distributing the stresses created around the hole). Recent works show the continuing interest of researchers in uncovering unknown aspects of stress distribution in VSCLs with curvilinear fibres [9,75–78]. Senocak and Tanriover [9] studied VSCL plates subjected to in-plane loading, using Galerkin method. In references [76–78], buckling, failure and interlaminar stresses of VSCL plates were investigated using ABAQUS finite element software. The studies included normal deflection and normal stresses of the plate. In another analysis [79], a generalised differential quadrature method together with a Newton–Raphson iterative scheme was presented for non-linear analysis of variable stiffness conical shell panels.

Ref. [74] showed that stiffness tailoring improves the buckling performance of VSCL plates by allowing re-distribution of loads from the critical regions of the plate. In Ref. [74], a differential quadrature method (DQM) was investigated for performing buckling analysis of VSCL panels. In another study [80], it was demonstrated that the stiffness tailoring of VSCL plates through the design of fibre orientation distributions can improve the buckling resistance, which is mainly due to the non-uniform, in-plane load re-distribution. The postbuckling performance of VSCL plates under a compression loading was assessed by studying both the maximum transverse displacement and the end-shortening strain in Ref. [81]. For this analysis, an efficient tool based on the variational principle and the Rayleigh-Ritz method was developed in Ref. [81]. In another reference [82], the postbuckling behaviour of the VSCL plates with perturbation method was discussed. There, optimised variable stiffness plates for maximum buckling load, demonstrating significant improvements in load-carrying capacity, were used.

In paper [83], the authors presented a layerwise theory, p-version finite element method for static analysis of unsymmetric laminates with curvilinear fibres, including von Kármán strains. A displacement field that varies linearly along the thickness of each layer was considered. For unsymmetric laminates in the linear and non-linear regimes, it was observed that a VSCL plate that experiences larger deflection in the linear regime, is not necessarily the one that suffers larger deflections in the non-linear regime. Also, it was shown that unsymmetric stacking sequences often decrease the overall stiffness of the plates, both in the linear and in the non-linear regimes; consequently, leading to larger deflection amplitudes [83]. The same authors mentioned the effects of the curved fibres in re-distributing the static applied load within the plates in non-linear regime [84]. They showed that although the distributed load was the same in all the studies, the maximum deflection did not occur at the central point in VSCL plates.

Analyses on the effect of transverse shear deformation and embedded manufacturing defects (gaps and overlaps during manufacturing process) on the deflection of VSCL plates were given in Ref. [41]. This reference presented the governing equations obtained via classical and shear deformation theories, and then solved them by using the hybrid Fourier–Galerkin method. It showed for moderately-thick plates with length-to-thickness ratio $a/h = 10$, major differences emerge between CLPT and TSDT predictions, in a way that discrepancy up to 23% was observed

for the maximum out-of-plane deflection. This reference showed the important role played by shear deformation in moderately-thick VSCL plates [41].

There are several publications addressing deflections and stresses aspects on CSCL (constant stiffness composite laminated) plates, i.e. in laminates with straight fibres. One can find 3-D elasticity exact solution for static analysis of multilayered (CSCL) plates in Ref. [85]. Ref. [86] showed experimental and classical plate theory (CPT) results on the deflection of CSCL plates in the non-linear regime. Putcha and Reddy [87] presented a refined mixed shear flexible finite element for the non-linear analysis of CSCL plates. Zhang and Kim [88] offered a 3-node triangular element for linear and geometrically non-linear analysis of deflections of laminated composite plates. A very comprehensive review including geometric non-linear finite element analysis of CSCL plates can be found in Ref. [89]. A particular mixed-enhanced finite element for linear bending analysis of CSCL plates based on first-order shear deformation theory (FSDT) was presented in Refs. [90–92]. There, even though FSDT was used, transverse shear stresses in composite plates were quite well computed. Most of the results given in this chapter have already been published in Ref. [93].

3.2 Modelling of VSCL Plates Considering Geometrical Non-linearity

The displacement field described in Chapter 2, Equations (2.1), excluding imperfection is used here. Non-linear terms based on von Kármán strain–displacement relations, a simplified version of Green's strain tensor, Equations (2.4), for moderate geometric non-linearity, are here introduced (for simplicity we write $\varepsilon(x,y,z,t)$ as ε, etc.).

$$\varepsilon_x = \frac{\partial u^0}{\partial x} + \left(z - cz^3\right)\frac{\partial \phi_x}{\partial x} - cz^3\left(\frac{\partial^2 w^0}{\partial x^2}\right) + \frac{1}{2}\left(\frac{\partial w^0}{\partial x}\right)^2,$$

$$\varepsilon_y = \frac{\partial v^0}{\partial y} + \left(z - cz^3\right)\frac{\partial \phi_y}{\partial y} - cz^3\left(\frac{\partial^2 w^0}{\partial y^2}\right) + \frac{1}{2}\left(\frac{\partial w^0}{\partial y}\right)^2,$$

$$\varepsilon_z = 0,$$

$$\gamma_{xy} = \frac{\partial u^0}{\partial y} + \frac{\partial v^0}{\partial x} + \left(z - cz^3\right)\left(\frac{\partial \phi_x}{\partial y} + \frac{\partial \phi_y}{\partial x}\right) + \frac{\partial w^0}{\partial x}\frac{\partial w^0}{\partial y} - 2cz^3\frac{\partial^2 w^0}{\partial x \partial y},$$

$$\gamma_{yz} = \left(1 - 3cz^2\right)\left(\phi_y(x,y,t) + \frac{\partial w^0}{\partial y}\right),$$

$$\gamma_{xz} = \left(1 - 3cz^2\right)\left(\phi_x(x,y,t) + \frac{\partial w^0}{\partial x}\right). \tag{3.1}$$

These expressions are in general accurate enough for static analysis of VSCL plates in the non-linear regime. If more accurate expressions are needed, the Equations (3.1) can be improved retaining all the non-linear terms. Now, strains can be presented in matrix form as

$$\begin{Bmatrix} \varepsilon_x \\ \varepsilon_y \\ \gamma_{xy} \end{Bmatrix} = \begin{bmatrix} 1 & 0 & 0 & z & 0 & 0 & -cz^3 & 0 & 0 \\ 0 & 1 & 0 & 0 & z & 0 & 0 & -cz^3 & 0 \\ 0 & 0 & 1 & 0 & 0 & z & 0 & 0 & -cz^3 \end{bmatrix} \boldsymbol{\varepsilon}$$

$$\boldsymbol{\varepsilon} = \begin{Bmatrix} \boldsymbol{\varepsilon}_o^p \\ \boldsymbol{\varepsilon}_o^b \\ \boldsymbol{\varepsilon}_o^b \end{Bmatrix} + \begin{Bmatrix} \boldsymbol{\varepsilon}_o^{p1} \\ \mathbf{0} \\ \boldsymbol{\varepsilon}_o^{b1} \end{Bmatrix} \tag{3.2}$$

in which $\boldsymbol{\varepsilon}_o^p$, $\boldsymbol{\varepsilon}_o^b$ and $\boldsymbol{\varepsilon}_o^{b1}$ are introduced already in Section 2.2, Equations (2.7) - (2.9). $\boldsymbol{\varepsilon}_o^{p1}$ is the non-linear in-plane strain as

$$\boldsymbol{\varepsilon}_o^{p1} = \begin{Bmatrix} \frac{1}{2}\left(w^0_{,x}\right)^2 \\ \frac{1}{2}\left(w^0_{,y}\right)^2 \\ w^0_{,x} w^0_{,y} \end{Bmatrix} \tag{3.3}$$

By introducing the mid-plane displacements of Equation (2.2) in the non-linear in-plane strain, above, one can obtain

$$\boldsymbol{\varepsilon}_o^{p1} = \frac{1}{2} \begin{Bmatrix} w^0_{,x}\mathbf{N}^{\mathbf{w}}_{,x} \\ w^0_{,y}\mathbf{N}^{\mathbf{w}}_{,y} \\ w^0_{,x}\mathbf{N}^{\mathbf{w}}_{,y} + w^0_{,y}\mathbf{N}^{\mathbf{w}}_{,x} \end{Bmatrix} \mathbf{q}_{\mathbf{w}}. \tag{3.4}$$

Using the method introduced in Section 2.2, the virtual work of the elastic restoring (internal) forces, Equation (2.25), extends as

$$\delta W_{in} = -\int_\Omega \Big(\delta\boldsymbol{\varepsilon}_o^{pT} \mathbf{A} \boldsymbol{\varepsilon}_o^p + \delta\boldsymbol{\varepsilon}_o^{bT} \left(\mathbf{C} + 2\mathbf{E} + \mathbf{F}\right) \boldsymbol{\varepsilon}_o^b + \delta\boldsymbol{\varepsilon}_o^{bT} \left(\mathbf{E} + \mathbf{F}\right) \boldsymbol{\varepsilon}_o^{b1} + \delta\boldsymbol{\varepsilon}_o^{b1^T} \left(\mathbf{E} + \mathbf{F}\right) \boldsymbol{\varepsilon}_o^b +$$

$$\delta\boldsymbol{\varepsilon}_o^{b1^T} \mathbf{F} \boldsymbol{\varepsilon}_o^{b1} + \delta\boldsymbol{\gamma}_o^{pT} \left(\mathbf{G} + 2\mathbf{H} + \mathbf{I}\right) \boldsymbol{\gamma}_o^p + \delta\boldsymbol{\varepsilon}_o^{p1^T} \mathbf{A} \boldsymbol{\varepsilon}_o^p + \delta\boldsymbol{\varepsilon}_o^{pT} \mathbf{A} \boldsymbol{\varepsilon}_o^{p1} + \delta\boldsymbol{\varepsilon}_o^{p1^T} \mathbf{A} \boldsymbol{\varepsilon}_o^{p1} \Big) \, d\Omega. \tag{3.5}$$

The first six terms are exactly as defined in Section 2.2, the last three terms are changed as given below. The seventh term is

$$\delta\boldsymbol{\varepsilon}_o^{p1^T} \mathbf{A} \boldsymbol{\varepsilon}_o^p = \frac{1}{2} \delta\mathbf{q}_{\mathbf{w}}{}^T \begin{Bmatrix} w^0_{,x}\mathbf{N}^{\mathbf{w}}_{,x} \\ w^0_{,y}\mathbf{N}^{\mathbf{w}}_{,y} \\ w^0_{,x}\mathbf{N}^{\mathbf{w}}_{,y} + w^0_{,y}\mathbf{N}^{\mathbf{w}}_{,x} \end{Bmatrix}^T \mathbf{A} \begin{bmatrix} \mathbf{N}^{\mathbf{u}\,T}_{,x} & \mathbf{0} \\ \mathbf{0} & \mathbf{N}^{\mathbf{u}\,T}_{,y} \\ \mathbf{N}^{\mathbf{u}\,T}_{,y} & \mathbf{N}^{\mathbf{u}\,T}_{,x} \end{bmatrix} \begin{Bmatrix} \mathbf{q}_{\mathbf{u}} \\ \mathbf{q}_{\mathbf{v}} \end{Bmatrix} =$$

$$\delta\mathbf{q}_{\mathbf{w}}{}^T \begin{bmatrix} \mathbf{K}^{31}_{\mathbf{NL}} & \mathbf{K}^{32}_{\mathbf{NL}} \end{bmatrix} \begin{Bmatrix} \mathbf{q}_{\mathbf{u}} \\ \mathbf{q}_{\mathbf{v}} \end{Bmatrix} \tag{3.6}$$

The eighth term is transpose of the seventh term and written as

$$\delta \boldsymbol{\varepsilon}_o^{pT} \mathbf{A} \boldsymbol{\varepsilon}_o^{p1} = \delta \left\{ \begin{array}{c} \mathbf{q_u} \\ \mathbf{q_v} \end{array} \right\}^T \left[\begin{array}{c} \mathbf{K}_{\mathbf{NL}}^{13} \\ \mathbf{K}_{\mathbf{NL}}^{23} \end{array} \right] \mathbf{q_w} \tag{3.7}$$

where

$$\left[\begin{array}{c} \mathbf{K}_{\mathbf{NL}}^{13} \\ \mathbf{K}_{\mathbf{NL}}^{23} \end{array} \right] = \left[\begin{array}{cc} \mathbf{K}_{\mathbf{NL}}^{31} & \mathbf{K}_{\mathbf{NL}}^{32} \end{array} \right]^T \tag{3.8}$$

The ninth term is defined as

$$\delta \boldsymbol{\varepsilon}_o^{p1^T} \mathbf{A} \boldsymbol{\varepsilon}_o^{p1} = \frac{1}{4} \delta \mathbf{q_w}^T \left\{ \begin{array}{c} w_{,x}^0 \mathbf{N}_{,x}^{\mathbf{w}} \\ w_{,y}^0 \mathbf{N}_{,y}^{\mathbf{w}} \\ w_{,x}^0 \mathbf{N}_{,y}^{\mathbf{w}} + w_{,y}^0 \mathbf{N}_{,x}^{\mathbf{w}} \end{array} \right\}^T \mathbf{A} \left\{ \begin{array}{c} w_{,x}^0 \mathbf{N}_{,x}^{\mathbf{w}} \\ w_{,y}^0 \mathbf{N}_{,y}^{\mathbf{w}} \\ w_{,x}^0 \mathbf{N}_{,y}^{\mathbf{w}} + w_{,y}^0 \mathbf{N}_{,x}^{\mathbf{w}} \end{array} \right\} \mathbf{q_w} = \delta \mathbf{q_w}^T \mathbf{K}_{\mathbf{NL}}^{33} \mathbf{q_w} \tag{3.9}$$

The internal virtual work, given in Equation (3.5), can be written as

$$\delta W_{in} = -\int_\Omega \delta \left\{ \begin{array}{c} \mathbf{q_u} \\ \mathbf{q_v} \\ \mathbf{q_w} \\ \mathbf{q}_{\boldsymbol{\phi}_\mathbf{x}} \\ \mathbf{q}_{\boldsymbol{\phi}_\mathbf{y}} \end{array} \right\}^T \left[\begin{array}{ccccc} \mathbf{K}_{\mathbf{L}}^{11} & \mathbf{K}_{\mathbf{L}}^{12} & \mathbf{0} & \mathbf{0} & \mathbf{0} \\ & \mathbf{K}_{\mathbf{L}}^{22} & \mathbf{0} & \mathbf{0} & \mathbf{0} \\ & & \mathbf{K}_{\mathbf{L}}^{33} & \mathbf{K}_{\mathbf{L}}^{34} & \mathbf{K}_{\mathbf{L}}^{35} \\ & & & \mathbf{K}_{\mathbf{L}}^{44} & \mathbf{K}_{\mathbf{L}}^{45} \\ sym & & & & \mathbf{K}_{\mathbf{L}}^{55} \end{array} \right] \left\{ \begin{array}{c} \mathbf{q_u} \\ \mathbf{q_v} \\ \mathbf{q_w} \\ \mathbf{q}_{\boldsymbol{\phi}_\mathbf{x}} \\ \mathbf{q}_{\boldsymbol{\phi}_\mathbf{y}} \end{array} \right\} d\Omega$$

$$-\int_\Omega \delta \left\{ \begin{array}{c} \mathbf{q_u} \\ \mathbf{q_v} \\ \mathbf{q_w} \\ \mathbf{q}_{\boldsymbol{\phi}_\mathbf{x}} \\ \mathbf{q}_{\boldsymbol{\phi}_\mathbf{y}} \end{array} \right\}^T \left[\begin{array}{ccccc} \mathbf{0} & \mathbf{0} & \mathbf{K}_{\mathbf{NL}}^{13}(\mathbf{q_w}) & \mathbf{0} & \mathbf{0} \\ \mathbf{0} & \mathbf{0} & \mathbf{K}_{\mathbf{NL}}^{23}(\mathbf{q_w}) & \mathbf{0} & \mathbf{0} \\ \mathbf{K}_{\mathbf{NL}}^{31}(\mathbf{q_w}) & \mathbf{K}_{\mathbf{NL}}^{32}(\mathbf{q_w}) & \mathbf{K}_{\mathbf{NL}}^{33}(\mathbf{q_w}) & \mathbf{0} & \mathbf{0} \\ \mathbf{0} & \mathbf{0} & \mathbf{0} & \mathbf{0} & \mathbf{0} \\ \mathbf{0} & \mathbf{0} & \mathbf{0} & \mathbf{0} & \mathbf{0} \end{array} \right] \left\{ \begin{array}{c} \mathbf{q_u} \\ \mathbf{q_v} \\ \mathbf{q_w} \\ \mathbf{q}_{\boldsymbol{\phi}_\mathbf{x}} \\ \mathbf{q}_{\boldsymbol{\phi}_\mathbf{y}} \end{array} \right\} d\Omega \tag{3.10}$$

Above, generalised coordinates $\mathbf{q_k}, (\mathbf{k} = \mathbf{u}, \mathbf{v}, \mathbf{w}, \boldsymbol{\phi}_\mathbf{x}, \boldsymbol{\phi}_\mathbf{y})$ are variables, the linear stiffness matrix is symmetric and constituted by sub-matrices $\mathbf{K}_{\mathbf{L}}^{ij}, (i, j = 1-5)$, which are all constant, already defined in Section 2.2. $\mathbf{K}_{\mathbf{NL}}^{ij}, (i, j = 1-5)$ are designated as non-linear stiffness sub-matrices, because they lead to non-linear terms. With the exception of $\mathbf{K}_{\mathbf{NL}}^{33}$, sub-matrices $\mathbf{K}_{\mathbf{NL}}^{ij}$ depend linearly on the transverse deflection. Matrix $\mathbf{K}_{\mathbf{NL}}^{33}$ is a quadratic function of the transverse deflections.

The virtual work of external forces is

$$\delta W_{ex} = \int_\Omega \left(\delta u f_u(x,y,t) + \delta v f_v(x,y,t) + \delta w f_w(x,y,t) + \delta \phi_x f_{\phi_x}(x,y,t) + \delta \phi_y f_{\phi_y}(x,y,t) \right) d\Omega =$$

$$\int_{\Omega} \delta \begin{Bmatrix} \mathbf{q_u} \\ \mathbf{q_v} \\ \mathbf{q_w} \\ \mathbf{q_{\phi_x}} \\ \mathbf{q_{\phi_y}} \end{Bmatrix}^T \begin{bmatrix} \mathbf{N^u}(x,y) & \mathbf{0} & \mathbf{0} & \mathbf{0} & \mathbf{0} \\ \mathbf{0} & \mathbf{N^u}(x,y) & \mathbf{0} & \mathbf{0} & \mathbf{0} \\ \mathbf{0} & \mathbf{0} & \mathbf{N^w}(x,y) & \mathbf{0} & \mathbf{0} \\ \mathbf{0} & \mathbf{0} & \mathbf{0} & \mathbf{N^{\phi_x}}(x,y) & \mathbf{0} \\ \mathbf{0} & \mathbf{0} & \mathbf{0} & \mathbf{0} & \mathbf{N^{\phi_y}}(x,y) \end{bmatrix} \begin{Bmatrix} f_u(x,y,t) \\ f_v(x,y,t) \\ f_w(x,y,t) \\ f_{\phi_x}(x,y,t) \\ f_{\phi_y}(x,y,t) \end{Bmatrix} d\Omega \tag{3.11}$$

in which f_w is the transverse load, f_u and f_v are the in-plane loads, and f_{ϕ_x} and f_{ϕ_y} are moments about axis y and x, respectively. All the forces and moments are per unit area.

Defining the virtual work of the internal and external forces, and applying the principle of virtual work, the equations of equilibrium are obtained as $\delta W_{in} + \delta W_{ex} = 0$. These equations are of the following form:

$$\begin{bmatrix} \mathbf{K_L^{11}} & \mathbf{K_L^{12}} & \mathbf{0} & \mathbf{0} & \mathbf{0} \\ & \mathbf{K_L^{22}} & \mathbf{0} & \mathbf{0} & \mathbf{0} \\ & & \mathbf{K_L^{33}} & \mathbf{K_L^{34}} & \mathbf{K_L^{35}} \\ & & & \mathbf{K_L^{44}} & \mathbf{K_L^{45}} \\ sym & & & & \mathbf{K_L^{55}} \end{bmatrix} \begin{Bmatrix} \mathbf{q_u} \\ \mathbf{q_v} \\ \mathbf{q_w} \\ \mathbf{q_{\phi_x}} \\ \mathbf{q_{\phi_y}} \end{Bmatrix} + \begin{bmatrix} \mathbf{0} & \mathbf{0} & \mathbf{K_{NL}^{13}}(\mathbf{q_w}) & \mathbf{0} & \mathbf{0} \\ \mathbf{0} & \mathbf{0} & \mathbf{K_{NL}^{23}}(\mathbf{q_w}) & \mathbf{0} & \mathbf{0} \\ \mathbf{K_{NL}^{31}}(\mathbf{q_w}) & \mathbf{K_{NL}^{32}}(\mathbf{q_w}) & \mathbf{K_{NL}^{33}}(\mathbf{q_w}) & \mathbf{0} & \mathbf{0} \\ \mathbf{0} & \mathbf{0} & \mathbf{0} & \mathbf{0} & \mathbf{0} \\ \mathbf{0} & \mathbf{0} & \mathbf{0} & \mathbf{0} & \mathbf{0} \end{bmatrix} \begin{Bmatrix} \mathbf{q_u} \\ \mathbf{q_v} \\ \mathbf{q_w} \\ \mathbf{q_{\phi_x}} \\ \mathbf{q_{\phi_y}} \end{Bmatrix}$$

$$= \begin{Bmatrix} \mathbf{f_u} \\ \mathbf{f_v} \\ \mathbf{f_w} \\ \mathbf{f_{\phi_x}} \\ \mathbf{f_{\phi_y}} \end{Bmatrix} \tag{3.12}$$

The vector of generalised external forces on the right-hand side of Equation (3.12) is obtained from virtual work of external forces. In the numerical applications, we will only consider transverse forces, so only $\mathbf{f_w}$ is not zero.

3.2.1 Solution of the Equations of Equilibrium by Newmark Method

Equations (3.12) is a non-linear algebraic equation which can be solved by Newton-Raphson method; however, because it worked quite well, an in-house code based on Newmark method [62, 94] is used, being time an artificial parameter. The Newmark Method for static analysis is used here as a special case of dynamic analysis; the same method is applied to dynamic problems in the next chapter. To use Newmark method, one needs the mass in equations of equilibrium, we already have it from Equations (2.40). We may write the Equation of equilibrium (3.12) as

$$\mathbf{Kq} = \mathbf{f} \tag{3.13}$$

To facilitate the explanation of Newmark method [94] for a more generalised equation of motion, let's take a general form of

$$\mathbf{M}\ddot{\mathbf{q}} + \mathbf{C}\dot{\mathbf{q}} + \mathbf{K}\mathbf{q} = \mathbf{f} \tag{3.14}$$

with **M**, **C**, **K**, **f**, and **q** representing mass, damping, stiffness, force and generalised coordinates, respectively.

Before describing the Newmark method, a brief introduction should be written about the Linear Acceleration Method. By discretising the time τ into n instants $\tau_j, j = 1 \ldots n$ and assuming that acceleration change with respect to the time (in a small length of the time Δt) is linear, one can write

$$\ddot{\mathbf{q}}(\tau) = \ddot{\mathbf{q}}_j + \frac{1}{\Delta t}\left(-\ddot{\mathbf{q}}_j + \ddot{\mathbf{q}}_{j+1}\right)\tau \qquad 0 \leq \tau \leq \Delta t \tag{3.15}$$

where $\tau = 0$ at point j; and $\tau = \Delta t$ at point $j+1$. By integrating with respect to time, one has

$$\dot{\mathbf{q}}(\tau) = \dot{\mathbf{q}}_j + \ddot{\mathbf{q}}_j\tau + \frac{1}{2\Delta t}\left(-\ddot{\mathbf{q}}_j + \ddot{\mathbf{q}}_{j+1}\right)\tau^2 \tag{3.16}$$

with another integration one has

$$\mathbf{q}(\tau) = \mathbf{q}_j + \dot{\mathbf{q}}_j\tau + \frac{1}{2}\ddot{\mathbf{q}}_j\tau^2 + \frac{1}{6\Delta t}\left(-\ddot{\mathbf{q}}_j + \ddot{\mathbf{q}}_{j+1}\right)\tau^3. \tag{3.17}$$

At $\tau = \Delta t$:

$$\dot{\mathbf{q}}_{j+1} = \dot{\mathbf{q}}_j + \Delta t\left(\frac{1}{2}\ddot{\mathbf{q}}_j + \frac{1}{2}\ddot{\mathbf{q}}_{j+1}\right),$$

$$\mathbf{q}_{j+1} = \mathbf{q}_j + \dot{\mathbf{q}}_j\Delta t + \Delta t^2\left(\frac{1}{3}\ddot{\mathbf{q}}_j + \frac{1}{6}\ddot{\mathbf{q}}_{j+1}\right). \tag{3.18}$$

Newmark method is a generalisation of the linear acceleration method, where

$$\dot{\mathbf{q}}_{j+1} = \dot{\mathbf{q}}_j + \Delta t\left((1-\gamma)\ddot{\mathbf{q}}_j + \gamma\ddot{\mathbf{q}}_{j+1}\right),$$

$$\mathbf{q}_{j+1} = \mathbf{q}_j + \dot{\mathbf{q}}_j\Delta t + \Delta t^2\left(\left(\frac{1}{2} - \beta\right)\ddot{\mathbf{q}}_j + \beta\ddot{\mathbf{q}}_{j+1}\right). \tag{3.19}$$

If $\gamma = \frac{1}{2}$ and $\beta = \frac{1}{6}$ the Newmark method is equal to the Linear Acceleration Method. Assuming average acceleration $\ddot{\mathbf{q}}(t) = \frac{\ddot{\mathbf{q}}_j + \ddot{\mathbf{q}}_{j+1}}{2}$ so $\dot{\mathbf{q}}_{j+1} = \dot{\mathbf{q}}_j + \Delta t\frac{\ddot{\mathbf{q}}_j + \ddot{\mathbf{q}}_{j+1}}{2}$ and $\mathbf{q}_{j+1} = \mathbf{q}_j + \dot{\mathbf{q}}_j\Delta t + \frac{1}{2}\Delta t^2\frac{\ddot{\mathbf{q}}_j + \ddot{\mathbf{q}}_{j+1}}{2}$. By this definition, if $\gamma = \frac{1}{2}$ and $\beta = \frac{1}{4}$ the Newmark method is equal to the Constant Average Acceleration Method.

Now, using the Newmark method one can obtain the acceleration and the velocity at a new point, namely $j+1$, using the generalised coordinate of the new point $j+1$ and the acceleration, the velocity and the generalised coordinate of the last point j. The acceleration and the velocity at the new point are

$$\ddot{\mathbf{q}}_{j+1} = \frac{1}{\beta\Delta t^2}\left(\mathbf{q}_{j+1} - \mathbf{q}_j\right) - \frac{1}{\beta\Delta t}\dot{\mathbf{q}}_j - \left(\frac{1}{2\beta} - 1\right)\ddot{\mathbf{q}}_j,$$

$$\dot{\mathbf{q}}_{j+1} = \frac{\gamma}{\beta\Delta t}\left(\mathbf{q}_{j+1} - \mathbf{q}_j\right) + \left(1 - \frac{\gamma}{\beta}\right)\dot{\mathbf{q}}_j + \Delta t\left(1 - \frac{\gamma}{2\beta}\right)\ddot{\mathbf{q}}_j. \tag{3.20}$$

One can write them with constants a_{1-6} as

$$\ddot{\mathbf{q}}_{j+1} = a_1\left(\mathbf{q}_{j+1} - \mathbf{q}_j\right) - a_3\dot{\mathbf{q}}_j - a_5\ddot{\mathbf{q}}_j,$$

$$\dot{\mathbf{q}}_{j+1} = a_2\left(\mathbf{q}_{j+1} - \mathbf{q}_j\right) + a_4\dot{\mathbf{q}}_j + a_6\ddot{\mathbf{q}}_j. \tag{3.21}$$

Applying these definitions in the general form of Equation (3.14), one can find generalised coordinates for the new point $\mathbf{q}_{j+1}$ using information of previous point ($\mathbf{q}_j$, $\dot{\mathbf{q}}_j$ and $\ddot{\mathbf{q}}_j$) and the force at the new point, as

$$\left(a_1\mathbf{M} + a_2\mathbf{C} + \mathbf{K}\right)\mathbf{q}_{j+1} = \mathbf{f}_{j+1} + \left(a_1\mathbf{M} + a_2\mathbf{C}\right)\mathbf{q}_j + \left(a_3\mathbf{M} - a_4\mathbf{C}\right)\dot{\mathbf{q}}_j + \left(a_5\mathbf{M} - a_6\mathbf{C}\right)\ddot{\mathbf{q}}_j. \tag{3.22}$$

The only problem is to find information of the first point $j = 0$. By knowing the initial condition for velocity, $\dot{\mathbf{q}}_0$, and displacement, $\mathbf{q}_0$, at point $j = 0$, one can obtain initial acceleration from

$$\mathbf{M}\ddot{\mathbf{q}}_0 = \mathbf{f}_0 - \mathbf{C}\dot{\mathbf{q}}_0 - \mathbf{K}\mathbf{q}_0. \tag{3.23}$$

In linear vibration, the Newmark method is unconditionally stable when $\gamma \geq \frac{1}{2}$ and $\beta \geq \frac{1}{4}\left(\gamma + \frac{1}{2}\right)^2$, [94]. The constant average acceleration method is unconditionally stable (regardless of the time step) and linear acceleration method is conditionally stable (regarding to time step). For good accuracy, the constant average acceleration method with time step given by $\frac{\omega_0\Delta t}{2\pi} = 0.01$ or $\Delta t = 0.01\tau_0$ may be used, in which ω_0 and τ_0 are fundamental frequency and period of vibration [94]. In this study, the constant average acceleration method (where $\gamma = \frac{1}{2}$ and $\beta = \frac{1}{4}$) is used.

3.3 Numerical Results and Comparison Study

In this section, large deflections and stresses of various VSCL and CSCL plates are given. The study aims to show that the *p*-element proposed provides accurate results, to examine how does variable stiffness influence the deflections and stresses, and to investigate if plates with different thickness and with different loading conditions (as depicted in Figure 3.1) are affected in a diverse way by the variation of the fibre orientation. The properties of the plates analysed herein are defined in Table 3.1.

Here, in the case of non-linear analysis of VSCLs via a model based on TSDT, numerical tests were carried out with the goal of verifying if an accurate *p*-version model can be constructed with

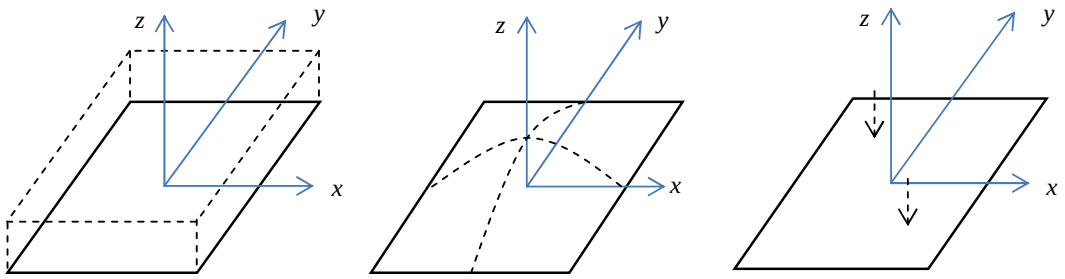

Uniform loading Sinusoidally loading Two point loading

Figure 3.1: Plate under three different loads.

a small number of degrees of freedom (DOF). It was verified that the 245 DOF ($p = p_u = p_w = p_\phi = 7$) model provides solutions quite close to models with more degrees of freedom. Moreover, we will show that this p-element (with $p = p_u = p_w = p_\phi = 7$) stands successfully comparisons with other approaches (examples in ensuing Tables 3.2 - 3.4). Since it also requires a reasonable computational time, this number of degrees of freedom is used in the analyses that follow, unless otherwise specified.

Table 3.1: Characteristics of the plates studied.

a (m)	b (m)	h (m)	E_1 (GPa)	E_2 (GPa)	G_{12} (GPa)	G_{13} (GPa)	G_{23} (GPa)	ν_{12}
Plate 1								
0.3048	0.3048	0.00244	12.605	12.628	2.16	2.16	2.16	0.25
Plate 2								
0.5	0.5	Various	25	1	0.50	0.50	0.20	0.25
Plate 3								
1	1	Various	173	7.2	3.76	3.76	3.76	0.29

The model introduced in the previous section is now partially validated by comparing its results with the deflections and stresses obtained elsewhere, either in the linear regime or in the geometrically non-linear regime. For that purpose, the model is applied to a CSCL $[0^o, 90^o]_{sym}$ plate, with different uniform loadings (of magnitude f_w) in the non-linear regime, in Figure 3.2 and Table 3.2, and to a plate with the same layup, but subjected to very small sinusoidally distributed loading (so that the plate is in the linear regime), in Table 3.3.

The plate of Figure 3.2 is Plate 1 in Table 3.1, with clamped boundaries. The deflections computed with the present TSDT are very close to the ones of references [88] and [95], where Reissner-Mindlin or FSDT theory was followed (identified by RDKQ and LDT18 in the figure), and to the displacements from Ref. [87], where TSDT was employed (identified by TSDT in the figure). The agreement between the deflections of the present method and the experimental results [86] is reasonable (the data from reference [86] was read in reference [87]), particularly if one takes into account that it is somewhat difficult to impose clamped boundary conditions in practice

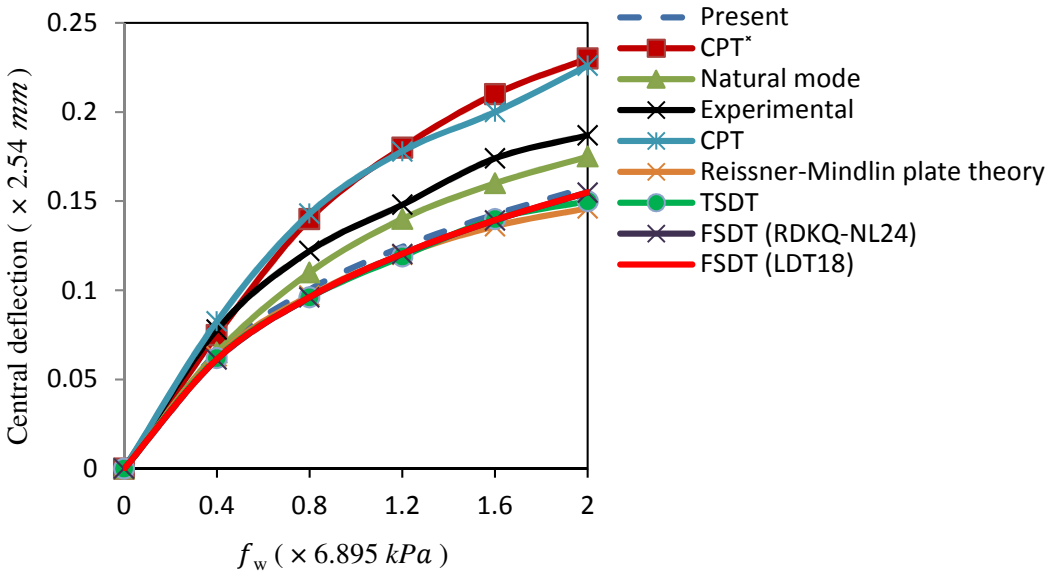

Figure 3.2: Central deflection of CSCL Plate 1 of Table 3.1 under different uniform loads, computed with various methods.

and that imperfections that often appear in real plates, influence the results [71]. The deflections computed by the approach here proposed deviate from the ones of reference [96] (denoted by FSDT Natural Mode in the figure) as the displacement magnitude increases (deflection results from Ref. [96] was read from a graph in Ref. [97], where a three-node multilayered triangular facet element based on a so called "natural mode method" and FSDT was used) and deviate even more from the thin plate theory based data of references [86] and [97] (CPT and CPT* in the Figure). In Figure 3.2, a difference between CPT and higher-order theories is observed which is slightly strange, because the plate is quite thin.

For a plate with edges simply-supported and immovable (SSSS-1) (for boundary conditions, see Appendix A), with different thicknesses, Table 3.2 shows a good comparison between the present deflections and deflections computed with other methods, including analytical results. Here, a plate similar to Plate 2 of Table 3.1, but with a and b equal to 1 m, is used. In this table, methods from Refs. [88,98–100] including a 4-node quadrilateral displacement-based laminated element (RDKQ-NL24), a displacement-based 3-node, 18-degree-of-freedom flat triangular plate/shell element (LDT18), a so-called material finite element (MFE), HSDT, and analytical solution are involved.

Table 3.3 tabulates deflections, and normal and shear stresses, using constitutive and equilibrium equations, for a simply-supported plate with movable edges (SSSS-2) that is under a sinusoidally distributed transverse load. Plate 2 in Table 3.1 (but with $a = b = 1$ m) is used. The following non-dimensional parameters are adopted [85]:

$$\overline{w} = w^0(0,0)\left(\frac{\pi^4 Q h^3}{12 a^4 f_w}\right),$$

Table 3.2: Central deflection of simply-supported CSCL Plate 2 of Table 3.1 under uniform loading.

$\frac{f_w a^4}{E_2 h^4}$	Central deflection $\frac{w^0(0,0)}{h}$					
	Present	HSDT [98]	FSDT (RDKQ-NL24) [88]	FSDT (LDT18) [88]	Analytical [99]	FSDT (MFE) [100]
$h = 0.025$						
50	0.2938	0.293	0.2941	0.2829	0.293	0.293
100	0.4641	0.464	0.4673	0.4513	0.464	0.463
150	0.5805	0.582	0.5866	0.5678	0.582	0.578
200	0.6686	0.664	0.6786	0.6577	0.664	0.666
250	0.7415	0.738	0.7541	0.7317	0.738	-
$h = 0.05$						
50	0.3126	0.320	0.3280	0.2955	0.320	0.314
100	0.4808	0.493	0.4949	0.4626	0.486	0.482
150	0.5929	0.592	0.6080	0.5768	0.592	0.593
200	0.6785	0.680	0.6948	0.6649	0.680	0.678
250	0.7486	0.752	0.7663	0.7373	0.752	-
$h = 0.1$						
50	0.3608	0.360	0.3704	0.3317	0.356	0.366
100	0.5179	0.520	0.5249	0.4922	0.510	0.522
150	0.6212	0.624	0.6290	0.6002	0.610	0.625
200	0.7005	0.696	0.7099	0.6834	0.689	0.703
250	0.7659	0.760	0.7770	0.7521	0.747	-

$$
\begin{aligned}
Q &= 4G_{12} + \frac{E_1 + E_2\,(1+2\nu)}{1-\nu^2}, \\
\overline{\sigma}_x &= \sigma_x\left(0,0,\frac{h}{2}\right)\left(\frac{h^2}{a^2 f_w}\right), \\
\overline{\sigma}_y &= \sigma_y\left(0,0,\frac{h}{4}\right)\left(\frac{h^2}{a^2 f_w}\right), \\
\overline{\tau}_{xy} &= \tau_{xy}\left(-\frac{a}{2},-\frac{b}{2},\frac{h}{2}\right)\left(\frac{h^2}{a^2 f_w}\right), \\
\overline{\tau}_{xz} &= \tau_{xz}\left(-\frac{a}{2},0,0\right)\left(\frac{h}{a f_w}\right), \\
\overline{\tau}_{yz} &= \tau_{yz}\left(0,-\frac{b}{2},0\right)\left(\frac{h}{a f_w}\right),
\end{aligned}
\tag{3.24}
$$

where f_w is the magnitude of the sinusoidally distributed load $f_w(x,y) = f_w \cos\left(\frac{x\pi}{a}\right)\cos\left(\frac{y\pi}{b}\right)$. The constitutive transverse shear stresses - τ^c_{xz} and τ^c_{yz} - and the in-plane stresses - σ_x, σ_y and τ_{xy} - are obtained from the constitutive relations, Equation (2.17). As is well known, the transverse shear

Table 3.3: Deflection and stresses of simply-supported CSCL Plate 2 of Table 3.1 under sinusoidally distributed transverse load.

a/h	Source	$\overline{w}$	$\overline{\sigma}_x$	$\overline{\sigma}_y$	$\overline{\tau}_{xy}$	$\overline{\tau}_{xz}$	$\overline{\tau}_{yz}$
100	3D-Elasticity [85]	1.008	0.539	0.271	0.022	0.337	0.141
	HSDT [101]	-	0.539	0.271	0.021	0.372	0.128
	Karama et al. [102]	-	0.538	0.270	0.021	0.324	0.118
	HSDT [103]	-	0.538	0.270	0.021	0.290	0.112
	Present - Constitutive Eq.	1.007	0.540	0.272	0.020	0.289	0.111
	Present - Equilibrium Eq.					0.333	0.136
20	3D-Elasticity [85]	1.189	0.543	0.308	0.023	0.328	0.156
	HSDT [101]	-	0.543	0.306	0.023	0.362	0.142
	Karama et al. [102]	-	0.541	0.306	0.023	0.316	0.131
	HSDT [103]	-	0.539	0.304	0.023	0.283	0.123
	Present - Constitutive Eq.	1.182	0.541	0.307	0.022	0.282	0.123
	Present - Equilibrium Eq.					0.327	0.152
10	3D-Elasticity [85]	1.709	0.559	0.401	0.028	0.301	0.196
	HSDT [101]	-	0.561	0.395	0.028	0.335	0.177
	Karama et al. [102]	-	0.553	0.393	0.027	0.294	0.163
	HSDT [103]	-	0.546	0.389	0.027	0.264	0.153
	Present - Constitutive Eq.	1.695	0.549	0.397	0.026	0.263	0.154
	Present - Equilibrium Eq.					0.304	0.192
4	3D-Elasticity [85]	4.491	0.720	0.663	0.047	0.219	0.292
	HSDT [101]	-	0.740	0.635	0.048	0.254	0.269
	Karama et al. [102]	-	0.699	0.637	0.046	0.226	0.253
	HSDT [103]	-	0.665	0.632	0.044	0.206	0.239
	Present - Constitutive Eq.	4.570	0.680	0.644	0.043	0.204	0.241
	Present - Equilibrium Eq.					0.228	0.298

stresses that result from the constitutive equations are not continuous at the interfaces between different oriented layers, and are therefore not realistic. One way of solving this issue, which was also adopted in this work, is using the equilibrium equations of 3-D elasticity to compute the stresses, i.e. using the following equations:

$$\tau_{xz}^{e} = -\int_{\frac{h}{2}}^{z} (\sigma_{x,x} + \tau_{xy,y})\, dz,$$

$$\tau_{yz}^{e} = -\int_{\frac{h}{2}}^{z} (\sigma_{y,y} + \tau_{xy,x})\, dz. \tag{3.25}$$

Equations (3.25) are obtained from the equilibrium equations of 3-D elasticity in directions x and y, without acceleration (static analysis), body or surface forces in those directions [51]. In this work, the external loads are always in the z direction. One verifies in Table 3.3 that the deflection, the normal stresses, the membrane shear stresses and the shear stresses computed by equilibrium equations are in good agreement with the 3D-elasticity results of reference [85]. It is noteworthy that this good agreement between the present results and 3D-elasticity occurs even in the very thick plate where $a/h = 4$. Moreover, the deflection, the normal and membrane shear stresses computed with the present approach are generally very close to the ones provided by other references. The transverse shear stresses computed by constitutive relation here and in Ref. [103] are also quite close. Furthermore, one verifies that the transverse shear stresses τ_{xz} computed via the constitutive relations differ less than 14% from the equilibrium relation stresses. In what transverse shear stresses τ_{yz} are concerned, the relative difference is always smaller than 20%. The constitutive relation based stresses are smaller than the equilibrium relation ones. The comparisons presented in this section indicate that the model here introduced and the computational code implemented are correct.

For the sake of completeness and to further verify the model, Table 3.4 shows an example that illustrates the convergence and accuracy on deflection and stress computation, by comparison with 3-D elasticity solutions taken from reference [85]. The considered CSCL square plate is simply-supported with movable edges (SSSS-2), with fibre configuration $[0^{o}, 90^{o}, 0^{o}, 90^{o}, 0^{o}]$, and has the mechanical properties of Plate 2 in Table 3.1 (but with $a = b = 1$ m). The plate is under a static load, with sinusoidal distribution and of small intensity – that means the analysis is in the linear regime; the non-linear terms are not included in the model. In Table 3.2, there was a somewhat similar example, but in a different plate and, although small displacements were considered, the non-linear model was used. The non-dimensional parameters mentioned in Equations (3.24) are used except, after [85], $\overline{\sigma}_{y} = \sigma_{y}\left(0, 0, \frac{h}{3}, t\right)\left(\frac{h^2}{a^2 f_w}\right)$.

p-Version finite elements with 180, 245, 405, and 500 DOFs are used and the transverse shear stresses are calculated by the equilibrium equations, to satisfy continuity requirements. The present method, with only 180 or 245 DOF, gives results that are generally very close to the 3-D elasticity results.

Table 3.4: Comparison of deflection and stresses of a CSCL plate subjected to static sinusoidal load.

a/h	Method	$\overline{w}$	$\overline{\sigma}_x$	$\overline{\sigma}_y$	$\overline{\tau}_{xy}$	$\overline{\tau}_{xz}$	$\overline{\tau}_{yz}$
100	3D-Elasticity [85]	1.006	0.539	0.360	-0.0213	0.272	0.205
	Present 180 DOF	1.004	0.539	0.356	-0.0200	0.265	0.206
	Present 245 DOF	1.005	0.541	0.358	-0.0201	0.260	0.200
	Present 405 DOF	1.005	0.541	0.358	-0.0201	0.264	0.203
	Present 500 DOF	1.005	0.541	0.358	-0.0201	0.264	0.203
50	3D-Elasticity [85]	1.023	0.539	0.363	-0.0214	0.271	0.206
	Present 245 DOF	1.020	0.540	0.360	-0.0202	0.260	0.200
20	3D-Elasticity [85]	1.145	0.539	0.380	-0.0222	0.268	0.212
	Present 245 DOF	1.122	0.540	0.373	-0.0207	0.257	0.207
10	3D-Elasticity [85]	1.570	0.545	0.430	-0.0246	0.258	0.223
	Present 245 DOF	1.480	0.542	0.410	-0.0223	0.246	0.223
	Present 500 DOF	1.480	0.542	0.410	-0.0223	0.247	0.226

3.3.1 Deflection of VSCL Plates

Initially, we consider a clamped four-layer VSCL plate $[\langle T_0, T_1\rangle, \langle 90^o + T_0, 90^o + T_1\rangle]_{sym}$. For this plate $a = b = 0.5$ m, $h = 0.005$ m; the other characteristics are the ones given for Plate 3 in Table 3.1. The plate is subjected to a uniformly transverse distributed static pressure of 1×10^5 Nm^{-2}. The analyses of static deformation on this plate indicate that, for any fibre angle variation $\langle T_0, T_1\rangle$, deflection is symmetric about the centre of the plate, we mean that the following relation holds: $w^0(x,y) = w^0(-x,-y)$. This symmetry condition is a consequence of the function used to define the curvilinear fibre, Equation (1.3), of the symmetry of load and boundaries. Four points in half of this plate are analysed in Figure 3.3; due to the symmetry condition given, these four points roughly provide an overall picture of the plate behaviour. Here, a dashed line represents CSCL plates (where T_0 and T_1 are equal) and the hatched area represents VSCL plates that cannot be manufactured, sub-section 1.4.4. The figure shows that VSCL plates can experience less deflection than any CSCL in specific points. For instance, at point $(x,y) = \left(\frac{a}{4}, -\frac{b}{4}\right)$, the deflection ratio $w^0\left(\frac{a}{4}, -\frac{b}{4}\right)/h = 0.3905$ of the VSCL plate with $[\langle 70^o, 20^o\rangle, \langle 160^o, 110^o\rangle]_{sym}$ is 77% of the deflection ratio ($w^0\left(\frac{a}{4}, -\frac{b}{4}\right)/h = 0.5043$) of the CSCL plate with $[0^o, 90^o]_{sym}$. At the other points considered in the figure (i.e. (x,y) equal to $(0,0)$, $(a/4, b/4)$ and $(0, b/4)$), CSCL plates show minimum deflection.

Deflection ratios $w^0(x,y)/h$ of a four-layer CSCL plate and of a VSCL plate are depicted in Figure 3.4. The plate's characteristics and the loading condition used in Figures 3.3 and 3.4 are the same; the two plates in Figure 3.4 share the same fibre orientation at $x = 0$. An area in lighter blue indicates larger deflection and the red arrow shows the point of maximum deflection. This figure shows that, in the VSCL as in the CSCL, the largest deflection occurs at the centre of the plate and also that deflections are symmetric with respect to the centre of the plate. But it is clear that due to the change in the fibre orientation from CSCL to VSCL, the pattern of deflection at the plate changes.

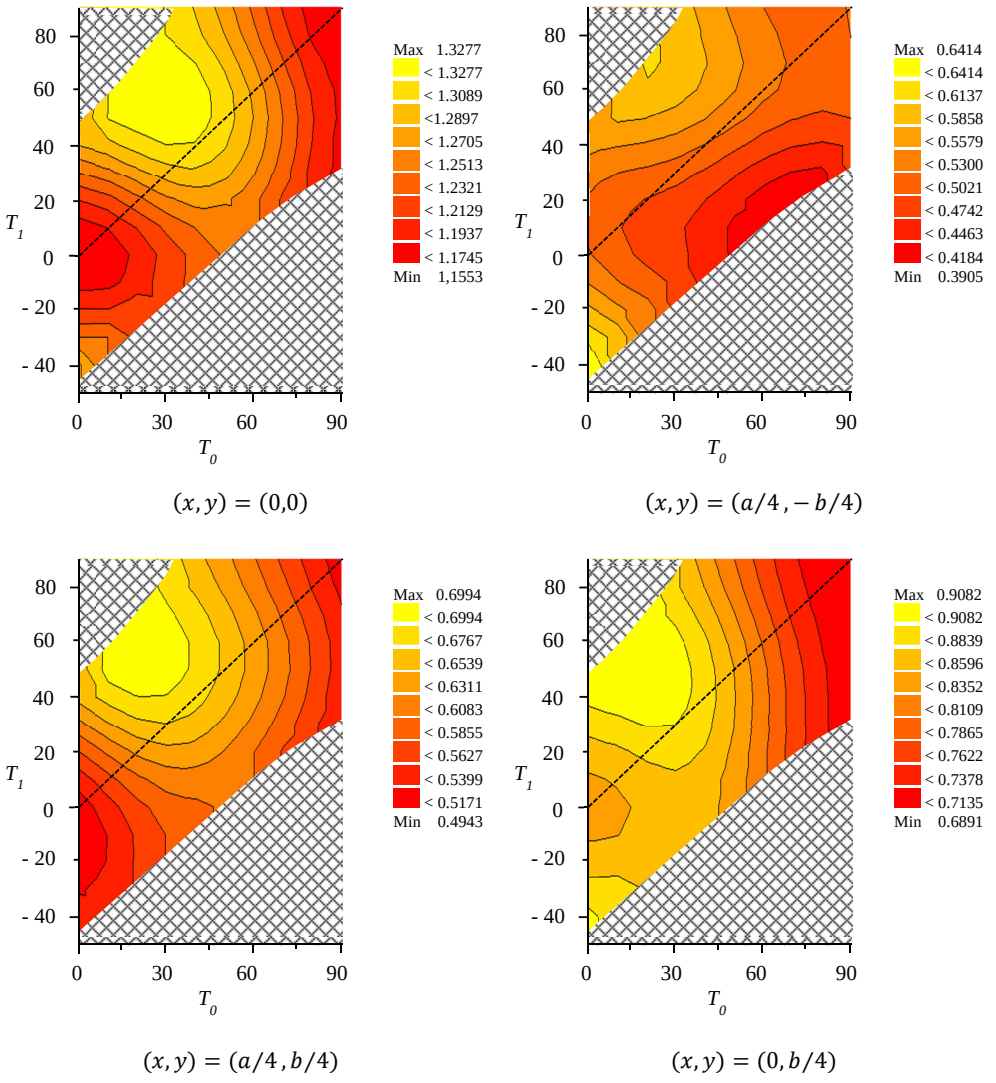

Figure 3.3: Deflection ratio $\frac{w^0(x,y)}{h}$ contour plots of four-layer VSCL Plates 3 of Table 3.1 with different fibre angles. The plate is subjected to a uniform load.

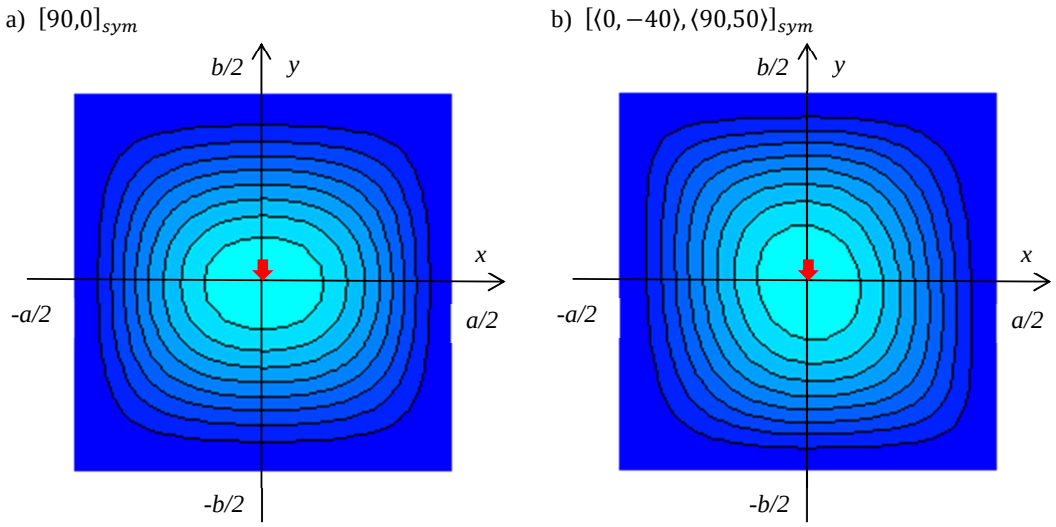

Figure 3.4: Deflection of CSCL and of VSCL Plate 3 of Table 3.1. (a) $[0^o,90^o]_{sym}$ and (b) $[\langle 0^o,-40^o\rangle,\langle 90^o,50^o\rangle]_{sym}$

In the case presented in Figure 3.3, we understood that with VSCL plates one achieves smaller deflection around point $(x,y)=(a/4,-b/4)$ in comparison with CSCL plates. This indicates that the VSCL plates with fibre paths considered here may be advantageous if the loads are out-of-centre point loads, instead of uniform, sinusoidal or loads applied in the plate centre. To test the preceding idea and look for advantages of VSCLs over CSCLs, plates subjected to two point loads of 3×10^4 N at $(x,y)=(-a/4,b/4)$ and $(a/4,-b/4)$ (see Figure 3.1), with different fibre angles, but with the same geometric and material properties (the ones of plates in Figure 3.3) are analysed. Here, unlike in Figure 3.4, the maximum deflection does not occur at the centre of the plate and the position of maximum deflection changes slightly by altering the fibre orientation angles. Figure 3.5(a) depicts deflection ratios for a VSCL plate with $[\langle 70^o,20^o\rangle,\langle 160^o,110^o\rangle]_{sym}$ fibre angles. In order to find the maximum deflection W, 1600 different points of this plate are analysed and the maximum deflection among these points is chosen. Figure 3.5(b) portrays the maximum deflection of these VSCL plates with different fibre orientation angles. As this figure demonstrates, there are many VSCL plates whose maximum deflections are smaller than any possible CSCL plate; this is especially – but not only – true below the dash-line of CSCL plates in Figure 3.5(b). For example, by choosing the VSCL plate with $[\langle 60^o,10^o\rangle,\langle 150^o,100^o\rangle]_{sym}$ the maximum deflection is reduced around 8% in comparison with the $[0^o,90^o]_{sym}$ CSCL plate.

3.3.2 Stress Distribution in VSCL plates

In Table 3.3, a simply-supported plate with movable edges (SSSS-2) was analysed in order to compare stresses and deflections computed here with published ones. The lack of results in the

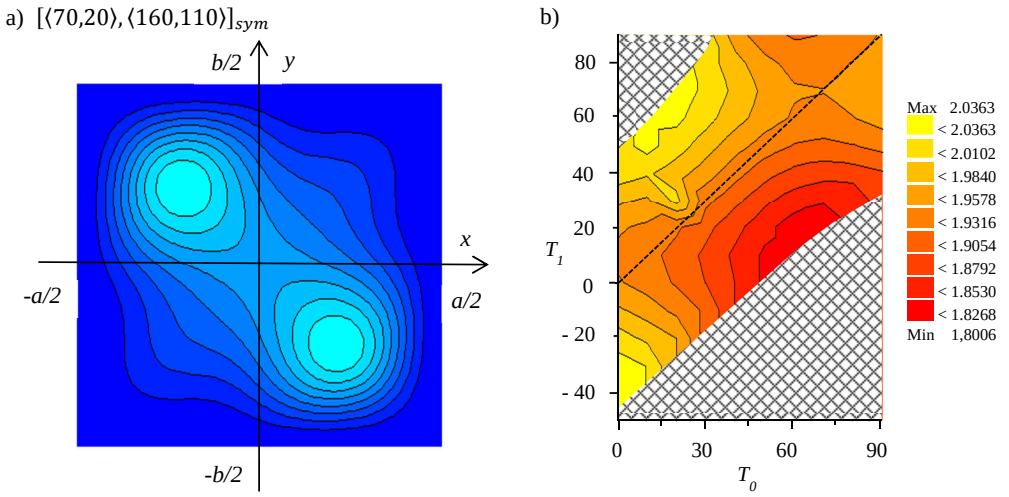

Figure 3.5: (a) Deflection in VSCL Plate 3 of Table 3.1 subjected to two point loads $[\langle 70^{\circ}, 20^{\circ}\rangle, \langle 160^{\circ}, 110^{\circ}\rangle]_{sym}$, and (b) Contour plot of maximum deflection ratio W/h of the VSCL Plate 3 with different fibre angles.

literature on stresses in CSCL plates with clamped edges, as well as in plates with edges simply-supported and immovable (SSSS-1), now motivates the author to present a few results in Table 3.5. These can be used by other researchers in future investigations. The stresses and deflections presented in Table 3.5 are for a plate with the geometry and loading conditions of the plate in Table 3.3, but with the just mentioned boundary conditions. Here, the results are for $\overline{w}(0,0)$, $\overline{\sigma}_x(0,0,h/2)$, $\overline{\sigma}_y(0,0,h/4)$, $\overline{\tau}_{xy}(-a/4,-b/4,h/2)$, $\overline{\tau}_{xz}(-a/4,-b/4,0)$, $\overline{\tau}_{yz}(-a/4,-b/4,0)$, i.e. Tables 3.3 and 3.5 show the shear stresses at different points. For clamped and simply-supported with immovable edges (SSSS-1) boundary conditions, the transverse shear stresses of the present model computed with the constitutive equations are zero or very small at the edges of the plate, and this is the reason why these stresses are now examined in a different point. Normal stresses and deflection are calculated in the centre of the plate in both tables. The results of Tables 3.3 and 3.5, which are obtained with a load of small magnitude, show that the deflection and normal stresses for simply-supported plates with movable (SSSS-2) or immovable (SSSS-1) edges are the same in the linear regime (as would be expected). Both tables show an increase in the non-dimensional parameters $\overline{w}$, $\overline{\sigma}_x$ (with one exception in the thin clamped plate at Table 3.5), $\overline{\sigma}_y$, $\overline{\tau}_{xy}$, and $\overline{\tau}_{yz}$ and a decrease in $\overline{\tau}_{xz}$ when the plate gets thicker (with another exception in Table 3.5, from $a/h = 100$ to $a/h = 20$ when using the equilibrium equations).

Increasing the load, the difference between deflection and stresses on plates with the two boundary conditions appears. If we increase the magnitude of the load to 1 Pa, which is much larger than the small load – in the scale of 10^{-3} Pa – used in Table 3.3, we get $w^0(x,y)/h = 0.4$ for the simply-supported plate with movable edges and $w^0(x,y)/h = 0.33$ for the plate simply-supported with immovable edges (SSSS-2). Therefore, applying higher loads, the two plates with

Table 3.5: Deflection and stresses of clamped and simply-supported CSCL Plate 2 of Table 3.1.

a/h		$\overline{w}$ $(0,0)$	$\overline{\sigma}_x$ $\left(0,0,\frac{h}{2}\right)$	$\overline{\sigma}_y$ $\left(0,0,\frac{h}{4}\right)$	$\overline{\tau}_{xy}$ $\left(\frac{-a}{4},\frac{-b}{4},\frac{h}{2}\right)$	$\overline{\tau}_{xz}$ $\left(\frac{-a}{4},\frac{-b}{4},0\right)$	$\overline{\tau}_{yz}$ $\left(\frac{-a}{4},\frac{-b}{4},0\right)$
Clamped							
100	Constitutive Eqs.	0.254	0.221	0.102	0.0045	0.136	0.037
	Equilibrium Eqs.					0.155	0.049
20	Constitutive Eqs.	0.425	0.205	0.155	0.0052	0.115	0.068
	Equilibrium Eqs.					0.164	0.088
10	Constitutive Eqs.	0.848	0.218	0.227	0.0068	0.100	0.106
	Equilibrium Eqs.					0.145	0.146
4	Constitutive Eqs.	3.048	0.416	0.277	0.0139	0.085	0.127
	Equilibrium Eqs.					0.097	0.202
Simply-supported with immovable edges							
100	Constitutive Eqs.	1.007	0.541	0.272	0.0109	0.145	0.055
	Equilibrium Eqs.					0.170	0.069
20	Constitutive Eqs.	1.184	0.542	0.308	0.0108	0.141	0.062
	Equilibrium Eqs.					0.165	0.077
10	Constitutive Eqs.	1.695	0.549	0.397	0.0128	0.132	0.077
	Equilibrium Eqs.					0.153	0.097
4	Constitutive Eqs.	4.570	0.680	0.644	0.0213	0.102	0.121
	Equilibrium Eqs.					0.114	0.151

different simply-supported boundary conditions (SSSS-1 and SSSS-2) experience different deflection and hence different stress.

Now, numerical results are provided for a VSCL plate subjected to a sinusoidally distributed transverse load. These may serve as a benchmark for future studies in the non-linear regime. Table 3.6 presents deflections and stresses for a VSCL plate that is either clamped or simply-supported with movable edges (SSSS-2). The plate has four layers with fibre angles defined by $[\langle 45^o, 0^o\rangle, \langle 135^o, 90^o\rangle]_{sym}$; the remaining characteristics are the ones of Plate 3 in Table 3.1. The deflection is divided by the plate thickness and the stresses are in GPa; deflection and stresses are computed at particular points, specifically: $w^0(0,0)/h$, $\sigma_x = \sigma_x(0,0,h/2)$, $\sigma_y = \sigma_y(0,0,h/4)$, $\tau_{xy} = \tau_{xy}(-a/4,-b/4,h/2)$, $\tau_{xz} = \tau_{xz}(-a/4,-b/4,0)$, and $\tau_{yz} = \tau_{yz}(-a/4,-b/4,0)$.

The force magnitudes were chosen so that the non-dimensional transverse displacement at $x = y = 0$ is more or less equal to the plate thickness. As might be expected, normal stresses are larger in thicker than in thin plates, experiencing displacements with similar non-dimensional magnitude, irrespectively of the boundary conditions. Proportionally, the normal stresses and the membrane shear stresses experience very different variations with the thickness in clamped and simply-supported with movable edges plates (SSSS-2). In fact, whilst, for example, the normal stress σ_x increases about 20 times when the boundaries are fully clamped, it increases about 4 times in the case of simply-supported with movable edges. In what transverse shear stresses are concerned, one realizes that even though a third-order shear deformation theory is being used, equilibrium and constitutive equations results are markedly different, significantly more than what occurred in Tables 3.3 and 3.5. This is an effect of geometrical non-linearity that we will examine

in more detail in the following paragraphs.

Table 3.6: Deflection and stresses (GPa) of VSCL Plate 3 of Table 3.1 under sinusoidally distributed transverse load (here xEy means $x \times 10^y$).

h/a	f_w (Pa)	$\frac{w^0(0,0)}{h}$	σ_x	σ_y	τ_{xy}	τ^c_{xz}	τ^e_{xz}	τ^c_{yz}	τ^e_{yz}
Clamped									
0.01	10E5	1.04	0.81E-1	0.61E-1	0.31E-2	0.10E-2	0.20E-2	0.37E-3	0.39E-3
0.05	5.0E7	1.01	0.16E1	0.12E1	0.58E-1	0.10	0.19	0.43E-1	0.53E-1
Simply-supported with movable edges (SSSS-2)									
0.01	2.0E4	0.98	0.22	0.27	0.36E-1	0.10	0.77E-2	0.37E-1	0.41E-2
0.05	1.1E7	0.98	0.89	0.72	0.28E-1	0.14E-1	0.64E-1	0.56E-1	0.30E-2

Altering the fibre orientations in a VSCL plate changes the stress field. So, not only the stress magnitudes, but also the place where the maximum stress is attained change with the curvilinear paths. Imagine for example a clamped $[\langle T_0, T_1\rangle, \langle 90^o + T_0, 90^o + T_1\rangle]_{sym}$ plate like Plate 3 of Table 3.1 (but with $a = b = 0.5$ m, $h = 0.005$ m), which is subjected to two point loads with magnitude 10^4 N, applied as shown in Figure 3.1. Figure 3.6 shows the maximum normal and in-plane stresses attained (for $\sigma_x(x,y,h/2)$, $\sigma_y(x,y,h/4)$, $\tau_{xy}(x,y,h/2)$) and their locations on the plane; and Figure 3.7 displays these results for $\tau_{xz}(x,y,0)$ and $\tau_{yz}(x,y,0)$. Only a quarter of the plate is analysed, because with this loading and fibre distribution, we expect the location of maximum stress to be in this particular quarter (and, with the same value, on the opposite quarter).

Figure 3.6 shows that the maximum value of σ_x is very sensitive to changes in the fibre orientation angle. For many fibre angles, this stress is low (red area), but a minor change in fibre angles can alter σ_x very much. The behaviour of σ_y is similar. Some CSCL plates with higher T_0 are the plates where a lower maximum normal stresses σ_x and σ_y is attained. In the quarter of the plate investigated, there are three distinct areas where points with maximum stress, for both normal stresses σ_x and σ_y, exist. One of these areas is close to the load and the other two are at the edges. No easy pattern can be found between these three areas and the fibre angles, but we acknowledge that these areas are prone to sustain local effects with the appearance of larger stresses. In-plane stress τ_{xy} is sensitive to fibre angle change, and it has a high amount (yellow areas in the figure) for many angles. The maximum stress τ_{xy} is achieved in two distinct areas, one is close to the load, and the other starts from one of the edges, and continues to the next edge. The transverse shear stresses τ^c_{xz} and τ^c_{yz} show opposite patterns, Figure 3.7. With constant T_0 and T_1, if one transverse stress is maximum, the other transverse stress is minimum. About the place of these maximum stresses, both transverse stresses are maximum in just one small area, but not the same, inside the quarter of the plate. Curiously, τ^e_{xz} and τ^e_{yz} show a more similar variation with the fibre angles, although one transverse shear stress, τ^e_{yz}, varies in a quite more regular way than the other, τ^e_{xz}. It would be expected that the maximum values of transverse shear stresses would occur in two distinct adjacent edges (at $x = \pm a/2$ and $y = \pm b/2$, respectively; it is recalled that $z = 0$). Figure 3.7 confirms this and shows exactly the points where the maximum values of τ^e_{xz} and τ^e_{yz} are attained under the hypothesis behind the present model.

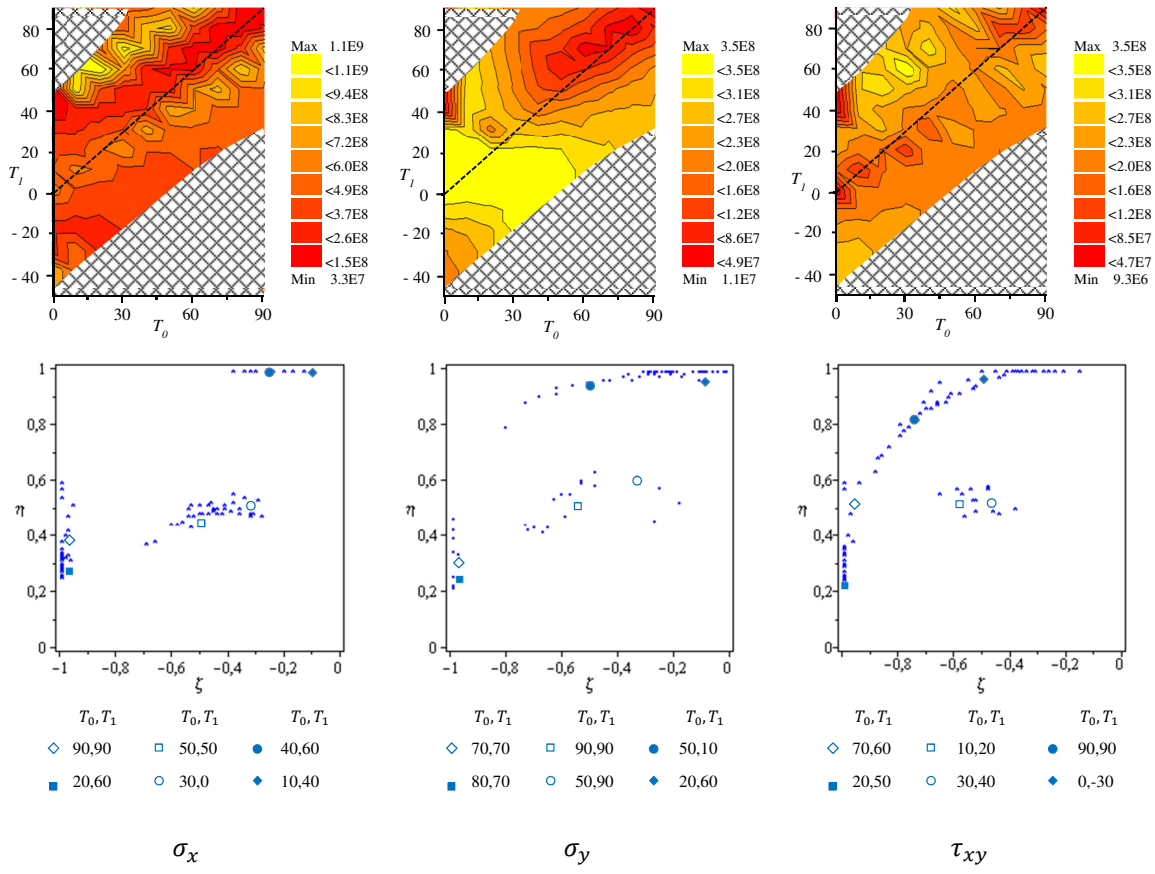

Figure 3.6: Maximum normal and in-plane shear stresses and change of their locations for VSCL Plate 3 of Table 3.1, subjected to two point loads, with different fibre angles.

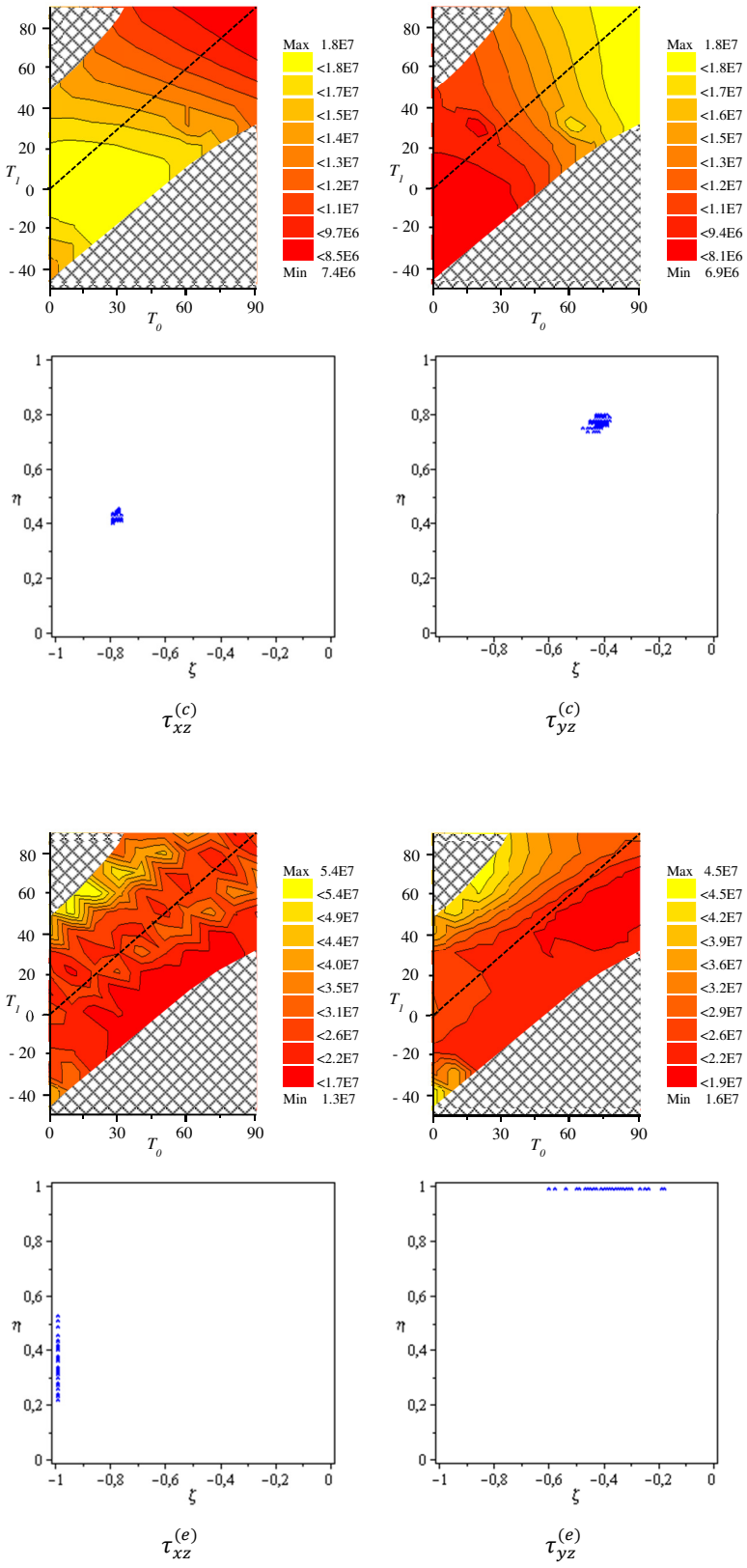

Figure 3.7: Maximum transverse shear stresses and change of their locations for VSCL Plate 3 of Table 3.1, subjected to two point loads, with different fibre angles.

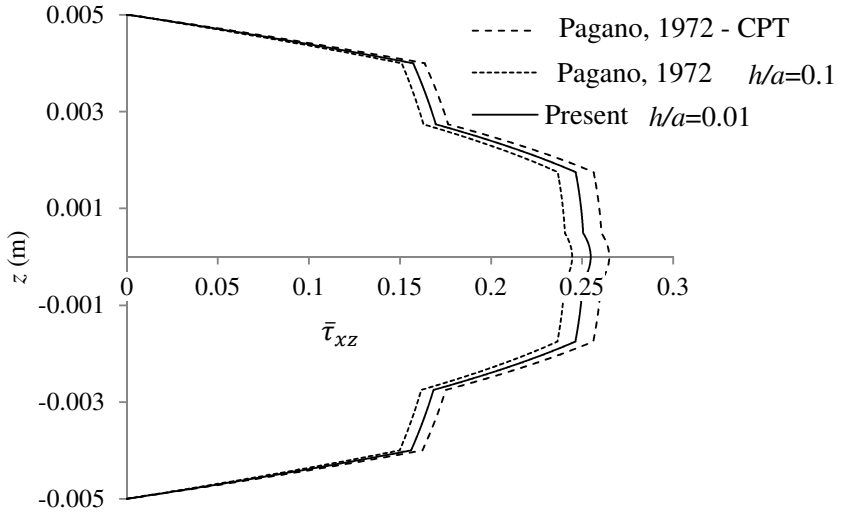

Figure 3.8: Shear stress distribution through the thickness simply-supported nine-layer CSCL Plate 2 of Table 3.1 in linear regime.

The previous paragraphs were focused on the variation of stresses with coordinates x and y. We now address the variation of stresses along the plate thickness (where $x = -a/2$ and $y = 0$). If one computes the transverse shear stresses by the equilibrium equations in the way expressed by Equations (3.25), zero stresses are obtained at the bottom surface of the plate. This zero shear stress in the bottom surface is due to the absence of integration constant in Equations (3.25) and is reasonable in the linear regime, where the deformed bottom surface remains almost parallel to the original xy plane. Using Equations (3.25) and with strain-displacement relation in the linear regime, the stresses at the top surface of the plate are also zero (see Figure 3.8), again a realistic result in the absence of large displacements and of tangential forces in the surface. We note that Figure 3.8 shows a good comparison between the present solution and Ref. [85], in the linear regime, for a nine-layer $[0^o, 90^o, 0^o, 90^o, 0^o, 90^o, 0^o, 90^o, 0^o]$ CSCL plate.

However, increasing the load, therefore, increasing the displacements and making non-linearity more meaningful, the equilibrium Equations (3.25), lead to non-zero transverse shear stresses at the top surface of a plate. Figure 3.9 shows this issue for a three-layer $[0^o, 90^o, 0^o]$ CSCL plate (where $x = -a/2$ and $y = 0$). In this figure, $\bar{\bar{\tau}}_{xz}$ is a non-dimensional stress parameter calculated by dividing the shear stress by its maximum value, in order to facilitate comparisons. Here, the properties of Plate 2 in Table 3.1, with simply-supported boundaries and movable edges (SSSS-2), are used. We consider that the appearance of non-zero values on the surface is correct, because the surface has an inclination with respect to the xy plane (at $x = -a/2$ and $y = 0$). Hence, even if the absence of forces tangential to the surface would lead to zero shear along this tangent, this is not in a direction parallel to y or z. Although often ignored, the appearance of non-zero shear transverse stresses at the top surface of the plate in the non-linear regime is not unknown and has been addressed in detail in Ref. [104].

By introducing relatively small changes in the fibre angles on VSCL plates, different stresses

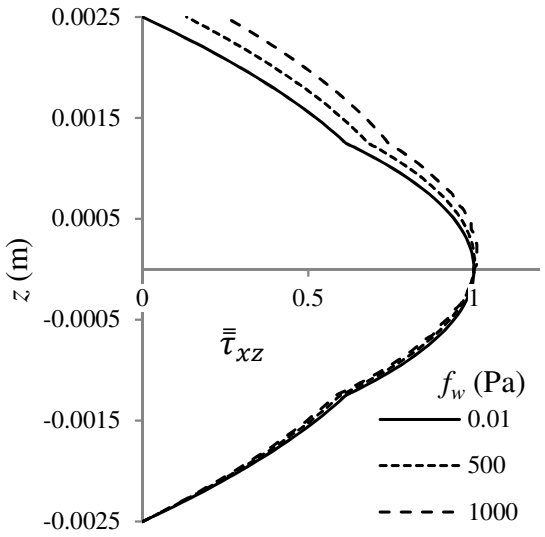

Figure 3.9: Shear stress distribution through the thickness of a simply-supported three-layer CSCL Plate 2 of Table 3.1 in non-linear regime, with increasing sinusoidally distributed transverse load.

are achieved. Hence, one can exploit the change of the fibre orientation in VSCL plates to avoid damages and failure, by adjusting the curvilinear fibre to the particular application of the plate. This idea is going to be further examined in the next chapter. For now, to illustrate the variations that occur through the thickness of a VSCL plate, plates of the type $[\langle T_0, T_1\rangle, \langle 90^o + T_0, 90^o + T_1\rangle]_{sym}$, with different angles T_0 and T_1, are analysed. Figure 3.10 shows these stress distributions under sinusoidally distributed loading (with magnitude 10^3 N) for $\sigma_x = \sigma_x(0,0,z)$, $\sigma_y = \sigma_y(0,0,z)$, $\tau_{xy} = \tau_{xy}(-a/2,-b/2,z)$, $\tau_{xz} = \tau_{xz}(-a/2,0,z)$, and $\tau_{yz} = \tau_{yz}(0,-b/2,z)$. The properties are the ones of Plate 3 in Table 3.1 (but with $a = b = 0.5, h = 0.005$ m). In this figure, transverse shear stresses computed by constitutive relation are continuous because of the similar shear transverse moduli.

Figure 3.11 shows the stresses for a VSCL $[\langle 90^o, 40^o\rangle, \langle 180^o, 130^o\rangle]_{sym}$ plate, under sinusoidally distributed loading. Other properties are similar to the plate used in Figure 3.10. Also, the deflection ratio of the plate at section $y = 0$ is given. The distributions of σ_x and σ_y demonstrate that the inner and outer layers react differently to the increase in load, with large values of σ_x in the inner layers and large values of σ_y in the outer layers. As might be expected, the upper layers are in compression and the lower ones in traction. But the point where σ_x is zero – which in Figure 3.11 has coordinates $(0,0,z)$ – moves, because its coordinate z increases with the load as a consequence of non-linear effects. In the case studied, increasing the load first leads to positive τ^c_{yz} stresses and then to negative. Moreover, whilst the absolute values of σ_x and σ_y increase less than the load (again a consequence of non-linearity), the absolute values of τ^c_{xz} and τ^c_{yz} experience large variations as non-linearity becomes more important.

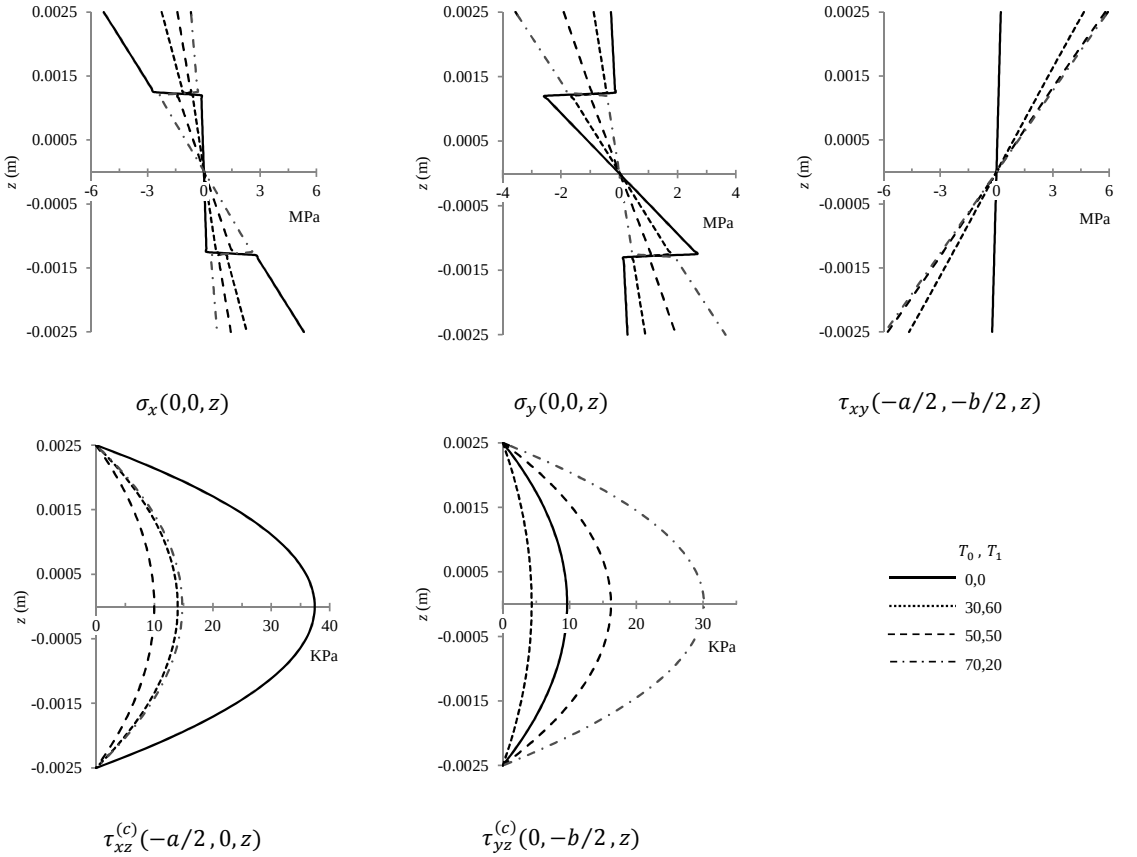

Figure 3.10: In-plane and shear stress distribution through the thickness of simply-supported VSCL Plates 3 of Table 3.1, with movable edges, under sinusoidally distributed loading, with different fibre angles.

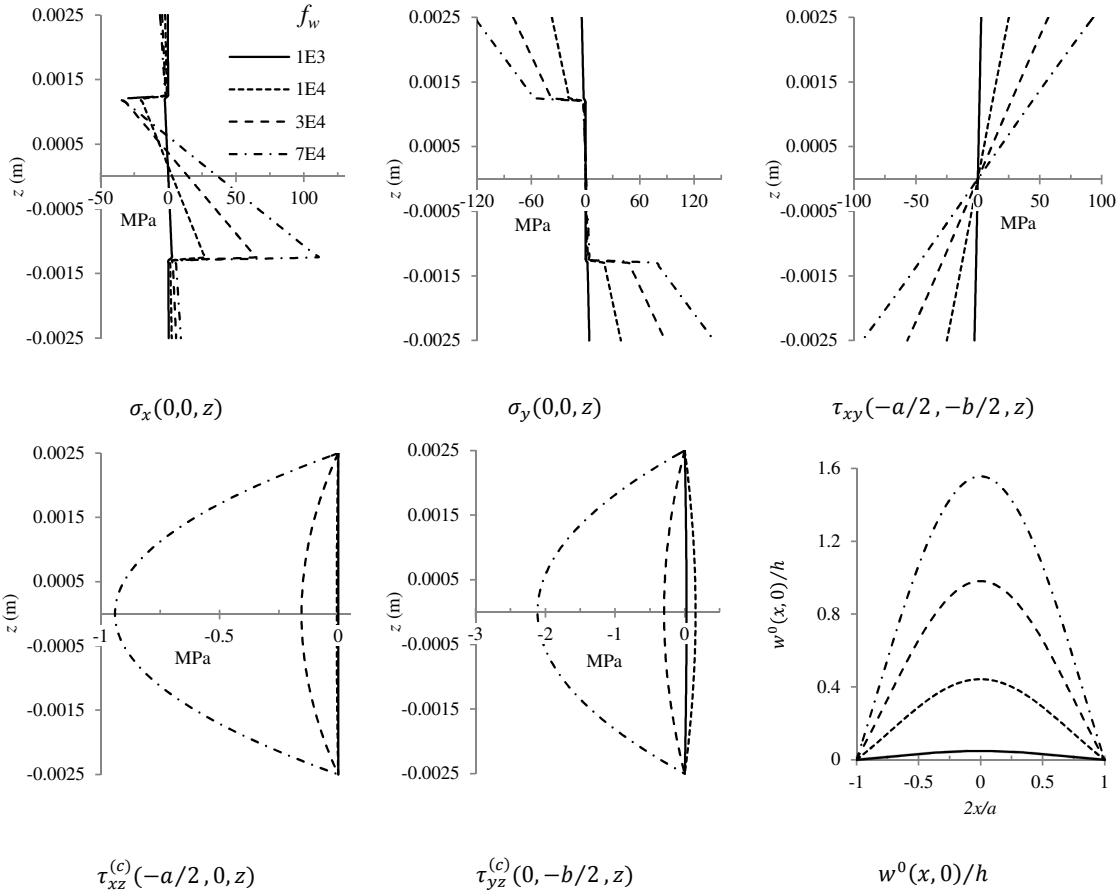

Figure 3.11: In-plane and shear stress distribution through the thickness as well as deflection in the section of the plate of simply-supported VSCL Plate 3 of Table 3.1, with movable edges, under increasingly sinusoidally distributed loading.

3.4 Conclusions

In this chapter, variable stiffness composite laminated plates with curvilinear fibres were analysed with the p-version finite element, using a third-order shear deformation theory. Due to the absence of data on VSCL plates, the formulation was verified by means of comparisons with published data on traditional, constant stiffness, laminates. The effects of using curvilinear fibres instead of straight fibres in laminated composite plates on (large) deflections and stresses were investigated. Several boundary conditions, plate thicknesses, and different loadings were considered. The tests carried out did not show that, for the fibre paths considered, VSCL always surpass CSCL. But it was found that using VSCL plates with linear variation of the fibre angle can lead to smaller displacement at certain points or even, for special loadings like eccentric point loads, diminish deflections of the plate overall. Curvilinear fibres also lead to changes in the stresses, as altering the position of maximum stress at the plate. These changes in maximum stresses magnitudes and locations may be exploited to improve damage resistance in particular applications. The transverse shear stresses computed by equilibrium equations was investigated in the non-linear regime and it was shown that non-zero shear stresses occur in the surfaces of the plate. This is due to the deformation of the outer planes, which are far from parallel to the xy plane when the displacements are large.

Chapter 4

Damage Onset of VSCL Plates: Statics and Dynamics

4.1 Introduction

With knowledge of the published literature on VSCL, the author believes that the developed *p*-version finite element, with non-linear strain-displacement relations, as described in Chapter 3, can be used to properly estimate the damage onset on VSCL plates. The *p*-version finite element method (FEM) has to its advantage a fast convergence rate and the high degree of continuity in the domain [48, 56, 63, 93]. The *p*-version finite element with hierarchical basis functions, based on a Third-Order Shear Deformation Theory (TSDT) in the linear strain-displacement regime, was already proposed to analyse the natural modes of vibration of VSCLs, in Chapter 2. In Chapter 3, the author explored VSCL plates subjected to static loads, to investigate the stress distributions and their dependence on non-uniform stiffness. In this chapter, the *p*-version finite element based on TSDT is applied in the geometrically non-linear regime to VSCL plates, in order to further assess their structural properties. Large deflections and damage onset of VSCL plates, when they are subjected to different static and dynamic loads, as uniform, partial (localised), sinusoidal, and impact loads, are studied.

To predict damage onset in VSCL plates, the well-known and widely used [105–107] stress based Tsai-Wu failure criterion is utilized here. The aim is to define an in-plane damage onset index and the safety factor for CSCL and VSCL plates. The stress computation with the present model was verified in [93] by comparison with other models and is here further verified by comparison with a 3-D elasticity based analysis.

4.1.1 Literature Review

Using curvilinear fibres, the stiffnesses become a function of the position [108]; these non-homogenous, locally orthotropic layers lead to VSCL, in which modification of load paths offers the possibility to distribute stresses in a more advantageous way [76, 109]. Improved structural performances accessible by VSCL plates – like less deflection and smaller likelihood of damage onset under static

and dynamic loads – are sought in this chapter. The analyses presented in this chapter are already given in Refs. [110, 111]. Although this chapter looks to the concept of load carrying capacity from the damage onset viewpoint, many other researchers investigate this concept using buckling and postbuckling behaviour of the VSCL plates. Accordingly, buckling and postbuckling is very often mentioned in the literature review.

Reference [112], a review paper on works published before 2010, lists pros and cons of parameterisation and optimisation algorithms used in the design of VSCLs. Recently, tailoring the fibre orientations, to maximize natural frequency, load carrying capacity or to minimise deflections has attracted a few researchers. Tailoring VSCLs to optimise natural frequency and deflection is essentially related with stiffness (mass also influences the natural frequency, but it is generally assumed that using curvilinear fibres does not affect mass distribution); this is different from maximizing the damage load, which depends on local strength [10]. In Ref. [77], the postbuckling first-ply failure response characteristics of VSCLs – modelled in the commercial finite element package Abaqus – are analysed using a set of physically-based criteria developed in [76]. In Ref. [78], the onset of delamination, an important failure mechanism in laminated plates, is evaluated using Abaqus to estimate interlaminar stresses in VSCLs. Delamination initiations are addressed in Ref. [113] by studying the response to impacts and the compression after impact, again using Abaqus to model VSCL plates. A multi-objective optimisation approach, with a non-dominated sorting genetic algorithm (NSGA-II), is employed in [114] to optimise either the strength around a circular hole with Tsai-Wu failure criterion, or the fundamental frequency, in a VSCL plate. Another design tailoring problem – the pressure pillowing of a fuselage VSCL panel – is addressed in [109], where Abaqus is yet again used with the goal of maximizing the load carrying capacity and the buckling capacity. References [75, 115] draw attention to the fact that thick laminates are more likely to experience failure than buckling, because the in-plane failure strains are an order of magnitude smaller than the buckling strains.

In Ref. [116], an optimisation (Global Response Surface Method as well as Abaqus) of a VSCL fuselage window belt demonstrated 26% postbuckling stability improvement compared to a CSCL design. The evaluations revealed that the optimal VSCL panel has 23% lower Tsai-Wu failure index and 10% reduction in in-plane shear stiffness compared to the CSCL design [116]. In another work [117], the authors optimised composite beams subjected to different loading for maximum failure load and proved the additional capacity of variable stiffness concept over the conventional straight-fiber concept due to re-distribution of loads.

Buckling, progressive damage and failure analyses were conducted on VSCL panels with and without central cut-outs in Ref. [118]. A continuum damage model in a commercially available code ABAQUS was applied for the simulation of the response of composite panels with increasing compression loads. Ref. [118] demonstrated that VSCLs, mainly with overlaps in the fibers, show improvements on the retardation of damage initiation and on the increase of structural strength by about 55%. It was shown in the same reference that the central hole is not the main geometrical cause for failure of notched panels, although stress re-distribution due to the cut-out may be playing a role. It is concluded in Ref. [118] that VSCLs with curvilinear fibres can redirect load

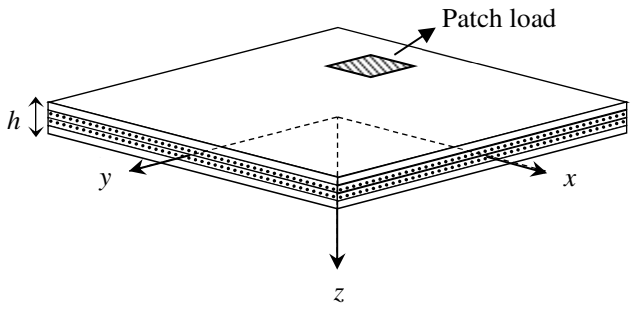

Figure 4.1: Configuration of a laminate. A rectangle where a localised distributed load is applied (a "patch load") is represented.

fluxes from the central regions to their stiffer edges, hence increasing buckling loads and delaying the initiation of damage and final structural failure to higher applied load levels. In another study, Ref. [119] gave the experimental results for variable stiffness flat panels with central circular holes and presented the buckling performance improvements attainable by elastic tailoring of composite laminates.

A semi-analytical variational approach was developed in Ref. [120] to perform postbuckling analysis of VSCL plates under uniform axial compression loading. It was demonstrated that enhanced results are given by the VSCL laminates, in which only small amounts of stiffness reduction occur in the postbuckling regime and simultaneously their overall stiffness and critical buckling load are maintained relatively high [120].

Ref. [41] presented an analysis on the effect of transverse shear deformation and embedded manufacturing defects (gaps and overlaps during manufacturing process) on the critical buckling load of VSCL plates using classical and shear deformation theories. A hybrid Fourier–Galerkin method was used to solve the governing equations. It was demonstrated that the discrepancy between critical buckling load obtained by CLPT and TSDT predictions is up to 33% for moderately-thick plates with length-to-thickness ratio $a/h = 10$, showing the importance of shear deformation theory in moderately-thick plates [41].

4.2 Damage Onset by a Non-linear Model for VSCL Plates

Here, rectangular symmetric laminates will be studied. In Figure 4.1, a plate is represented, together with Cartesian coordinates, the origin of which is the plate centroid. The curvilinear fibre paths are as they introduced in Section 1.4.1. A p-version finite element, with hierarchical basis functions and following TSDT, is employed to investigate if damage appears on laminates, under the action of various static and dynamic loads.

The virtual works of inertia in the non-linear regime of strain-displacements (already given in Section 2.2), internal and external forces (already given in Section 3.2) are defined and applied in the principle of virtual work, to find the equations of motion below; details on these matrices were given in the past chapters. A stiffness proportional damping, a special case of viscous damping, is

introduced in the equations of motion, with α representing the factor of proportionality [121,122]. The vector on the right-hand side of Equation (4.1) is the vector of generalised external forces. In the following numerical examples, we only consider transverse forces, so only $\mathbf{f_w}$ is not zero. To solve these non-linear differential equations, we use an in-house code written in FORTRAN, that implements Newmark method [62,94] (also see Section 3.2.1). This code was used to find static solutions using time as an artificial parameter, and to find steady-state and transient responses to dynamic loads, including impact loads.

$$
\begin{bmatrix}
\mathbf{M}^{11} & \mathbf{0} & \mathbf{0} & \mathbf{0} & \mathbf{0} \\
 & \mathbf{M}^{22} & \mathbf{0} & \mathbf{0} & \mathbf{0} \\
 & & \mathbf{M}^{33} & \mathbf{M}^{34} & \mathbf{M}^{35} \\
 & & & \mathbf{M}^{44} & \mathbf{0} \\
\textit{sym} & & & & \mathbf{M}^{55}
\end{bmatrix}
\begin{Bmatrix}
\ddot{\mathbf{q}}_{\mathbf{u}} \\ \ddot{\mathbf{q}}_{\mathbf{v}} \\ \ddot{\mathbf{q}}_{\mathbf{w}} \\ \ddot{\mathbf{q}}_{\boldsymbol{\phi}_x} \\ \ddot{\mathbf{q}}_{\boldsymbol{\phi}_y}
\end{Bmatrix}
+\alpha
\begin{bmatrix}
\mathbf{K}_{\mathbf{L}}^{11} & \mathbf{K}_{\mathbf{L}}^{12} & \mathbf{0} & \mathbf{0} & \mathbf{0} \\
 & \mathbf{K}_{\mathbf{L}}^{22} & \mathbf{0} & \mathbf{0} & \mathbf{0} \\
 & & \mathbf{K}_{\mathbf{L}}^{33} & \mathbf{K}_{\mathbf{L}}^{34} & \mathbf{K}_{\mathbf{L}}^{35} \\
 & & & \mathbf{K}_{\mathbf{L}}^{44} & \mathbf{K}_{\mathbf{L}}^{45} \\
\textit{sym} & & & & \mathbf{K}_{\mathbf{L}}^{55}
\end{bmatrix}
\begin{Bmatrix}
\dot{\mathbf{q}}_{\mathbf{u}} \\ \dot{\mathbf{q}}_{\mathbf{v}} \\ \dot{\mathbf{q}}_{\mathbf{w}} \\ \dot{\mathbf{q}}_{\boldsymbol{\phi}_x} \\ \dot{\mathbf{q}}_{\boldsymbol{\phi}_y}
\end{Bmatrix}
+
$$

$$
\begin{bmatrix}
\mathbf{K}_{\mathbf{L}}^{11} & \mathbf{K}_{\mathbf{L}}^{12} & \mathbf{0} & \mathbf{0} & \mathbf{0} \\
 & \mathbf{K}_{\mathbf{L}}^{22} & \mathbf{0} & \mathbf{0} & \mathbf{0} \\
 & & \mathbf{K}_{\mathbf{L}}^{33} & \mathbf{K}_{\mathbf{L}}^{34} & \mathbf{K}_{\mathbf{L}}^{35} \\
 & & & \mathbf{K}_{\mathbf{L}}^{44} & \mathbf{K}_{\mathbf{L}}^{45} \\
\textit{sym} & & & & \mathbf{K}_{\mathbf{L}}^{55}
\end{bmatrix}
\begin{Bmatrix}
\mathbf{q}_{\mathbf{u}} \\ \mathbf{q}_{\mathbf{v}} \\ \mathbf{q}_{\mathbf{w}} \\ \mathbf{q}_{\boldsymbol{\phi}_x} \\ \mathbf{q}_{\boldsymbol{\phi}_y}
\end{Bmatrix}
+
\begin{bmatrix}
\mathbf{0} & \mathbf{0} & \mathbf{K}_{\mathbf{NL}}^{13}(\mathbf{q_w}) & \mathbf{0} & \mathbf{0} \\
\mathbf{0} & \mathbf{0} & \mathbf{K}_{\mathbf{NL}}^{23}(\mathbf{q_w}) & \mathbf{0} & \mathbf{0} \\
\mathbf{K}_{\mathbf{NL}}^{31}(\mathbf{q_w}) & \mathbf{K}_{\mathbf{NL}}^{32}(\mathbf{q_w}) & \mathbf{K}_{\mathbf{NL}}^{33}(\mathbf{q_w}) & \mathbf{0} & \mathbf{0} \\
\mathbf{0} & \mathbf{0} & \mathbf{0} & \mathbf{0} & \mathbf{0} \\
\mathbf{0} & \mathbf{0} & \mathbf{0} & \mathbf{0} & \mathbf{0}
\end{bmatrix}
\begin{Bmatrix}
\mathbf{q}_{\mathbf{u}} \\ \mathbf{q}_{\mathbf{v}} \\ \mathbf{q}_{\mathbf{w}} \\ \mathbf{q}_{\boldsymbol{\phi}_x} \\ \mathbf{q}_{\boldsymbol{\phi}_y}
\end{Bmatrix}
$$

$$
=
\begin{Bmatrix}
\mathbf{f}_{\mathbf{u}} \\ \mathbf{f}_{\mathbf{v}} \\ \mathbf{f}_{\mathbf{w}} \\ \mathbf{f}_{\boldsymbol{\phi}_x} \\ \mathbf{f}_{\boldsymbol{\phi}_y}
\end{Bmatrix}
\tag{4.1}
$$

As written in the introduction, different failure criteria have been used for composites and, specifically, for variable stiffness laminates. Various failure modes, namely, fibre failure, matrix failure, interfacial failure, delamination, and buckling, interact and can occur to cause the onset of damage. In the maximum stress and strain criteria, individual stress or strain components have specific limits, which are not affected by the other components; there is no interaction between stress or strain components. Here, we will use a quadratic, interactive Tsai-Wu failure criterion, taking into consideration a multi-axial stress state and how the combination of different stress components affect the damage onset [123]. Accordingly, damage starts when the following condition is satisfied

$$
\frac{1}{X_t X_c}\sigma_1^2 + \frac{1}{Y_t Y_c}\left(\sigma_2^2 + \sigma_3^2\right) + \frac{1}{S_{12}^2}\left(\tau_{12}^2 + \tau_{13}^2\right) + \frac{1}{S_{23}^2}\left(\tau_{23}^2 - \sigma_2\sigma_3\right) + \left(\frac{1}{X_t} - \frac{1}{X_c}\right)\sigma_1 +
$$

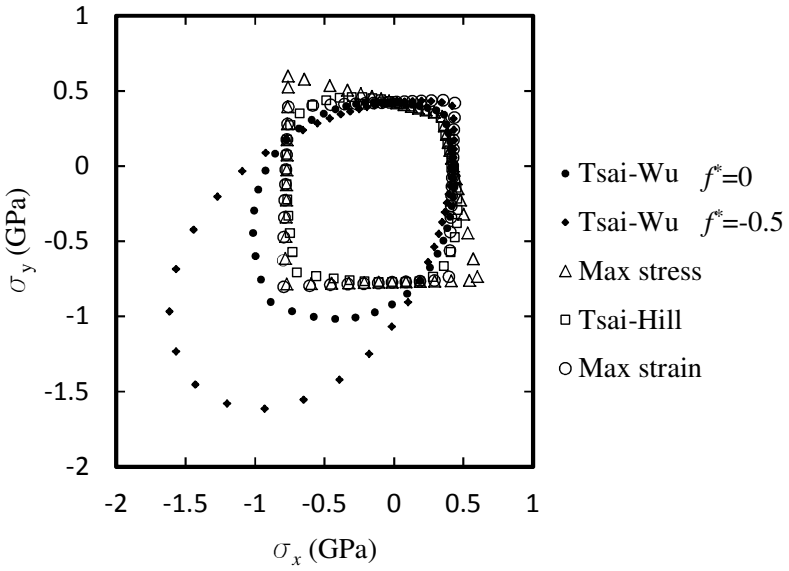

Figure 4.2: Various failure envelopes for a [0°,90°,90°,0°] plate.

$$\left(\frac{1}{Y_t}-\frac{1}{Y_c}\right)(\sigma_2+\sigma_3)+\frac{2f^*}{\sqrt{X_tX_cY_tY_c}}\sigma_1(\sigma_2+\sigma_3)=\text{ Damage index }\geq 1. \tag{4.2}$$

Interaction parameter $f^*, -0.5 \leq f^* \leq 0$, is a constant; f^* equal to zero is generally used in more conservative damage onset prediction, but in this chapter we make it equal to -0.5, to include the interaction effect between normal stresses [123]. Finding the actual value of the interaction parameter is not possible only with uni-directional strength tests, it requires bi-axial test results instead; taking this parameter equal to -0.5 is, in isotropic materials, the same as using the von Mises yield criterion [123].

Tsai-Wu criterion is often defended in the literature as a good first-ply failure criterion. To illustrate the difference between this and other criteria, different failure criteria (maximum strain and stress criteria, Tsai-Hill criterion and Tsai-Wu criterion, i.e. Equation (4.2), with f^* equal to 0 or to -0.5) are assessed for a CSCL plate and their envelopes are shown in Figure 4.2. The plate lay-up is $[0^o, 90^o, 90^o, 0^o]$ with geometric and mechanical properties defined as $E_1 = 172.37$ GPa, $E_2 = 6.89$ GPa, $G_{12} = G_{13} = 3.45$ GPa, $G_{23} = 1.38$ GPa, $\nu = 0.25$. The envelopes are obtained using the software Helius: CompositePro[1]. As Figure 4.2 describes, the maximum stress envelope does not show any interaction between normal stresses, while maximum strain envelope reveals such interaction. Of the criteria under consideration here, Tsai-Hill criterion is the most conservative that assumes interaction. For most stresses, Tsai-Wu criterion is more conservative when taking interaction parameter equal to 0 rather than -0.5. Only when both stresses are compressive, Tsai-Wu criterion with interaction parameter equal to -0.5 is less safe.

Equation (4.2) can be described either with a damage onset index or using a safety factor. Ref. [106] suggests replacing stresses σ and τ with $\lambda\sigma$ and $\lambda\tau$; the λ that results in beginning of

[1] Helius: CompositePro Software

the damage is recognized as the safety factor. Among different laminates, the one with lower λ would be the laminate where damage onset is less likely.

4.3 Numerical Results

Differences between CSCL plates and VSCL plates with curvilinear fibres are discussed in this section. We are chiefly interested in the damage onset in the non-linear regime and the criterion expressed by the Equation (4.2) is evaluated on the different plates, under various static and dynamic loading conditions. In the dynamic case, the steady state response to harmonic loads is considered first, and, after, the transient response of a VSCL plate under an impact is shown.

4.3.1 Deflection and Damage Onset in the Non-Linear Regime

The p-version finite element method can treat laminates with diverse curvilinear fibres, different sequence stacking and number of layers, but in this section we will consider a four-layer variable stiffness laminate with curvilinear fibre configuration $[\langle T_0, T_1\rangle, 90^o + \langle T_0, T_1\rangle]_{sym}$ in order to restrict the domain of the study. For the laminates with straight fibres, T_0 is equal to T_1 and can take values 0^o or 45^o, so that strength and stiffness are greater in two specific directions; but for the laminates with curvilinear fibres T_0 – that takes one of the following values: 20^o, 40^o, 45^o, 60^o, 80^o – is different than T_1 (that can be -20^o, 0^o, 20^o, 40^o, 60^o or 80^o); these angles take into account the manufacturing limitation on fibre curvatures (see 1.4.4). The VSCL plate considered here and in the remaining examples in this chapter is fully clamped and with the geometry $a = b = 0.5$ m, $h = 0.005$ m and mechanical properties of AS4/3501-6 carbon epoxy (after [106]): $E_1 = 142$ GPa, $E_2 = 10.3$ GPa, $G_{12} = G_{13} = G_{23} = 7.2$ GPa, $\nu_{12} = 0.27$, $\rho = 1580$, kg/m^3, $X_t = 2280$ MPa, $X_c = 1440$ MPa, $Y_t = 57$ MPa, $Y_c = 228$ MPa, $S = 71$ MPa.

The four-layer laminate with curvilinear fibre configuration $[\langle 45^o, 80^o\rangle, \langle 135^o, 170^o\rangle]_{sym}$ is selected to verify the convergence of results with the number of shape functions in the non-linear regime. Deflections at the centre of the plate and damage onset safety factors, computed using two p-version finite elements, one with 245 DOF, the other with 405 DOF, are compared in Table 4.1. The minimum safety factor is the one reported here; in order to find it, a grid of $40 \times 40 \times 100$ points (along the width, length and thickness, respectively) is defined and the safety factor is computed in each node. An acceptable agreement between the damage onset safety factors and non-dimensional deflections computed with the two approaches is observed in this table. Taking into account that the computational effort is very large if more than 81 (9×9) shape functions are used per displacement component, and taking into consideration the former comparison between p-version models, as well as comparisons carried out in the last chapters, we decided to use 405 DOF for the ensuing analyses in this chapter. Different transverse loadings, namely uniform load, $f_w(x,y,t) = 10^4 \cos(\omega t)$, sinusoidally distributed load, $f_w(x,y,t) = 10^4 \cos(\pi x/a)\cos(\pi y/b)\cos(\omega t)$, and a partial load defined as

$$f_w(x,y,t) = 5 \times 10^5 \cos(\omega t) \tag{4.3}$$

if

$$(-0.3a \leq x \leq -0.2a, 0.2b \leq y \leq 0.3b) \text{ or } (0.2a \leq x \leq 0.3a, -0.3b \leq y \leq -0.2b)$$

are applied to the plates. These partial, or patch, loads correspond to concentrated (point) loads if the patches are small. Unlike a concentrated load, patch loads do not lead to infinite stresses at the application point; they also have the advantage of requiring less shape functions for convergence. The loads are either static or dynamic, with dynamic here meaning harmonic and with an excitation frequency ω equal to the fundamental natural frequency of the laminate.

Table 4.1: Non-dimensional deflection and damage onset safety factor of a VSCL plate under different dynamic and static loads (Difference is calculated taking 405 DOF as reference).

	Non-dimensional deflection, W/h		Damage onset safety factor	
Loading	245 DOF	405 DOF	245 DOF	405 DOF
Harmonic uniform	0.8737 ($\approx 1.1\%$)	0. 8835	3.16 ($\approx 5.4\%$)	3.34
Static uniform	0.2828 ($\approx 0.0\%$)	0.2828	13.85 ($\approx 2.1\%$)	14.14
Harmonic sinusoidal	0.8155 ($\approx 0.3\%$)	0.8181	4.70 ($\approx 0.2\%$)	4.69
Static sinusoidal	0.2089 ($\approx 0.0\%$)	0.2088	23.62 ($\approx 0.1\%$)	23.59
Harmonic partial	0.8234 ($\approx 0.4\%$)	0.8267	3.55 ($\approx 7.3\%$)	3.83
Static partial	0.1765 ($\approx 1.6\%$)	0.1793	8.95 ($\approx 6.7\%$)	8.39

Real-life structures have some kind of energy dissipation mechanism or damping. Here, we employ small damping factors, academic but consistent with the fact that structural damping is small in most structures [122]. It is valuable to mention that to find the actual value of damping, one may follow methods defined in Refs. [121, 122]. In the example of Table 4.1, the proportional damping parameter α in Equation (4.1) is taken as 10^{-5}.

Figure 4.3 compares deflection ratios, represented by a solid circle, and safety factors – shown by column bars – of different laminates with straight and curvilinear fibres. The deflection ratios were defined by dividing the value of maximum deflection, which does not necessarily take place at the centroid, of the laminate under analysis, by the maximum deflection of the cross-ply laminate $[0^o, 90^o, 90^o, 0^o]$ (i.e. $[\langle 0^o, 0^o\rangle, \langle 90^o, 90^o\rangle]_{sym}$ or simply $T_0, T_1 = 0^o, 0^o$ in the figure), subjected to the same loading condition. Each part of this figure exemplifies the results for the laminates subjected to different harmonic, static, or impact loads. In this figure, harmonic loads have as excitation frequency, ω, the fundamental natural frequency, and impact loads are defined as half-sine functions of time with duration equal to half a fundamental period of vibration of the laminate. The proportional damping parameter is taken as 5×10^{-5}. Starting with Figure 4.3(a), deflection ratios, defined as W/h, and damage onset when the plates are oscillating at steady-state under the action of a harmonic load located only in two specific regions of the plate – partial loads, Equation (4.3) – and with amplitude 10^6 Nm^{-2}, are assessed. The laminate with curvilinear fibre configuration $[\langle 60^o, 20^o\rangle, \langle 150^o, 110^o\rangle]_{sym}$ (simply $T_0, T_1 = 60^o, 20^o$ in the figure) has minimum deflection. VSCL plate $[\langle 45^o, 80^o\rangle, \langle 135^o, 170^o\rangle]_{sym}$ is the safest configuration albeit it experiences deflection larger than $[\langle 60^o, 20^o\rangle, \langle 150^o, 110^o\rangle]_{sym}$; thus, the former laminate is more flexible and develops lower stresses at the edges than the latter. Still in the case of loads harmonic in time and comparing

with the CSCL laminates, VSCL $[\langle 45^o, 80^o\rangle, \langle 135^o, 170^o\rangle]_{sym}$ experiences a deflection of similar magnitude, with a substantially larger safety factor. For all plates but one, the point with the minimum safety factor is found at the edge and bottom surface; however, it is not always exactly at the same position. In the unique case of $[\langle 45^o, 80^o\rangle, \langle 135^o, 170^o\rangle]_{sym}$, the point where the safety factor is minimum is not at the bottom of the plate, but still is at the edge. With loads of the same intensity, but static, different results are estimated in Figure 4.3(b). In general, changing the load, from harmonic to static, decreases the deflection magnitude and reduces the probability of damage onset, as shown by the increase in the safety factors in Figure 4.3(b). So with the same load intensity, the harmonic load at the linear natural frequency is more likely than the static load to cause a start of damage. Minimum deflection and highest safety factor occur in variable stiffness laminates, respectively with configurations $[\langle 60^o, 20^o\rangle, \langle 150^o, 110^o\rangle]_{sym}$ and $[\langle 45^o, 80^o\rangle, \langle 135^o, 170^o\rangle]_{sym}$. In all but one of the fibre angle configurations, the damage onset occurs on the bottom surface, at the edges of the plate, only for $[\langle 45^o, 80^o\rangle, \langle 135^o, 170^o\rangle]_{sym}$ plate (that also has the highest safety factor), the damage starts on the patch load area, at the upper surface and far from edges. Another result, not shown in the figure, is that the maximum deflection of the laminates subjected to two harmonic partial loads occurs at its centre, while for the laminates under static partial load it does not necessarily happen at the centre of the plate. In the latter case, the location that experiences maximum deflection depends on the fibre orientation. In the former case – harmonic excitation at the natural frequency – the plates experience deflections with a shape that approaches the first linear mode of vibration, with maximum amplitude at the centre.

Figure 4.3(c) and (d) present a similar analysis, with harmonic and static sinusoidal force with intensity 2×10^4 Nm^{-2}. Due to the load spatial distribution, the maximum deflection always takes place at the plate's centre. Laminates under harmonic and static sinusoidal load have the minimum deflection in the cross-ply configuration $[0^o, 90^o, 90^o, 0^o]$, while in the static case the laminate with curvilinear fibre $T_0, T_1 = 80^o, 40^o$ experiences very low deflection with a high safety factor. The VSCL with fibre arrangement $[\langle 45^o, 80^o\rangle, \langle 135^o, 170^o\rangle]_{sym}$ has the maximum safety factor, and the minimum safety factor is for VSCL laminate $[\langle 40^o, 0^o\rangle, \langle 130^o, 90^o\rangle]_{sym}$. Another difference between laminates under harmonic and static sinusoidal loads is the high safety factor of laminates under static load, confirming the fact that, for the same load intensity, harmonic loading can be more critical than static loading. Different CSCL and VSCL plates, under both loading cases, experience damage onset at the edges, on the bottom surface. The exception is plate with curvilinear fibre $T_0, T_1 = 45^o, 80^o$, where damage starts at the edge, somewhere between the upper and bottom surfaces (close to a layer interface), also this plate is, as mentioned above, the one that has maximum damage onset safety factor.

Maximum deflection magnitudes and minimum safety factors of transient responses of laminates subjected to impacts are displayed in the last two figures of Figure 4.3. Figure 4.3(e) corresponds to a uniform load, with intensity 3×10^4 N/m^{-2}, and Figure 4.3(f) to an impact by a partial load with intensity 2×10^6 Nm^{-2} applied at $-0.3a \leq x \leq -0.2a, 0.2b \leq y \leq 0.3b$. In the case of uniform impact, maximum deflections are found at the centre of the plates, but when the impact is due to a partial load, the maximum deflection does not necessarily occur at the centre of

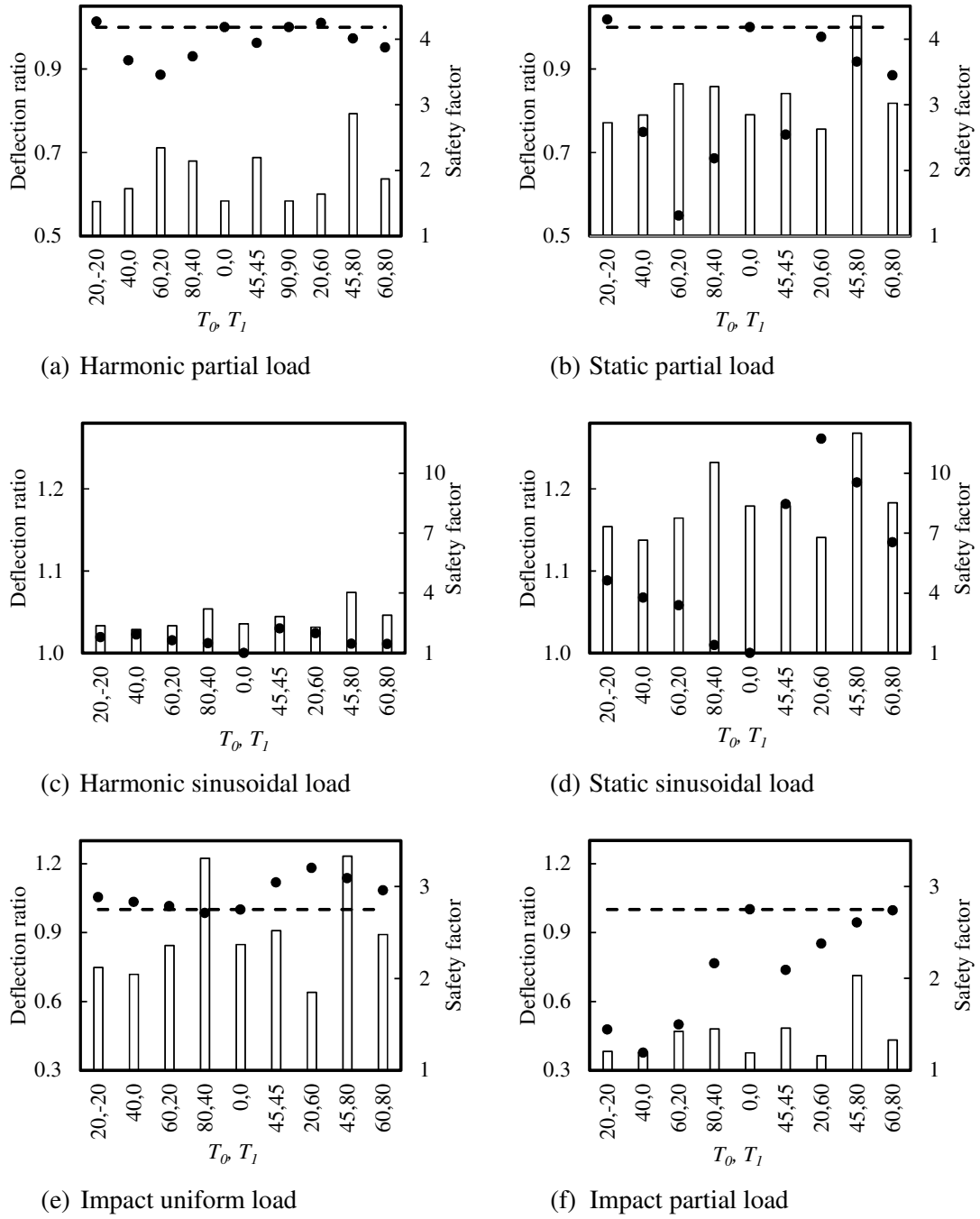

(a) Harmonic partial load

(b) Static partial load

(c) Harmonic sinusoidal load

(d) Static sinusoidal load

(e) Impact uniform load

(f) Impact partial load

Figure 4.3: Deflection ratios (solid circles) and damage safety factors (column bars) of laminates with straight and curvilinear fibres under different types of loads. Dashed-lines represent deflection ratio equal to one.

the plate and its location depends on the fibre orientation. If the laminates are under the impact of a uniformly distributed load, by choosing the arrangement $[\langle 80^o, 40^o\rangle, \langle 170^o, 130^o\rangle]_{sym}$, keeping the deflection almost equal to the cross-ply case $[0^o, 90^o, 90^o, 0^o]$, one obtains a safer laminate. When applying an impact by a partial load, taking the curvilinear fibres $[\langle 40^o, 0^o\rangle, \langle 130^o, 90^o\rangle]_{sym}$ would be as safe as the cross-ply case $[0^o, 90^o, 90^o, 0^o]$, while the VSCL plate has the minimum deflection and the cross-ply has maximum deflection. In summary, the diverse load cases in Figure 4.3 lead to some common conclusions; although the laminate with the curvilinear fibre $[\langle 45^o, 80^o\rangle, \langle 135^o, 170^o\rangle]_{sym}$ has usually high deflection, it has the largest safety factor. Curvilinear fibre format $[\langle 80^o, 40^o\rangle, \langle 170^o, 130^o\rangle]_{sym}$ usually has the second highest safety factor among the cases studied.

4.3.2 Transient Response of a Sample VSCL Plate in the Non-Linear Regime

In this section, the response to impact loads of a VSCL plate is analysed in more detail. Figure 4.3 shows that using VSCL instead of CSCL plates may avoid damage onset; the reason is that laminates with straight fibres have uniform stiffness and strength while laminates with curved fibres have non-uniform stiffness and strength. Non-constant stiffness in a laminate changes deflections; moreover non-constant stiffness and strength together influence the damage onset, an action stemming from a different stress re-distribution throughout the laminate.

In addition to the effect of curvilinear fibres in stress re-distribution (more about stresses in VSCL plates can be found in Chapter 3), non-linear relation between strains (and subsequently stresses) and displacements changes meaningfully the order of magnitude of normal and shear stresses, which are applied in the damage criterion, Equation (4.2). The damage safety factor is influenced by both the non-uniform strengths, and in the non-linear regime, by a significant change in the order of magnitude of the stresses, shown in Figure 4.4. This figure shows stresses and maximum damage index for the laminate with fibres $[\langle 60^o, 20^o\rangle, \langle 150^o, 110^o\rangle]_{sym}$, loaded by a partial impact equal to the one of Figure 4.3(f), but when the force intensity is increasing. The displayed stresses belong to the location of maximum damage index. The figure shows the analysis done either in the linear or in the non-linear regime. The proportional damping parameter α was assumed to be 5×10^{-5}.

Figure 4.4(a), presenting results in the non-linear regime with the load magnitude ranging from 0.5 MPa to 4 MPa, shows that increasing the load has a uniform effect on the in-plane stresses, whereas its increase to values greater than 2 MPa has more influence on σ_x than on σ_y. Another result that is not shown in the figure is that increasing the load alters the location of maximum damage index (although it happens always at the line belonging to the horizontal edge and bottom surfaces, i.e. $y = b/2$ and $z = -h/2$), which is a consequence of the fact that the stresses' magnitudes change differently. For the load magnitude between 0.5 to 2 MPa, σ_y is the largest stress, and Tsai-Wu index changes from 0.15 to 0.63; in this range, the maximum damage index is found to be around point $(x/a, y/b, z/h) = (-0.15, 0.5, -0.5)$. Increasing the load magnitude from 3 MPa to 4 MPa raises the Tsai-Wu index from 0.96 to 1.27, in this range σ_x is the largest stress, and the maximum damage index happens near point $(x/a, y/b, z/h) =$

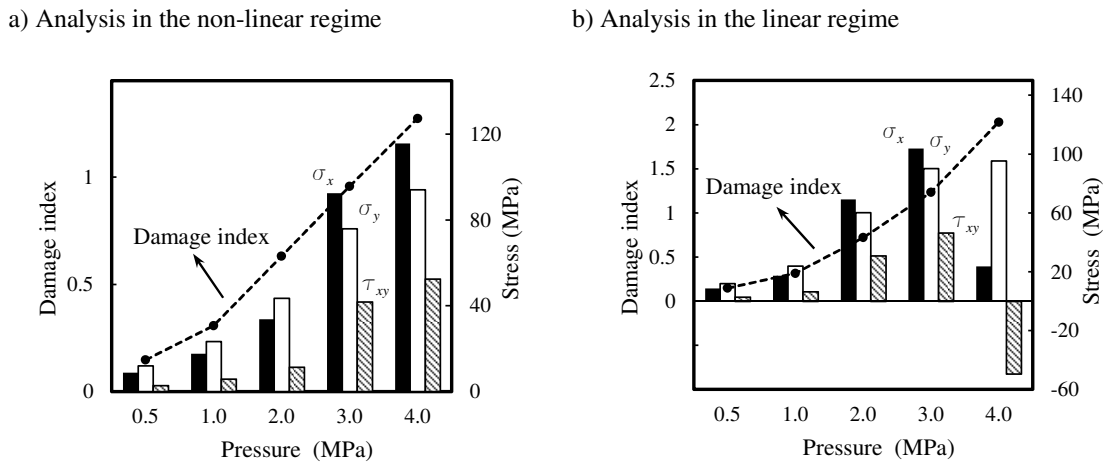

Figure 4.4: Effect of increasing the load on the damage index. (a) Analysis in the non-linear regime; (b) Analysis in the linear regime.

$(-0.125, 0.5, -0.5)$. The maximum Tsai-Wu index always takes place at the bottom surface of the plate.

Figure 4.4(b) gives the results for the same problem but in the linear regime. In the linear regime, damage appears when the load magnitude is around 2.5 MPa, while in the non-linear regime it appears when the load magnitude is around 3 MPa. In the linear regime, σ_x is smaller when the load magnitude is 4 MPa than when it is 3 MPa. When the load magnitude is 4 MPa, τ_{xy} is negative. It should be re-called that the stresses given here belong to the location of maximum damage index, which changes with the load magnitude. Here, if the load magnitude is 0.5 MPa or 1 MPa then the maximum damage index is around 0.15 and 0.32, respectively, and it occurs around point $(x/a, y/b, z/h) = (-0.15, 0.5, -0.5)$. Increasing the load magnitude from 2 MPa to 3 MPa raises the maximum damage index from 0.72 to 1.23 and changes its location, which becomes close to point $(x/a, y/b, z/h) = (-0.125, 0.5, -0.5)$. When the load magnitude is 4 MPa, the maximum damage index is around 2 and takes place at point $(x/a, y/b, z/h) = (-0.225, 0.4, -0.5)$. These analyses indicate that the geometrical non-linearity, represented in the strain-displacement relation, can lead to a change in the position of damage onset.

Time-response and damage indices of this VSCL plate under the impact of one partial load with intensity 3×10^6 Nm^{-2} – applied at $-0.3a \leq x \leq -0.2a, 0.2b \leq y \leq 0.3b$ – are plotted in Figure 4.5. The half-sine impact duration is a quarter of, half of, or equal to the first natural period of vibration, $2\pi/\omega_1$. To simplify the comparison of the curves, non-dimensional force is plotted (by means of dividing it by its maximum); deflections are divided by the thickness. The unsymmetrical impact load causes the maximum deflection to happen at a place different than the centre of the plate. If the impact duration is small, say a quarter of first natural period of vibration given in Figure 4.5(a), the plate experiences damage onset at almost $t = 0.0006$ s, so the results after this moment are not valid, because the model does not account for damage or its propagation. If the impact duration is half of the first natural period of vibration, given in Figure

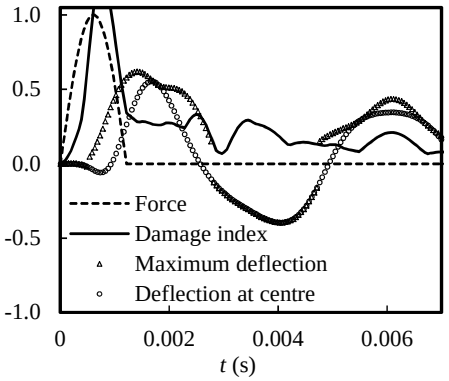

a) Force duration is a quarter of the first natural period of vibration

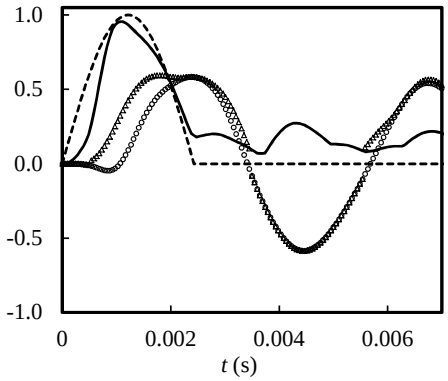

b) Force duration is half of the first natural period of vibration

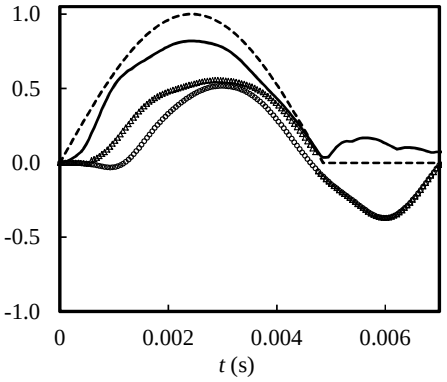

c) Force duration is equal to the first natural period of vibration

Figure 4.5: Transient time response, force, and damage index of a VSCL plate under an impact of partial load.

4.5(b), the maximum deflection and damage index occur respectively later and before the moment of maximum force. It is interesting that before the force exceeds its maximum value, the laminate almost touches its onset of damage, but later at the moment of maximum force, the plate damage index is smaller. The maximum damage index almost reaches 1 and the maximum deflection and deflection at the centre (W/h) are almost 0.6, meaning that the non-linear terms are important. Increasing the load can lead to damage onset in the plate. With an impact load of longer duration, as given in Figure 4.5(c) (equal to first natural period of vibration), the maximum damage index occurs when the load has its maximum amount.

4.4 Conclusions

Laminates with different straight and curvilinear fibre orientations (various angles at centre and edges of the plate) under various static, harmonic, and impact loads are investigated. The effect of half-sine impact loads with different durations on VSCL plates is studied. Deflections and

damage onset of the laminates in the non-linear regime are given for several fibre configurations. The stress computation with the present model was verified by comparison with a 3-D elasticity based analysis. The following conclusions emerge from this study:

1. Under different studied harmonic, static, and impact loads, laminate with curvilinear fibre orientation $[\langle 45^o, 80^o\rangle, \langle 135^o, 170^o\rangle]_{sym}$ has the largest safety factor (among the plates considered), in what concerns resistance to damage onset. This configuration represents a VSCL plate that is locally angle-ply in the plate centroid (due to 45° and -45°, that is 135°, fibres placed at the centroid). This VSCL plate, $[\langle 45^o, 80^o\rangle, \langle 135^o, 170^o\rangle]_{sym}$, shows more resistance to the appearance of damage than the traditional angle-ply CSCL laminate with the same number of layers and mechanical properties $[\langle 45^o, 45^o\rangle, \langle -45^o, -45^o\rangle]_{sym}$ or $([45^o, -45^o]_{sym})$.

2. In comparison with $[\langle 45^o, 80^o\rangle, \langle 135^o, 170^o\rangle]_{sym}$, another fibre configuration $[\langle 80^o, 40^o\rangle, \langle 170^o, 130^o\rangle]_{sym}$ has a reasonable high safety factor, with less deflection magnitude. The numerical tests indicate that the existence of fibres with 40° and -50° (that is 130°), close to the edges can increase the damage resistance of the plate.

3. In the considered loading conditions, the angle-ply $[45^o, -45^o, -45^o, 45^o]$ laminate is safer than cross-ply configuration $[0^o, 90^o, 90^o, 0^o]$.

4. Changing the load, from harmonic with a frequency equal to the natural frequency to static, decreases the deflection magnitude and reduces the probability of damage occurrence.

5. It is hence concluded that damage onset can be avoided with VSCL, under certain static and dynamic loads.

6. The duration of impacts has a significant influence not only on the deflection variation with time, but also on the damage onset. Regarding the latter, impacts with smaller time span and the same intensity can be more dangerous than longer impacts.

Chapter 5

Free Geometrically Non-linear Oscillations of Perfect and Imperfect VSCL Plates

5.1 Introduction

In this chapter, the author intends to include the effect of imperfections and study in detail the free vibration of imperfect VSCL plates. A *p*-version finite element model, based on a TSDT that applies to imperfect (out-of-planarity) VSCL plates with curvilinear fibres will be presented. The reference fibre path, introduced by a function of horizontal coordinate x, is shifted along Cartesian coordinate y, in the rectangular VSCL plate as described in Section 1.4.1. The edges of the laminates are clamped, except in comparison studies, where simply-supported conditions are applied. The finite element model, later designated as ”full model”, may be statically condensed [124], leading to a model that will be designated as the ”statically condensed model”. The number of degrees of freedom (DOF) of the model are further reduced using modal coordinates [125]. Periodic solutions of the plate in the absence of external loads, in the geometrically non-linear regime, are calculated using the shooting method and Runge-Kutta-Fehlberg method modified with Cash-Karp method to control the error with adaptive stepsize. Branches that bifurcate from the fundamental backbone curves are found and studied in detail using phase plane plots, time histories plots and Fourier spectra. Here, "phase plane plot" means a plot that is obtained by projecting trajectories in the plane defined by the transverse displacement and the transverse velocity at a point.

Adding to the consideration of geometrical imperfections in VSCL, this chapter has a distinctive feature that the shooting method is employed to analyse non-linear free vibrations of VSCL. The displacement field is modelled by TSDT and the equations of motion (full model), in the time-domain, are obtained using a *p*-version finite element method. The shooting method allows one to solve non-linear boundary value problems [126], therefore it can be applied to find periodic solutions. Unlike perturbation methods, shooting is not restricted to small amplitude oscillations

and its application in systems with many degrees of freedom is not – in what concerns the algorithm – excessively complicated. In comparison with harmonic balance – or similar – methods the Fourier spectra of the solution is not artificially restricted. Although time domain integration is also performed, shooting is a more straightforward procedure of obtaining periodic solutions in a certain frequency range than direct integration methods applied on their own. In comparison with harmonic balance, shooting has the disadvantages of suffering from numerical issues and requiring longer computational times [126, 127]. The application of the shooting technique to the problem at hand is assessed on this chapter.

5.1.1 Literature Review

The *p*-version FEM was employed to investigate the linear frequencies of vibration in Chapter 2, deformations and stresses in the geometrically non-linear regime in Chapter 3, damage onset in the non-linear regime in Chapter 4 and non-linear forced and free vibrations of VSCL plates in Refs. [63] and [44]. About the free non-linear vibration of VSCL panels with curvilinear fibres few papers were published, Refs. [44, 128, 129], but using the harmonic balance method, with either a thin panel [128, 129] or a FSDT model [44]. Furthermore, the plates were considered to be perfect in Refs. [44] and [128].

Ref. [129] gave a *p*-version finite element for geometrically non-linear vibrations of thin shallow shells. This reference showed the influence of the different fibre paths in the non-linear oscillations not only on backbone curves and shapes, but also by projections of trajectories in a phase plane. Different hardening and softening behaviour of the backbones curves of VSCL panels were also studied [129]. Here, harmonic balance method was used.

For a long time, geometric imperfections have been considered as a reason for discrepancies between experimental and numerical results. They have a key effect on the non-linear vibration of structures. Even if two structures are manufactured by the same technique, it has been observed that eigenfrequencies and non-linear behavior can be different [71, 130]. Many studies found that the initial deflections of structures, which are unavoidable when manufacturing, are major causes for explaining the significant discrepancies detected between theoretical results (calculated assuming a perfect structure) and experimental observations, Refs. [51, 131, 132]. According to Refs. [71, 130, 131], numerically computed natural frequencies of vibration of plates agree better with experimental ones, when geometrical imperfections are taken into account in the formulation. Different types of geometrical imperfections are shown in Ref. [133], where Nanda and Pradyumna investigated the effect of geometrical imperfections on linear and non-linear frequencies, as well as on the transient response of laminated shells. Even if the number of published papers on VSCL plates is growing, the behavior of such plates in the presence of imperfections was not extensively studied (except Ref. [134]), where most of the results given in this chapter are published.

5.2 Modelling of Free Vibration of VSCL Plates

This section starts with the derivation of a full model, by the p-version hierarchical finite element, for rectangular plates with von Kármán theory. After, the full model is condensed using a technique named static condensation. Finally, both the full and the condensed models are transformed to a reduced model using modal coordinates.

5.2.1 p-Version Finite Element Full Model

In TSDT, the displacement components, Equations (2.1) of Section 2.2, are used. Initial geometric imperfection in the normal direction, w_i, associated with zero initial stress, is considered in the formulation. Then, mid-plane displacements can be written as in Equation (2.2).

In the cases studied here, the non-linear vibration amplitude of the clamped laminates will not exceed 1.5 times the laminate thickness. So, it is not necessary to retain geometric non-linearities in the in-plane displacements; and taking the von Kármán non-linearity terms (i.e. those involving the normal displacement only) is adequate [135,136]. In the case of non-linear vibration of simply-supported shells, Amabili [135, 136] showed that inaccurate results are obtained by keeping only non-linear terms of the von Kármán type for vibration amplitudes of about two times the shell thickness; so he involved geometric non-linearities in the in-plane displacements. In this chapter, the strain-displacement relations, with the von Kármán strains, are (already given without non-linear term in Equations (2.5)):

$$\varepsilon_x = \frac{\partial u^0}{\partial x} + \left(z - cz^3\right)\frac{\partial \phi_x}{\partial x} - cz^3\left(\frac{\partial^2 w^0}{\partial x^2}\right) + \frac{1}{2}\left(\frac{\partial w^0}{\partial x}\right)^2 + \frac{\partial w^0}{\partial x}\frac{\partial w_i}{\partial x},$$

$$\varepsilon_y = \frac{\partial v^0}{\partial y} + \left(z - cz^3\right)\frac{\partial \phi_y}{\partial y} - cz^3\left(\frac{\partial^2 w^0}{\partial y^2}\right) + \frac{1}{2}\left(\frac{\partial w^0}{\partial y}\right)^2 + \frac{\partial w^0}{\partial y}\frac{\partial w_i}{\partial y},$$

$$\varepsilon_z = 0,$$

$$\gamma_{xy} = \frac{\partial u^0}{\partial y} + \frac{\partial v^0}{\partial x} + \left(z - cz^3\right)\left(\frac{\partial \phi_x}{\partial y} + \frac{\partial \phi_y}{\partial x}\right) + \frac{\partial w^0}{\partial x}\frac{\partial w^0}{\partial y} - 2cz^3\frac{\partial^2 w^0}{\partial x \partial y} + \frac{\partial w^0}{\partial x}\frac{\partial w_i}{\partial y} + \frac{\partial w^0}{\partial y}\frac{\partial w_i}{\partial x},$$

$$\gamma_{yz} = \left(1 - 3cz^2\right)\left(\phi_y(x,y,t) + \frac{\partial w^0}{\partial y}\right),$$

$$\gamma_{xz} = \left(1 - 3cz^2\right)\left(\phi_x(x,y,t) + \frac{\partial w^0}{\partial x}\right). \tag{5.1}$$

These equations are generally accurate enough for non-linear vibrations of plates; if more accurate expressions are required, more non-linear terms can be included. If the approximations in the

above equation are not applied, the problem becomes more complex. Now, strains can be presented in matrix form as

$$\begin{Bmatrix} \varepsilon_x \\ \varepsilon_y \\ \gamma_{xy} \end{Bmatrix} = \begin{bmatrix} 1 & 0 & 0 & z & 0 & 0 & -cz^3 & 0 & 0 \\ 0 & 1 & 0 & 0 & z & 0 & 0 & -cz^3 & 0 \\ 0 & 0 & 1 & 0 & 0 & z & 0 & 0 & -cz^3 \end{bmatrix} \boldsymbol{\varepsilon}$$

$$\boldsymbol{\varepsilon} = \begin{Bmatrix} \boldsymbol{\varepsilon}_o^p \\ \boldsymbol{\varepsilon}_o^b \\ \boldsymbol{\varepsilon}_o^b \end{Bmatrix} + \begin{Bmatrix} \boldsymbol{\varepsilon}_o^{p1} \\ \mathbf{0} \\ \boldsymbol{\varepsilon}_o^{b1} \end{Bmatrix} \tag{5.2}$$

in which $\boldsymbol{\varepsilon}_o^p$, $\boldsymbol{\varepsilon}_o^b$ and $\boldsymbol{\varepsilon}_o^{b1}$ are introduced already in Section 2.2, Equations (2.7) - (2.9). $\boldsymbol{\varepsilon}_o^{p1}$ is the non-linear in-plane strain including imperfection and is defined as

$$\boldsymbol{\varepsilon}_o^{p1} = \begin{Bmatrix} \frac{1}{2}\left(w_{,x}^0\right)^2 + w_{,x}^0 w_{i,x} \\ \frac{1}{2}\left(w_{,y}^0\right)^2 + w_{,y}^0 w_{i,y} \\ w_{,x}^0 w_{,y}^0 + w_{,x}^0 w_{i,y} + w_{,y}^0 w_{i,x} \end{Bmatrix} \tag{5.3}$$

By introducing mid-plane displacements of Equation (2.2) in the equation above

$$\boldsymbol{\varepsilon}_o^{p1} = \frac{1}{2} \begin{Bmatrix} \left(w_{i,x} + w_{,x}^0\right) \mathbf{N}_{,x}^{\mathbf{w}} \\ \left(w_{i,y} + w_{,y}^0\right) \mathbf{N}_{,y}^{\mathbf{w}} \\ w_{,x}^0 \mathbf{N}_{,y}^{\mathbf{w}} + w_{,y}^0 \mathbf{N}_{,x}^{\mathbf{w}} + w_{i,x} \mathbf{N}_{,y}^{\mathbf{w}} + w_{i,y} \mathbf{N}_{,x}^{\mathbf{w}} \end{Bmatrix} \mathbf{q}_{\mathbf{w}} \tag{5.4}$$

Now, Using the method introduced in the 2.2, the virtual work of the elastic restoring (internal) forces, Equation (2.25), extends as

$$\delta W_{in} = -\int_\Omega \Big(\delta \boldsymbol{\varepsilon}_o^{pT} \mathbf{A} \boldsymbol{\varepsilon}_o^p + \delta \boldsymbol{\varepsilon}_o^{bT} \left(\mathbf{C} + 2\mathbf{E} + \mathbf{F}\right) \boldsymbol{\varepsilon}_o^b + \delta \boldsymbol{\varepsilon}_o^{bT} \left(\mathbf{E} + \mathbf{F}\right) \boldsymbol{\varepsilon}_o^{b1} + \delta \boldsymbol{\varepsilon}_o^{b1\,T} \left(\mathbf{E} + \mathbf{F}\right) \boldsymbol{\varepsilon}_o^b +$$

$$\delta \boldsymbol{\varepsilon}_o^{b1\,T} \mathbf{F} \boldsymbol{\varepsilon}_o^{b1} + \delta \boldsymbol{\gamma}_o^{pT} \left(\mathbf{G} + 2\mathbf{H} + \mathbf{I}\right) \boldsymbol{\gamma}_o^p + \delta \boldsymbol{\varepsilon}_o^{p1\,T} \mathbf{A} \boldsymbol{\varepsilon}_o^p + \delta \boldsymbol{\varepsilon}_o^{pT} \mathbf{A} \boldsymbol{\varepsilon}_o^{p1} + \delta \boldsymbol{\varepsilon}_o^{p1\,T} \mathbf{A} \boldsymbol{\varepsilon}_o^{p1} \Big) \, d\Omega \tag{5.5}$$

The first six terms are introduced in Section 2.2, the last three terms are corrected below. The seventh term is

$$\delta \boldsymbol{\varepsilon}_o^{p1\,T} \mathbf{A} \boldsymbol{\varepsilon}_o^p = \frac{1}{2} \delta \mathbf{q}_{\mathbf{w}}{}^T \begin{Bmatrix} \left(w_{i,x} + w_{,x}^0\right) \mathbf{N}_{,x}^{\mathbf{w}} \\ \left(w_{i,y} + w_{,y}^0\right) \mathbf{N}_{,y}^{\mathbf{w}} \\ \left(w_{i,x} + w_{,x}^0\right) \mathbf{N}_{,y}^{\mathbf{w}} + \left(w_{i,y} + w_{,y}^0\right) \mathbf{N}_{,x}^{\mathbf{w}} \end{Bmatrix}^T \mathbf{A} \begin{bmatrix} \mathbf{N}_{,x}^{\mathbf{u}\,T} & \mathbf{0} \\ \mathbf{0} & \mathbf{N}_{,y}^{\mathbf{u}\,T} \\ \mathbf{N}_{,y}^{\mathbf{u}\,T} & \mathbf{N}_{,x}^{\mathbf{u}\,T} \end{bmatrix} \begin{Bmatrix} \mathbf{q}_{\mathbf{u}} \\ \mathbf{q}_{\mathbf{v}} \end{Bmatrix} =$$

$$\delta \mathbf{q}_{\mathbf{w}}{}^T \begin{bmatrix} \mathbf{K}_{\mathbf{L3}}^{31} + \mathbf{K}_{\mathbf{NL}}^{31} & \mathbf{K}_{\mathbf{L3}}^{32} + \mathbf{K}_{\mathbf{NL}}^{32} \end{bmatrix} \begin{Bmatrix} \mathbf{q}_{\mathbf{u}} \\ \mathbf{q}_{\mathbf{v}} \end{Bmatrix} \tag{5.6}$$

The eighth term is transpose of the seventh term and written as

$$\delta \boldsymbol{\varepsilon}_o^{p^T} \mathbf{A} \boldsymbol{\varepsilon}_o^{p1} = \delta \left\{ \begin{array}{c} \mathbf{q_u} \\ \mathbf{q_v} \end{array} \right\}^T \left[\begin{array}{c} \mathbf{K}_{\mathbf{L3}}^{13} + \mathbf{K}_{\mathbf{NL}}^{13} \\ \mathbf{K}_{\mathbf{L3}}^{23} + \mathbf{K}_{\mathbf{NL}}^{23} \end{array} \right] \mathbf{q_w} \tag{5.7}$$

where

$$\left[\begin{array}{c} \mathbf{K}_{\mathbf{L3}}^{13} + \mathbf{K}_{\mathbf{NL}}^{13} \\ \mathbf{K}_{\mathbf{L3}}^{23} + \mathbf{K}_{\mathbf{NL}}^{23} \end{array} \right] = \left[\begin{array}{cc} \mathbf{K}_{\mathbf{L3}}^{31} + \mathbf{K}_{\mathbf{NL}}^{31} & \mathbf{K}_{\mathbf{L3}}^{32} + \mathbf{K}_{\mathbf{NL}}^{32} \end{array} \right]^T \tag{5.8}$$

The ninth term is defined as

$$\delta \boldsymbol{\varepsilon}_o^{p1^T} \mathbf{A} \boldsymbol{\varepsilon}_o^{p1} = \frac{1}{4} \delta \mathbf{q_w}^T \left\{ \begin{array}{c} \left(w_{i,x} + w_{,x}^0\right) \mathbf{N}_{,x}^{\mathbf{w}} \\ \left(w_{i,y} + w_{,y}^0\right) \mathbf{N}_{,y}^{\mathbf{w}} \\ \left(w_{i,x} + w_{,x}^0\right) \mathbf{N}_{,y}^{\mathbf{w}} + \left(w_{i,y} + w_{,y}^0\right) \mathbf{N}_{,x}^{\mathbf{w}} \end{array} \right\}^T \mathbf{A}$$

$$\left\{ \begin{array}{c} \left(w_{i,x} + w_{,x}^0\right) \mathbf{N}_{,x}^{\mathbf{w}} \\ \left(w_{i,y} + w_{,y}^0\right) \mathbf{N}_{,y}^{\mathbf{w}} \\ \left(w_{i,x} + w_{,x}^0\right) \mathbf{N}_{,y}^{\mathbf{w}} + \left(w_{i,y} + w_{,y}^0\right) \mathbf{N}_{,x}^{\mathbf{w}} \end{array} \right\} \mathbf{q_w} = \delta \mathbf{q_w}^T \left(\mathbf{K}_{\mathbf{L3}}^{33} + \mathbf{K}_{\mathbf{NL}}^{33}\right) \mathbf{q_w} \tag{5.9}$$

In the absence of external forces, the summation of the virtual work of inertia (from Section 2.2) and internal force should be zero,

$$\int_V \rho \left(\delta u \ddot{u} + \delta v \ddot{v} + \delta w \ddot{w}\right) dV + \int_V \sigma_{ij} \delta \varepsilon_{ij} = 0 \tag{5.10}$$

where ρ is density and V represents volume. Equation (5.11) gives the time-domain ordinary differential equations in generalised coordinates (namely the full model)

$$\left[\begin{array}{ccccc} \mathbf{M}^{11} & \mathbf{0} & \mathbf{0} & \mathbf{0} & \mathbf{0} \\ & \mathbf{M}^{22} & \mathbf{0} & \mathbf{0} & \mathbf{0} \\ & & \mathbf{M}^{33} & \mathbf{M}^{34} & \mathbf{M}^{35} \\ & & & \mathbf{M}^{44} & \mathbf{0} \\ sym & & & & \mathbf{M}^{55} \end{array} \right] \left\{ \begin{array}{c} \ddot{\mathbf{q}}_{\mathbf{u}} \\ \ddot{\mathbf{q}}_{\mathbf{v}} \\ \ddot{\mathbf{q}}_{\mathbf{w}} \\ \ddot{\mathbf{q}}_{\boldsymbol{\phi}_\mathbf{x}} \\ \ddot{\mathbf{q}}_{\boldsymbol{\phi}_\mathbf{y}} \end{array} \right\} + \left[\begin{array}{ccccc} \mathbf{K}_{\mathbf{L}}^{11} & \mathbf{K}_{\mathbf{L}}^{12} & \mathbf{K}_{\mathbf{L}}^{13} & \mathbf{0} & \mathbf{0} \\ & \mathbf{K}_{\mathbf{L}}^{22} & \mathbf{K}_{\mathbf{L}}^{23} & \mathbf{0} & \mathbf{0} \\ & & \mathbf{K}_{\mathbf{L}}^{33} & \mathbf{K}_{\mathbf{L}}^{34} & \mathbf{K}_{\mathbf{L}}^{35} \\ & & & \mathbf{K}_{\mathbf{L}}^{44} & \mathbf{K}_{\mathbf{L}}^{45} \\ sym & & & & \mathbf{K}_{\mathbf{L}}^{55} \end{array} \right] \left\{ \begin{array}{c} \mathbf{q_u} \\ \mathbf{q_v} \\ \mathbf{q_w} \\ \mathbf{q}_{\boldsymbol{\phi}_\mathbf{x}} \\ \mathbf{q}_{\boldsymbol{\phi}_\mathbf{y}} \end{array} \right\}$$

$$+ \left[\begin{array}{ccccc} \mathbf{0} & \mathbf{0} & \mathbf{K}_{\mathbf{NL}}^{13}(\mathbf{q_w}) & \mathbf{0} & \mathbf{0} \\ \mathbf{0} & \mathbf{0} & \mathbf{K}_{\mathbf{NL}}^{23}(\mathbf{q_w}) & \mathbf{0} & \mathbf{0} \\ \mathbf{K}_{\mathbf{NL}}^{31}(\mathbf{q_w}) & \mathbf{K}_{\mathbf{NL}}^{32}(\mathbf{q_w}) & \mathbf{K}_{\mathbf{NL}}^{33}(\mathbf{q_w}) & \mathbf{0} & \mathbf{0} \\ \mathbf{0} & \mathbf{0} & \mathbf{0} & \mathbf{0} & \mathbf{0} \\ \mathbf{0} & \mathbf{0} & \mathbf{0} & \mathbf{0} & \mathbf{0} \end{array} \right] \left\{ \begin{array}{c} \mathbf{q_u} \\ \mathbf{q_v} \\ \mathbf{q_w} \\ \mathbf{q}_{\boldsymbol{\phi}_\mathbf{x}} \\ \mathbf{q}_{\boldsymbol{\phi}_\mathbf{y}} \end{array} \right\} = \mathbf{0} \tag{5.11}$$

where all mass sub-matrices are already given in Equations (2.40). Non-linear stiffness sub-matrices and the linear ones related to imperfection are presented in Equations (5.6) - (5.9); while the rest of linear sub-matrices (not including imperfection) were already defined in Equations (2.26) - (2.31). In the linear stiffness matrix, terms $\mathbf{K}_{\mathbf{L}}^{13}$ and $\mathbf{K}_{\mathbf{L}}^{23}$ appear due to the imperfection;

term $\mathbf{K}_{\mathbf{L}}^{33}$ - already exists in the equations of perfect plates; but now it is affected by the imperfection. In the non-linear stiffness matrix, term $\mathbf{K}_{\mathbf{NL}}^{33}$ is affected by the deflection amplitude of imperfect plate. The linear stiffness matrix and its sub-matrices are already defined in Equations (2.37) in Section 2.2. Equations (5.11) - mentioned as the full model in this chapter - are a set of $2\times p_u^2+2\times p_w^2+2\times p_\phi^2$ equations.

5.2.2 Reduced Model by Statically Condensation

For the clamped plate, absence of in-plane external loads and the transverse deflection less than 2 times the plate's thickness suggest that the in-plane displacements are not very pronounced and the corresponding in-plane inertia can be neglected [137]. This process is known as *Static Condensation* [124]; it reduces the number of equations (where the new number of DOF is $2\times p_w^2+2\times p_\phi^2$) but changes the bandwidth of the stiffness matrix. Putting the in-plane inertia equal to zero, one obtains the in-plane displacements by

$$\left\{\begin{array}{c}\mathbf{q_u}\\ \mathbf{q_v}\end{array}\right\}=-\left[\begin{array}{cc}\mathbf{K}_{\mathbf{L}}^{11} & \mathbf{K}_{\mathbf{L}}^{12}\\ \mathbf{K}_{\mathbf{L}}^{21} & \mathbf{K}_{\mathbf{L}}^{22}\end{array}\right]^{-1}\left[\begin{array}{c}\mathbf{K}_{\mathbf{L}}^{13}+\mathbf{K}_{\mathbf{NL}}^{13}(\mathbf{q_w})\\ \mathbf{K}_{\mathbf{L}}^{23}+\mathbf{K}_{\mathbf{NL}}^{23}(\mathbf{q_w})\end{array}\right]\mathbf{q_w} \tag{5.12}$$

The equations of motion that result from Equations (5.11), where the effect of in-plane displacements is taken into account, but not in-plane inertia, are

$$\left[\begin{array}{ccc}\mathbf{M}^{33} & \mathbf{M}^{34} & \mathbf{M}^{35}\\ & \mathbf{M}^{44} & \mathbf{0}\\ sym & & \mathbf{M}^{55}\end{array}\right]\left\{\begin{array}{c}\ddot{\mathbf{q}}_{\mathbf{w}}\\ \ddot{\mathbf{q}}_{\boldsymbol{\phi}_{\mathbf{x}}}\\ \ddot{\mathbf{q}}_{\boldsymbol{\phi}_{\mathbf{y}}}\end{array}\right\}+\left[\begin{array}{ccc}\mathbf{K}_{\mathbf{LS}}^{33} & \mathbf{K}_{\mathbf{L}}^{34} & \mathbf{K}_{\mathbf{L}}^{35}\\ & \mathbf{K}_{\mathbf{L}}^{44} & \mathbf{K}_{\mathbf{L}}^{45}\\ sym & & \mathbf{K}_{\mathbf{L}}^{55}\end{array}\right]\left\{\begin{array}{c}\mathbf{q}_{\mathbf{w}}\\ \mathbf{q}_{\boldsymbol{\phi}_{\mathbf{x}}}\\ \mathbf{q}_{\boldsymbol{\phi}_{\mathbf{y}}}\end{array}\right\}+$$

$$\left[\begin{array}{ccc}\mathbf{K}_{\mathbf{NLS}}^{33}(\mathbf{q_w}) & \mathbf{0} & \mathbf{0}\\ & \mathbf{0} & \mathbf{0}\\ sym & & \mathbf{0}\end{array}\right]\left\{\begin{array}{c}\mathbf{q}_{\mathbf{w}}\\ \mathbf{q}_{\boldsymbol{\phi}_{\mathbf{x}}}\\ \mathbf{q}_{\boldsymbol{\phi}_{\mathbf{y}}}\end{array}\right\}=\mathbf{0} \tag{5.13}$$

Linear term $\mathbf{K}_{\mathbf{LS}}^{33}$ is constant as

$$\mathbf{K}_{\mathbf{LS}}^{33}=\mathbf{K}_{\mathbf{L1}}^{33}+\mathbf{K}_{\mathbf{L2}}^{33}+\mathbf{K}_{\mathbf{L3}}^{33}+\mathbf{K}_{\mathbf{L4}}^{33}$$

where

$$\mathbf{K}_{\mathbf{L4}}^{33}=-\left[\begin{array}{c}\mathbf{K}_{\mathbf{L3}}^{13}\\ \mathbf{K}_{\mathbf{L3}}^{23}\end{array}\right]^{T}\left[\begin{array}{cc}\mathbf{K}_{\mathbf{L}}^{11} & \mathbf{K}_{\mathbf{L}}^{12}\\ \mathbf{K}_{\mathbf{L}}^{21} & \mathbf{K}_{\mathbf{L}}^{22}\end{array}\right]^{-1}\left[\begin{array}{c}\mathbf{K}_{\mathbf{L3}}^{13}\\ \mathbf{K}_{\mathbf{L3}}^{23}\end{array}\right].$$

$\mathbf{K}_{\mathbf{NLS}}^{33}(\mathbf{q_w})$ has terms that depend linearly and terms that depend quadratically on the transverse deflection

$$\mathbf{K}_{\mathbf{NLS}}^{33}(\mathbf{q_w})=\mathbf{K}_{\mathbf{NL1}}^{33}(\mathbf{q_w})+\mathbf{K}_{\mathbf{NL2}}^{33}(\mathbf{q_w})+\mathbf{K}_{\mathbf{NL3}}^{33}(\mathbf{q_w})$$

where

$$\mathbf{K}_{\mathbf{NL3}}^{33}(\mathbf{q}_{\mathbf{w}}) = -2\begin{bmatrix} \mathbf{K}_{\mathbf{NL1}}^{13} \\ \mathbf{K}_{\mathbf{NL1}}^{23} \end{bmatrix}^{T} \begin{bmatrix} \mathbf{K}_{\mathbf{L}}^{11} & \mathbf{K}_{\mathbf{L}}^{12} \\ \mathbf{K}_{\mathbf{L}}^{21} & \mathbf{K}_{\mathbf{L}}^{22} \end{bmatrix}^{-1} \begin{bmatrix} \mathbf{K}_{\mathbf{NL1}}^{13} \\ \mathbf{K}_{\mathbf{NL1}}^{23} \end{bmatrix}.$$

5.2.3 Reduced Model by Modal Summation Method

For simplicity, either Equation (5.11) or Equation (5.13) can be written in a compact form

$$\mathbf{M}\ddot{\mathbf{q}}(t) + \mathbf{K}_{\mathbf{L}}\mathbf{q}(t) + \mathbf{K}_{\mathbf{NL}}(\mathbf{q}(t))\,\mathbf{q}(t) = \mathbf{0}. \tag{5.14}$$

Knowing that we will analyse the lower-order modes, very high-order modes will probably not be excited. Therefore, we would be justified in assuming that the free vibration is the superposition of only a few of the lower-frequency modes [125], lets say m modes (the procedure on how to select these m modes are given in Section 5.2.5). Using a reduced modal matrix $\mathbf{\Phi}$ composed of only m normal modes $\boldsymbol{\phi}_i$, the generalised displacements $\mathbf{q}$ can be related to modal displacements $\mathbf{q}_{\mathbf{m}}$ by

$$\mathbf{q}(t) = \mathbf{\Phi}\mathbf{q}_{\mathbf{m}}(t) \tag{5.15}$$

Premultiplying Equation (5.14) by the transpose $\mathbf{\Phi}^T$ and substituting Equation (5.15) gives m equations of motion as

$$\overline{\mathbf{M}}\ddot{\mathbf{q}}_{\mathbf{m}}(t) + \overline{\mathbf{K}}_{\mathbf{L}}\mathbf{q}_{\mathbf{m}}(t) + \overline{\mathbf{K}}_{\mathbf{NL}}(\mathbf{q}_{\mathbf{m}}(t))\,\mathbf{q}_{\mathbf{m}}(t) = \mathbf{0}. \tag{5.16}$$

Here, the modal mass $\overline{\mathbf{M}}$ and linear stiffness matrices $\overline{\mathbf{K}}_{\mathbf{L}}$ are diagonal, but the modal non-linear stiffness $\overline{\mathbf{K}}_{\mathbf{NL}}$ matrix is not. The use of an expansion, based on a truncated number of normal modes, reduces the number of equations to the number of modes employed.

5.2.4 Periodic Free Vibration Solutions by the Shooting Method

Equation (5.16) is an autonomous system of equations. In autonomous systems, period T is not known in advance. Here, we overcome this by fixing T, by using it as a parameter. Free periodic solutions of the time-domain Equation (5.16) may be found by treating the equation as a two-point boundary value problem and using the shooting method [138]. The periodicity condition is

$$\begin{Bmatrix} \mathbf{y}(0) \\ \mathbf{q}_{\mathbf{m}}(0) \end{Bmatrix} = \begin{Bmatrix} \mathbf{y}(T) \\ \mathbf{q}_{\mathbf{m}}(T) \end{Bmatrix}$$

where $\dot{\mathbf{q}}_{\mathbf{m}} = \mathbf{y}$ and T is the period of the free vibration. Therefore, it is only natural — but not obligatory — to convert the system of m second-order ordinary equations of motion (5.16) to $2m$ first-order ordinary differential equations on state-space coordinates (Ref. [138])

$$\begin{bmatrix} \mathbf{0} & \overline{\mathbf{M}} \\ \overline{\mathbf{M}} & \mathbf{0} \end{bmatrix} \begin{Bmatrix} \dot{\mathbf{y}}(t) \\ \dot{\mathbf{q}}_{\mathbf{m}}(t) \end{Bmatrix} + \begin{bmatrix} -\overline{\mathbf{M}} & \mathbf{0} \\ \mathbf{0} & \overline{\mathbf{K}}_{\mathbf{L}} + \overline{\mathbf{K}}_{\mathbf{NL}}(\mathbf{q}_{\mathbf{m}}(t)) \end{bmatrix} \begin{Bmatrix} \mathbf{y}(t) \\ \mathbf{q}_{\mathbf{m}}(t) \end{Bmatrix} = \mathbf{0} \tag{5.17}$$

Taking the phase-space vector $\mathbf{X}\left(\begin{Bmatrix} \mathbf{y}(0) \\ \mathbf{q}_{\mathbf{m}}(0) \end{Bmatrix}, t\right) = \begin{Bmatrix} \mathbf{y}(t) \\ \mathbf{q}_{\mathbf{m}}(t) \end{Bmatrix}$, an initial value problem can be written

$$\dot{\mathbf{X}} = -\begin{bmatrix} \mathbf{0} & \overline{\mathbf{M}} \\ \overline{\mathbf{M}} & \mathbf{0} \end{bmatrix}^{-1} \begin{bmatrix} -\overline{\mathbf{M}} & \mathbf{0} \\ \mathbf{0} & \overline{\mathbf{K}}_{\mathbf{L}} + \overline{\mathbf{K}}_{\mathbf{NL}}(\mathbf{q}_{\mathbf{m}}(t)) \end{bmatrix} \mathbf{X},$$

$$\mathbf{X}\left(\begin{Bmatrix} \mathbf{y}(0) \\ \mathbf{q}_{\mathbf{m}}(0) \end{Bmatrix}, 0\right) = \begin{Bmatrix} \mathbf{y}(0) \\ \mathbf{q}_{\mathbf{m}}(0) \end{Bmatrix} \tag{5.18}$$

Equation (5.18) is solved when $\mathbf{X}\left(\begin{Bmatrix} \mathbf{y}(0) \\ \mathbf{q}_{\mathbf{m}}(0) \end{Bmatrix}, T\right)$ is equal to $\mathbf{X}\left(\begin{Bmatrix} \mathbf{y}(0) \\ \mathbf{q}_{\mathbf{m}}(0) \end{Bmatrix}, 0\right)$.

The initial condition $\begin{Bmatrix} \mathbf{y}(0) \\ \mathbf{q}_{\mathbf{m}}(0) \end{Bmatrix}$ for the first two points of backbone curves (which are very close to the linear solution) is chosen with modal displacement $\mathbf{q}_{\mathbf{m}}(0)$ taken in the form of the first linear mode shape with its velocity $\mathbf{q}_{\mathbf{m}}(0)$ equal to zero. For the following points of the response curve, a secant predictor is used [139]. Then, the set of $2m$ ordinary differential equations are integrated by an initial value method arriving at the other boundary $\mathbf{X}\left(\begin{Bmatrix} \mathbf{y}(0) \\ \mathbf{q}_{\mathbf{m}}(0) \end{Bmatrix}, T\right)$; we use Runge–Kutta–Fehlberg method modified with Cash–Karp method to control the error with *Adaptive Stepsize* [138]. The purpose of this *adaptive stepsize Control* is to achieve some prefixed accuracy in the solution with the minimum computational effort. Here, the dimension of phase space (i.e. two times the modal coordinates) does not exceed 30; using this phase space, it was possible to carry out the non-linear vibration examinations almost without any numerical issue. If a researcher needs to have a higher-dimensional phase space, it could be preferable to use Adams–Gear method designed for stiff equations [51], to avoid spurious nonstationary and divergent motions.

To achieve the periodicity conditions, the initial values are corrected until convergence, by

$$\mathbf{X}\left(\begin{Bmatrix} \mathbf{y}(0) \\ \mathbf{q}_{\mathbf{m}}(0) \end{Bmatrix}, 0\right)^{i+1} = \mathbf{X}\left(\begin{Bmatrix} \mathbf{y}(0) \\ \mathbf{q}_{\mathbf{m}}(0) \end{Bmatrix}, 0\right)^{i} + \delta\mathbf{X} \tag{5.19}$$

The correction $\delta\mathbf{X}$ solves the system of equations

$$\left[\frac{\partial \mathbf{X}\left(\left\{\begin{array}{c}\mathbf{y}(0)\\ \mathbf{q_m}(0)\end{array}\right\},T\right)}{\partial\left\{\begin{array}{c}\mathbf{y}(t)\\ \mathbf{q_m}(t)\end{array}\right\}}-[I]\right]\delta\mathbf{X}=\mathbf{X}\left(\left\{\begin{array}{c}\mathbf{y}(0)\\ \mathbf{q_m}(0)\end{array}\right\},0\right)-\mathbf{X}\left(\left\{\begin{array}{c}\mathbf{y}(0)\\ \mathbf{q_m}(0)\end{array}\right\},T\right). \quad (5.20)$$

The following initial values for the free oscillations may be found using a secant predictor, given for example in Refs. [127, 139].

It is possible to reach to turning points in the backbone curves in the free vibration of imperfect plates. To find a solution after the turning point, one can reverse the trend of the initial values (for instance, during hardening behaviour, the following initial guess corresponds to a higher frequency; a guess for a solution after the turning point can be obtained using an initial guess with a decrease in the frequency). Reaching to the solution around the turning point also depends to the frequency intervals between guesses. If a large interval prevent the prediction of a turning point, so a smaller frequency interval (i.e. a more exact guess after turning point) maybe solve the problem and identify the turning point (afterward hardening behaviour changes to softening or vice versa).

Finding probable bifurcations in backbone curves also is possible with this technique. The most important issue in arriving to a bifurcation and continuing to the bifurcated solution branch is selecting relevant modes in the modal coordinates. In addition to the inclusion of the corresponding modes in the modal coordinates of the reduced-model, always a good choice of the error parameters in the Runge-Kutta-Fehlberg method with adaptive stepsize (to read about these error variable see Ref. [138]) is necessary to find bifurcated branches of the solution.

5.2.5 Selection of Modes for Reduced Model by the Modal Summation Method

Selecting the appropriate modes to be used in the reduced order model by modal summation method has a decisive role in the exactness of the final results (here, transverse displacements); also these modes have an effect on the detection of bifurcations in the frequency-response curves. Obviously, taking all the linear modes in this method would lead to the most exact result, but running the final code in Fortran would take a long time. In result, selecting a limited number of the most important linear modes can help the code to give enough exact results after an acceptable running time.

In this study, the procedure that is used to select the most important linear modes is as follows: the main frequency response curve is first determined using two modes in modal summation method, including always the first linear mode plus an arbitrary extra mode; then the results (in this case, maximum transverse displacement) are saved. Then, the transverse displacements obtained with different couple of modes are compared and the linear modes related to the largest results are selected. The largest deflection results corresponds to those modes which give more flexibility to the laminate. This stage can be performed using more than two modes (usually, it is necessary). By the end, a limited number of linear modes including the first mode are selected for

calculation of the main frequency response curve. Depending on the modes included, bifurcations may be detected or not.

5.3 Numerical Results

The matrices in the equations of motion (5.11) have been obtained by using Maple 13 software with 30 digits of accuracy to avoid matrix ill-conditioning when performing surface integrals of shape functions (already given in "Appendix A"). An in-house code written in Intel Visual Fortran 11.1 utilizes a shooting procedure with Runge–Kutta–Fehlberg method [138] to find periodic solutions of Equation (5.18), detect bifurcations as well as follow branches of the solution.

In what follows, perfect VSCL plates are considered first, to assess the convergence and compare present results with published ones. Then, the effect of curvilinear fibres on frequency response curves of perfect VSCL is evaluated in detail, with examples of bifurcations. Later, imperfect VSCL plates are studied. Because of the lack of published data for comparison in imperfect VSCL plates, the non-linear frequencies are compared when the fibres are straight. In Chapter 2, a section on the verification and comparison of the linear frequencies of imperfect CSCL plates is given. Finally, the effect of sinusoidal imperfection on the backbone curves is assessed. The mechanical properties of the plates here studied are given in Table 5.1. In addition, all the layers of the laminated plates have the same thicknesses. As written in Section 1.4.4, a restriction during manufacturing VSCLs is the radius of curvature of fibres. In this chapter, the fibre angles are chosen considering this limitation.

Table 5.1: Mechanical properties of the composite plates studied.

a (m)	b (m)	h (m)	E_1 (GPa)	E_2 (GPa)	G_{12} (GPa)	G_{13} (GPa)	G_{23} (GPa)	ν_{12}	ρ (kg/m^3)
Plate 1									
0.5	0.5	0.005	24.028	1	0.522	0.522	0.522	0.29	1000
Plate 2									
0.5	0.5	0.005	173	7.2	3.76	3.76	3.76	0.29	1540
Plate 3									
1	1	0.1	181	10.3	7.17	7.17	6.21	0.28	1000

5.3.1 Convergence and Comparison Study for Free Oscillation of Perfect VSCL plates

Evaluations of plate p-version finite elements, based on the hierarchic sets of polynomial shape functions employed here and using different deformation theories, including TSDT, on the computation of linear frequencies of perfect VSCL plates, are given in the past chapters. So this section starts with non-linear vibrations. In order to verify the p-version finite element model and the shooting method implemented, a convergence study and a comparison with another author's results are performed in Table 5.2. The number of unidimensional shape functions ($p_u = p_w = p_\phi = p$)

is increased from 4 to 8. The fundamental non-linear frequency parameters $\Omega_{NL} = \omega_l a\sqrt{\rho/E_2}$ (ω_l represents the fundamental linear frequency) of the four-layered VSCL $[\langle 40^o, 80^o\rangle, -\langle 40^o, 80^o\rangle]_{sym}$ are calculated with $p = 4,5,6,7$, and 8 shape functions and compared with data from Ref. [128]. The non-linear frequency parameters are calculated as a function of the maximum amplitude-to-thickness ratio w_{max}/h, where the point of maximum amplitude is located at the centre of the plate. The laminate has clamped edges and the mechanical properties of Plate 1 in Table 5.1. Three modal coordinates are considered. In order to find an accurate reduced order model, the non-linear frequencies using five modal coordinates were calculated (but not included in Table 5.2) and compared with the results using three modal coordinates. There was a good agreement between both results. In what convergence is concerned, we see that the relative difference between the non-linear frequency parameter computed with 125 DOF (i.e. $p = p_u = p_w = p_\phi = 5$) and with 320 DOF (i.e. $p = 8$) is always below 0.7%. Furthermore, the non-linear frequency parameter of the present approach is in very good agreement with the one computed in Ref. [128]. In Ref. [128], a thin plate theory, hierarchical finite element method (HFEM) is applied to obtain ordinary differential equations of motion, which are passed to the frequency domain via the harmonic balance method (HBM), considering solely one harmonic. The frequency domain equations are solved using the linearized updated mode method. Hereafter, based on this study, 245 DOF will be employed for the full models of the VSCL plates.

Table 5.2: Convergence and comparison study of fundamental non-linear frequency parameter Ω_{NL} of the $[\langle 40^o, 80^o\rangle, -\langle 40^o, 80^o\rangle]_{sym}$ laminate

w_{max}/h	p					Data from Ref. [128]
	4	5	6	7	8	
0.2	0.273	0.269	0.268	0.268	0.268	0.269
0.4	0.278	0.274	0.273	0.273	0.273	0.275
0.6	0.288	0.283	0.282	0.282	0.282	0.283
0.8	0.301	0.295	0.294	0.293	0.293	0.295
1.0	0.316	0.310	0.308	0.308	0.308	0.309

Still to verify the present model and solution method, comparisons of the non-linear frequency parameter with data on VSCL plates from Ref. [128] are given in Table 5.3. The geometry and mechanical properties of the laminates are the same as in the example given in Table 5.2. The studied VSCL plates have different curvilinear fibre angles T_1. To calculate the non-linear frequency parameters, static condensation is applied to the full 245 DOF model, and then, four modal coordinates are used. An analysis with the same conditions, but including eight modal coordinates, was also done. The first five digits of the non-linear frequencies computed with these two modal reduced models were the same. In Table 5.3, the difference between Ref. [128] and the present frequencies is less than 1%. However, our experience showed that it may be required to include a few modal coordinates, in order to accurately compute frequencies in the non-linear regime, as well as to find bifurcations from main backbone curves. When depicting maximum deflection ratio $w_{max}(0,0,t)/h$ at the centre of the plate against frequency ratio ω/ω_{l1}, secondary branches that

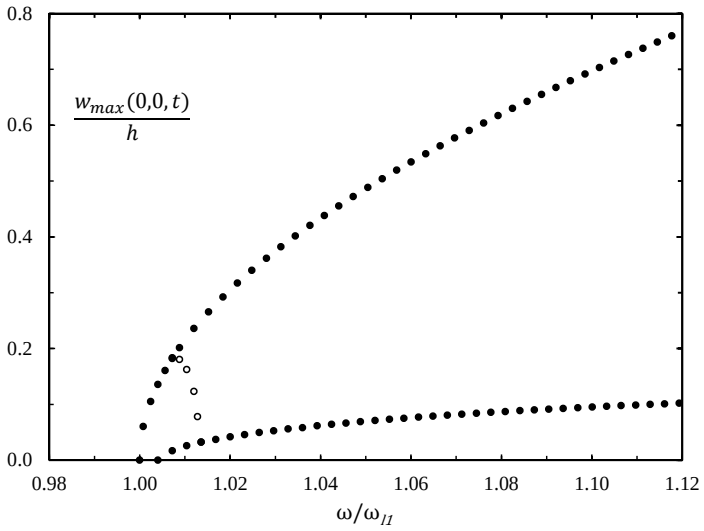

Figure 5.1: Main branches (solid dots) and a secondary branch (hollow dots) for the VSCL plate with $[\langle 40^o, 20^o\rangle, -\langle 40^o, 20^o\rangle]_{sym}$.

bifurcate from the main branch were observed. For instance, one of them, which was observed in the analyses of VSCL $[\langle 40^o, 20^o\rangle, -\langle 40^o, 20^o\rangle]_{sym}$ plate, is shown in Figure 5.1.

Here, the main branches, shown in solid dot, designate branches that contain a solution that simultaneously obeys the following: occurs at zero vibration amplitude, corresponding to a linear mode shape and occurs at a linear natural frequency or at a sub-harmonic of a linear natural frequency. A secondary branch, with the hollow dots, is one that bifurcates from a main branch. A secondary branch that bifurcates from the main fundamental branch (dominated by the first harmonic and containing the first linear mode of vibration) connects the latter with another main branch dominated by the third harmonic. These bifurcations were not found in Ref. [128].

Table 5.3: Comparison of fundamental non-linear frequency parameter Ω_{NL} of the VSCL $[\langle T_0, T_1\rangle, -\langle T_0, T_1\rangle]_{sym}$ plates.

Fibre orientation angle	Method	w_{max}/h				
		0.2	0.4	0.6	0.8	1.0
$[\langle 40^o, 20^o\rangle, -\langle 40^o, 20^o\rangle]_{sym}$	Ref. [128]	0.318	0.326	0.338	0.355	0.375
	Present	0.315	0.323	0.336	0.353	0.374
$[\langle 40^o, 40^o\rangle, -\langle 40^o, 40^o\rangle]_{sym}$	Ref. [128]	0.297	0.305	0.316	0.331	0.350
	Present	0.295	0.302	0.314	0.330	0.349
$[\langle 40^o, 60^o\rangle, -\langle 40^o, 60^o\rangle]_{sym}$	Ref. [128]	0.278	0.284	0.294	0.307	0.322
	Present	0.276	0.282	0.292	0.305	0.321

5.3.2 Effect of Fibre Angles on Free Vibration of Perfect VSCL Plates

The effect of changes in the curvilinear fibre angles T_0 and T_1 on the fundamental non-linear frequency parameter $\Omega_{NL} = \omega_{l1} a\sqrt{\rho/E_2}$ of a square VSCL plate is investigated in Figure 5.2,

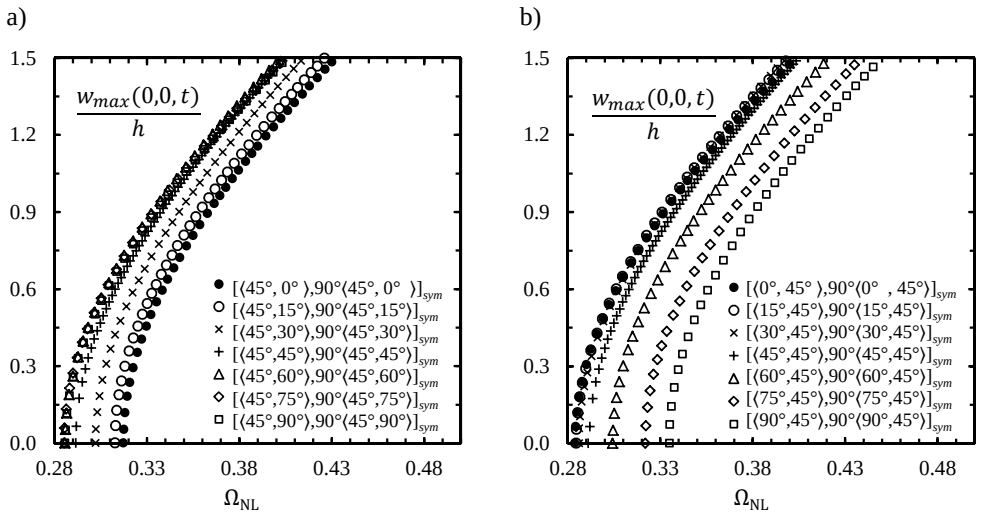

Figure 5.2: Fundamental backbone curves of (a) the VSCL $[\langle 45^o, T_1\rangle, 90^o + \langle 45^o, T_1\rangle]_{sym}$, and (b) the VSCL $[\langle T_0, 45^o\rangle, 90^o + \langle T_0, 45^o\rangle]_{sym}$.

with increasing vibration amplitude. The mechanical properties of Plate 2 in Table 5.1 are used. Fibre angles T_1 and T_0 are independently changed, respectively, in Figure 5.2(a) and (b), in a four-layer symmetric Ω_{NL} of VSCL $[\langle T_0, T_1\rangle, 90^o + \langle T_0, T_1\rangle]_{sym}$ plate. In Figure5.2(a), the fibre angle at the plate centre is constant, $T_0 = 45^o$, and is changing at the edges, $T_1 = 0^o...90^o$, but in Figure 5.2(b) the fibre angles at the edges are constant 45^o and angles at the plate centre are different. Backbone curves of these perfect plates always show hardening effect. There is no significant change in the non-linear frequencies of laminates when the curvilinear fibre angle at the edges, T_1, varies between 60^o and 90^o. Selecting the larger fibre angle T_1 at the edge decreases the non-linear frequencies; on the contrary, choosing larger fibre angle T_0 at the centre increases the non-linear frequencies. If fibre angles T_0 at the centre change from 0^o to 30^o, there will be no meaningful difference in the non-linear frequencies. It also results from the analysis of Figure 5.2 that the effect of T_0 on the non-linear frequency is larger than the effect of T_1.

While calculating non-linear frequencies around the first linear frequency, in the examples above, some bifurcations to other branches were observed. This is, by way of example, demonstrated in Figure 5.3 for two VSCLs, namely $[\langle 45^o, 15^o\rangle, 90^o + \langle 45^o, 15^o\rangle]_{sym}$ and $[\langle 45^o, 75^o\rangle, 90^o + \langle 45^o, 75^o\rangle]_{sym}$. The figure shows two secondary branches that bifurcate from the fundamental backbone and another main branch, for each fibre configuration. Time histories along at least an oscillation period (trajectories in black run for four periods; this was confirmed analysing the phase plane plot), phase plane plots and frequency Fourier spectra, in various frequency ratios in the second, third and fourth branches, are given in Figure 5.4 (the second and third - secondary - branches and the fourth - main - branch of each laminate can be found in Figure 5.3). The non-linear frequency parameters related to points P1 (from second branch), P2 (from fourth branch) and P3 (from third branch) are $\Omega_{NL} = 0.3103, 0.3159$ and 0.3159 for VSCL $[\langle 45^o, 75^o\rangle, 90^o + \langle 45^o, 75^o\rangle]_{sym}$. In points P4 (from second branch), P5 (from fourth branch) and

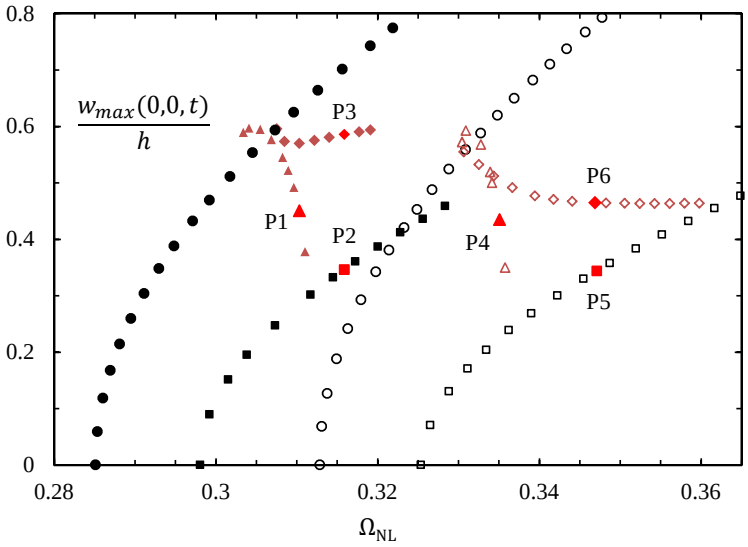

Figure 5.3: Fundamental backbone ●, second (secondary) branch ▲, third (secondary) branch ◆ and fourth (main) branch ■ of the VSCL $[\langle 45^o, 75^o\rangle, 90^o + \langle 45^o, 75^o\rangle]_{sym}$; fundamental backbone ○, second (secondary) branch △, third (secondary) branch ◇ and fourth (main) branch □ of the VSCL $[\langle 45^o, 15^o\rangle, 90^o + \langle 45^o, 15^o\rangle]_{sym}$.

P6 (from third branch), non-linear frequency parameters are $\Omega_{NL} = 0.3351, 0.3466$ and 0.3466 for VSCL $[\langle 45^o, 15^o\rangle, 90^o + \langle 45^o, 15^o\rangle]_{sym}$.

It is seen that for $[\langle 45^o, 75^o\rangle, 90^o + \langle 45^o, 75^o\rangle]_{sym}$ configuration, in addition to the first, the fifth harmonic is excited in the third branch, whereas for $[\langle 45^o, 15^o\rangle, 90^o + \langle 45^o, 15^o\rangle]_{sym}$ configuration, in addition to the first, the third harmonic is also stimulated. In the second branch, the fourth harmonic is excited in both VSCLs, but for $[\langle 45^o, 75^o\rangle, 90^o + \rangle 45^o, 75^o\rangle]_{sym}$ laminate, also third and fifth harmonics are slightly excited. In these six statuses (P1,..., P6), sectional views of the plate are depicted in Figures 5.5 and 5.6. These figures display sectional views ($y = 0$) of the vibration, as well as five transverse deflection plots during vibration for each P1 to P6 points. The deflection plots display deflection of the plate in different - but not necessarily separated by equal intervals - sequential times in the oscillation period of Figure 5.4(a) and (d). In all six points, except P2 and P5, more than one vibrational mode is observed. For both the VSCLs $[\langle 45^o, 75^o\rangle, 90^o + \langle 45^o, 75^o\rangle]_{sym}$ and $[\langle 45^o, 15^o\rangle, 90^o + \langle 45^o, 15^o\rangle]_{sym}$, the first mode is essential in the fundamental branch and the seventh mode in the fourth branch. The relations between the seventh linear frequency and the fundamental linear frequency of the $[\langle 45^o, 75^o\rangle, 90^o + \langle 45^o, 75^o\rangle]_{sym}$ plate is $\omega_{l7}/\omega_{l1} = 4.180$ and of the $[\langle 45^o, 15^o\rangle, 90^o + \langle 45^o, 15^o\rangle]_{sym}$ plate is $\omega_{l7}/\omega_{l1} = 4.163$. Therefore, internal resonances of order 1:4 due to coupling between modes one and seven occurred in the second secondary branches, in both VSCLs.

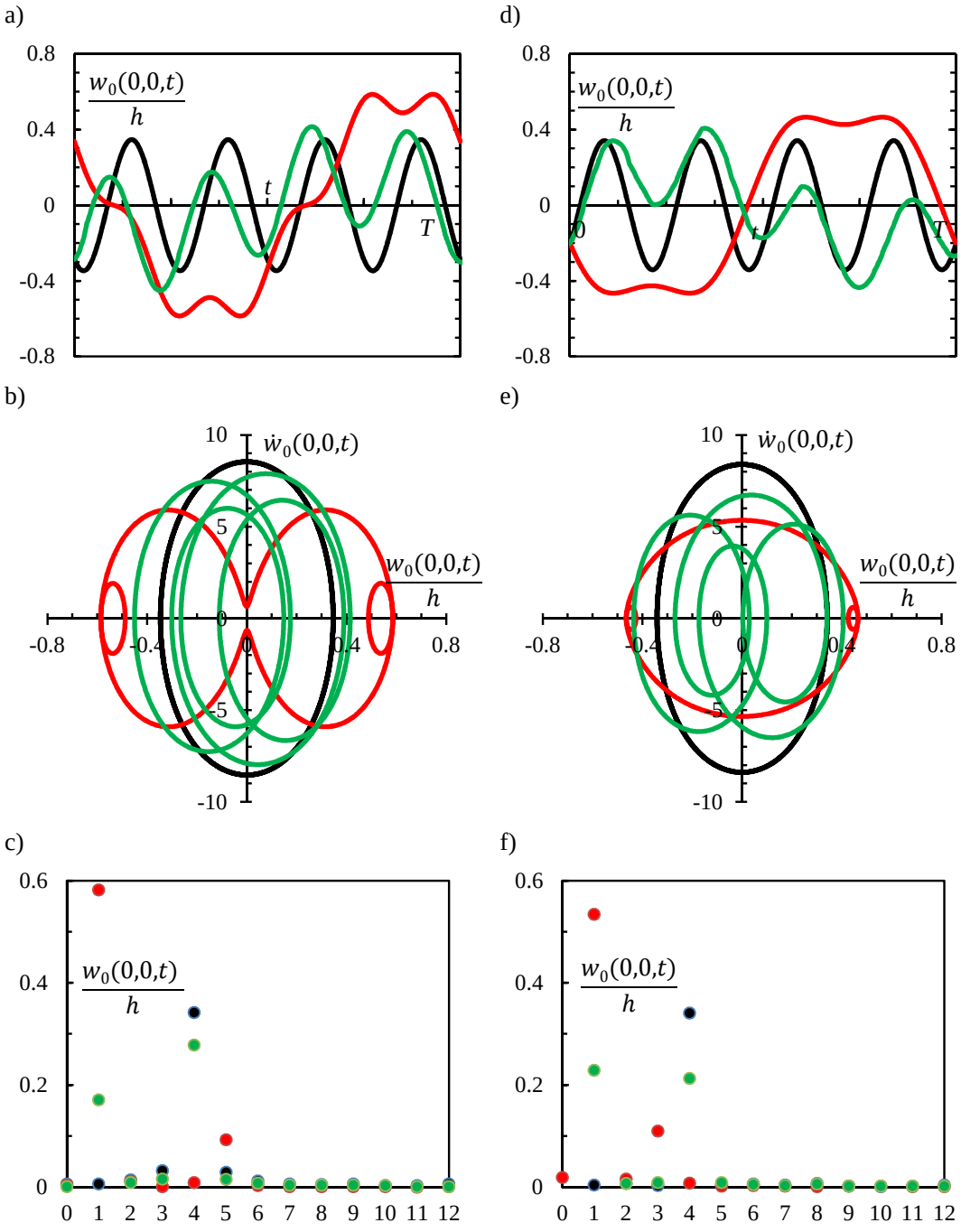

Figure 5.4: Time histories in a periodic cycle, phase plane plot and frequency spectrum for VSCLs. (a)–(c) VSCL $[\langle 45^o, 75^o\rangle, 90^o + \langle 45^o, 75^o\rangle]_{sym}$, in points P1 (second branch, $\Omega_{NL} = 0.3103$ indicated with green colour), P2 (fourth branch, $\Omega_{NL} = 0.3159$, black colour) and P3 (third branch, $\Omega_{NL} = 0.3159$, red colour), and (d)–(f) VSCL $[\langle 45^o, 15^o\rangle, 90^o + \langle 45^o, 15^o\rangle]_{sym}$, in points P4 (second branch, $\Omega_{NL} = 0.3351$, green colour), P5 (fourth branch, $\Omega_{NL} = 0.3466$, black colour) and P6 (third branch, $\Omega_{NL} = 0.3466$, red colour).

a) Point P1 (second branch, Ω_{NL}=0.3103)

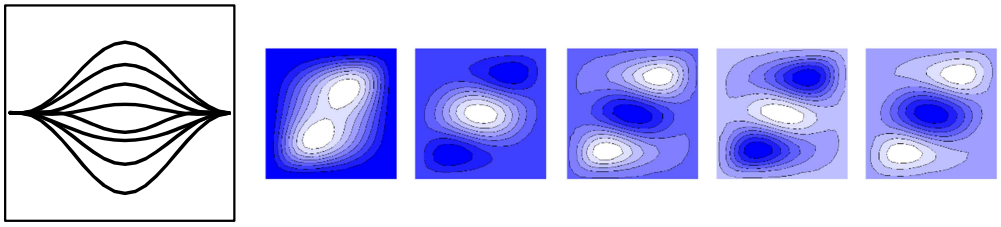

b) Point P2 (fourth branch, Ω_{NL}=0.3159)

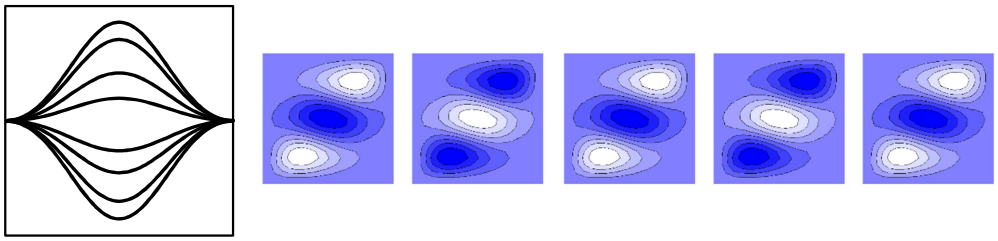

c) Point P3 (third branch, Ω_{NL}=0.3159)

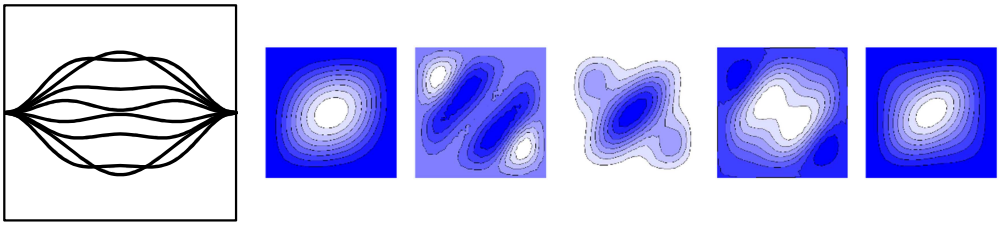

Figure 5.5: Sectional views, at $y = 0$, of transverse vibration in points P1, P2 and P3 for the VSCL $[\langle 45^{\mathrm{o}}, 75^{\mathrm{o}}\rangle, 90^{\mathrm{o}} + \langle 45^{\mathrm{o}}, 75^{\mathrm{o}}\rangle]_{sym}$, as well as its transverse deflection contour plots in five consequential and different times in the related periodic cycle. (a) Point P1 (second branch, $\Omega_{NL} = 0.3103$). (b) Point P2 (fourth branch, $\Omega_{NL} = 0.3159$). (c) Point P3 (third branch, $\Omega_{NL} = 0.3159$).

a) Point P4 (second branch, Ω_{NL}=0.3351)

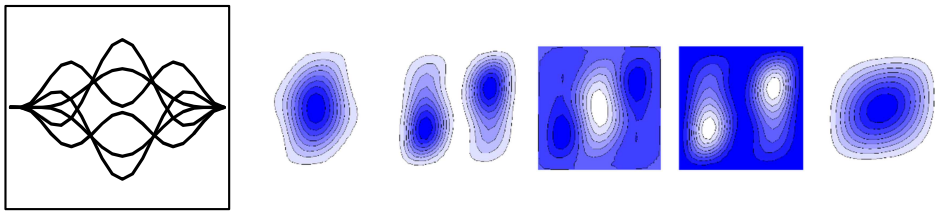

b) Point P5 (fourth branch, Ω_{NL}=0. 3466)

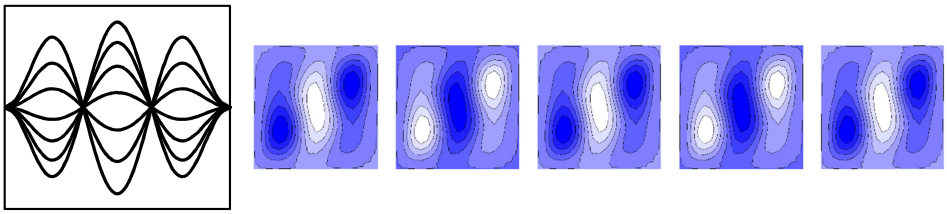

c) Point P6 (third branch, Ω_{NL}=0. 3466)

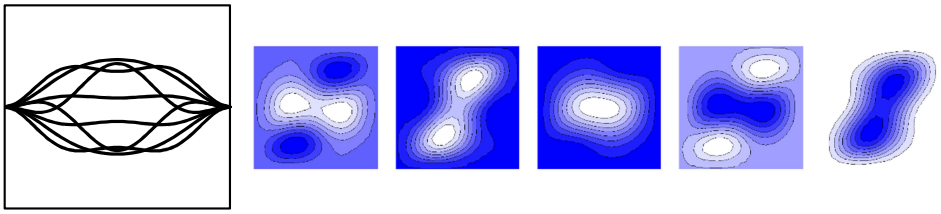

Figure 5.6: Sectional views, at $y = 0$ of transverse vibration in points P4, P5 and P6 for the VSCL $[\langle 45^{\mathrm{o}}, 15^{\mathrm{o}}\rangle, 90^{\mathrm{o}} + \langle 45^{\mathrm{o}}, 15^{\mathrm{o}}\rangle]_{sym}$, as well as its transverse deflection contour plots in five consequential and different times in the related periodic cycle. (a) Point P4 (second branch, $\Omega_{NL} = 0.3351$). (b) Point P5 (fourth branch, $\Omega_{NL} = 0.3466$). (c) Point P6 (third branch, $\Omega_{NL} = 0.3466$).

5.3.3 Comparison of Non-linear Frequencies of Imperfect VSCL plate

Although any type of geometry imperfection can be integrated in the model, sinusoidal imperfection, $w_i = h_0 \times \cos(\pi x/a)\cos(\pi y/b)$, is applied into the formulation, as was done in Ref. [71], in which h_0 is the imperfection magnitude at the centre of the plate. To validate the model, some examples of non-linear frequencies of imperfect laminates are compared with published data. Because data on imperfect VSCL plates are not available, the comparisons are made with CSCL plates. In the comparison studies on imperfect plates, a specific simply-supported boundary condition, with restrained normal displacement at the plate edges and fully free in-plane displacements (SSSS-3) (the boundary condition is given in Appendix A), has been used [71, 73, 140].

The comparison, given in Table 5.4, is for a laminated CSCL square cross-ply $[0^o, 90^o, 0^o]$ imperfect plate (i.e. $[\langle 0^o, 0^o\rangle, \langle 90^o, 90^o\rangle, \langle 0^o, 0^o\rangle]$), with simply-supported edges (SSSS-3). The magnitude of the imperfection is $h_0 = 0.1h$. The mechanical properties are the ones of plate 3 of Table 5.1. The normalized non-linear frequency (presented as ratio between non-linear and linear frequency) of the present method with 15 modal coordinates is compared with data from Refs. [73, 140] based on a third-order shear deformation plate theory and a parabolic shear deformation theory. The present linear frequency parameter Ω_1 (where $\Omega_1^2 = \omega_{l1}^2 a^4 \rho (1 - \nu_{12}\nu_{21})/h^2 E_2$) and the one from Ref. [140] differ by 2%. Possibly, the difference between the non-linear results—which ranges from 0.77 to 5.7% - is due to the single-mode techniques used in Refs. [73, 140].

Table 5.4: Comparison of non-linear frequency ratio ω_{nl}/ω_1 for cross-ply CSCL Plate 3 of Table 5.1 with imperfection ($h_0 = 0.1h$)

$\frac{w_{max}}{h}$	Ref. [73] Single mode approach	Ref. [140] Single mode approach $\Omega_l = 12.141$	Present 25 modal coordinates $\Omega_l = 11.900$
0	1	1	1
0.2	1.034	1.03	1.04
0.4	1.142	1.13	1.141
0.6	1.301	1.289	1.272
0.8	1.496	1.482	1.416
1.0	1.708	1.694	1.681

5.3.4 Effect of Imperfections on Backbone Curves in Free Vibration of VSCL Plates

Some analyses are done for imperfect CSCL ($[\langle 45^o, 45^o\rangle, 90^o + \langle 45^o, 45^o\rangle]_{sym}$) and imperfect VSCL ($[\langle 45^o, 15^o\rangle, 90^o + \langle 45^o, 15^o\rangle]_{sym}$, $[\langle 45^o, 75^o\rangle, 90^o + \langle 45^o, 75^o\rangle]_{sym}$, $[\langle 15^o, 45^o\rangle, 90^o + \langle 15^o, 45^o\rangle]_{sym}$ and $[\langle 75^o, 45^o\rangle, 90^o + \langle 75^o, 45^o\rangle]_{sym}$) plates with different imperfection ratios $h_0/h = 0, ..., 1.0$. The plate geometry and mechanical properties are the ones of the example in Figure 5.2 (Plate 2 of Table 5.1). Backbones of the CSCL and VSCLs with imperfection are shown in Figure 5.7. The perfect laminate has, always, the smallest linear frequency parameter, and with increasing the imperfection, the linear frequency of the VSCL laminate increases. The non-linear frequency

response ($\Omega_{NL} = \omega_{l1} a\sqrt{\rho/E_2}$) of the perfect plate shows hardening effect, but increasing the amount of imperfection this behaviour changes to softening for small deflections, returning to hardening for larger deflections. A comparison between VSCLs curves in Figure 5.7(b), (c) and CSCL curves in Figure 5.7(a) shows that when the fibre angle at the edge T_1 is large, the imperfect plate is more affected by softening. Comparing the VSCL curves in Figure 5.7(d), (e) with the CSCL curves in Figure 5.7(a), one verifies that non-linear frequencies of imperfect plates are more affected by softening when the fibre angle at the centre of the plate T_0 is small. Of all these plates, the one with larger linear natural frequencies and which experiences less softening is the VSCL plate $[\langle 75^o, 45^o\rangle, 90^o + \langle 75^o, 45^o\rangle]_{sym}$.

5.4 Conclusions

In this chapter, a TSDT-based *p*-version finite element for geometrical non-linear vibrations of imperfect VSCL plates was presented. The number of degrees of freedom (DOF) was first reduced by neglecting in-plane inertia (i.e. by static condensation) and later by using modal reduction, i.e. by considering a truncated set of modal coordinates. Periodic, free, geometrically non-linear oscillations were studied. The periodic boundary value problem was treated using the shooting method, with adaptive step-size control in the integration of the reduced set of equations of motion. The experience of using shooting method - where, unlike in other methods, the degree of the non-linearity is not forcefully small or the frequency content of the response artificially limited - showed that the results for the periodic boundary value problem can be found very fast by controlling the error parameter in adaptive step-size control algorithm. Obviously, a model with more modal coordinates (i.e. with more DOFs) requires more computational time to be solved and more computational memory. As shown in a convergence study, in the *p* -version finite element method, seven one-dimensional shape functions in each individual displacement variable are enough to accurately calculate the non-linear frequencies of interest in this chapter. The effects that varying fibre angles at the vertical edges and at the centre of the ply have on the non-linear free vibrations of VSCL plates were studied. These effects were shown in backbone curves as well as resorting to time histories, phase - plane plots and Fourier spectra. Sectional views of two VSCL plates in different branches were plotted. Later in this chapter, the effect of imperfection on non-linear free vibration of VSCL plates was investigated. A CSCL plate against some VSCL plates with different imperfection magnitudes was examined, and corresponding backbone curves were depicted. Softening and hardening behaviours were found. The effect of varying fibre angle at the centre and the edges of the plate on non-linear frequency of imperfect plates was assessed. Of the particular set of plates analysed, the one that experienced less softening, and showed large natural frequencies, both in the linear and in the non-linear regimes, for different imperfection magnitudes, was VSCL plate $[\langle 75^o, 45^o\rangle, 90^o + \langle 75^o, 45^o\rangle]_{sym}$.

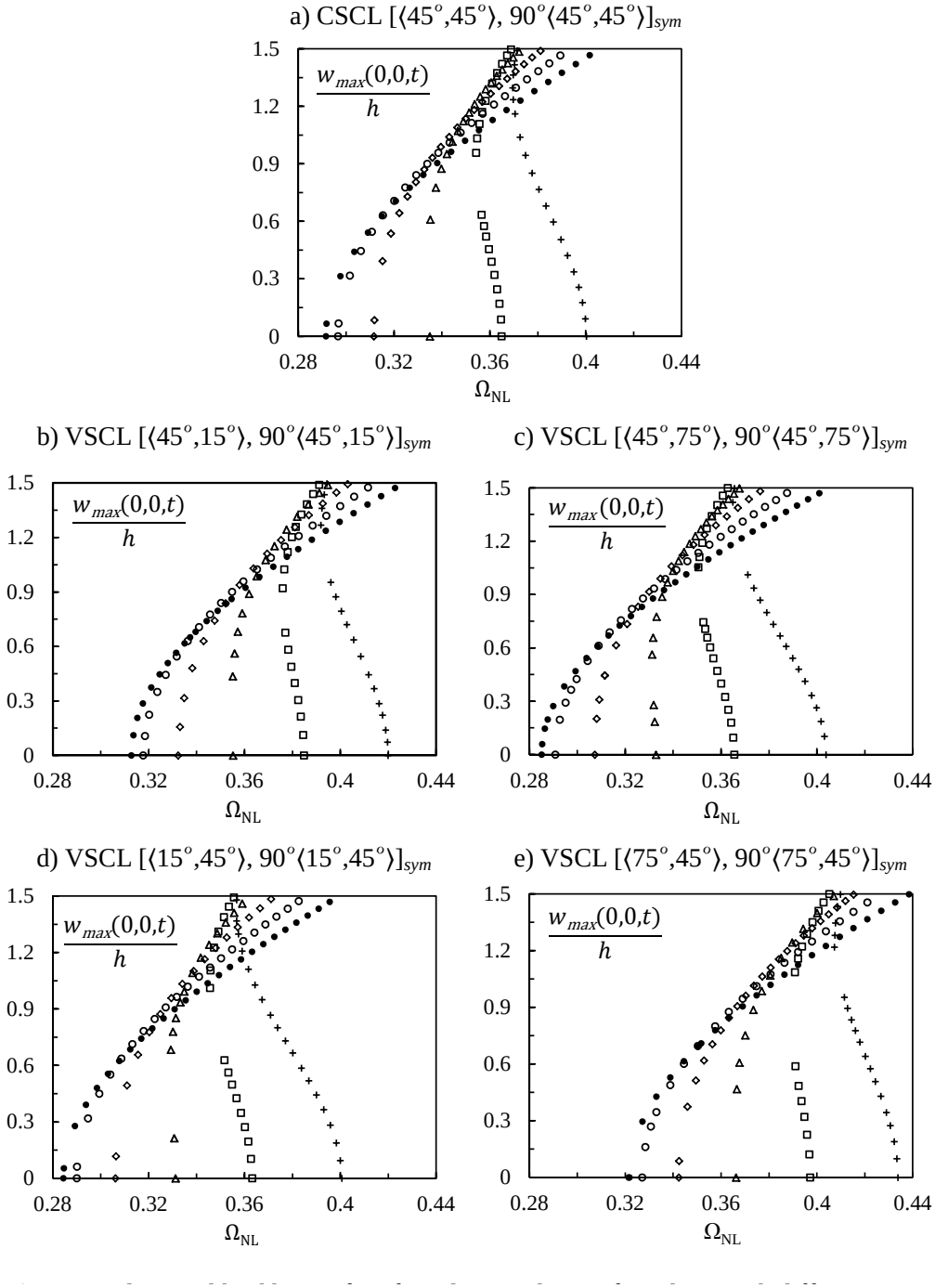

Figure 5.7: Fundamental backbone of perfect plates and imperfect plates with different imperfection magnitude, shown, in (a) for a CSCL plate, and, in (b)-(e), for various VSCL plates with different fibre angles T_0 and T_1; perfect plate: •, $h_0/h = 0.2$: ○, $h_0/h = 0.4$: ◇, $h_0/h = 0.6$: △, $h_0/h = 0.8$: □, $h_0/h = 1.0$: +.

Chapter 6

Forced Geometrically Non-linear Periodic Oscillations of VSCL Plates

6.1 Introduction

Large-amplitude forced vibration, before damage onset, of variable stiffness composite laminated plates with curvilinear fibres are studied in this chapter. As in the previous chapters, the fibre paths considered change linearly in relation to one Cartesian coordinate. The plates are rectangular and with clamped edges. The displacement field is modelled by a third order shear deformation theory and the equations of motion, in the time domain, are obtained using a *p*-version finite element method. The in-plane inertia is neglected, still taking into consideration the in-plane displacements, and the model is statically condensed [124]. The condensed model is transformed to modal coordinates [125] in order to have a reduced model with a smaller number of degrees-of-freedom. A shooting method [126, 127, 138, 139, 141, 142] using fifth-order Runge-Kutta method [138], as well as adaptive stepsize control, is used to find periodic solutions of the equations of motion. Frequency-response curves [51] of composite laminates with different curvilinear fibre angles and various thicknesses are plotted and compared. Tsai-Wu criterion is employed in order to predict the damage onset [105–107, 143]. When it is detected that damaged started, the continuation method is interrupted and no further points of the response curve are computed. The reason behind this interruption is that the model does not include the effects of damage. Examples of bifurcations are presented and studied in detail, using projections of trajectories in a phase plane and Fourier spectra [144–147]. The time histories and frequency spectra of steady-state stresses are plotted for VSCL plates with different fibre angles. The steady-state stresses are also displayed for bifurcated branches of the solutions.

6.1.1 Literature Review

Behaviours of VSCL panels on forced and free vibrations are studied respectively in Ref. [63, 148] and Ref. [44]. In papers [44, 63, 148] diverse *p*-version finite elements with hierarchical basis functions are used; Ref. [63] includes studies about transient and periodic forced vibration of

VSCL plates with curvilinear fibres using Newmark method. In Ref. [44], the harmonic balance method is applied to study the periodic free vibration of such panels. We note that Newmark method based procedures, as the one employed in Ref. [63] or Chapter 3, do not allow to recognise bifurcations and instabilities in forced oscillations.

Ref. [148] presented a non-linear model for VSCL cylindrical shallow shells; the simulation was performed using the harmonic balance method and via a procedure in the complex domain, with which one can employ as many harmonics as one wishes. The resulting algebraic equation was solved by an arc-length continuation method. The authors in this reference employed a large number of harmonics in their numerical tests; as well as static condensation. They did not reduced the DOF by modal analysis, so the complete statically condensed model was solved. Their study showed non-linear frequency response curves and phase plane plots of shells with different fibre orientations, demonstrating that the variation of the fibre orientation leads to significant changes on the response of the shell. They introduced different alterations between hardening and softening behaviour, the vibration shape, and the relative importance of the harmonics of the responses. They also demonstrated that depending on fibre path adopted, more or less parts of the shells can vibrate in phase opposition [148].

Unlike CSCL, VSCL plates have local strengths that vary along the plate; tailoring the fibre orientations to improve damage and failure properties of composites is one of the goals of using VSCL plates [10, 76, 78, 82, 109, 149]. Ref. [78] studied postbuckling first-ply failure response and onset of delamination to estimate interlaminar stresses in VSCLs. Initiation of delamination is addressed in [113] by studying the response to impacts and the compression after impact. An example of design tailoring problem (the pressure pillowing of a fuselage VSCL panel) is given in [109] with the goal of maximizing the load carrying capacity. The analyses of Refs. [78, 109, 113] were carried out using the commercial finite element software Abaqus. An optimisation approach is employed in [114] to optimise the strength around a circular hole, with Tsai-Wu failure criterion, in a VSCL plate. References [75, 115] investigated in-plane and buckling responses of VSCL plates and considered that, because the laminates were thin, the in-plane failure strains would be an order of magnitude larger than the buckling strains. Consequently, considerations for the in-plane strength failure were avoided. In studies on the vibration of laminates, failure analyses is more often than not neglected; (an exception is Ref. [150], where it is arrived at the conclusion that in a moderately thick plate, the material usually fails before the maximum deflection reaches the magnitude of the thickness). The author believes that, especially when a moderately thick laminate is considered, it is interesting to investigate if failure appeared due to the vibrations. Most of the works shown in this chapter are already published in Ref. [151].

6.2 Modelling of Forced Vibration of VSCL Plates

First, a rectangular plate is modelled by a *p*-version finite element in the time domain considering large deflections, using the so called von Kármán strain-displacement relations; the corresponding theoretical model is designated as the full model. Then a technique named static condensa-

tion [124] is applied to decrease the number of degrees of freedom (statically condensed model). The condensed model is converted to a reduced model using the modal summation method [125] (reduced model).

6.2.1 Full Model of VSCL Plates

Taking the full model as described in Chapter 5 as well as putting a proportional damping matrix, as for example, is found in Equation (4.1), and the external force vector in the formulation, we will have the equations of motion in the matrix form of (here terms related to imperfection are excluded)

$$\begin{bmatrix} \mathbf{M}^{11} & \mathbf{0} & \mathbf{0} & \mathbf{0} & \mathbf{0} \\ & \mathbf{M}^{22} & \mathbf{0} & \mathbf{0} & \mathbf{0} \\ & & \mathbf{M}^{33} & \mathbf{M}^{34} & \mathbf{M}^{35} \\ & & & \mathbf{M}^{44} & \mathbf{0} \\ sym & & & & \mathbf{M}^{55} \end{bmatrix} \begin{Bmatrix} \ddot{\mathbf{q}}_{\mathbf{u}} \\ \ddot{\mathbf{q}}_{\mathbf{v}} \\ \ddot{\mathbf{q}}_{\mathbf{w}} \\ \ddot{\mathbf{q}}_{\boldsymbol{\phi}_{\mathbf{x}}} \\ \ddot{\mathbf{q}}_{\boldsymbol{\phi}_{\mathbf{y}}} \end{Bmatrix} + \begin{bmatrix} \mathbf{K}_{\mathbf{L}}^{11} & \mathbf{K}_{\mathbf{L}}^{12} & \mathbf{0} & \mathbf{0} & \mathbf{0} \\ & \mathbf{K}_{\mathbf{L}}^{22} & \mathbf{0} & \mathbf{0} & \mathbf{0} \\ & & \mathbf{K}_{\mathbf{L}}^{33} & \mathbf{K}_{\mathbf{L}}^{34} & \mathbf{K}_{\mathbf{L}}^{35} \\ & & & \mathbf{K}_{\mathbf{L}}^{44} & \mathbf{K}_{\mathbf{L}}^{45} \\ sym & & & & \mathbf{K}_{\mathbf{L}}^{55} \end{bmatrix} \times$$

$$\left(\alpha \times \begin{Bmatrix} \dot{\mathbf{q}}_{\mathbf{u}} \\ \dot{\mathbf{q}}_{\mathbf{v}} \\ \dot{\mathbf{q}}_{\mathbf{w}} \\ \dot{\mathbf{q}}_{\boldsymbol{\phi}_{\mathbf{x}}} \\ \dot{\mathbf{q}}_{\boldsymbol{\phi}_{\mathbf{y}}} \end{Bmatrix} + \begin{Bmatrix} \mathbf{q}_{\mathbf{u}} \\ \mathbf{q}_{\mathbf{v}} \\ \mathbf{q}_{\mathbf{w}} \\ \mathbf{q}_{\boldsymbol{\phi}_{\mathbf{x}}} \\ \mathbf{q}_{\boldsymbol{\phi}_{\mathbf{y}}} \end{Bmatrix} \right) + \begin{bmatrix} \mathbf{0} & \mathbf{0} & \mathbf{K}_{\mathbf{NL}}^{13}(\mathbf{q}_{\mathbf{w}}) & \mathbf{0} & \mathbf{0} \\ \mathbf{0} & \mathbf{0} & \mathbf{K}_{\mathbf{NL}}^{23}(\mathbf{q}_{\mathbf{w}}) & \mathbf{0} & \mathbf{0} \\ \mathbf{K}_{\mathbf{NL}}^{31}(\mathbf{q}_{\mathbf{w}}) & \mathbf{K}_{\mathbf{NL}}^{32}(\mathbf{q}_{\mathbf{w}}) & \mathbf{K}_{\mathbf{NL}}^{33}(\mathbf{q}_{\mathbf{w}}) & \mathbf{0} & \mathbf{0} \\ \mathbf{0} & \mathbf{0} & \mathbf{0} & \mathbf{0} & \mathbf{0} \\ \mathbf{0} & \mathbf{0} & \mathbf{0} & \mathbf{0} & \mathbf{0} \end{bmatrix} \begin{Bmatrix} \mathbf{q}_{\mathbf{u}} \\ \mathbf{q}_{\mathbf{v}} \\ \mathbf{q}_{\mathbf{w}} \\ \mathbf{q}_{\boldsymbol{\phi}_{\mathbf{x}}} \\ \mathbf{q}_{\boldsymbol{\phi}_{\mathbf{y}}} \end{Bmatrix}$$

$$= \begin{Bmatrix} \mathbf{0} \\ \mathbf{0} \\ \mathbf{f}_{\mathbf{w}} \\ \mathbf{0} \\ \mathbf{0} \end{Bmatrix} \tag{6.1}$$

The set of equations of motion (6.1), regarded here as the full model, has $2 \times p_u^2 + 2 \times p_w^2 + 2 \times p_\phi^2$ degrees of freedom.

6.2.2 Statically Condensation of the Full Model

As explained in the Section 5.2.2, in a clamped plate, knowing that the in-plane inertia is very small, a technique called static condensation [124] can be applied to reduce the number of degrees of freedom in Equation (6.1). The idea comes because the in-plane accelerations are not very pronounced due to the clamped edges of the plate, the lack of in-plane external forces, and the fact that the transverse deflection is not bigger than 2 times the plate's thickness. Therefore, the in-plane inertia can be neglected, particularly if, as is the case, only periodic oscillations are of interest

[137]. Still, the in-plane displacements are retained in the equations. The process condenses the number of equations to $2\times p_w^2+2\times p_\phi^2$ degrees of freedom, but changes the bandwidth of the non-linear stiffness matrix.

Putting the in-plane inertia and damping equal to zero, one obtains the in-plane displacements by

$$\left\{\begin{array}{c}\mathbf{q_u}\\ \mathbf{q_v}\end{array}\right\}=-\left[\begin{array}{cc}\mathbf{K_L^{11}} & \mathbf{K_L^{12}}\\ \mathbf{K_L^{21}} & \mathbf{K_L^{22}}\end{array}\right]^{-1}\left[\begin{array}{c}\mathbf{K_{NL}^{13}}(\mathbf{q_w})\\ \mathbf{K_{NL}^{23}}(\mathbf{q_w})\end{array}\right]\mathbf{q_w} \tag{6.2}$$

Hence, the in-plane displacements depend quadratically on the transverse displacements. The condensed equations of motion will be

$$\left[\begin{array}{ccc}\mathbf{M^{33}} & \mathbf{M^{34}} & \mathbf{M^{35}}\\ & \mathbf{M^{44}} & \mathbf{0}\\ sym & & \mathbf{M^{55}}\end{array}\right]\left\{\begin{array}{c}\ddot{\mathbf{q}}_\mathbf{w}\\ \ddot{\mathbf{q}}_{\boldsymbol{\phi}_\mathbf{x}}\\ \ddot{\mathbf{q}}_{\boldsymbol{\phi}_\mathbf{y}}\end{array}\right\}+\left[\begin{array}{ccc}\mathbf{K_L^{33}} & \mathbf{K_L^{34}} & \mathbf{K_L^{35}}\\ & \mathbf{K_L^{44}} & \mathbf{K_L^{45}}\\ sym & & \mathbf{K_L^{55}}\end{array}\right]\left(\alpha\times\left\{\begin{array}{c}\dot{\mathbf{q}}_\mathbf{w}\\ \dot{\mathbf{q}}_{\boldsymbol{\phi}_\mathbf{x}}\\ \dot{\mathbf{q}}_{\boldsymbol{\phi}_\mathbf{y}}\end{array}\right\}+\left\{\begin{array}{c}\mathbf{q_w}\\ \mathbf{q}_{\boldsymbol{\phi}_\mathbf{x}}\\ \mathbf{q}_{\boldsymbol{\phi}_\mathbf{y}}\end{array}\right\}\right)+$$

$$\left[\begin{array}{ccc}\mathbf{K_{NLS}^{33}}(\mathbf{q_w}) & \mathbf{0} & \mathbf{0}\\ & \mathbf{0} & \mathbf{0}\\ sym & & \mathbf{0}\end{array}\right]\left\{\begin{array}{c}\mathbf{q_w}\\ \mathbf{q}_{\boldsymbol{\phi}_\mathbf{x}}\\ \mathbf{q}_{\boldsymbol{\phi}_\mathbf{y}}\end{array}\right\}=\left\{\begin{array}{c}\mathbf{f_w}\\ \mathbf{0}\\ \mathbf{0}\end{array}\right\} \tag{6.3}$$

In the equation above, the non-linear stiffness term, $\mathbf{K_{NLS}^{33}}(\mathbf{q_w})$, is defined as

$$\mathbf{K_{NLS}^{33}}(\mathbf{q_w})=\mathbf{K_{NL1}^{33}}(\mathbf{q_w})+\mathbf{K_{NL2}^{33}}(\mathbf{q_w})$$

$$\mathbf{K_{NL2}^{33}}(\mathbf{q_w})=-2\left[\begin{array}{c}\mathbf{K_{NL1}^{13}}\\ \mathbf{K_{NL1}^{23}}\end{array}\right]^T\left[\begin{array}{cc}\mathbf{K_L^{11}} & \mathbf{K_L^{12}}\\ \mathbf{K_L^{21}} & \mathbf{K_L^{22}}\end{array}\right]^{-1}\left[\begin{array}{c}\mathbf{K_{NL1}^{13}}\\ \mathbf{K_{NL1}^{23}}\end{array}\right]$$

Here, the non-linear stiffness term due to static condensation, $\mathbf{K_{NL2}^{33}}(\mathbf{q_w})$, includes quadratic terms depending on transverse coordinates.

6.2.3 Modal Summation Method

In simplified notation, Equation (6.3) can be written as

$$\mathbf{M}\ddot{\mathbf{q}}(t)+\mathbf{K_L}(\alpha\dot{\mathbf{q}}(t)+\mathbf{q}(t))+\mathbf{K_{NL}}(\mathbf{q}(t))\,\mathbf{q}(t)=\mathbf{f_w}(t). \tag{6.4}$$

Using the *Modal Summation Method* (already given in Section 5.2.3) and the simplified equation above, we will have

$$\overline{\mathbf{M}}\ddot{\mathbf{q}}_\mathbf{m}(t)+\overline{\mathbf{K}}_\mathbf{L}(\alpha\dot{\mathbf{q}}_\mathbf{m}(t)+\mathbf{q_m}(t))+\overline{\mathbf{K}}_\mathbf{NL}(\mathbf{q_m}(t))\,\mathbf{q_m}(t)=\bar{\mathbf{f}}(t) \tag{6.5}$$

where $\bar{\mathbf{f}}(t)=\boldsymbol{\Phi}^T\mathbf{f_w}(t)$.

6.2.4 Periodic Forced Vibration Solutions by the Shooting Method

The forced periodic vibration problem associated with Equation (6.5) is a two-point boundary value problem [138]. To apply the procedure here suggested, first, the second-order differential Equation (6.5) is rewritten, using $\dot{\mathbf{q}}_{\mathbf{m}}(t) = \mathbf{y}(t)$, as a set of $2m$ first-order differential equations

$$\begin{bmatrix} \mathbf{0} & \overline{\mathbf{M}} \\ \overline{\mathbf{M}} & \alpha\overline{\mathbf{K}}_{\mathbf{L}} \end{bmatrix} \begin{Bmatrix} \dot{\mathbf{y}}(t) \\ \dot{\mathbf{q}}_{\mathbf{m}}(t) \end{Bmatrix} + \begin{bmatrix} -\overline{\mathbf{M}} & \mathbf{0} \\ \mathbf{0} & \overline{\mathbf{K}}_{\mathbf{L}} + \overline{\mathbf{K}}_{\mathbf{NL}}(\mathbf{q}_{\mathbf{m}}(t)) \end{bmatrix} \begin{Bmatrix} \mathbf{y}(t) \\ \mathbf{q}_{\mathbf{m}}(t) \end{Bmatrix} = \begin{Bmatrix} \mathbf{0} \\ \bar{\mathbf{f}}(t) \end{Bmatrix} \tag{6.6}$$

The system of equations (6.6) is non-autonomous. The two boundaries of the above equation respect the periodicity condition

$$\begin{Bmatrix} \mathbf{y}(0) \\ \mathbf{q}_{\mathbf{m}}(0) \end{Bmatrix} = \begin{Bmatrix} \mathbf{y}(T) \\ \mathbf{q}_{\mathbf{m}}(T) \end{Bmatrix} \tag{6.7}$$

with T as the period of the response. Taking the phase-space vector $\mathbf{X}\left(\begin{Bmatrix} \mathbf{y}(0) \\ \mathbf{q}_{\mathbf{m}}(0) \end{Bmatrix}, t\right) = \begin{Bmatrix} \mathbf{y}(t) \\ \mathbf{q}_{\mathbf{m}}(t) \end{Bmatrix}$, an initial value problem is obtained from the boundary value problem of Equations (6.6) and (6.7)

$$\dot{\mathbf{X}} = \begin{bmatrix} \mathbf{0} & \overline{\mathbf{M}} \\ \overline{\mathbf{M}} & \alpha\overline{\mathbf{K}}_{\mathbf{L}} \end{bmatrix}^{-1} \left(\begin{Bmatrix} \mathbf{0} \\ \bar{\mathbf{f}}(t) \end{Bmatrix} - \begin{bmatrix} -\overline{\mathbf{M}} & \mathbf{0} \\ \mathbf{0} & \overline{\mathbf{K}}_{\mathbf{L}} + \overline{\mathbf{K}}_{\mathbf{NL}}(\mathbf{q}_{\mathbf{m}}(t)) \end{bmatrix} \mathbf{X} \right),$$

$$\mathbf{X}\left(\begin{Bmatrix} \mathbf{y}(0) \\ \mathbf{q}_{\mathbf{m}}(0) \end{Bmatrix}, 0\right) = \begin{Bmatrix} \mathbf{y}(0) \\ \mathbf{q}_{\mathbf{m}}(0) \end{Bmatrix} \tag{6.8}$$

The boundary value problem is solved when $\mathbf{X}\left(\begin{Bmatrix} \mathbf{y}(0) \\ \mathbf{q}_{\mathbf{m}}(0) \end{Bmatrix}, T\right)$ is equal to $\mathbf{X}\left(\begin{Bmatrix} \mathbf{y}(0) \\ \mathbf{q}_{\mathbf{m}}(0) \end{Bmatrix}, 0\right)$.

The initial conditions $\begin{Bmatrix} \mathbf{y}(0) \\ \mathbf{q}_{\mathbf{m}}(0) \end{Bmatrix}$ for the first two points of the frequency response curve are taken as the linear solutions of Equation (6.6). Taking as generalised load a sinusoidal one, $\mathbf{f}_{\mathbf{w}}(t) = \mathbf{p}\sin(\omega t)$, with ω the excitation frequency, and generalised displacements as $\mathbf{q}_{\mathbf{m}}(t) = \mathbf{q}_{\mathbf{c}}\cos(\omega t) + \mathbf{q}_{\mathbf{s}}\sin(\omega t)$, the first and second initial values are

$$\begin{Bmatrix} \mathbf{y}(0) \\ \mathbf{q}_{\mathbf{m}}(0) \end{Bmatrix} = \begin{Bmatrix} \omega\mathbf{q}_{\mathbf{s}} \\ \mathbf{q}_{\mathbf{c}} \end{Bmatrix}$$

For the following points of the frequency response curve, a secant predictor is used [66]. Then the set of $2m$ ordinary equations are integrated by the initial value method, fifth-order Runge-Kutta using adaptive stepsize control [138], arriving at the other boundary $\mathbf{X}\left(\begin{Bmatrix} \mathbf{y}(0) \\ \mathbf{q}_{\mathbf{m}}(0) \end{Bmatrix}, T\right)$. The purpose of this adaptive stepsize control is to achieve some prefixed accuracy in the solution with

the minimum computational effort. To achieve the periodicity conditions, the initial values are corrected until convergence by

$$\mathbf{X}\left(\left\{\begin{array}{c}\mathbf{y}(0)\\ \mathbf{q_m}(0)\end{array}\right\},0\right)^{i+1}=\mathbf{X}\left(\left\{\begin{array}{c}\mathbf{y}(0)\\ \mathbf{q_m}(0)\end{array}\right\},0\right)^{i}+\delta\mathbf{X} \tag{6.9}$$

The correction $\delta\mathbf{X}$ solves the system of equations

$$\left[\frac{\partial\mathbf{X}\left(\left\{\begin{array}{c}\mathbf{y}(0)\\ \mathbf{q_m}(0)\end{array}\right\},T\right)}{\partial\left\{\begin{array}{c}\mathbf{y}(t)\\ \mathbf{q_m}(t)\end{array}\right\}}-[I]\right]\delta\mathbf{X}=\mathbf{X}\left(\left\{\begin{array}{c}\mathbf{y}(0)\\ \mathbf{q_m}(0)\end{array}\right\},0\right)-\mathbf{X}\left(\left\{\begin{array}{c}\mathbf{y}(0)\\ \mathbf{q_m}(0)\end{array}\right\},T\right). \tag{6.10}$$

To see more details on correcting the first guess using Newton's algorithm, as well as on the use of the monodromy matrix to investigate the stability of the solutions, one can refer to Refs. [126,127,139] and references therein. The following initial values of the forced response are here found using a secant predictor, given for example in Refs. [127,139]. The monodromy matrix is equal to $\dfrac{\partial\mathbf{X}\left(\left\{\begin{array}{c}\mathbf{y}(0)\\ \mathbf{q_m}(0)\end{array}\right\},T\right)}{\partial\left\{\begin{array}{c}\mathbf{y}(t)\\ \mathbf{q_m}(t)\end{array}\right\}}$. Using Floquet multipliers, as the eigenvalues of monodromy matrix, one can find the stability of the periodic vibration. If one or more of the Floquet multipliers lie outside the unit circle, the periodic solution is unstable. If two or more Floquet multipliers are located on the unit circle, the periodic solution is non-hyperbolic periodic solution. The solution is unstable if one or more of the related Floquet multipliers lie outside the unit circle. If none of the multipliers lie outside of the unit circle, a non-linear analysis should be used to determine the stability of the non-hyperbolic periodic solution (see Ref. [126]).

6.3 Numerical Results on Forced Periodic Vibration of VSCL Plates

This section gives the properties of the plates that are studied in the numerical tests that follow. Due to limitation of data for comparison, instead of a VSCL plate, a clamped CSCL plate with mechanical properties of Plate 1 in Table 6.1 is analysed. The laminate has three layers $[45^{\circ},-45^{\circ},45^{\circ}]$ with equal thickness. The laminate is under a uniform harmonic transverse pressure $3454.665\times\sin(\omega t)$. The same laminate was the subject of examination in references [66,152].

To analyse the influence of the fibre angle in the forced vibrations of VSCL plates, a clamped plate with mechanical properties of AS4/3501-6 carbon epoxy (Plate 2 in Table 6.1, after Ref. [106]) is used. Longitudinal tensile and compressive strengths, transverse tensile and compressive strengths and shear strength of the ply are, respectively, $X_t=2280$ MPa, $X_c=1440$ MPa,

$Y_t = 57$ MPa, $Y_c = 280$ MPa and $S = 71$ MPa (also from reference [106]). The laminate has four variable stiffness layers, with configuration $[\langle T_0, T_1\rangle, \langle 90^o + T_0, 90^o + T_1\rangle]_{sym}$ represented as $[\langle T_0, T_1\rangle, 90^o + \langle T_0, T_1\rangle]_{sym}$. The fibre angles at the centre and the edges of the first and fourth layers are respectively T_0 and T_1 degrees; on the second and third layers, they are $T_0 + 90^o$ and $T_1 + 90^o$. All layers have equal thickness. The laminate is subjected to transverse pressure, uniform in space and harmonic in time, given by $2 \times 10^4 \times \sin(\omega t)$ Nm^{-2}.

Table 6.1: Mechanical properties of the composite plates studied.

a (m)	b (m)	h (m)	E_1 (GPa)	E_2 (GPa)	G_{12} (GPa)	G_{13} (GPa)	G_{23} (GPa)	ν_{12}	ρ (kg/m^3)
Plate 1 (CSCL)									
0.3048	0.3048	0.003048	206.84	5.171	2.5855	2.5855	2.5855	0.25	2564.856
Plate 2 (VSCL)									
0.5	0.5	0.01	142	10.3	7.2	7.2	7.2	0.27	1580

In this analysis, the full model has equal numbers of in-plane, transverse and rotational shape functions. It was already found in other studies (e.g. in Refs. [66, 132] that retaining more in-plane than out-of-plane generalised coordinates facilitates the convergence of solutions when the vibration amplitude is large, i.e, when membrane effects become more important. On the other hand, retaining more transverse and rotational components is first of all important to achieve convergence in the linear regime and in the non-linear regime in the presence of internal resonances. We decided to use the same number of shape functions for all components in order to turn the convergence analysis more concise and systematic, avoiding a large number of studies, individually related to the diverse displacement components.

6.3.1 Verification and Convergence with the Number of Normal Modes in the Reduced Model

To verify the modal model (with static condensation and modal coordinates - but including all normal modes in modal matrix $\mathbf{\Phi}$), it was compared with the full model without static condensation and in the generalised displacements $\mathbf{q}$; in the former case, the shooting method was applied, but in the latter the Newmark method was used (for details on the Newmark method refer to [62] or Section 3.2.1; the Newmark code applied here was validated in Chapter 3). Because of the need to employ damping in the Newmark method, in order to dissipate transients and find the steady-state solution, we used a very small damping factor. The test plate here was the CSCL plate previously introduced. For the sake of easiness, two hierarchical shape functions were taken for each variable (that is $p_u = p_w = p_\phi = 2$). The full model (i.e. 20 DOF) of Equation (6.1) was solved by the Newmark method. Equation (6.5) - as written with static condensation and in modal coordinates, but including all linear normal modes (i.e. 12 DOF) - was solved by the shooting method presented in this chapter. The results of both methods (not shown) were in very good agreement. This supports the earlier claim, according to which considering membrane inertia is

not really necessary in the problem under study. Furthermore, this agreement showed that the transformation into modal coordinates and the shooting procedure were well implemented.

In another analysis, the full model, Equation (6.1), solved via the Newmark method, is used as a benchmark for the reduced order model, solved by the shooting method. Three hierarchical shape functions in each direction are used for each variable ($p_u = p_w = p_\phi = 3$). Therefore, the full model has 45 DOF; in the reduced order model, different numbers of normal modes are considered: 10, 15, and 24 modes (Table 6.2). A damping parameter α equal to 10^{-5} is adopted in the Newmark method, again in order to dissipate transients. It is shown that taking 10 normal modes and applying the shooting method, gives results very similar to the ones of the full model, solved by the Newmark method. By further increasing the number of modes, almost total agreement is achieved.

Table 6.2: Convergence of the results of the present reduced order model with the number of normal modes.

	ω/ω_l			
	Full model Equation (6.1) 45 DOF	Reduced model Equation (6.5) 10 DOF	Reduced model Equation (6.5) 15 DOF	Reduced model Equation (6.5) 24 DOF
w_{max}/h	Newmark method	shooting method	shooting method	shooting method
0.2	0.783	0.783	0.783	0.783
-0.2	1.192	1.193	1.193	1.193
0.6	1.011	1.011	1.011	1.011
1.0	1.164	1.166	1.164	1.164

Proceeding with the verification of the procedures implemented in this work, the displacement amplitudes due to harmonic forces, uniformly distributed, are computed with the present TSDT model (with $p_u = p_w = p_\phi = 7$) and are compared with published data, which was obtained applying classical plate theory. In Ref. [66] a p-version FEM with hierarchical basis functions and the harmonic balance method (HBM) were used, with $p_u = 6$ and $p_w = 4$, then the model was statically condensed to 16 DOF. Ref. [152] used an h-version type FEM with 36 elements. The plate studied is the CSCL plate introduced above. All results in Table 6.3 are for an undamped plate, except the ones computed by Newmark method, where a small damping is introduced, for the reason explained above. The fundamental linear natural frequencies of vibration, ω_l, are also given. The different values obtained for ω_l reflect the different theories and degrees of discretization employed. In the non-linear regime, the difference between the vibration amplitudes/excitation frequencies of references [66, 152] and the ones of present full model, computed using Newmark method, is below 1.2%. Again, given the diverse theories and degrees of discretization employed, this is a quite reasonable agreement. Results by shooting method with 10 linear normal modes differ at most 2.3% from the ones computed by the full model (Newmark method, 245 DOF). Given the computational cost that ensues from using more modes in the shooting method, and the very close agreement already achieved in Table 6.3, more modes are not used in the rest of this chapter.

Table 6.3: Comparison of excitation frequencies against vibration amplitudes by different methods.

CPT [66] 16 DOF			FEM CPT [152]	Newmark 245 DOF	Equation (6.5) by shooting method 10 DOF	15 DOF	20 DOF	24 DOF
w_{max}/h	ω/ω_l	w_{max}/h	ω/ω_l	ω/ω_l	ω/ω_l			
0.2016	0.734	0.2	0.7219	0.730	0.730	0.718	0.718	0.718
-0.1971	1.2466	-0.2	1.2333	1.248	1.249	1.240	1.240	1.240
0.5997	1.0085	0.6	1.0085	1.012	1.018	1.018	1.018	1.018
1.0005	1.1756	1.0	1.1787	1.187	1.215	1.216	1.214	1.214
ω_l (rad/s)	1580.36		1592.3	1562.43	1562.43			

6.3.2 Effects of Fibre Angle at the Centre on the Forced Vibration of VSCL Plates

To investigate the effect of fibre angles at the centre of the plate on the forced vibration of variable stiffness plate with configuration $[\langle T_0, T_1\rangle, \langle 90^o + T_0, 90^o + T_1\rangle]_{sym}$, the angle T_0 changes from 0^o to 90^o by intervals of 15^o, while angle T_1 is constant, equal to 45^o. The maximum deflection amplitude (w_{max}/h) at the centre of the plate against non-dimensional excitation frequency $\Omega_{NL} = \omega a\sqrt{\rho/E_2}$) is depicted in Figure 6.1(a). To calculate this data, the full model with seven shape functions ($p_u = p_w = p_\phi = 7$), i.e. 245 DOF, is obtained first, then (generally) the first ten normal modes are used in the reduced model of the VSCL plate.

To determine the stability of the periodic solutions, the Floquet multipliers were computed, by calculating the eigenvalues of the monodromy matrix [126]. Only linear terms in the disturbance were kept in the stability analysis, so when some of the Floquet multipliers are on the unit circle, and none is outside, we know that the solution is non-hyperbolic, but not necessarily stable [126]. Solutions of this type are prone to appear in an undamped analysis; they will be simply designated as "non-hyperbolic". When one, or more, Floquet multipliers are outside the unit circle, the solution is beyond doubt unstable, even if it is non-hyperbolic; these solutions will be designated as "unstable". Non-hyperbolic (with stability status not determined) and unstable solutions of vibration are shown in hollow and solid circles, respectively.

During calculation of the forced vibrations, the damage index is controlled in the plate and the analysis is stopped when the start of damage is detected. So, the curves end when damage starts (wherein the maximum deflection ratio is roughly between 0.6 and 1). In VSCL $[\langle T_0, 45^o\rangle, 90^o + \langle T_0, 45^o\rangle]_{sym}$ plates, two different scenarios happen, one when increasing the fibre angle at the centre of the plate, T_0, from 0^o to 30^o, the other when increasing from 30^o to 90^o. In the first scenario, the increase of T_0 from 0^o to 30^o barely affects the relations between frequency and deflection amplitudes, but causes damage onset to appear earlier. Actually, among all VSCL plates of the form $[\langle T_0, 45^o\rangle, 90^o + \langle T_0, 45^o\rangle]_{sym}$, the one with $T_0 = 30^o$ experiences damage first, when $w_{max}/h \approx 0.64$. The position of damage onset is at the bottom surface, at coordinates $(x/a, y/b) = (1, 0.35)$. This is a consequence of stress distribution by the curvilinear fibres in VSCL plates, already found in Chapter 3 and Refs. [110, 111]. In the second scenario, when the fibre angle T_0 is increased from 30^o to 90^o, the frequency response curves of the VSCL plates are

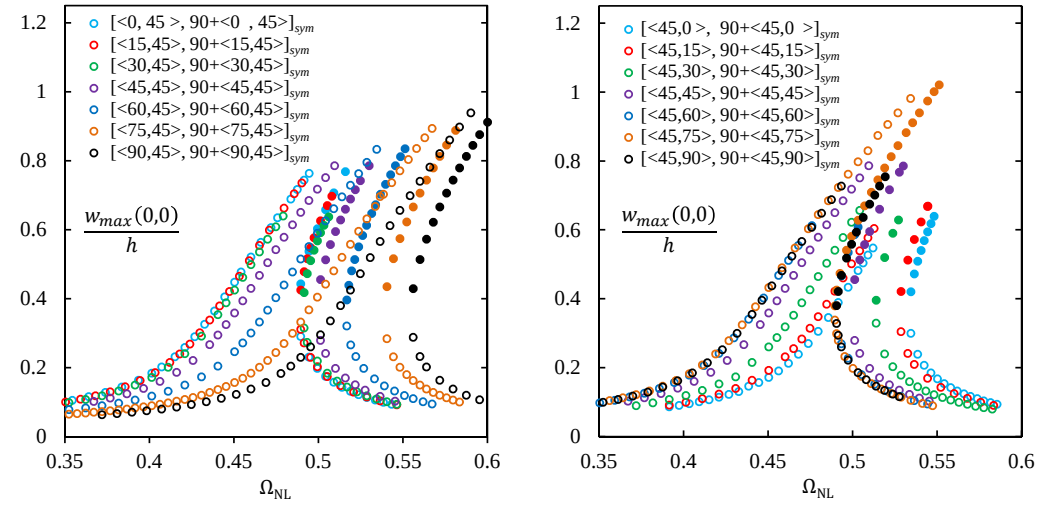

Figure 6.1: Frequency response curves, showing deflection (w_{max}/h) against non-dimensional excitation frequency, for VSCL $[\langle T_0, T_1\rangle, \langle 90^o + T_0, 90^o + T_1\rangle]_{sym}$ plates when changing fibre angle at the centre of the plate, T_0, shown at (a) and when changing fibre angle at the edges of the plate, T_1, shown at (b). Hollow and solid circles show non-hyperbolic and unstable vibrations, respectively.

shifted to the right, because the natural frequencies increase, and hardening becomes stronger. So, to achieve similar deflection with the same force amplitude, the plate should be excited at higher frequency. Interestingly, the damage onset occurs later, when the plates undergo larger deflection, being plate with $T_0 = 90^o$ the one that can experience larger vibration amplitudes, achieving $w_{max}/h \approx 0.94$. In the last case, the damage position is at the bottom surface, at coordinates $(x/a, y/b) = (1, 0.25)$. It is obvious that the use of curvilinear fibres in VSCL plates experiencing periodic oscillations changes the vibration amplitude and the frequency at which damage onset occurs. The precise position where damage onset appears also depends on the curvilinear fibre path in periodic oscillations, as it did in transient oscillations of VSCL [110, 111]. However, in the examples of Figure 6.1, damage onset always occurred in one of the boundaries, very often either at the top or at the bottom surface. Of this set of plates, the constant stiffness plate is not the one where larger vibration amplitude can occur without damage onset.

6.3.3 Effects of Fibre Angle at Edges on Forced Vibration of VSCL Plates

To see how forced vibration is influenced by changes in the fibre angles at the edges of the VSCL plates, the fibre angle at the centre, T_0, is taken as 45^o, and the fibre angle at the edges of the plate, T_1, is varied from 0^o to 90^o by intervals of 15^o, see Figure 6.1(b). Again, non-hyperbolic (and with stability undetermined) and unstable solutions are shown in hollow and solid circles, respectively. Like above, but now in VSCL $[\langle 45^o, T_1\rangle, 90^o + \langle 45^o, T_1\rangle]_{sym}$ plates, two scenarios are observed: the first increasing the fibre angle at the edges, T_1, from 0^o to 60^o, and the second

scenario increasing T_1 from 60^o to 90^o. In the first scenario, increasing T_1 from 0^o to 60^o in VSCL plates, affects the forced vibration curves by shifting them to the left, while slightly reducing the hardening effect. So, similar deflection amplitudes are achieved at lower excitation frequencies in laminates with larger fibre angle T_1. We believe that, particularly when the first mode shape is important, fibre angles nearly perpendicular to the boundaries tend to increase the stiffness in comparison to other angles, because the fibres exert a stronger opposition to bending. In the second scenario, when T_1 is increased from 60^o to 90^o, the change in the fibre path has almost no effect on the relation between the deflection amplitudes and the frequency of excitation; however, it has a major effect on the amplitude at which damage onset occurs. These three are the less stiff plates, overall. In both scenarios, no distinct pattern for damage onset could be recognized. But, the change in fibre paths significantly affects the frequency and the amplitude at which damage onset occurs; the VSCL plate where damage onset appears at lower vibration amplitude is plate $[\langle 45^o, 0^o\rangle, 90^o + \langle 45^o, 0^o\rangle]_{sym}$, where damage appears at $w_{max}/h \approx 0.56$, and occurs at the bottom surface of the plate, coordinates $(x/a, y/b) = (0.3, 1)$. The CSCL is not the one that can experience larger amplitude deflections without damage starting.

6.3.4 Stresses in Forced Vibration of VSCL Plates

The study of stresses is important for damage and fatigue analysis; here, we examine the stresses in some of the plates analysed in the previous section. It was shown in Ref. [93] that the magnitude of transverse shear stresses is significantly smaller than the one of in-plane stresses, when the VSCL plate is under sinusoidal or uniform transverse loads. Consequently, transverse shear stresses are not so important for the application of Tsai-Wu criterion in this section, and only normal stresses, σ_x, σ_y, and shear stress σ_{xy} are given here. Figure 6.2 shows normal stresses along a period of vibration and its frequency spectra, σ_x, σ_y, and σ_{xy}, for the reference CSCL plate, $[\langle 45^o, 45^o\rangle, 90^o + \langle 45^o, 45^o\rangle]_{sym}$, and four VSCL plates with various configurations: $[\langle 30^o, 45^o\rangle, 90^o + \langle 30^o, 45^o\rangle]_{sym}$, $[\langle 75^o, 45^o\rangle, 90^o + \langle 75^o, 45^o\rangle]_{sym}$, $[\langle 45^o, 0^o\rangle, 90^o + \langle 45^o, 0^o\rangle]_{sym}$, and $[\langle 45^o, 75^o\rangle, 90^o + \langle 45^o, 75^o\rangle]_{sym}$. These are stresses at the centre of the plates, by way of example. The steady state stresses develop under a uniform loading with frequency 2300 rad/s ($\Omega_{NL} \approx 0.45$) (the fundamental frequency of the reference CSCL plate is 2365 rad/s) and the amplitude of the force per unit area is 2×10^4 Pa. The stresses are calculated at the top and bottom surfaces of the plate, because (when finding damage onset in the VSCLs of Figure 6.1) we saw that the onset of damage, calculated using Equation (4.2), generally occurs in one of these two surfaces. The frequency spectra of the steady state harmonic stresses are also given in this figure.

Among the plates studied, the stress in direction x is maximum in the VSCL plate $[\langle 30^o, 45^o\rangle, 90^o + \langle 30^o, 45^o\rangle]_{sym}$, while stress in direction y is maximum in the plate $[\langle 45^o, 75^o\rangle, 90^o + \langle 45^o, 75^o\rangle]_{sym}$. VSCL plate $[\langle 75^o, 45^o\rangle, 90^o + \langle 75^o, 45^o\rangle]_{sym}$ has the minimum normal stress σ_x and minimum in-plane shear stress, σ_{xy}. Stress σ_y is lowest in VSCL plate $[\langle 45^o, 0^o\rangle, 90^o + \langle 45^o, 0^o\rangle]_{sym}$; σ_x and σ_{xy} are also low in this plate. The CSCL plate is not among the plates with maximum or minimum stresses. The frequency spectra of the stresses show that, in these solutions, the first harmonic is more excited than other harmonics. Nevertheless, the second harmonic and the constant element

of the spectra are also stimulated, in some cases introducing a visible asymmetry in the variation of stresses with time. This data shows that using curvilinear fibres can significantly change the magnitude of in-plane stresses and their variation along a vibration period.

6.3.5 Examples of Bifurcation on Forced Vibration of VSCL Plates

Depending on the modes used in the calculation, the main fundamental branch (in this context, a "main branch" is understood as a branch that starts in the static solution, and contains solutions dominated by the first harmonic and by one mode of vibration; word "fundamental" indicates that, in the particular cases of this section, this mode is the first mode of vibration) may bifurcate to a branch that will be designated as "bifurcated" or "secondary" in this section; in the latter type of branch a higher harmonic is important. These bifurcations are due to internal resonances, with indirect excitation of higher modes. Two of these branches are shown in Figure 6.3. The main branches were formed with the first ten linear normal modes, except the third, fourth, and fifth, which were estimated to be less important in these branches. The secondary (bifurcated) branches include the first ten normal modes and are shown in the figure with square marks. They bifurcate from the main branch of VSCL $[\langle 45^o, 75^o\rangle, 90^o + \langle 45^o, 75^o\rangle]_{sym}$ (shown in hollow red circles) and from the main branch of VSCL $[\langle 75^o, 45^o\rangle, 90^o + \langle 75^o, 45^o\rangle]_{sym}$ (shown in hollow black circles). In Figure 6.3, the main branches of these two VSCLs start from P1 and O1 (with a small deflection), and end at P2 and O2 where damage onsets happen. In the bifurcated branches, points P3 and O3 mark the end of the curves and correspond to the onset of damage. As displayed, in the bifurcated branches damage onset happens at a relatively small deflection amplitude (at the centre of the plate, it is around 0.3 or 0.4, depending on the plate), while in the main branches the damage onset, points P2 and O2, occurs when the amplitude of deflection at the centre of the plate is reasonably large (around 0.9 or 1.0). Here, the peak amplitude is not at the centre of the plate.

In VSCL $[\langle 45^o, 75^o\rangle, 90^o + \langle 45^o, 75^o\rangle]_{sym}$, the relation between the fourth linear frequency ($\omega_{l4} = 6374$ rad/s) and the excitation frequency close to the bifurcation ($\omega = 2132$ rad/s) is $\omega_{l4}/\omega = 2.99$. The first linear natural frequency is 2310 rad/s, so $\omega_{l1}/\omega = 1.08$. Here, the first mode is important in the first harmonic and the fourth mode in the third harmonic. These two important modes are shown in Figure 6.4(a). Hence, an internal resonance of order 1:3 occurred, originating a bifurcation. For the VSCL $[\langle 75^o, 45^o\rangle, 90^o + \langle 75^o, 45^o\rangle]_{sym}$, the relations of the fifth linear frequency ($\omega_{l5} = 7601$ rad/s) and the tenth linear frequency ($\omega_{l10} = 12723$ rad/s) to the excitation frequency close to the bifurcation ($\omega = 2555$ rad/s) are, respectively, $\omega_{l5}/\omega = 2.97$ and $\omega_{l10}/\omega = 4.98$. The first natural frequency is 2576 rad/s, hence $\omega_{l1}/\omega = 1.01$.The first mode is important in the first harmonic and the fifth mode in the third harmonic; the tenth mode appears in connection with the fifth harmonic, but with less influence than the former modes. The significant modes are depicted in Figure 6.4(b).

To better understand the vibrational behaviour of the VSCL plates, Figure 6.5 displays the non-dimensional displacements along a period of vibration, as well as phase plane plots and frequency spectra for the two VSCL plates studied in Figure 6.3. The displacements and the velocities are computed at the centre of the plates. At first, we study VSCL $[\langle 45^o, 75^o\rangle, 90^o + \langle 45^o, 75^o\rangle]_{sym}$.

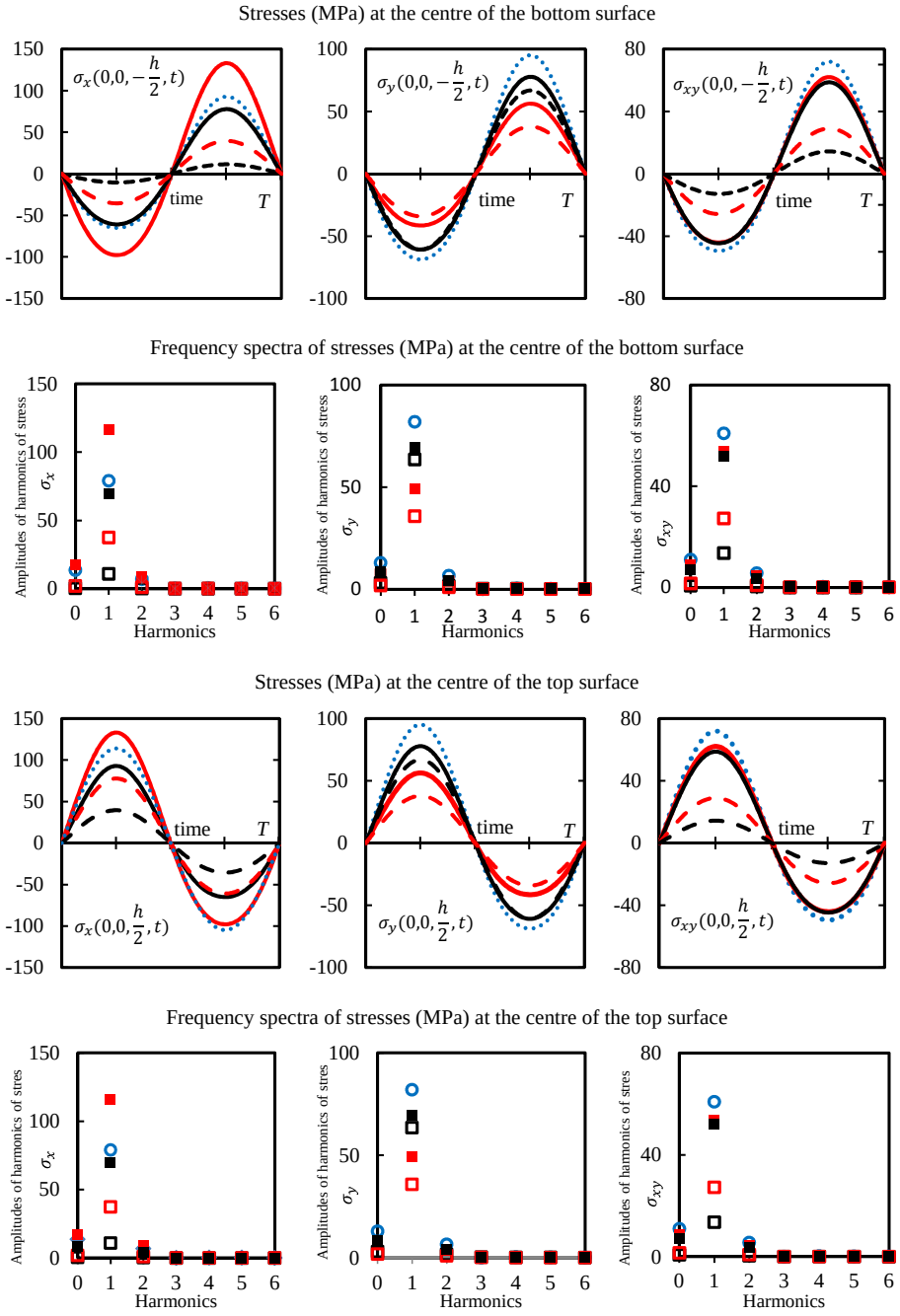

Figure 6.2: Steady state normal stress histories and their frequency spectra for various VSCL plates $[\langle 30^o,45^o\rangle,90^o+\langle 30^o,45^o\rangle]_{sym}$: ——— and ■; $[\langle 75^o,45^o\rangle,\ 90^o+\langle 75^o,45^o\rangle]_{sym}$: - - - and □; $[\langle 45^o,0^o\rangle,90^o+\langle 45^o,0^o\rangle]_{sym}$: - - - and □; $[\langle 45^o,75^o\rangle,90^o+\langle 45^o,75^o\rangle]_{sym}$: - - - and ○; reference CSCL plate $[\langle 45^o,45^o\rangle,90^o+\langle 45^o,45^o\rangle]_{sym}$: ——— and ■

Increasing the frequency (that consequently here increases the amplitude of deflection) leads to damage onset in points P2 and P3, at the main and the secondary branch, respectively. Looking to the frequency spectrum on the point of damage onset on the main branch (P2), one sees that essentially the first harmonic is excited. On the other hand, as written in the previous paragraph, in the secondary branch (P3) the first and third harmonics are excited. The differences between the time histories and between the phase plane plots at these two onset points are obvious from Figure 6.5(a) and (c). A somewhat similar pattern occurs in VSCL $[\langle 75^{\circ}, 45^{\circ}\rangle, 90^{\circ} + \langle 75^{\circ}, 45^{\circ}\rangle]_{sym}$, as can be observed in Figure 6.5(b) and (d). At the points of damage onset, O2 and O3, in the main and secondary branch, respectively, the first harmonic is excited in the main branch while the first, third and fifth harmonics are stimulated in the secondary branch.

The shapes of plates in situations P2, P3, O2, and O3 are shown in Figure 6.6. The shape of the plates when damage starts, at points P2 and O2, shows that mainly the first mode is excited. In contrast, when damage starts in the bifurcated branches, i.e. at points P3 and O3, higher modes are present. In point P3, the shape of the plate displays mainly domination of a higher mode (fourth mode), while in point O3, the plate is affected by the fifth and tenth mode.

6.3.6 Stresses in Main and Bifurcation Branches of Frequency Response Curves

Figure 6.7 shows times histories of normal stresses along a period of vibration in points P1, P2 and P3 and the respective frequency spectra. The stresses were computed in the centre of the top surface - i.e., at point $(0,0,h/2)$ - and at the centre of the bottom surface - i.e., at point $(0,0,-h/2)$ - of VSCL plate $[\langle 45^{\circ}, 75^{\circ}\rangle, 90^{\circ} + \langle 45^{\circ}, 75^{\circ}\rangle]_{sym}$. Only normal stresses σ_x and σ_y, and shear stress σ_{xy} are given, for the reasons specified above. At point P1, where the deflection amplitude is small, $w_{max}/h \approx 0.15$, the positive and negative amplitudes of the two in-plane normal stress, σ_x, σ_y, and of the in-plane shear stress, σ_{xy}, are similar; furthermore, the spectra show that only the first harmonic is excited. At point P2, where onset of damage occurs at the end of the main branch, $w_{max}/h \approx 1$, the maximum compressive and tensile stresses are not similar, both in σ_x and σ_y, and neither are the absolute values of the maximum and minimum in-plane shear stress; the second harmonic and the constant term are added to the first harmonic in the frequency spectra. All the former characteristics are due to the non-linear effects. At the onset of damage in the bifurcated branch (secondary branch), point P3, only the first and third harmonics are excited, without the constant term, here $w_{max}/h \approx 0.35$. This figure shows that higher harmonics occur in the spectra of stresses, when the amplitude of deflection increases or where bifurcations happen. The appearance of higher harmonics in stresses may be relevant for fatigue life studies (see for example [153]), because the number of cycles increases.

6.3.7 Direct Excitation of Higher Modes in VSCL Plates

We saw that higher order modes appear in branches that were defined by following bifurcations of the main branch of the response curve. Damage onset was detected at lower amplitudes in these

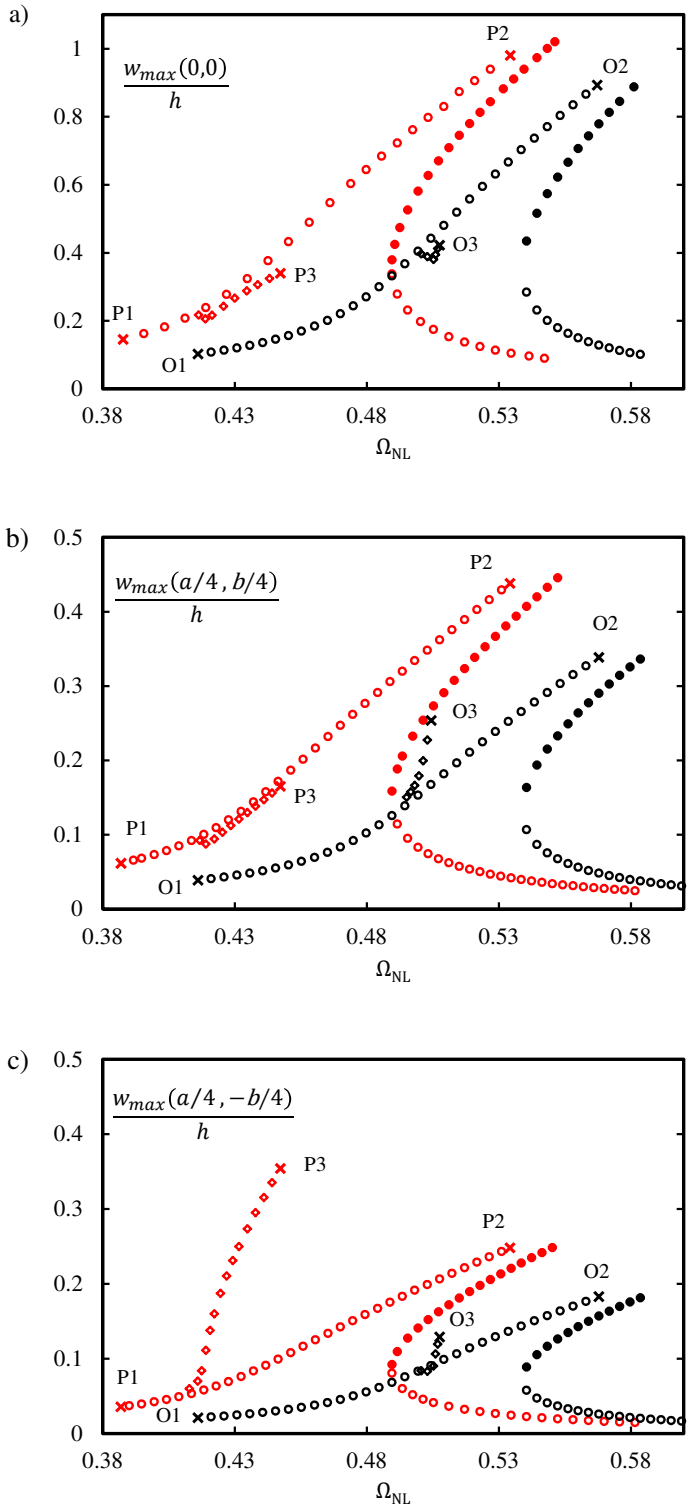

Figure 6.3: Bifurcations to other branches from the main branch, VSCL $[\langle 45^o, 75^o\rangle, 90^o + \langle 45^o, 75^o\rangle]_{sym}$, shown by ○, and VSCL $[\langle 75^o, 45^o\rangle, 90^o + \langle 75^o, 45^o\rangle]_{sym}$, shown by ○. Results are shown for three points $(x, y) = (0,0), (a/2, b/2), (a/2, -b/2)$. The solutions resulting from bifurcations are shown by ◇ and ◇, respectively. Non-hyperbolic results are represented by hollow symbols (○, ○, ◇, ◇), while unstable results are shown by solid circles (●, ●).

a) VSCL [<45°,75°>, 90°+<45°,75°>]$_{sym}$

Mode 1 (ω_{l1} =2310 rad/s) Mode 4 (ω_{l4} =6374 rad/s)

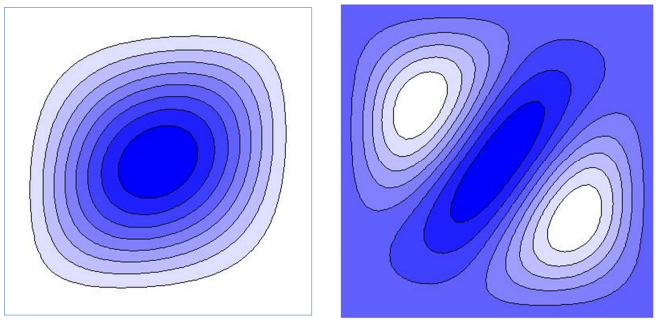

b) VSCL [<75°,45°>, 90°+<75°,45°>]$_{sym}$

Mode 1 (ω_{l1} =2576 rad/s) Mode 5 (ω_{l5} =7601 rad/s) Mode 10 (ω_{l10} =12723 rad/s)

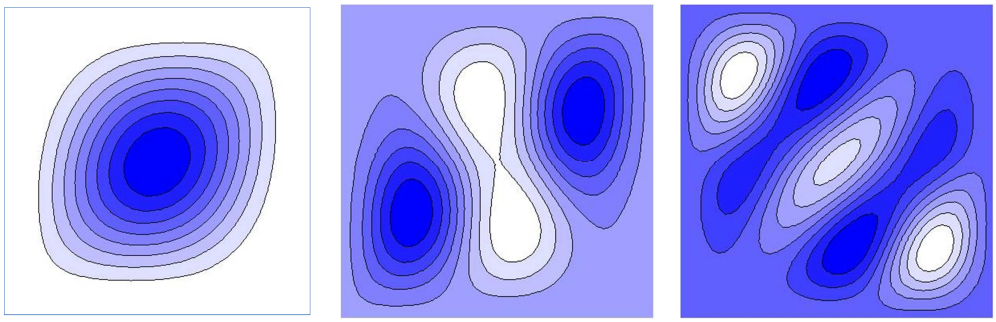

Figure 6.4: Significant modes in the secondary branches separated from the main branch of (a) VSCL $[\langle 45^o, 75^o\rangle, 90^o + \langle 45^o, 75^o\rangle]_{sym}$ and (b) VSCL $[\langle 75^o, 45^o\rangle, 90^o + \langle 75^o, 45^o\rangle]_{sym}$.

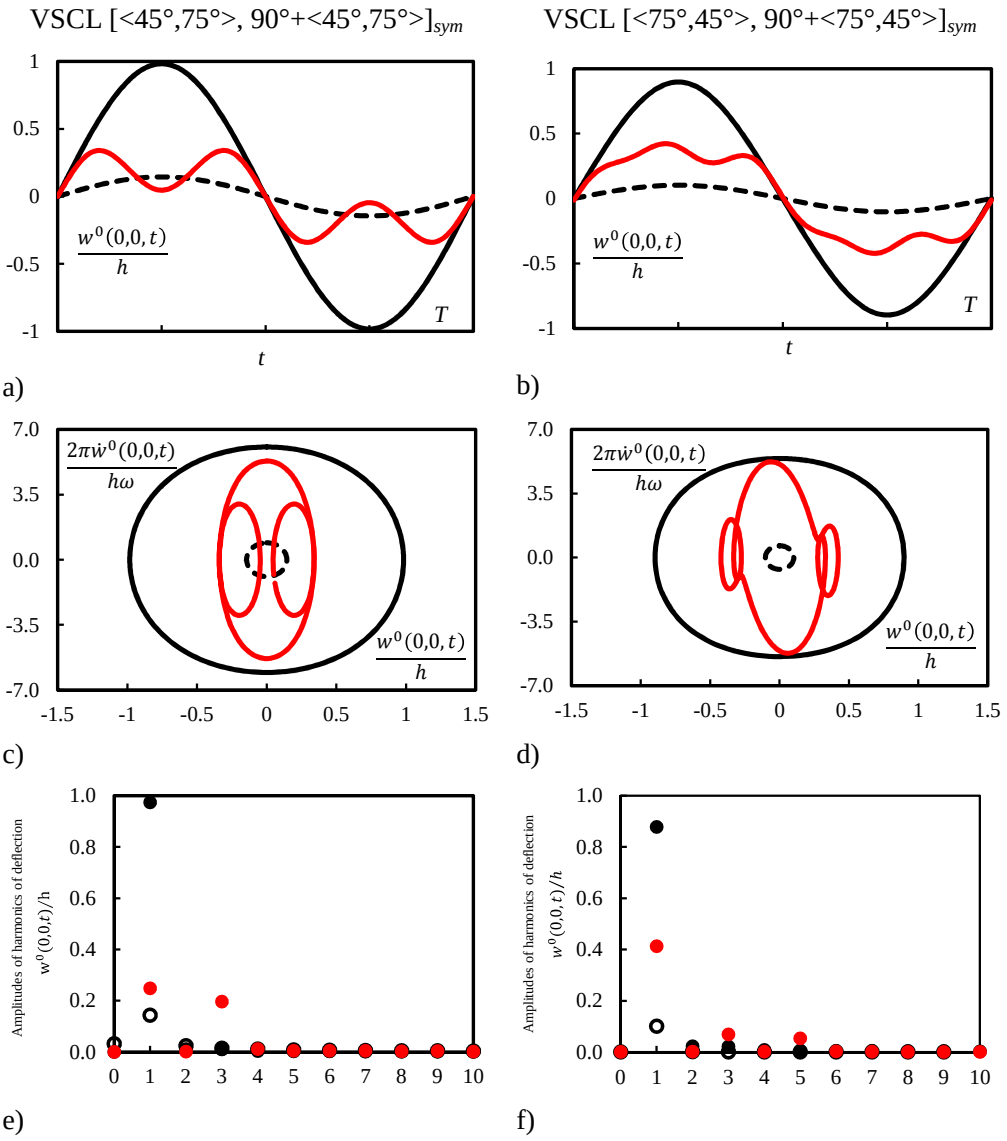

Figure 6.5: (a) and (b): Time histories along a period of vibration; (c) and (d): phase plane plots; (e) and (f): frequency spectra for forced vibration of VSCL $[\langle 45^o, 75^o\rangle, 90^o + \langle 45^o, 75^o\rangle]_{sym}$ (shown in (a), (c) and (e)) and of VSCL $[\langle 75^o, 45^o\rangle, 90^o + \langle 75^o, 45^o\rangle]_{sym}$ (shown in (b), (d), and (f)). The analyses are carried out at points P1 and O1 of Figure 6.3: black dashed line - - - and hollow circle ○; P2 and O2: black solid line ——— and filled circle ●; P3 and O3: red solid line ——— and filled circle ●. In VSCL $[\langle 45^o, 75^o\rangle, 90^o + \langle 45^o, 75^o\rangle]_{sym}$: P1 is from the main branch with $\Omega_{NL} = 0.388$; P2 with $\Omega_{NL} = 0.534$; P3 with $\Omega_{NL} = 0.447$. In VSCL $[\langle 75^o, 45^o\rangle, 90^o + \langle 75^o, 45^o\rangle]_{sym}$: O1 is from the main branch with $\Omega_{NL} = 0.416$; O2 with $\Omega_{NL} = 0.567$; O3 with $\Omega_{NL} = 0.508$.

a) VSCL [<45°,75°>, 90°+<45°,75°>]$_{sym}$: Point P2

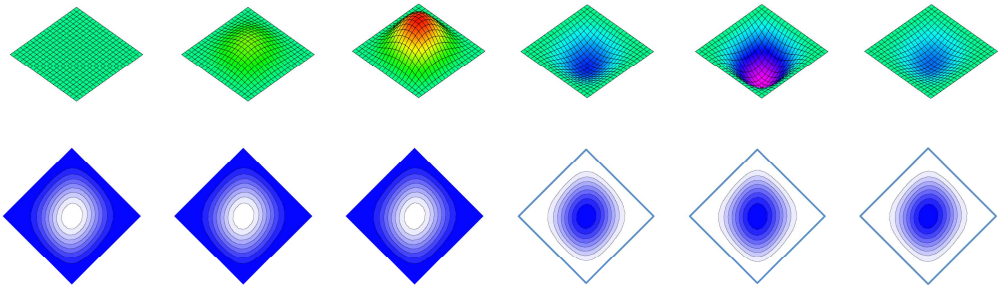

b) VSCL [<45°,75°>, 90°+<45°,75°>]$_{sym}$: Point P3

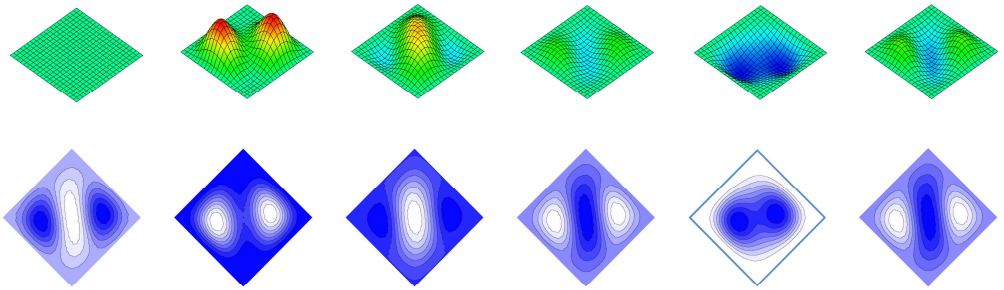

c) VSCL [<75°,45°>, 90°+<75°,45°>]$_{sym}$: Point O2

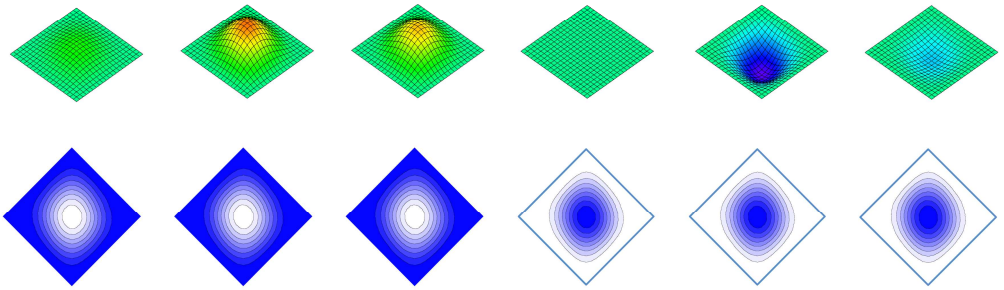

d) VSCL [<75°,45°>, 90°+<75°,45°>]$_{sym}$: Point O3

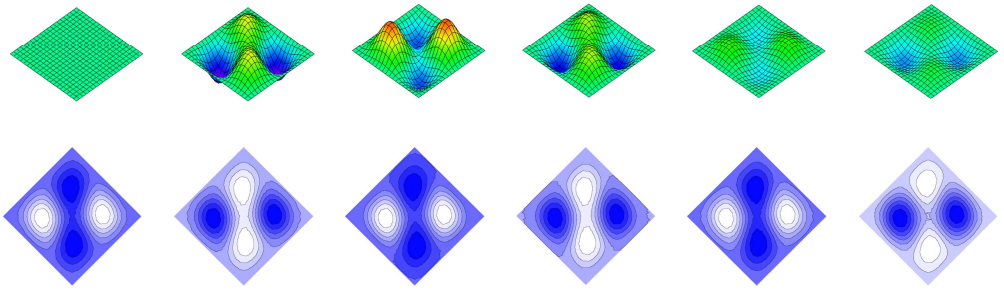

Figure 6.6: Perspectives and contour plots of shapes assumed by the plates in solutions P2, P3, O2 and O3 of Figure 6.3, in VSCLs $[\langle 45^o, 75^o\rangle, 90^o + \langle 45^o, 75^o\rangle]_{sym}$ and $[\langle 75^o, 45^o\rangle, 90^o + \langle 75^o, 45^o\rangle_{sym}$. The shapes are at sequential times in the related periodic cycle.

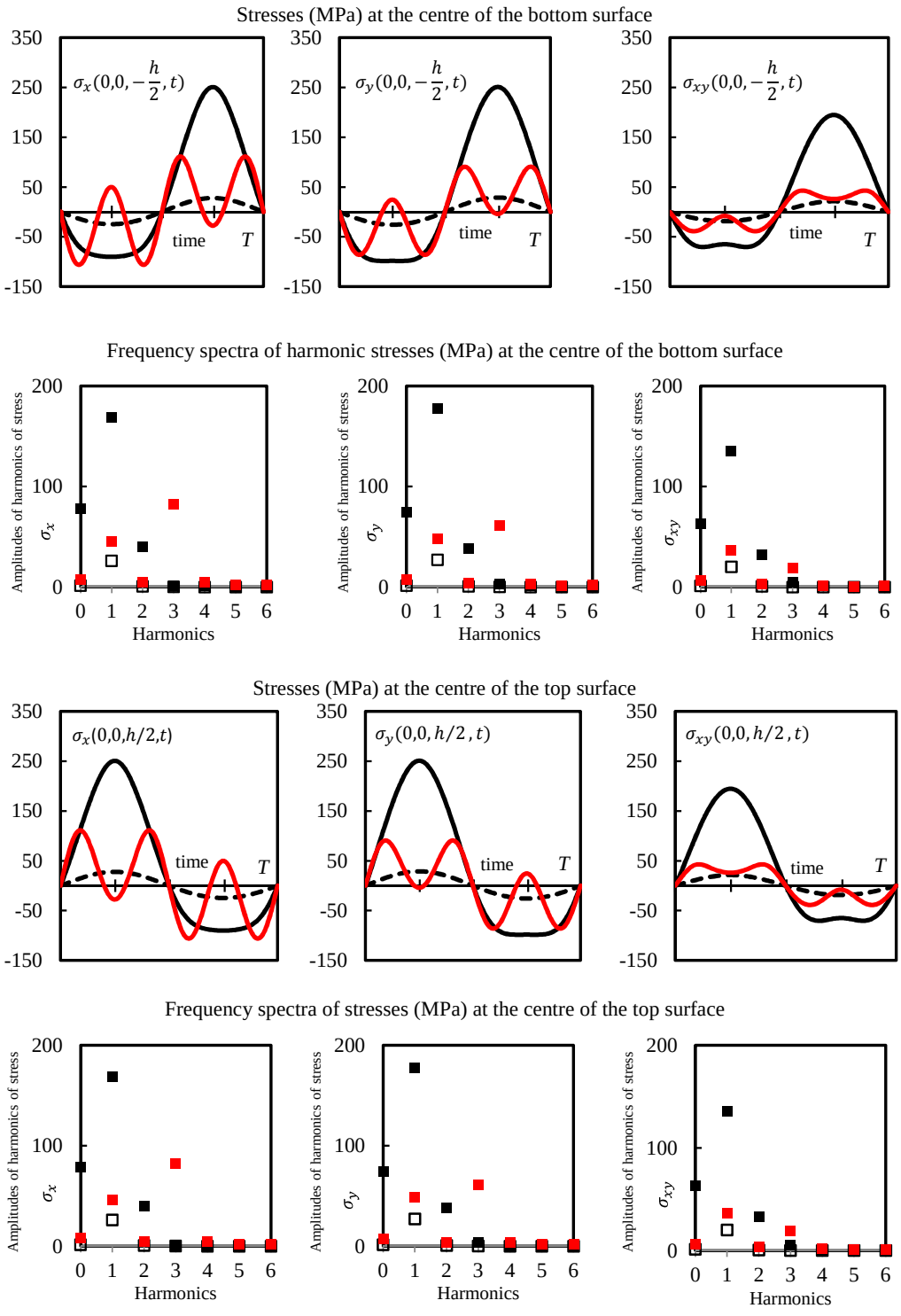

Figure 6.7: Normal stress time histories and frequency spectra for various points of the main and secondary branches of VSCL plate $[\langle 45^o, 75^o\rangle, 90^o + \langle 45^o, 75^o\rangle]_{sym}$; P1: black dashed line - - - and hollow square □; P2: black solid line ——— and filled square ■; P3: red solid line ——— and filled square ■; at the centre of the top and bottom surfaces.

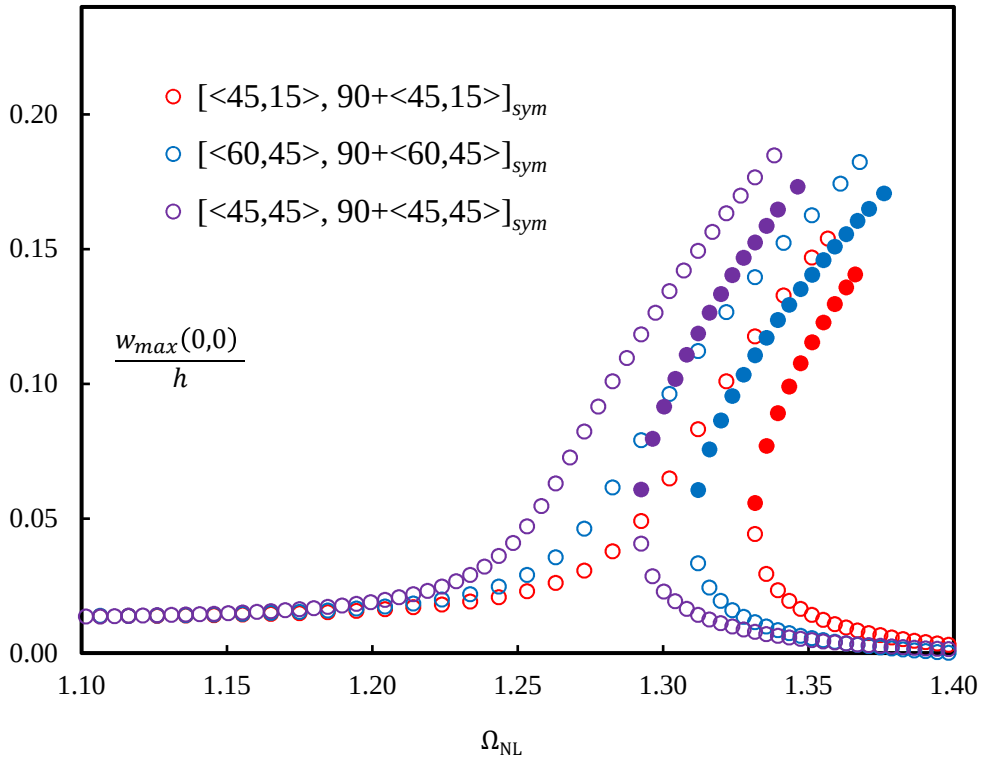

Figure 6.8: Frequency response curves at higher excitation frequencies for VSCLs $[\langle 45^o, 15^o\rangle, 90^o + \langle 45^o, 15^o\rangle]_{sym}$ and $[\langle 60^o, 45^o\rangle, 90^o + \langle 60^o, 45^o\rangle]_{sym}$, and for CSCL $[\langle 45^o, 45^o\rangle, 90^o + \langle 45^o, 45^o\rangle]_{sym}$. Non-hyperbolic results are represented by hollow symbols, while unstable results are shown in solid circles.

branches than in the main branch. It appears then that failure onset occurs at lower vibration amplitudes when higher order modes are excited. To somehow confirm this hypothesis, an investigation of higher order modes was carried out, directly exciting them, by applying forces at higher frequencies. Figure 6.8 displays deflection ratio against excitation frequency. Two different VSCLs - $[\langle 45^o, 15^o\rangle, 90^o + \langle 45^o, 15^o\rangle]_{sym}$, $[\langle 60^o, 45^o\rangle, 90^o + \langle 60^o, 45^o\rangle]_{sym}$ - and a reference CSCL plate, $[\langle 45^o, 45^o\rangle, 90^o + \langle 45^o, 45^o\rangle]_{sym}$, are excited near the natural frequency of a higher mode. When the plates are vibrating around their natural fundamental frequency (Frequency Response Curves shown in Figure 6.1), damage onset occurs when the maximum deflection ratio w_{max}/h is at least 0.6. Figure 6.8 shows that damage starts with a smaller deflection ratio (w_{max}/h between 0.15 and 0.2) if higher modes are (directly) excited. damage occurs at lower vibration amplitudes in the presence of higher modes because the shapes of these modes contain more waves, deforming more the plate. Stresses depend on the deformation of the plate, or, mathematically, on derivatives of the displacement components, as can be seen in the expressions for strains; to obtain the stresses one applies generalised Hooke's law, Equation (2.13).

6.3.8 Damage in VSCL Plates with Different Thickness

The purpose of Figure 6.9 is to show that damage starts at somewhat low non-dimensional vibration displacement amplitudes in thicker plates. A VSCL $[\langle 45^o, 75^o\rangle, 90^o + \langle 45^o, 75^o\rangle]_{sym}$ and a reference CSCL $[\langle 45^o, 45^o\rangle, 90^o + \langle 45^o, 45^o\rangle]_{sym}$ (i.e. angle-ply $[45^o, -45^o]_{sym}$) with different thickness h/a =0.01, 0.015, and 0.02 are analysed. It shows vibration amplitudes of oscillations with frequencies around the respective fundamental frequencies until damage starts. The plot reflects the fact that resonance in thicker plates occurs at higher excitation frequencies. The maximum deflection amplitudes correspond to the conditions when damage starts, so in thicker plates damage starts at a lower non-dimensional vibration displacement amplitude. This is physically because at equal non-dimensional vibration displacement amplitude w_{max}/h, displacement is larger in a thicker than in a thinner laminate and by generalised Hooke's law, stresses are directly related to the derivative of displacements (recall also that the in-plane dimensions were not changed, hence increasing the transverse displacement, the slope increases). Furthermore, when bending occurs, the in-plane strains increase with z, so their corresponding stresses tend to achieve larger values in a thicker plate (see equations of strain-displacements (3.1) and strain-stress relation (2.13)). Comparing the VSCL and CSCL plates, one verifies that damage onset occurs at larger amplitudes of vibration in the VSCL plate, especially when the laminate is thinner. To calculate these results, reduced order models with at least 10 normal modes are used. Figure 6.9 is quite important, because it shows that very large amplitude vibration analyses with a model that does not account for damage may well be useless, particularly in thick plates. This is somehow in accordance with Ref. [150]. However, we may disagree with the conclusion taken in this reference regarding the supposedly limited interest of non-linear shear deformation theories: non-linear shear deformation theories may still be interesting in not very thick plates, which can experience large amplitude vibrations without damage onset, because they lead to more accurate stress computations than theories based on Kirchhoff hypotheses. Furthermore, the fact that damage began in a specific point does not necessarily mean that the plate is due to fail.

6.4 Conclusions

In this chapter, the p-version finite element based on a third order shear deformation theory for VSCL plates is employed to study forced, periodic, non-linear, oscillations. Initially, static condensation is applied, neglecting in-plane inertia and, therefore, reducing the number of degrees of freedom. Then using a truncated set of modal coordinates the number of degrees of freedom is additionally reduced to the number of linear normal modes used. The final set of equations of motion in the form of second order differential equations is reformulated to a new set of first order differential equations, which are integrated in the time domain using a fifth-order Runge-Kutta method, with time steps controlled by an adaptive step size control algorithm. The periodic solution of the equations is treated as a boundary value problem by the shooting method. The application of the shooting method to the reduced models helps to find results very fast, in spite

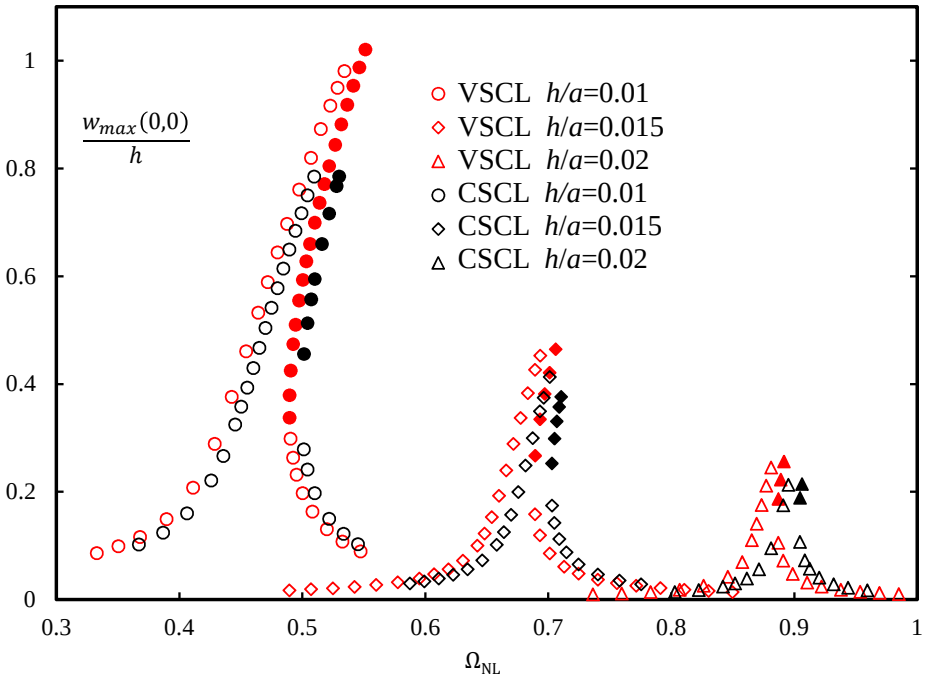

Figure 6.9: Frequency response curves for a VSCL $[\langle 45^o, 75^o \rangle, 90^o + \langle 45^o, 75^o \rangle]_{sym}$ and a CSCL $[\langle 45^o, 45^o \rangle, 90^o + \langle 45^o, 45^o \rangle]_{sym}$ plate with different thickness. Non-hyperbolic solutions are marked with hollow symbols and unstable ones with solid symbols.

of the non-linearities, and without any limitation on the frequency content of the response. As expected, models with more modal coordinates, require more computational time. The accuracy of the modal reduced models is verified by carrying comparisons with the full model using Newmark method. The results show that, in general, taking seven one-dimensional shape functions for each displacement component in the *p*-version finite element method and ten modal coordinates in the reduced models can lead to accurate models for the problems at hand.

Later, the effect of varying fibre angles by changing the governing angles, at the vertical edges and at the centre of the plies, on the forced vibration of VSCL plates is investigated. Results in the form of time histories, phase plane plots and Fourier spectra are shown for different vibrations in the main branch and in secondary branches. The secondary branches are due to bifurcations and involve higher modes of vibration. In all the analyses, a damage onset criterion is controlled and when the damage starts, the ongoing analyses are stopped. The dynamic behaviour of VSCL plates at the moment of damage occurrence is studied. Also, the steady-state in-plane normal and shear stresses at CSCL and various VSCL plates are analysed. These analyses are as well performed for the points of damage onset in branches found under bifurcations. In the set of plates studied, it is always a VSCL, not the CSCL, that leads to the limit cases (as experiencing maximum or minimum stress, or harmonics with larger or smaller amplitude).

In some oscillations, higher harmonics are quite important in stresses. This may affect the fatigue life of the plates, because it increases the number of cycles per second. Other analyses are done to evaluate the effect of the laminate thickness on the damage onset. It is verified that damage onset occurs at smaller non-dimensional deflections in thicker than in thinner laminates. Also, forced vibrations of laminates are assessed when higher modes of vibration are directly excited. Either due to internal resonances or to direct excitation at higher frequencies, it is apparent that damage starts with smaller deflection ratios in the presence of higher modes.

Chapter 7

Conclusion and Future Work

The work described in this thesis was concerned with the development of a p-version finite element model for non-linear vibration of variable stiffness laminated plates. A new model based on a third-order shear deformation theory was proposed. An investigation of the fibre angle change was presented on the linear modes of vibration and non-linear large deflection statics and dynamics of the plates. A number of interesting features of VSCL plates have been described and it was shown that the methods employed are effective and robust on predicting non-linear dynamic and static behaviours.

7.1 Thesis Conclusion

A general introduction of variable stiffness composite laminates was first presented in Chapter 1. With automated tow placement machines, the problem of producing plies with curved fibres has become easier. To remove the defects of the tow placement process, like gaps and overlaps between the fibres, other procedures and techniques are being developed.

There are two ways to put the fibres close to each other, the shifted method and the parallel method. Without looking to the advantages and disadvantages of these two methods, in this thesis, shifted method is considered. Anyway, the shifted method to produce other fibre paths from a reference fibre path is the easier case for implementation in the analysis. Hence, the objectives of this thesis were to evaluate the non-linear vibration and static analysis of composites with shifted curvilinear fibres. Another problem that usually happens during manufacturing of these VSCL plates is fibre kinking due to a restriction on the fibre radius curvature. This restriction limits the selection domain of fibre angles and was considered in this thesis.

A description of linear modes of vibration of VSCL plates, as well as the effect of geometrical imperfections on them, were given in Chapter 2. Generally, linear vibrational modes of VSCL plates depend on fibre angles. A change in the fibre angle can change meaningfully the natural frequency of the VSCL plate and its corresponding vibrational mode shape. This can lead to a different dynamic behaviour in the VSCL plate. It was also found that geometric imperfections affect the vibration modes. The VSCL model including imperfection was tested successfully.

Static analyses of VSCL plates using non-linear strain-displacement relations are given in Chapter 3. Different static loads were applied to the VSCL plate. The simulations were performed to see how deflection of different VSCL and traditional plates (CSCL) can change with the fibre path. Also, normal and shear stresses of the VSCL plates were analysed. It was shown that many VSCL plates can experience less deflection in comparison to the traditional composite laminates, with the same material and loadings. As was expected, the magnitude of normal and shear stresses changed significantly due to stress distribution. In this chapter, it was shown that varying the fibre angles in a VSCL plate can change the stress pattern completely. More details on the stress behaviour of these plates under various load magnitudes and fibre angles were given in Chapter 3.

In Chapter 4, different static and dynamic loads were applied to VSCL plates. A damage criterion (Tsai-Wu criterion) was used to see when and where the damage starts in the plates during an increase in the load magnitude. The analysis was done taking into account non-linear strain-displacements relations. To facilitate the comparison of damage index between different VSCL plates, a safety factor parameter was introduced. The simulation was carried out for deflection and safety factor of different VSCL plates under different loading conditions including static, harmonic dynamic and impact loads. It was demonstrated that VSCL plates can experience less deflection and they can have larger safety factor, in comparison to the traditional composite laminates, taking the same material and loading. Also, a small discussion was given about the location of damage, which was found to change when different VSCL plates are considered. Moreover, the growth of the normal and shear in-plane stresses due to increasing load magnitude until damage was displayed.

Development of a non-linear model for VSCL plates including imperfections, was performed in Chapter 5. The geometrically non-linear and periodic free vibration of VSCL plates was simulated using shooting and Runge-Kutta-Fehlberg methods. Runge-Kutta-Fehlberg integration technique is modified with Cash-Karp coefficients to control the error with adaptive stepsize. The model obtained using the p-version finite element, named as full-model, was reduced using static condensation. The statically condensed model neglects the in-plane inertia but includes the in-plane displacements. The reduced model was transformed to modal coordinates with a smaller number of degrees of freedom. Geometric imperfection were also included in the model of VSCL plates. Backbone curves of VSCL plates with different fibre angles were given and compared. When possible, bifurcations to secondary branches were detected using the shooting method. To have more details, phase plane plots and Fourier spectra of bifurcated branches of the solution were given. Some important sectional views of the vibration mode in fundamental backbone and bifurcated solutions were displayed. In addition, the effect of imperfection on the softening behaviour of backbone curves were detailed in this chapter.

Chapter 6 provided qualitative assessments for geometrically non-linear forced vibration of VSCL plates. Like in the previous chapter, the full model was statically condensed and transformed to modal coordinates. It was treated with the shooting method but now in presence of external load. The Tsai-Wu damage criterion was employed to see when the damage starts on VSCL plates under different loadings. Frequency response curves of VSCL plates with different

fibre angles were presented. Bifurcations were detected successfully and analysed using phase plane plots and Fourier spectra. The analysis continued till damage starts; it was shown that damage happens for lower vibration amplitudes in the bifurcated solutions. That is due to stimulation of higher modes of vibration when the solution bifurcates from the main branch. The behaviour of stresses in these bifurcated solutions are detailed in this chapter. Again, the sectional views of the plates under forced periodic vibrations (for the main and bifurcated branches of the solution) are displayed. This chapter ended with short discussion on the effect of higher modes and thickness on the forced vibration behaviour of VSCL plates.

7.2 Recommendation for Future Work

Although the results presented here demonstrated the effectiveness of VSCL plates, it could be further developed in a number of ways, as follows. There is clearly much more work to be done in the area of VSCL materials.

- **Forced vibration of VSCL plates including imperfection**:

  The proposed work will include the out-of-plane imperfections into account. Those imperfections are inevitable in manufacturing processes. The imperfection can take any shape (symmetrical or unsymmetrical). This would lead to a better tool for future comparisons between the simulation model and experimental results, although now there is a lack of experimental results in this field.

- **Experimental tests on dynamics of VSCL plates**:

  The applications of VSCL panels in the world are increasing, but still there is a lack of experimental analysis especially for dynamics of VSCL plates.

- **Flutter analysis on VSCL plates**:

  As VSCL plates are going to be used more and more in the aeronautical structures like airplanes, it is recommended to perform some flutter analysis on these plates. A flutter analysis can help to achieve a better design of airplane wings from VSCL materials.

Appendix A

Displacement Shape Functions and Boundary Conditions in the *p*-Version Finite Element

In what concerns the transverse displacements, a set of polynomials has been extensively applied [57, 59, 154, 155]. With this set, the boundary conditions and the conditions of continuity at the element boundaries are easily implemented, because only one of the first four shape functions has either value or derivative different from zero at the end of each element. All higher order hierarchical functions have zero magnitude and slopes at $\xi = -1$ and 1. This set of functions - which was designated as f - has also the advantage of requiring a small number of DOF and will be used here. Its form is

$$f_1(\xi) = \frac{1}{2} - \frac{3}{4}\xi + \frac{1}{4}\xi^3,$$

$$f_2(\xi) = \frac{1}{4} - \frac{1}{4}\xi - \frac{1}{4}\xi^2 + \frac{1}{4}\xi^3,$$

$$f_3(\xi) = \frac{1}{2} + \frac{3}{4}\xi - \frac{1}{4}\xi^3,$$

$$f_4(\xi) = -\frac{1}{4} - \frac{1}{4}\xi + \frac{1}{4}\xi^2 + \frac{1}{4}\xi^3,$$

$$f_r(\xi) = \sum_{n=0}^{INT\left(\frac{r}{2}\right)} \frac{(-1)^n (2r-2n-7)!!}{2^n n! (r-2n-1)!} \xi^{r-2n-1}, \quad r > 4 \tag{A.1}$$

and $r!! = r(r-2)\ldots(2\text{or}1)$, $0!! = (-1)!! = 1$ and $INT\left(\frac{r}{2}\right)$ denotes the integer part of $\frac{r}{2}$. A set of polynomials called the g set will be applied as in-plane shape functions. The derivatives of these g functions are not zero at the boundaries, but their value is. This set has also been applied with success in the analysis of beams and plates [57, 59, 154, 155], and is defined as

$$g_1(\xi) = \frac{1}{2} - \frac{1}{2}\xi,$$

$$g_2(\xi) = \frac{1}{2} + \frac{1}{2}\xi,$$

$$g_r(\xi) = \sum_{n=0}^{INT\left(\frac{r}{2}\right)} \frac{(-1)^n (2r-2n-5)!!}{2^n n!\,(r-2n-1)!}\xi^{r-2n-1}, \qquad r > 2 \tag{A.2}$$

The disadvantage of *p*-version finite elements is that they are not so simple as the common *h*-version finite elements. But by using a symbolic computation package to manipulate the shape functions, the element mass and stiffness matrices are accurately and easily evaluated.

In a completely free plate (FFFF), shape functions in Equations A.1 are used for transverse displacement and same shape functions in Equations A.2 are used for both in-plane and rotational displacements. In a fully clamped plate (CCCC), because the displacements and rotations are zero at the boundaries, the shape functions $f_1 - f_4$ and $g_{1-}g_2$ are not employed.

Three types of simply-supported conditions are considered here:

- **SSSS-1**: simply-supported with immovable edges, in which $u^0 = v^0 = w^0 = \phi_y = M_{xx} = 0$ at the edges $x = \pm a/2$; and $u^0 = v^0 = w^0 = \phi_x = M_{yy} = 0$ at the edges $y = \pm b/2$;
- **SSSS-2**: simply-supported with movable edges, in which $v^0 = w^0 = \phi_y = M_{xx} = N_{xx} = 0$ at the edges $x = \pm a/2$ and $u^0 = w^0 = \phi_x = M_{yy} = N_{yy} = 0$ at the edges $y = \pm b/2$;
- **SSSS-3**: simply-supported with fully free in-plane edges, in which $w^0 = \phi_y = M_{xx} = N_{xx} = N_{xy} = 0$ at the edges $x = \pm a/2$; and $w^0 = \phi_x = M_{yy} = N_{yy} = N_{xy} = 0$ at the edges $y = \pm b/2$; but $u^0, v^0 \neq 0$ at all edges;

In a simply-supported SSSS-1 plate, the transverse and rotation shape functions are taken from Equations A.2 and in-plane shape functions from A.1. In the simply-supported boundary condition, ϕ_y at the edges $x = \pm a/2$ and ϕ_x at the edges $y = \pm b/2$ are zero so some bi-dimensional rotational shape functions, which have not zero value at the related edges, must be removed from rotational shape function row vectors $\mathbf{N}^{\boldsymbol{\phi}_x}$ and $\mathbf{N}^{\boldsymbol{\phi}_y}$. Shape functions for simply-supported SSSS-2 are the same as for SSSS-1 conditions, but with lower restrictions. In this boundary conditions, $v^0 = 0$ at the edges $x = \pm a/2$ and $u^0 = 0$ at the edges $y = \pm b/2$ so some bi-dimensional in-plane shape functions, which have non zero values at the related edges, must be removed from in-plane shape function row vectors $\mathbf{N}^{\mathbf{u}}$ and $\mathbf{N}^{\mathbf{v}}$. In SSSS-3 boundary condition, no restriction is applied to the in-plane displacements, therefore shape functions $g_1(\xi)$ and $g_2(\xi)$ are employed both in displacements u^0 and v^0.

Appendix B

Experiments

Free boundary conditions were simulated by hanging the plate so that it stands vertically, as represented in Figure B.1. After some tests with a hammer, performed to obtain an idea of the values of the first natural frequencies, it was decided to extract modes with frequencies ranging from 0 to 200 Hz. For that purpose, the plate was excited with random excitation (white noise) via an electromagnetic shaker, which was also hanged in strings and another aluminium frame. A drive rod and a piezoelectric force transducer, Bruel & Kjaer model 8203, connected the shaker to the plate, so that the force was applied perpendicularly to it. A grid of 9×9 points was defined and the acceleration measured by a light-weight piezoelectric accelerometer, model 27 A11 of Endeveco. The frequency response functions were obtained in this pre-defined grid. An example of the FRFs obtained can be seen in Figure B.2, which represents the accelerance that corresponds to an acceleration at the point where the excitation was applied, hence the characteristic anti-resonances. From these eighty-one FRFs, natural frequencies, modal dampings and mode shapes of vibration were identified using a modal analysis software [70][1].

[1] Professors José Dias Rodrigues (jdr@fe.up.pt) and Pedro Ribeiro (pmleal@fe.up.pt) have performed the experiments; the natural frequencies and natural mode shapes of vibration from the experimental data were identified by Professors José Dias Rodrigues.

Figure B.1: Set-up for the freely VSCL plate (Ref. [70])

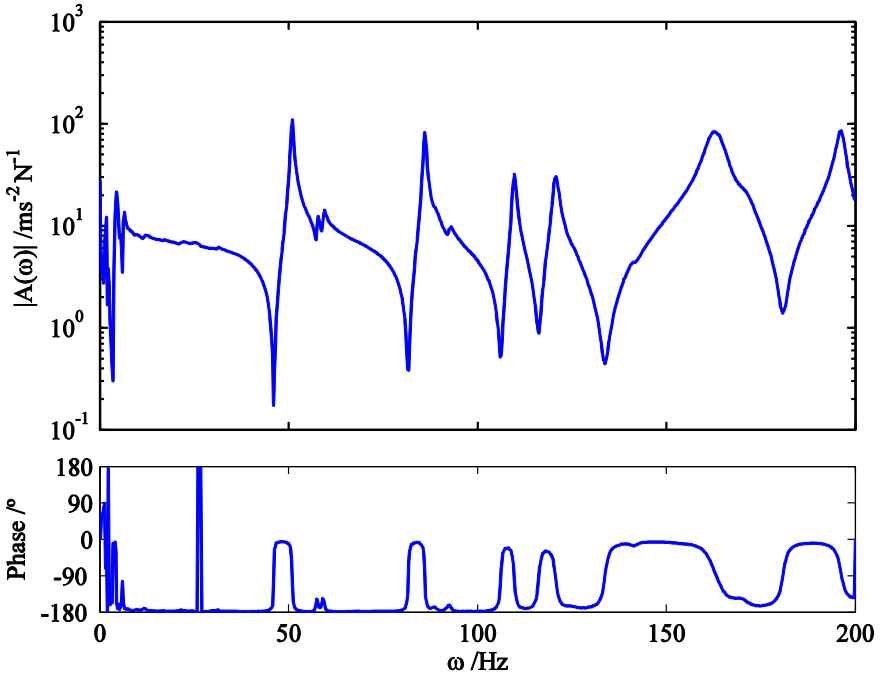

Figure B.2: Point accelerance (force and acceleration on the same point) [70].

References

[1] MW Hyer and RF Charette. Innovative design of composite structures: The use of curvilinear fiber format in composite structure design. Technical Report NASA-CR-186453, NASA, 1990. Cited on pp. 2, 4, and 30.

[2] MW Hyer and RF Charette. Use of curvilinear fiber format in composite structure design. *AIAA Journal*, 29(6):1011–1015, 1991. Cited on p. 2.

[3] MW Hyer and HH Lee. Innovative design of composite structures: the use of curvilinear fiber format to improve buckling resistance of composite plates with central circular holes. Technical Report NASA-CR-186454, NASA, 1990. Cited on pp. 2 and 4.

[4] MW Hyer and HH Lee. The use of curvilinear fiber format to improve buckling resistance of composite plates with central circular holes. *Composite Structures*, 18(3):239–261, 1991. Cited on p. 2.

[5] Z Gürdal and R Olmedo. In-plane response of laminates with spatially varying fiber orientations-variable stiffness concept. *AIAA Journal*, 31(4):751–758, 1993. Cited on p. 2.

[6] C Waldhart. Analysis of tow-placed, variable-stiffness laminates. Master's thesis, Virginia Polytechnic Institute and State University, 1996. Cited on pp. 2, 7, 8, 11, 33, and 41.

[7] BF Tatting. *Analysis and design of variable stiffness composite cylinders*. PhD thesis, Virginia Polytechnic Institute and State University, 1998. Cited on pp. 2 and 41.

[8] PT Langley. Finite element modeling of tow-placed variable-stiffness composite laminates. Master's thesis, Virginia Polytechnic Institute and State University, 1999. Cited on pp. 2 and 41.

[9] E Senocak and H Tanriover. Analysis of composite plates with variable stiffness using galerkin method. *Aeronautical Journal*, 111(1118):247–255, 2007. Cited on pp. 2 and 42.

[10] S Setoodeh, Z Gürdal, and LT Watson. Design of variable-stiffness composite layers using cellular automata. *Computer Methods in Applied Mechanics and Engineering*, 195(9):836–851, 2006. Cited on pp. 2, 68, and 102.

[11] JM Curry, ER Ohnson, and JH Tarnes. Effect of dropped plies on the strength of graphite-epoxy laminates. *AIAA Journal*, 30(2):449–456, 1992. Cited on pp. 2 and 4.

[12] A Mukherjee and B Varughese. A ply drop-off element for inclusion of drop-off in the global analysis of layered composite structures. *Computers & Structurest*, 54(5):865–870, 1995. Cited on p. 2.

[13] DS Cairns, JF Mandell, ME Scott, and JZ Maccagnano. Design and manufacturing considerations for ply drops in composite structures. *Composites Part B: Engineering*, 30(5):523–534, 1999. Cited on pp. 2 and 4.

[14] JE Herencia, PM Weaver, and MI Friswell. Optimization of anisotropic composite panels with t-shaped stiffeners including transverse shear effects and out-of-plane loading. *Structural and Multidisciplinary Optimization*, 37(2):165–184, 2008. Cited on p. 2.

[15] L Marín, D Trias, P Badalló, G Rus, and JA Mayugo. Optimization of composite stiffened panels under mechanical and hygrothermal loads using neural networks and genetic algorithms. *Composite Structures*, 94(11):3321–3326, 2012. Cited on p. 2.

[16] J Sliseris and K Rocens. Optimal design of composite plates with discrete variable stiffness. *Composite Structures*, 98:15–23, 2013. Cited on p. 2.

[17] DK Jha, T Kant, and RK Singh. A critical review of recent research on functionally graded plates. *Composite Structures*, 96:833–849, 2013. Cited on p. 2.

[18] S Hosseini-Hashemi, HRD Taher, and H Akhavan. Vibration analysis of radially fgm sectorial plates of variable thickness on elastic foundations. *Composite Structures*, 92(7):1734–1743, 2010. Cited on p. 2.

[19] S Hosseini-Hashemi, H Akhavan, HRD Taher, N Daemi, and A Alibeigloo. Differential quadrature analysis of functionally graded circular and annular sector plates on elastic foundation. *Materials & Design*, 31(4):1871–1880, 2010. Cited on p. 2.

[20] EIS Flores, MI Friswell, and Y Xia. Variable stiffness biological and bio-inspired materials. *Journal of Intelligent Material Systems and Structures*, 24(5):529–540, 2013. Cited on p. 2.

[21] A Alhaj Ahmad. *Design tailoring of panels for pressure pillowing using tow-placed steered fibers*. PhD thesis, Delft University of Technology, 2008. Cited on p. 4.

[22] BF Tatting and Z Gürdal. Design and manufacture of elastically tailored tow placed plates. Technical Report CR-2002-211919, NASA, 2002. Cited on pp. 4, 5, and 42.

[23] BF Tatting and Z Gürdal. Automated finite element analysis of elastically-tailored plates. Technical Report CR-2003-212679, NASA, 2003. Cited on pp. 4, 5, and 42.

[24] HJAL Dirk, C Ward, and KD Potter. The engineering aspects of automated prepreg layup: History, present and future. *Composites Part B: Engineering*, 43(3):997–1009, 2012. Cited on pp. 4 and 5.

[25] Z Gürdal, BF Tatting, and KC Wu. Tow-placement technology and fabrication issues for laminated composite structures. In *Proceedings of the Aiaa/Asme/Asce/Ahs/Asc structures, 46th structural dynamics & materials conference*, 2005. Cited on p. 5.

[26] CS Lopes. *Damage and failure of non-conventional composite laminates*. PhD thesis, TU Delft, 2009. Cited on p. 5.

[27] J Barth. Fabrication of complex composite structures using advanced fiber placement technology. In *International SAMPE Symposium and Exhibition, 35 th, Anaheim, CA*, pages 710–720, 1990. Cited on p. 5.

[28] ML Enders and PC Hopkins. Developments in the fiber placement process. In *36th International SAMPE Symposium*, pages 778–790, 1991. Cited on p. 5.

[29] F Bullock, S Kowalski, and R Young. Automated prepreg tow placement for composite structures. *35th International SAMPE Symposium*, 1:734–745, 1990. Cited on p. 5.

[30] BC Kim, K Potter, and PM Weaver. Continuous tow shearing for manufacturing variable angle tow composites. *Composites Part A: Applied Science and Manufacturing*, 43(8):1347–1356, 2012. Cited on p. 5.

[31] P Mattheij, K Gliesche, and D Feltin. Tailored fiber placement-mechanical properties and applications. *Journal of Reinforced Plastics and Composites*, 17(9):774–786, 1998. Cited on p. 5.

[32] A Spickenheuer, M Schulz, K Gliesche, and G Heinrich. Using tailored fibre placement technology for stress adapted design of composite structures. *Plastics, Rubber and Composites*, 37(5):227–232, 2008. Cited on p. 5.

[33] AW Blom. *Structural performance of fiber-placed, variable-stiffness composite conical and cylindrical shells*. PhD thesis, Delft University of Technology, 2010. Cited on p. 8.

[34] JN Reddy. *Mechanics of laminated composite plates and shells: theory and analysis*. CRC Press, 2004. Cited on pp. 11, 13, 17, 18, 19, and 41.

[35] JN Reddy. *Mechanics of laminated composite plates- Theory and analysis*. CRC Press, 1997. Cited on pp. 11, 17, 18, and 41.

[36] JN Reddy. *Theory and analysis of elastic plates and shells*. CRC press, 2006. Cited on pp. 11 and 41.

[37] M Levinson. An accurate, simple theory of the statics and dynamics of elastic plates. *Mechanics Research Communications*, 7(6):343–350, 1980. Cited on pp. 11 and 13.

[38] M Levinson. On higher order beam and plate theories. *Mechanics Research Communications*, 14(5-6):421–424, 1987. Cited on p. 11.

[39] BF Vlasov. On the equations of bending of plates. *Dokla Ak Nauk Azerbeijanskoi-SSR*, 3:955–979, 1957. Cited on pp. 11 and 13.

[40] C-P Wu and C-Y Lee. Differential quadrature solution for the free vibration analysis of laminated conical shells with variable stiffness. *International Journal of Mechanical Sciences*, 43(8):1853–1869, 2001. Cited on p. 12.

[41] AH Akbarzadeh, MA Nik, and D Pasini. The role of shear deformation in laminated plates with curvilinear fiber paths and embedded defects. *Composite Structures*, 118:217–227, 2014. Cited on pp. 12, 42, 43, and 69.

[42] S Yazdani and P Ribeiro. A layerwise p-version finite element formulation for free vibration analysis of thick composite laminates with curvilinear fibres. *Composite Structures*, 120:531–542, 2015. Cited on p. 12.

[43] P Ribeiro, H Akhavan, A Teter, and J Warmiński. A review on the mechanical behaviour of curvilinear fibre composite laminated panels. *Journal of Composite Materials*, page 0021998313502066, 2013. Cited on p. 12.

[44] P Ribeiro. Non-linear free periodic vibrations of variable stiffness composite laminated plates. *Nonlinear Dynamics*, 70(2):1535–1548, 2012. Cited on pp. 12, 82, 101, and 102.

[45] S Honda and Y Narita. Natural frequencies and vibration modes of laminated composite plates reinforced with arbitrary curvilinear fiber shape paths. *Journal of Sound and Vibration*, 331(1):180–191, 2012. Cited on p. 12.

[46] MM Abdalla, S Setoodeh, and Z Gürdal. Design of variable stiffness composite panels for maximum fundamental frequency using lamination parameters. *Composite Structures*, 81(2):283–291, 2007. Cited on p. 13.

[47] AW Blom, S Setoodeh, JMAM Hol, and Z Gürdal. Design of variable-stiffness conical shells for maximum fundamental eigenfrequency. *Computers & Structures*, 86(9):870–878, 2008. Cited on p. 13.

[48] H Akhavan and P Ribeiro. Natural modes of vibration of variable stiffness composite laminates with curvilinear fibers. *Composite Structures*, 93(11):3040–3047, 2011. Cited on pp. 13 and 67.

[49] BA Szabo and AK Mehta. p-convergent finite element approximations in fracture mechanics. *International Journal for Numerical Methods in Engineering*, 12(3):551–560, 1978. Cited on p. 14.

[50] I Babuska and B Szabo. On the rates of convergence of the finite element method. *International Journal for Numerical Methods in Engineering*, 18(3):323–341, 1982. Cited on p. 15.

[51] M Amabili. *Nonlinear vibrations and stability of shells and plates*. Cambridge University Press, 2008. Cited on pp. 15, 53, 82, 88, and 101.

[52] C-Y Chia. *Nonlinear analysis of plates*. McGraw-Hill International Book Company, 1980. Cited on p. 17.

[53] ML Bucalem and K-J Bathe. *The mechanics of solids and structures-hierarchical modeling and the finite element solution*. Springer Science & Business Media, 2011. Cited on p. 18.

[54] MS Qatu. *Vibration of laminated shells and plates*. Elsevier, 2004. Cited on p. 19.

[55] RM Jones. *Mechanics of composite materials*. Crc Press, 1998. Cited on p. 19.

[56] BA Szabo and I Babuška. *Finite element analysis*. John Wiley & Sons, 1991. Cited on pp. 26 and 67.

[57] A Houmat. Hierarchical finite element analysis of the vibration of membranes. *Journal of Sound and Vibration*, 201(4):465–472, 1997. Cited on pp. 26 and 129.

[58] P Ribeiro. A hierarchical finite element for geometrically non-linear vibration of thick plates. *Meccanica*, 38(1):117–132, 2003. Cited on p. 26.

[59] NS Bardell. Free vibration analysis of a flat plate using the hierarchical finite element method. *Journal of Sound and Vibration*, 151(2):263–289, 1991. Cited on pp. 26 and 129.

[60] W Han and M Petyt. Linear vibration analysis of laminated rectangular plates using the hierarchical finite element method-i. free vibration analysis. *Computers & Structures*, 61(4):705–712, 1996. Cited on p. 26.

[61] P Ribeiro. First-order shear deformation, p-version, finite element for laminated plate non-linear vibrations. *AIAA Journal*, 43(6):1371–1379, 2005. Cited on pp. 26, 27, 29, and 30.

[62] M Petyt. *Introduction to finite element vibration analysis*. Cambridge university press, 2010. Cited on pp. 26, 46, 70, and 107.

[63] P Ribeiro and H Akhavan. Non-linear vibrations of variable stiffness composite laminated plates. *Composite Structures*, 94(8):2424–2432, 2012. Cited on pp. 26, 67, 82, 101, and 102.

[64] S Wang and Y Zhang. Vibration analysis of rectangular composite laminated plates using layerwise b-spline finite strip method. *Composite Structures*, 68(3):349–358, 2005. Cited on pp. 27 and 29.

[65] A Nosier, RK Kapania, and JN Reddy. Free vibration analysis of laminated plates using a layerwise theory. *AIAA Journal*, 31(12):2335–2346, 1993. Cited on pp. 27 and 29.

[66] P Ribeiro and M Petyt. Non-linear vibration of composite laminated plates by the hierarchical finite element method. *Composite Structures*, 46(3):197–208, 1999. Cited on pp. 27, 29, 105, 106, 107, 108, and 109.

[67] P Ribeiro. Forced periodic vibrations of laminated composite plates by a p-version, first order shear deformation, finite element. *Composites Science and Technology*, 66(11):1844–1856, 2006. Cited on pp. 27 and 29.

[68] G-L Qian, SV Hoa, and X Xiao. A new rectangular plate element for vibration analysis of laminated composites. *Journal of Vibration and Acoustics*, 120(1):80–86, 1998. Cited on pp. 27 and 30.

[69] KS Sivakumaran. Frequency analysis of symmetrically laminated plates with free edges. *Journal of Sound and Vibration*, 125(2):211–225, 1988. Cited on pp. 27, 29, and 30.

[70] JD Rodrigues, P Ribeiro, and H Akhavan. Experimental and finite element modal analysis of variable stiffness composite laminated plates. In *Proceedings of the 11th Biennial International Conference on Vibration Problems (ICOVP-2013)*, 2013. Cited on pp. 30 and 131.

[71] M Amabili. Theory and experiments for large-amplitude vibrations of rectangular plates with geometric imperfections. *Journal of Sound and Vibration*, 291(3):539–565, 2006. Cited on pp. 34, 36, 50, 82, and 98.

[72] M Rafiee, XQ He, and KM Liew. Non-linear dynamic stability of piezoelectric functionally graded carbon nanotube-reinforced composite plates with initial geometric imperfection. *International Journal of Non-Linear Mechanics*, 59:37–51, 2014. Cited on pp. 34 and 36.

[73] S Kitipornchai, J Yang, and KM Liew. Semi-analytical solution for nonlinear vibration of laminated fgm plates with geometric imperfections. *International Journal of Solids and Structures*, 41(9):2235–2257, 2004. Cited on pp. 36 and 98.

[74] G Raju, Z Wu, and PM Weaver. Buckling analysis of variable angle tow composite plates using differential quadrature method. *Journal of the Indian Institute of Science*, 93(4):689–698, 2013. Cited on pp. 41 and 42.

[75] Z Gürdal, BF Tatting, and KC Wu. Variable stiffness composite panels: effects of stiffness variation on the in-plane and buckling response. *Composites Part A: Applied Science and Manufacturing*, 39(5):911–922, 2008. Cited on pp. 42, 68, and 102.

[76] CS Lopes, Z Gürdal, and PP Camanho. Variable-stiffness composite panels: Buckling and first-ply failure improvements over straight-fibre laminates. *Computers & Structures*, 86(9):897–907, 2008. Cited on pp. 42, 67, 68, and 102.

[77] CS Lopes, Z Gürdal, and PP Camanho. Tailoring for strength of composite steered-fibre panels with cutouts. *Composites Part A: Applied Science and Manufacturing*, 41(12):1760–1767, 2010. Cited on pp. 42 and 68.

[78] J Diaz, C Fagiano, MM Abdalla, Z Gürdal, and S Hernandez. A study of interlaminar stresses in variable stiffness plates. *Composite Structures*, 94(3):1192–1199, 2012. Cited on pp. 42, 68, and 102.

[79] S Maleki and M Tahani. Non-linear analysis of fiber-reinforced open conical shell panels considering variation of thickness and fiber orientation under thermo-mechanical loadings. *Composites Part B: Engineering*, 52:245–261, 2013. Cited on p. 42.

[80] Z Wu, PM Weaver, G Raju, and BC Kim. Buckling analysis and optimisation of variable angle tow composite plates. *Thin-walled Structures*, 60:163–172, 2012. Cited on p. 42.

[81] Z Wu, PM Weaver, and G Raju. Postbuckling optimisation of variable angle tow composite plates. *Composite Structures*, 103:34–42, 2013. Cited on p. 42.

[82] T Rahman, ST Ijsselmuiden, MM Abdalla, and EL Jansen. Postbuckling analysis of variable stiffness composite plates using a finite element-based perturbation method. *International Journal of Structural Stability and Dynamics*, 11(04):735–753, 2011. Cited on pp. 42 and 102.

[83] S Yazdani and P Ribeiro. Geometrically non-linear static analysis of unsymmetric composite plates with curvilinear fibres: p-version layerwise approach. *Composite Structures*, 118:74–85, 2014. Cited on p. 42.

[84] S Yazdani, P Ribeiro, and JD Rodrigues. A p-version layerwise model for large deflection of composite plates with curvilinear fibres. *Composite Structures*, 108:181–190, 2014. Cited on p. 42.

[85] NJ Pagano and HJ Hatfield. Elastic behavior of multilayered bidirectional composites. *AIAA Journal*, 10(7):931–933, 1972. Cited on pp. 43, 50, 52, 53, 54, and 62.

[86] SA Zaghloul and JB Kennedy. Nonlinear behavior of symmetrically laminated plates. *Journal of Applied Mechanics*, 42(1):234–236, 1975. Cited on pp. 43, 49, and 50.

[87] NS Putcha and JN Reddy. A refined mixed shear flexible finite element for the nonlinear analysis of laminated plates. *Computers & Structures*, 22(4):529–538, 1986. Cited on pp. 43 and 49.

[88] YX Zhang and KS Kim. A simple displacement-based 3-node triangular element for linear and geometrically nonlinear analysis of laminated composite plates. *Computer Methods in Applied Mechanics and Engineering*, 194(45):4607–4632, 2005. Cited on pp. 43, 49, 50, and 51.

[89] YX Zhang and CH Yang. Recent developments in finite element analysis for laminated composite plates. *Composite Structures*, 88(1):147–157, 2009. Cited on p. 43.

[90] F Auricchio and E Sacco. A mixed-enhanced finite-element for the analysis of laminated composite plates. *International Journal for Numerical Methods in Engineering*, 44(10):1481–1504, 1999. Cited on p. 43.

[91] F Auricchio, C Lovadina, and E Sacco. Analysis of mixed finite elements for laminated composite plates. *Computer Methods in Applied Mechanics and Engineering*, 190(35):4767–4783, 2001. Cited on p. 43.

[92] F Auricchio, E Sacco, and G Vairo. A mixed fsdt finite element for monoclinic laminated plates. *Computers & Structures*, 84(8):624–639, 2006. Cited on p. 43.

[93] H Akhavan, P Ribeiro, and MFSF de Moura. Large deflection and stresses in variable stiffness composite laminates with curvilinear fibres. *International Journal of Mechanical Sciences*, 73:14–26, 2013. Cited on pp. 43, 67, and 111.

[94] K-J Bathe and EL Wilson. *Numerical methods in finite element analysis*. Prentice-Hall Englewood Cliffs, NJ, 1976. Cited on pp. 46, 47, 48, and 70.

[95] M Ganapathi, O Polit, and M Touratier. A c0 eight-node membrane-shear-bending element for geometrically non-linear (static and dynamic) analysis of laminates. *International Journal for Numerical Methods in Engineering*, 39(20):3453–3474, 1996. Cited on p. 49.

[96] J Argyris and L Tenek. Linear and geometrically nonlinear bending of isotropic and multilayered composite plates by the natural mode method. *Computer Methods in Applied Mechanics and Engineering*, 113(3):207–251, 1994. Cited on p. 50.

[97] J Yang and L Zhang. Nonlinear analysis of imperfect laminated thin plates under transverse and in-plane loads and resting on an elastic foundation by a semi-analytical approach. *Thin-walled Structures*, 38(3):195–227, 2000. Cited on p. 50.

[98] T Kant and JR Kommineni. C 0 finite element geometrically non-linear analysis of fibre reinforced composite and sandwich laminates based on a higher-order theory. *Computers & Structures*, 45(3):511–520, 1992. Cited on pp. 50 and 51.

[99] M Gorji. On large deflection of symmetric composite plates under static loading. *Proceedings of the Institution of Mechanical Engineers, Part C: Journal of Mechanical Engineering Science*, 200(1):13–19, 1986. Cited on pp. 50 and 51.

[100] VS Thankam, G Singh, GV Rao, and AK Rath. Shear flexible element based on coupled displacement field for large deflection analysis of laminated plates. *Computers & Structures*, 81(5):309–320, 2003. Cited on pp. 50 and 51.

[101] JL Mantari, AS Oktem, and CG Soares. A new higher order shear deformation theory for sandwich and composite laminated plates. *Composites Part B: Engineering*, 43(3):1489–1499, 2012. Cited on p. 52.

[102] M Karama, KS Afaq, and S Mistou. A new theory for laminated composite plates. *Proceedings of the Institution of Mechanical Engineers, Part L: Journal of Materials Design and Applications*, 223(2):53–62, 2009. Cited on p. 52.

[103] JN Reddy and CF Liu. A higher-order shear deformation theory of laminated elastic shells. *International Journal of Engineering Science*, 23(3):319–330, 1985. Cited on pp. 52 and 53.

[104] TD Canisius and RO Foschi. Some aspects in the calculation of transverse shear stresses in mindlin plates. *Communications in Numerical Methods in Engineering*, 9(8):681–685, 1993. Cited on p. 62.

[105] F París. A study of failure criteria of fibrous composite materials. Technical Report NASA/CR 2001-210661, NASA, 2001. Cited on pp. 67 and 101.

[106] IM Daniel and O Ishai. *Engineering mechanics of composite materials*, volume 3. Oxford university press New York, 1994. Cited on pp. 67, 71, 72, 101, 106, and 107.

[107] ST IJsselmuiden. *Optimal design of variable stiffness composite structures using lamination parameters*. PhD thesis, TU Delft, Delft University of Technology, 2011. Cited on pp. 67 and 101.

[108] S Honda and Y Narita. Vibration design of laminated fibrous composite plates with local anisotropy induced by short fibers and curvilinear fibers. *Composite Structures*, 93(2):902–910, 2011. Cited on p. 67.

[109] A Alhajahmad, MM Abdalla, and Z Gürdal. Optimal design of tow-placed fuselage panels for maximum strength with buckling considerations. *Journal of Aircraft*, 47(3):775–782, 2010. Cited on pp. 67, 68, and 102.

[110] H Akhavan, P Ribeiro, and MFSF de Moura. Damage onset on tow-placed variable stiffness composite laminates. *Composite Structures*, 113:419–428, 2014. Cited on pp. 68, 109, and 110.

[111] H Akhavan, P Ribeiro, and MFSF de Moura. Composite laminates with linearly varying fiber angles under static and dynamic loads. In *Proceeding of 54th AIAA/ASME/ASCE/AHS/ASC Structures, Structural Dynamics, and Materials Conference and co-located Events*, pages 2013–1565, 2013. Cited on pp. 68, 109, and 110.

[112] H Ghiasi, K Fayazbakhsh, D Pasini, and L Lessard. Optimum stacking sequence design of composite materials part ii: Variable stiffness design. *Composite Structures*, 93(1):1–13, 2010. Cited on p. 68.

[113] TD Dang and SR Hallett. A numerical study on impact and compression after impact behaviour of variable angle tow laminates. *Composite Structures*, 96:194–206, 2013. Cited on pp. 68 and 102.

[114] S Honda, T Igarashi, and Y Narita. Multi-objective optimization of curvilinear fiber shapes for laminated composite plates by using nsga-ii. *Composites Part B: Engineering*, 45(1):1071–1078, 2013. Cited on pp. 68 and 102.

[115] MM Abdalla, Z Gürdal, and GF Abdelal. Thermomechanical response of variable stiffness composite panels. *Journal of Thermal Stresses*, 32(1-2):187–208, 2008. Cited on pp. 68 and 102.

[116] T Ungwattanapanit and H Baier. Postbuckling analysis and optimization of stiffened fuselage panels utilizing variable-stiffness laminates. In *Proceedings of 29th Congress of the International Council of the Aeronautical Sciences (ICAS2014)*, 2014. Cited on p. 68.

[117] Z Zamani, H Haddadpour, and MR Ghazavi. Curvilinear fiber optimization tools for design thin walled beams. *Thin-Walled Structures*, 49(3):448–454, 2011. Cited on p. 68.

[118] CS Lopes, PP Camanho, Z Gürdal, and BF Tatting. Progressive failure analysis of tow-placed, variable-stiffness composite panels. *International Journal of Solids and Structures*, 44(25):8493–8516, 2007. Cited on p. 68.

[119] Dawn C Jegley, Brian F Tatting, and Z Gürdal. Tow-steered panels with holes subjected to compression or shear loading. In *Proceedings of the AIAA/ASME/ASCE/AHS/ASC 46th Structures, Structural Dynamics and Materials (SDM) Conference, Austin, TX*, pages 2005–2017, 2005. Cited on p. 69.

[120] Z Wu, G Raju, and PM Weaver. Postbuckling analysis of variable angle tow composite plates. *International Journal of Solids and Structures*, 50(10):1770–1780, 2013. Cited on p. 69.

[121] S Adhikari. *Damping models for structural vibration*. PhD thesis, University of Cambridge, 2001. Cited on pp. 70 and 73.

[122] C Beards. *Structural vibration analysis*. John Wiley and Sons New York, 1983. Cited on pp. 70 and 73.

[123] HT Hahn and SW Tsai. *Introduction to composite materials*, volume 1. CRC Press, 1980. Cited on pp. 70 and 71.

[124] L Meirovitch. *Computational methods in structural dynamics*. Springer Science & Business Media, 1980. Cited on pp. 81, 86, 101, and 103.

[125] WT Thomas and MD Dahleh. *Theory of vibration with applications*. Prentice Hall, 1988. Cited on pp. 81, 87, 101, and 103.

[126] AH Nayfeh and B Balachandran. *Applied Nonlinear Dynamics: Analytical, Computational, and Experimental Methods*. Wiley-Interscience, NY, 1995. Cited on pp. 81, 82, 101, 106, and 109.

[127] P Ribeiro. Non-linear forced vibrations of thin/thick beams and plates by the finite element and shooting methods. *Computers & Structures*, 82(17):1413–1423, 2004. Cited on pp. 82, 89, 101, and 106.

[128] A Houmat. Nonlinear free vibration of laminated composite rectangular plates with curvilinear fibers. *Composite Structures*, 106:211–224, 2013. Cited on pp. 82, 91, and 92.

[129] P Ribeiro. Non-linear modes of vibration of thin cylindrical shells in composite laminates with curvilinear fibres. *Composite Structures*, 122:184–197, 2015. Cited on p. 82.

[130] M Amabili. Theory and experiments for large-amplitude vibrations of circular cylindrical panels with geometric imperfections. *Journal of Sound and Vibration*, 298(1):43–72, 2006. Cited on p. 82.

[131] C Camier, C Touzé, and O Thomas. Non-linear vibrations of imperfect free-edge circular plates and shells. *European Journal of Mechanics-A/Solids*, 28(3):500–515, 2009. Cited on p. 82.

[132] F Alijani, M Amabili, G Ferrari, and V D'Alessandro. Nonlinear vibrations of laminated and sandwich rectangular plates with free edges. part 2: Experiments & comparisons. *Composite Structures*, 105:437–445, 2013. Cited on pp. 82 and 107.

[133] N Nanda and S Pradyumna. Nonlinear dynamic response of laminated shells with imperfections in hygrothermal environments. *Journal of Composite Materials*, 45(20):2103–2112, 2011. Cited on p. 82.

[134] H Akhavan and P Ribeiro. Free geometrically nonlinear oscillations of perfect and imperfect laminates with curved fibres by the shooting method. *Nonlinear Dynamics*, pages 1–17, 2015. Cited on p. 82.

[135] M Amabili and JN Reddy. A new non-linear higher-order shear deformation theory for large-amplitude vibrations of laminated doubly curved shells. *International Journal of Non-Linear Mechanics*, 45(4):409–418, 2010. Cited on p. 83.

[136] M Amabili. A non-linear higher-order thickness stretching and shear deformation theory for large-amplitude vibrations of laminated doubly curved shells. *International Journal of Non-Linear Mechanics*, 58:57–75, 2014. Cited on p. 83.

[137] P Ribeiro. On the influence of membrane inertia and shear deformation on the geometrically non-linear vibrations of open, cylindrical, laminated clamped shells. *Composites Science and Technology*, 69(2):176–185, 2009. Cited on pp. 86 and 104.

[138] WH Press. *Numerical recipes 3rd edition: The art of scientific computing*. Cambridge university press, 2007. Cited on pp. 87, 88, 89, 90, 101, and 105.

[139] P Ribeiro. Periodic vibration of plates with large displacements. *AIAA Journal*, 40(1):185–188, 2002. Cited on pp. 88, 89, 101, and 106.

[140] A Bhimaraddi. Large amplitude vibrations of imperfect antisymmetric angle-ply laminated plates. *Journal of Sound and Vibration*, 162(3):457–470, 1993. Cited on p. 98.

[141] SM Ibrahim, BP Patel, and Y Nath. Modified shooting approach to the non-linear periodic forced response of isotropic/composite curved beams. *International Journal of Non-Linear Mechanics*, 44(10):1073–1084, 2009. Cited on p. 101.

[142] S Stoykov and S Margenov. Numerical computation of periodic responses of nonlinear large-scale systems by shooting method. *Computers & Mathematics with Applications*, 67(12):2257–2267, 2014. Cited on p. 101.

[143] RM Christensen. Stress based yield/failure criteria for fiber composites. *International Journal of Solids and Structures*, 34(5):529–543, 1997. Cited on p. 101.

[144] C Touzé, M Vidrascu, and D Chapelle. Direct finite element computation of non-linear modal coupling coefficients for reduced-order shell models. *Computational Mechanics*, 54(2):567–580, 2014. Cited on p. 101.

[145] O Weeger, U Wever, and B Simeon. Nonlinear frequency response analysis of structural vibrations. *Computational Mechanics*, 54(6):1477–1495, 2014. Cited on p. 101.

[146] F Boumediene, L Duigou, EH Boutyour, A Miloudi, and JM Cadou. Nonlinear forced vibration of damped plates coupling asymptotic numerical method and reduction models. *Computational Mechanics*, 47(4):359–377, 2011. Cited on p. 101.

[147] L-J Leu and C-H Tsou. Applications of a reduction method for reanalysis to nonlinear dynamic analysis of framed structures. *Computational Mechanics*, 26(5):497–505, 2000. Cited on p. 101.

[148] P Ribeiro and S Stoykov. Forced periodic vibrations of cylindrical shells in laminated composites with curvilinear fibres. *Composite Structures*, 2015. Cited on pp. 101 and 102.

[149] T Rahman, MM Abdalla, ST IJsselmuiden, and EL Jansen. Postbuckling analysis of variable stiffness composite panels using a finite element based perturbation method. In *ASME International Mechanical Engineering Congress and Exposition, Proceedings*, volume 10, pages 757–768, 2010. Cited on p. 102.

[150] MS Qatu. On the validity of nonlinear shear deformation theories for laminated plates and shells. *Composite Structures*, 27(4):395 – 401, 1994. Cited on pp. 102 and 121.

[151] H Akhavan and P Ribeiro. Non-linear forced periodic oscillations of laminates with curved fibres by the shooting method. *International Journal of Non-Linear Mechanics*, 76:176–189, 2015. Cited on p. 102.

[152] CK Chiang, C Mei, and CE Gray. Finite element large-amplitude free and forced vibrations of rectangular thin composite plates. *Journal of Vibration and Acoustics*, 113(3):309–315, 1991. Cited on pp. 106, 108, and 109.

[153] A Przekop and SA Rizzi. A reduced order method for predicting high cycle fatigue of nonlinear structures. *Computers & Structures*, 84(24):1606–1618, 2006. Cited on p. 114.

[154] W Han. *The analysis of isotropic and laminated rectangular plates including geometrical non-linearity using the P-version finite element method.* PhD thesis, University of Southampton, 1993. Cited on p. 129.

[155] P Ribeiro. *Geometrical nonlinear vibration of beams and plates by the hierarchical finite element method*. PhD thesis, University of Southampton, 1998. Cited on p. 129.

Index